Virtual chemical mechanisms optimized to capture pollutant formation in turbulent flames

Mélody Cailler

université PARIS-SACLAY

NNT : 2018SACLC084

CentraleSupélec

Virtual chemical mechanisms optimized to capture pollutant formation in turbulent flames

Thèse de doctorat de l'Université Paris-Saclay
préparée à CentraleSupélec

École doctorale n°579 : Sciences mécaniques et énergétiques, matériaux et géosciences (SMEMAG)
Spécialité de doctorat : Énergétique

Thèse présentée et soutenue à Gif-sur-Yvette le 08/10/2018, par

Mélody Cailler

Composition du Jury :

Perrine Pepiot Professeure, Cornell University	Rapporteur
Luc Vervisch Professeur, INSA de Rouen	Rapporteur
Ulrich Maas Professeur, Karlsruhe Institut of Technology	Président du jury
Olivier Colin Docteur, IFP Energies Nouvelles	Examinateur
Stéphane Richard Docteur, Safran Helicopter Engines	Examinateur
Lisa Bouheraoua Docteur, Safran Tech	Invitée
Benoît Fiorina Professeur, CentraleSupélec	Directeur de thèse
Nasser Darabiha Professeur, CentraleSupélec	Co-Directeur de thèse

Thèse de doctorat

Université Paris-Saclay
Espace Technologique / Immeuble Discovery
Route de l'Orme aux Merisiers RD 128 / 91190 Saint-Aubin, France

Remerciements

La rédaction de ces quelques lignes marque la fin d'une belle aventure, dont le dénouement a été possible grâce à de nombreuses personnes, que je souhaiterai remercier.

Je tiens tout d'abord à remercier l'ensemble des membres du jury pour avoir accepté d'évaluer mon travail de thèse. Je remercie Perrine Pepiot pour sa lecture attentive de mon manuscrit, son rapport détaillé et ses questions lors de la soutenance. Un grand merci également d'avoir fait le voyage depuis Cornell ! Je remercie Luc Vervisch d'avoir accepté de rapporter ma thèse. Merci pour les questions presque "philosophiques" qui m'ont permis une prise de recul essentielle sur mes travaux. Je remercie ensuite Ulrich Maas d'avoir lu mon manuscrit et présider le jury de la soutenance. Merci pour ses questions qui ont apporté une vision mathématique de l'approche de chimie virtuelle. Enfin, je remercie les examinateurs : Olivier Colin, Stéphane Richard et Lisa Bouheraoua d'avoir participer au jury. Merci d'avoir relu mon manuscrit, et merci pour vos questions et commentaires pendant la soutenance.

Je tiens ensuite à remercier Benoît Fiorina mon directeur de thèse. Avant tout, merci pour cette idée un peu folle : "partir d'une page blanche" pour construire petit à petit, après de nombreuses heures au tableau et discussions, un nouveau modèle : la "chimie virtuelle". Aussi, merci pour ton soutien continu et tes conseils qui m'ont beaucoup aidé à traverser ces 4 années. Enfin, merci pour la confiance que tu m'as accordée. Tu m'as en effet offert la possibilité de participer à plusieurs conférences, donner quelques cours, encadrer des projets et surtout tu m'as permis de travailler en collaboration avec tes doctorants, la désormais célèbre "Team Benoît" !

Un grand merci à tout le laboratoire EM2C qui aura été comme une deuxième famille pour moi. Mes remerciements vont naturellement à Nasser Darabiha pour sa gentillesse légendaire, sa disponibilité à toute épreuve (de longues heures passées derrière le mac) et naturellement pour Regath, code sans lequel la chimie virtuelle serait restée bien virtuelle ! Merci à Benedetta Franzelli pour avoir répondu à mes questions diverses et variées sur les schémas cinétiques, les flammes laminaires, le modèle TFLES, *etc*... Mais surtout, merci pour toutes les discussions sur la chimie virtuelle qui m'ont beaucoup aidé pour la rédaction du manuscrit et la préparation de la soutenance. J'ai une pensée toute particulière pour toute l'équipe de doctorants et post-doctorants que j'ai pu côtoyer pendant ces 4 années. J'ai partagé avec vous d'excellents moments qu'ils soient scientifiques, gustatifs, sportifs ou musicaux j'en garde de très bons souvenirs,

à renouveler sans modération ! Je tiens à remercier également tout le personnel administratif et informatique pour votre gentillesse et votre efficacité au quotidien.

Je souhaiterai aussi remercier toutes les personnes avec qui j'ai eu le plaisir de travailler à l'extérieur du laboratoire EM2C. Je remercie les équipes de choc qui contribuent au développement de deux grands codes AVBP et YALES2. Un merci spécial à Eléonore Riber et Bastien Rochette ainsi que Vincent Moureau et Patricia Domingo Alvarez qui m'ont accueilli au CERFACS et au CORIA pour des discussions passionnantes au sujet de l'énigmatique configuration Heron. Enfin, au cours de cette thèse, j'ai eu la chance de croiser le chemin d'un certain Renaud Mercier qui aura lui aussi œuvré au bon déroulement de ces 4 années. Merci pour ton investissement dans ces travaux, pour ta disponibilité, pour ton soutien et enfin pour ton enthousiasme constant.

Je profite de cette occasion pour remercier Vincent Brunet et Frédérique Feyel qui m'ont permis de finaliser mon manuscrit et préparer la soutenance dans les meilleures conditions. Aussi, un grand merci à l'ensemble de l'équipe CFD de Safran Tech pour m'avoir supporté et aidé pendant cette dernière année.

Enfin, je remercie toute ma famille et en particulier mes parents, ma sœur Mathilde et mon frère Pierre. Merci de m'avoir donné la possibilité d'arriver jusqu'ici. Merci pour votre soutien (quasi-journalier), vos encouragements permanents, vous avez été et êtes ma petite bulle d'oxygène.

Abstract

The conflicting nature of performance, operability and environmental constraints leads engine manufacturers to perform a fine optimization of the combustion chamber geometry to find the best design compromise. Large-Eddy Simulation (LES) is an attractive tool to achieve this challenging task and is routinely used in design office to capture macroscopic flow features. However, the prediction of phenomena influenced by complex kinetic effects, such as flame stabilization, extinction and pollutant formation, is still a crucial issue. Indeed, the comprehensive description of combustion chemistry effects requires the use of detailed models imposing prohibitive computational costs, numerical stiffness and difficulties related to model the coupling with unresolved turbulent scales. Reduced-cost chemistry description strategies must then be proposed to account for kinetic effects in LES of practical combustion chambers. In this thesis an original modeling approach, called virtual optimized chemistry, is developed. This strategy aims at describing the chemical flame structure and pollutant formation in relevant flame configurations, at a low computational cost. Virtual optimized kinetic schemes, composed by virtual reactions and virtual chemical species, are built through optimization of both kinetic rate parameters and virtual species thermo-chemical properties in order to capture reference target flame quantities.

Keywords: Chemical flame structure, Pollutant formation, Turbulent combustion, Large-Eddy Simulation, Virtual optimized chemistry.

Résumé

La nature conflictuelle des contraintes de performances, d'opérabilité et de respect des normes environnementales conduit les motoristes à optimiser finement la géométrie de la chambre de combustion afin d'identifier le meilleur design. La Simulation aux Grande Echelles (SGE) est aujourd'hui un outil performant et est déployé de manière courante dans les Bureaux d'Etudes pour la prédiction des propriétés macroscopiques des écoulements réactifs. Toutefois, la description des phénomènes influencés par les effets de chimie complexe, tels que la stabilisation, l'extinction de flamme et la formation des polluants, reste un problème crucial. En effet, la prédiction des effets de chimie complexe nécessite l'utilisation de modèles cinétiques détaillés imposant des coûts de calculs prohibitifs, des problèmes de raideur numérique et des difficultés de couplage avec les échelles non résolues turbulentes. Afin d'inclure une description des processus chimiques dans les simulations numériques de chambres de combustion industrielles des modèles réduits doivent être proposés. Dans cette thèse, une méthode originale, appelée chimie virtuelle optimisée, est développée. Cette stratégie a pour objectif la description de la structure chimique de la flamme et la formation des polluants dans des configurations de flamme représentatives. Les schémas cinétiques virtuels optimisés, composés de réactions virtuelles et d'espèces chimiques virtuelles, sont construits par optimisation des paramètres réactionnels et des propriétés thermo-chimiques des espèces virtuelles afin de capturer les propriétés de flamme d'intérêt.

Mots-clés: Structure de flamme, Prédiction des polluants, Combustion turbulente, Simulation aux Grandes Echelles, Chimie virtuelle optimisée.

Contents

List of publications

Peer-rewieved journals

- M. Cailler, N. Darabiha, and B. Fiorina, "Virtual chemistry for pollutant emissions prediction", Combustion and Flame, Under review.
- M. Cailler, N. Darabiha, D. Veynante and B. Fiorina, "Building-up virtual optimized mechanism for flame modeling", Proceedings of the Combustion Institute 36, Issue 1, 2017, Pages 1251-1258.
- G. Maio, M. Cailler, R. Mercier and B. Fiorina, "Virtual chemistry for temperature and CO prediction in LES of non-adiabatic turbulent flames", Proceedings of the Combustion Institute 37, In press.
- C. Mehl, M. Cailler, R. Mercier and V. Moureau, B. Fiorina, "Filtered optimized chemistry for Large Eddy Simulations of wrinkled flames", To be submitted.

Peer-rewieved conference publications

- M. Cailler, P. Domingo-Alvarez, V. Moureau, B. Fiorina, "Large-Eddy Simulation of Industrial Two-Phase Burner Using Virtual Optimized Chemistry", 57^{th} AIAA Aerospace Sciences Meeting, AIAA SciTech Forum, 2019, Submitted.
- M. Cailler, R. Mercier, V. Moureau, N. Darabiha, B. Fiorina, "Prediction of CO emissions in LES of turbulent stratified combustion using virtual chemistry", 55^{th} AIAA Aerospace Sciences Meeting, AIAA SciTech Forum, (AIAA 2017-0606).
- G. Maio, M. Cailler, R. Mercier, V. Moureau, B. Fiorina, "LES modeling of piloted jet flames with inhomogeneous inlets using tabulated chemistry methods", 55^{th} AIAA Aerospace Sciences Meeting, AIAA SciTech Forum, (AIAA 2017-1471).
- G. Maio, R. Mercier, M. Cailler, B. Fiorina, "Virtual chemistry for prediction of chemical flame structure in non adiabatic combustion", 8^{th} European Combustion Meeting, 2017.

Introduction

This PhD Thesis was co-supported by Safran Tech company and the Association Nationale Recherche Technologie (ANRT) under the grant CIFRE No. 2014/0701.

Challenges for the design of the next generation aeronautical combustion chambers

During the last 20 years, the world air traffic has increased considerably. The number of passengers more than doubled since 2000 to reach 4.0 billion in 2017, according to the International Civil Aviation Organization (ICAO). Moreover, this rising trend is expected to be heightened in the next 20 years (Fig. 1).

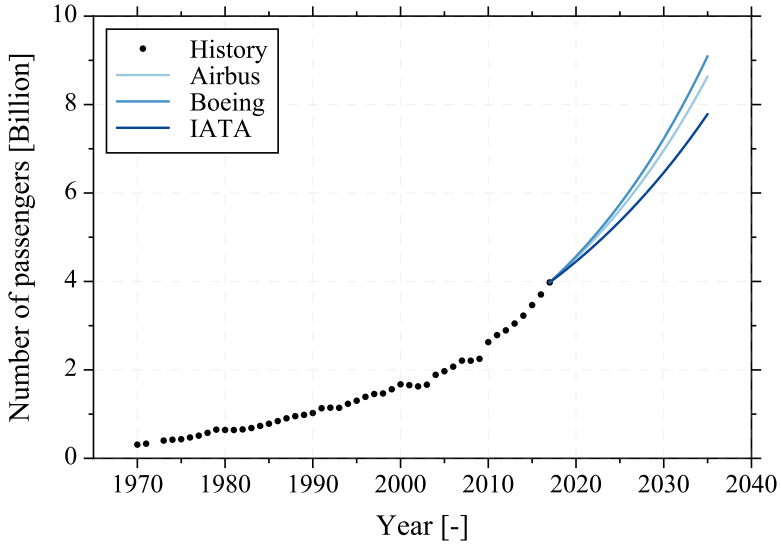

Figure 1: *Evolution and prediction of the number of passengers carried by air transport. Data collected from ICAO (2017) and forecasts provided by significant players of aeronautics: Airbus (2018), Boeing (2017) and IATA (2017).*

This vertiginous increase raises the important question of the environmental impact of civil aviation. Burnt gases issued from fossil fuels combustion include greenhouse gases (mainly CO_2) and pollutant species such as carbon monoxide (CO), nitrogen oxides (NO_x), sulfur oxides (SO_x) and soot particles whose

effects is detrimental for both environment (global warming, air quality deterioration, acid rains, visibility reduction) and human health (respiratory diseases, premature death). A thorough description of environmental and health effects due to jet aircraft emissions is provided in (United Stated Environmental Protection Agency 2018). Though aircraft traffic is currently responsible for only 3% of the total anthropogenic radiative forcing by all human activities, its relative contribution is predicted to grow significantly in the next decades because of the continuous increase of air traffic (see Fig. 2).

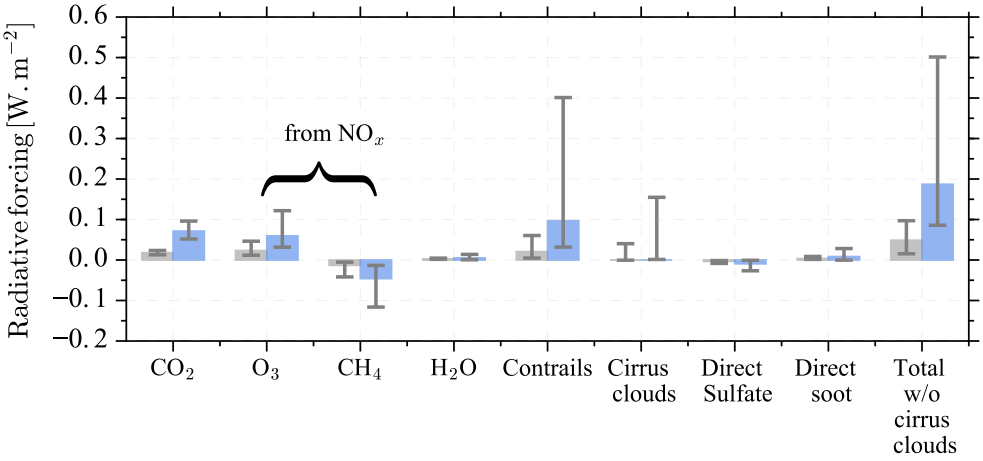

Figure 2: *Estimate of the perturbation to the energy balance of the Earth-atmosphere system (radiative forcing) due to air traffic. Positive values of radiative forcing imply a net warming, while negative values imply cooling. Grey lines correspond to the uncertainty range developed using the best knowledge and tools available. Adapted from (Penner et al. 1999).*

A first step towards limitation of aviation harmful impact was achieved by the ICAO in 1983 by establishing a technical committee aiming at formulating new policies regarding pollutant emissions. This organization regulates emissions of CO, NO_x, unburned hydrocarbons (HC_x) and smoke for a reference Landing and Take-Off (LTO) cycle. In 2001, the Advisory Council for Aviation Research and Innovation in Europe (ACARE) was created to establish a research agenda aiming at orienting the strategy for aeronautical developments. Following the first global objectives of the Vision 2020 program, a new set of targets has been defined for the horizon towards 2050. Concerning environment protection, the ACARE aims a 75 % reduction of CO_2 emissions, a 90 % decrease of NO_x emissions, and a reduction of perceived noise by 65 % (Flightpath 2011).

Main levers to achieve emissions constraints imposed by these norms is to optimize the propulsion system design and develop innovative technologies. However, in addition to environmental objectives, engine manufacturers must fulfill performance and operability requirements to provide an efficient and safe

burner (Lefebvre 2010). The main constraints that a combustor should satisfy are summarized in Table 1. An important issue raised when designing a combustor is related to the incompatibility between design objectives. For instance, solutions aiming at reducing NO_x formation may lead to the degradation of thermal efficiency, the increase in fuel consumption or the onset of thermo-acoustic instabilities. The conflicting nature of the performance, environmental and operability constraints leads engine designers to perform a fine optimization of the burner geometry to find the best compromise.

Performance requirements	**Operability requirements**
• High combustion efficiency	• Wide combustion stability limit
• Low pressure loss	• Reliable ignition in severe conditions
• Low fuel consumption	• Efficient altitude relight
• Efficient wall cooling	• Stable thermo-acoustic behavior
• Low noise levels	
• High lifespan	
• Good compactness	
• Low cost maintenance	
• **Low pollutant emissions**	

Table 1: *Performance and operability requirements for aeronautical engines.*

Numerical simulations an essential tool

Engine optimization design relies on three main tools intervening in the various stages of the development cycle:

- During the **pre-design step**, **0-D and 1-D models** are used to define the combustor shape, the cooling systems, and injectors characteristics so that global performance targets are satisfied. These tools, generally based on correlations (Lefebvre 2010; Mongia 2010) calibrated on experimental data, are very efficient for the prediction of global quantities in steady-state conditions.

- In a second stage, more **refined definition and validation** of the combustion chamber organs are performed through **experimental tests** and **3-D simulations**.
  Experimental measurements mainly rely on visualization, optical diagnostics and more basic systems such as thermocouples or gas analyzers. Data issued from measurement campaigns provide a reliable description of physical processes, and as such, are considered as reference. However, measurement techniques face numerous difficulties including: issues to set up in severe conditions, calibration problems and high costs. In addition,

experiments only provide a reduced number of flow (velocity components) and flame (major species, temperature) quantities on very limited spatial regions. Eventually, as experimental campaigns cannot be performed in flight conditions extrapolations of the measurements must be done to evaluate the engine behavior in real operating conditions.
On the other side, numerical simulations, based on the resolution of the governing flow equations, are generally less expensive, give access to an unsteady and complete description of all transported variables, and can be used to assess combustion chambers at high pressure and high temperature conditions. Nevertheless, their degree of predictivity and representativity strongly depends on the models used.
In practice, these two complementary strategies are used jointly to evaluate combustion efficiency, pollutant emissions, combustor exit temperature distribution, ignition and extinction limits.

- Finally, full engine performance and operability limits are **certified** on **test rigs** in representative conditions.

In the recent years, the combined increase in computational power and the progress in turbulent combustion modeling make the simulations a continuously more attractive tool. Today, simulations are used to guide the technological decisions by, for instance, studying the influence of combustion chamber components on the design objectives. It is also used to gain a better understanding of the complex non-stationary phenomena occurring in the combustion chamber.
Though numerical simulations appear as an efficient tool to guide the design of the next generation combustors, they should also face the challenges of predictivity and representativity at the lowest cost.

Challenges for numerical simulations

Turbulent flames encountered in aeronautical combustion chambers, and more generally in industrial devices, result from complex interactions between several phenomena including: spray break-up, evaporation, turbulent mixing, combustion chemistry and heat transfer. Figure 3 gives a simplified representation of the physical processes involved in turbulent combustion. The liquid fuel is injected in a swirled air environment where it undergoes instabilities leading to the break-up of the film into fine liquid ligaments. Due to air entrainment and destabilizing aerodynamic forces the ligaments are then divided into liquid droplets of varying size and velocity. The heat conducted from the flame induces pre-heated air and spray temperature increase leading to the evaporation of the liquid droplets. The newly-formed gaseous fuel is then mixed with air to form a partially-premixed reactive flow that feeds the flame front with fresh gases. In this zone, thousands of elementary reactions convert the reactive mixture into radical and intermediate species that are subsequently transformed

into final combustion products, namely CO_2, H_2O, CO, NO_x, soot precursors (PAH), and unburnt hydrocarbons. In addition to two-phase flow and kinetics effects, heat exchanges between the flow and the combustion chamber walls take place and affect the flame stabilization processes.

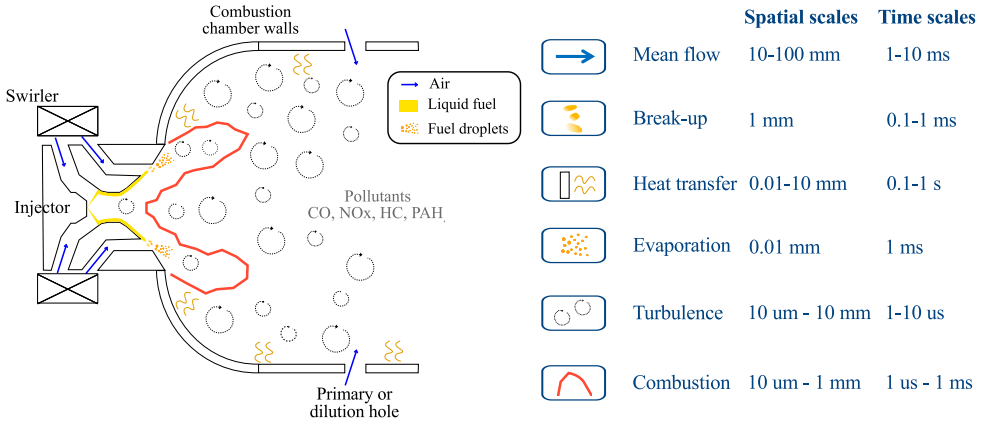

Figure 3: *Schematic representation of the physical phenomena observed in a combustion chamber. Characteristic spatial and time scales associated with each phenomenon are indicated on the right. Reproduced from (Richard 2015).*

All these strongly coupled phenomena feature a wide variety of spatial scales (see Fig. 3). As an example, fast reactions are characterized by thicknesses of less than ten microns, while liquid break-up and droplets transport occur on larger length scales of the order of the millimeter. Turbulence itself, due to its high intensity, exhibits a large spectrum of space scales ranging from the integral length scale of about 100 mm to the smallest eddy whose size is *circa* 10 μm. Physical phenomena occurring in a combustion chamber also present a great variability of time scales. For instance, combustion covers a wide range of time scales going from a few microseconds for radical species net production, to several milliseconds for slow NO_x chemistry.

The multi-physical character of the flow and the high disparity of both space and time scales, lead to a complex system of transport equations that requires highly refined meshes and very small timesteps. Unfortunately, the available computational resources are not sufficient to solve such a system. It is then necessary to simplify the set of equations by deriving mathematical models neglecting the less important phenomena and reliably describing the dominant ones.

If two-phase flow and heat transfer have definitely an impact on the overall behavior of the combustion chamber, the interactions between chemical combustion and flow dynamics are fundamental phenomena and therefore must be properly modeled.

Kinetic combustion modeling

Though turbulent combustion has received important interest in the scientific community, the modeling of turbulent reacting flows is still an open problem. Turbulent combustion models must indeed provide a reliable representation of the chemical processes transforming reactants into products, and their interactions with turbulent eddies.
As previously mentioned, combustion chemistry itself is a highly complex and non-linear phenomenon involving a large number of degree of freedoms. A precise and comprehensive description of the reacting chemical system may be achieved by using the so-called detailed kinetic schemes, involving hundreds of species and thousands of reactions. Unfortunately, the application of such detailed models in 3-D simulations of real scale configurations is prohibitive. The computational cost associated with the resolution of species transport equations, the numerical stability problems due to reaction rates stiffness and the potential modeling issues related to the coupling with turbulence limit the use of detailed schemes to simple configurations and light fuels. To take into account kinetic effects in simulations of real combustion chambers, various reduced-cost chemistry description strategies have been proposed in the literature:

- **Global and semi-global mechanisms** constitute one of the simplest descriptions of chemical effects. Semi-global kinetic schemes are generally based on 5 to 8 major species interacting through 1 to 4 global reactions. These reduced kinetic models, built to reproduce global flame properties such as laminar flame speed or auto ignition delay (Westbrook and Dryer 1981; Jones and Lindstedt 1988; Franzelli et al. 2010), are widely used for their low computational costs and relatively easy coupling with turbulence. However, global schemes are valid on a limited range of operating conditions and are not able to capture pollutant species formation processes. In addition, as global schemes are optimized to a specific combustion regime they fail to capture the chemical structure of complex flames encountered in practical combustion chambers.

- **Tabulated chemistry strategies** assume that the flame structure can be parametrized by a reduced set of control parameters (Peters 1984; Gicquel et al. 2000; Van Oijen et al. 2001; Pierce and Moin 2004). The chemical response of canonical problems (premixed, non-premixed, burner stabilized flames, *etc*) is stored in a chemical database as a function of representative variables. Though only 2 to 3 scalars are transported, tabulated chemistry allows the description of intermediate and pollutant species. If tabulated chemistry is very efficient when applied in simple configurations, it however raises numerous modeling issues (choice of the prototype flamelet and control variables, closure of trans-

port equations) and practical difficulties (storage issues) when used in real configurations. Indeed, the extension of tabulated chemistry capabilities in complex configurations requires the tabulation of additional flamelet solutions and the increase of the number of control variables.

- **Analytically-reduced mechanisms** are derived through a chemistry-driven approach consisting in i) eliminating redundant species and reactions of a detailed mechanism (Vajda et al. 1985; Lu and Law 2005; Pepiot-Desjardins and Pitsch 2008) and ii) applying Quasi-Steady State Approximation (QSSA) (Lam and Goussis 1994; Lepage 2000; Løvås et al. 2000). These mechanisms, composed by 10 to 40 species (depending on the fuel complexity), provide an accurate description of the flame structure and intermediate species on a wide range of conditions (Luche 2003; Lu and Law 2008). Moreover, as analytic schemes retain real chemical pathways, they can be used outside of the operating domain targeted during the reduction procedure (Felden 2017). Recently, the LES of the swirled SGT-100 burner demonstrated the capabilities of analytic chemistry to capture CO and NO_x emissions (Jaravel et al. 2017). Unfortunately, the computational cost associated with this methodology increases rapidly with the number of species transported. Analytically-reduced schemes also involve a wide range of chemical time scales that may lead to numerical stiffness and difficulties to model the coupling with turbulent structures.

- **Optimized reduced mechanisms** are generated through a fully automated procedure relying on i) the identification of chemical trajectories accessed in the target configuration, ii) the application of classical chemical reduction methods and iii) the optimization of reaction rate parameters (Jaouen et al. 2017). Since reduction and optimization procedure only target the chemical trajectories encountered in the simulated configuration, the size of the optimized reduced mechanisms is reduced in comparison with classical chemistry-driven reduction strategies. Unfortunately, the questions of the cost associated with the prediction of heavy molecules, and the coupling with turbulent flows are still unanswered.

This brief state of the art of the current chemistry description strategies motivates the development of an alternative method that would address the main limitations mentioned above. In this thesis a new modeling approach, called virtual optimized chemistry, has been therefore developed to describe quantities of interest such as flame temperature and pollutants at a reduced computational cost.

Contributions of the thesis

- **Development of a reduced-cost chemistry description approach:** An original chemistry description approach aiming at capturing selected flame properties (heat release, pollutant species) on a range of representative flame configurations is proposed. This new strategy, called virtual optimized chemistry, relies on virtual optimized mechanisms composed of virtual reactions and virtual species. Thermo-chemical properties of the virtual species and reaction rate parameters of the virtual reactions are optimized with the objective to reproduce the reference flame variables of interest on the targeted flame archetypes. Virtual mechanisms architecture is based on various sub-mechanisms dedicated to the prediction of a given flame property. In this thesis, a strategy is developed to derive i) main virtual schemes dedicated to retrieve flame temperature and ii) satellite-mechanisms devoted to CO formation description.

- **Numerical simulation of laminar premixed and non-premixed flames:** the virtual optimized chemistry approach has been then implemented in both the premixed and counter-flow solvers of the in-house laminar flow package REGATH (Darabiha and Candel 1992). The 1-D laminar flow codes are used to generate virtual premixed and non-premixed flame solutions for the optimization procedure and a-posteriori validations. The virtual chemistry approach was compared to main chemical description strategies in terms of predictive capabilities, numerical stiffness and computational cost.

- **Development of an optimization tool:** a constrained multi-objective optimization program has been developed to train the virtual reduced mechanisms to capture targeted flame properties of a reference flamelet library. This optimization tool, relying on an evolutionary algorithm, was coupled to the REGATH thermo-chemistry package to allow the evaluation of the solution fitness.

- **Large-Eddy Simulations of gaseous and two-phase turbulent burners:** the virtual optimized chemistry concept has been implemented in two official releases of the massively-parallel and compressible LES solver AVBP, co-developed at CERFACS and IFPEN (Schönfeld and Rudgyard 1999). The capabilities of the virtual kinetic mechanisms to capture the flame stabilization and dynamics as well as CO concentration was then assessed on two laboratory-scale gaseous turbulent combustors. The virtual optimized chemistry approach was finally applied to a two-phase industrial test-rig.

Outline of the manuscript

This manuscript is organized in four parts:

Part I

The first part discusses the difficulties raised by modeling reacting flows and draws a state of the art of the chemistry modeling strategies. In Chapter 1 governing equations for reacting flows and the challenges related with the closure of dominant phenomena are presented. Also, general concepts on canonical flame archetypes and on combustion regimes encountered in real applications are discussed. Chapter 2 reviews the main strategies used for chemistry description and discusses their applicability.

Part II

A new approach to describe kinetic effects at a reduced computational cost, called virtual optimized chemistry, is introduced. In Chapter 3, the concept of virtual mechanism is presented, and the methodology to build-up virtual optimized models dedicated to the capture of a given flame property is detailed. Chapter 4 concerns the application and validation of the newly developed approach. The virtual optimized approach is first applied to atmospheric methane/air combustion. Resulting virtual optimized schemes are subsequently validated on 1-D laminar flames and 2-D laminar burners. The performances of the virtual model in terms of prediction, computational cost, stiffness and robustness are compared against detailed, analytically-reduced, global and tabulated chemistry. Extension of the virtual optimized chemistry approach to aeronautical fuel is also presented.

Part III

The third part of this manuscript concentrates on the application of the virtual optimized strategy in turbulent configurations. Chapter 5 briefly introduces the difficulties associated with turbulent combustion modeling and presents the coupling of virtual optimized strategy with the Thickened Flame model for LES (TFLES) (Colin et al. 2000). Chapter 6 demonstrates the applicability of virtual optimized chemistry in two gaseous turbulent flame configurations. The premixed swirled combustor PRECCINSTA (Meier et al. 2007) serves as first test case to validate the coupling between virtual optimized chemistry and the Thickened Flame turbulent model. The Cambridge burner (Sweeney et al. 2011) is then simulated to assess the model capabilities to predict flame stabilization and CO formation in a stratified jet flame.

Part IV

In this last part, a focus is made on the application of the virtual optimized chemistry model in a two-phase flow environment. The modeling approach used to describe the dispersed phase dynamics and evaporation is described in Chapter 7. In Chapter 8 virtual kinetic schemes are then coupled with the TFLES model (Colin et al. 2000) and classical two-phase flow closures to be subsequently tested on the high pressure HERON test benchÂ (Salaün et al. 2016), experimentally investigated at CORIA laboratory. A particular attention is given to the capabilities of the virtual optimized approach to capture flame shape and stabilization.

Part I

Modeling of reacting flows

Chapter 1

Reacting flow modeling challenges

Contents

The objective of this chapter is to introduce the reader with the theoretical concepts and the challenges associated with the modeling of reacting flows. First, the governing balance equations for reacting flows are presented. As transport and kinetic phenomena are of paramount importance, a specific attention is given to the modeling of these two contributions. Then, general and essential concepts on flame regimes are discussed. After a brief introduction on the canonical flame archetypes used for chemistry modeling, the flame regimes encountered in real turbulent applications are analyzed. As the developed kinetic models are intended to be used in industrial burners, the combustion modes to consider during chemical model derivation must be properly identified.

1.1 Mathematical formalism

1.1.1 Governing equations

Under the hypothesis of continuous medium, the dynamics of a non-reacting flow is described by the Navier-Stokes equations. These equations are obtained by applying conservation laws of mass, momentum and energy to an elementary volume of fluid particles. The resolution of the system of equations enables the evaluation of the macroscopic flow properties such as velocities, temperature and pressure. When dealing with reacting flows, additional species conservation equations are required to account for the mixture composition variations due to chemical reactions and species diffusion. The full set of exact governing flow equations is hereinafter presented. The Einstein summation convention is used except for the k index referring to the k^{th} species of the mixture.

Mass balance equation
The equation for total mass conservation reads:

$$\frac{\partial \rho}{\partial t} + \frac{\partial}{\partial x_i}\left(\rho u_i\right) = 0 \tag{1.1}$$

where ρ is the mixture density and $\mathbf{u}\left(u_1, u_2, u_3\right)$ is the velocity vector.

Momentum balance equation
Conservation of momentum gives:

$$\frac{\partial \rho u_j}{\partial t} + \frac{\partial}{\partial x_i}\left(\rho u_i u_j\right) = \frac{\partial \sigma_{ij}}{\partial x_i} + \rho \sum_{k=1}^{N_s} Y_k f_{k,j} \tag{1.2}$$

where N_s is the total number of species included in the mixture and $f_{k,j}$ denotes the exterior volume force acting on species k in the j^{th} direction. The stress tensor σ_{ij} is the sum of a pressure and viscous tensor τ_{ij}:

$$\sigma_{ij} = -P\delta_{ij} + \tau_{ij} \tag{1.3}$$

where P denotes the static pressure, and δ_{ij} stands for the Kronecker symbol equal to unity if $i = j$ and zero otherwise. In combustion applications, as fluids are considered as Newtonian, the viscous contribution of the stress tensor is linearly proportional to the local rate of deformation:

$$\tau_{ij} = \left(\kappa - \frac{2}{3}\mu\right)\frac{\partial u_l}{\partial x_l}\delta_{ij} + \mu\left(\frac{\partial u_i}{\partial x_j} + \frac{\partial u_j}{\partial x_i}\right) \tag{1.4}$$

where κ is the volume viscosity and μ is the dynamic shear viscosity.

Species balance equation

The conservation equation for each species k considered in the mixture is given by:

$$\frac{\partial \rho Y_k}{\partial t} + \frac{\partial}{\partial x_i}\left(\rho Y_k u_i\right) = -\frac{\partial}{\partial x_i}\left(\rho Y_k V_{k,i}\right) + \dot{\omega}_k \tag{1.5}$$

where Y_k refers to the k^{th} species mass fraction, $V_{k,i}$ stands for the ith component of the diffusion velocity vector $\mathbf{V_k}\left(V_{k,1}, V_{k,2}, V_{k,3}\right)$ of the species k, and $\dot{\omega}_k$ refers to species reaction rate. The total mass conservation given in Eq. (1.1), ensures the two following relations:

$$\sum_{k=1}^{N_s} Y_k V_{k,i} = 0 \quad \text{and} \quad \sum_{k=1}^{N_s} \dot{\omega}_k = 0 \tag{1.6}$$

The molecular diffusion processes result from four contributions: i) species concentration gradients (direct effect), ii) pressure gradient (barodiffusive effect), iii) temperature gradient (Soret or thermodiffusion effect) and iv) species affected by different external forces. The kinetic theory of gases, leads to the general form of the diffusion velocity vector $\mathbf{V}_k$ (Ern and Giovangigli 1994):

$$\mathbf{V}_k = \sum_{l=1}^{N_s} D_{kl}^{MC} \mathbf{d}_l - D_k^T \frac{\nabla T}{T} \tag{1.7}$$

where D_{kl}^{MC} is the multi-component diffusion coefficient for the species pair (k,l). This term is non-linearly dependent on all the state variables $\psi = \{Y_1, ..., Y_{N_s}, T, P\}$. The thermal diffusion coefficient of species k is defined as $D_k^T = \sum_{l=1}^{N_s} D_{k,l}^{MC} \xi_l$, where ξ_l is the thermal diffusion ratio of species l. The species diffusion driving forces vector $\mathbf{d}_l$ is given by:

$$\mathbf{d}_l = \nabla X_l + \left(X_l - Y_l\right)\frac{\nabla P}{P} + \frac{\rho}{P}\sum_{m=1}^{N_s} Y_l Y_m \left(\mathbf{f}_m - \mathbf{f}_l\right) \tag{1.8}$$

where $X_k = (Y_k W)/W_k$ refers to the mole fraction of species k, with W_k the molecular weight of species k and W the mean molecular weight of the mixture.

Energy balance equation

Multiple forms of energy conservation equations can be written depending on the variable used to describe energy (see Table 1.1). When the total energy e_t is considered, the energy conservation equation expresses as:

$$\begin{aligned}\frac{\partial \rho e_t}{\partial t} + \frac{\partial}{\partial x_i}\left(\rho u_i e_t\right) = &-\frac{\partial q_i}{\partial x_i} + \frac{\partial}{\partial x_j}\left(\sigma_{ij} u_i\right) + \dot{Q} \\ &+ \rho \sum_{k=1}^{N_s} Y_k f_{k,i}\left(u_i + V_{k,i}\right)\end{aligned} \tag{1.9}$$

where $\dot{Q}$ is an external heat source term due for instance to radiative flux or electrical energy deposition. The energy flux q_i is the sum of three contributions given by:

$$q_i = -\lambda \frac{\partial T}{\partial x_i} + \rho \sum_{k=1}^{N_s} (h_k Y_k V_{k,i}) + P \sum_{k=1}^{N_s} (\xi_k V_{k,i}) \tag{1.10}$$

where h_k is the sensible chemical enthalpy of species k. The first term of the energy flux vector describes heat diffusion through Fourrier's Law ($\lambda \partial T / \partial x_i$) with λ the thermal conductivity. The second contribution is associated with the diffusion of species with different enthalpies. Eventually, the last term accounts for the Dufour heat flux induced by concentration gradients.

Form	Enthalpy	Energy
Sensible	$h_s = \int_{T_0}^{T} c_p(T')\, dT'$	$e_s = \int_{T_0}^{T} c_v(T')\, dT' - P/\rho$
Sensible chemical	$h = h_s + \sum_{k=1}^{N_s} \Delta h^0_{f,k} Y_k$	$e = e_s + \sum_{k=1}^{N_s} \Delta h^0_{f,k} Y_k$
Total chemical	$h_t = h + \frac{1}{2} u_i u_i$	$e_t = e + \frac{1}{2} u_i u_i$
Total non chemical	$H = h_s + \frac{1}{2} u_i u_i$	$E = e_s + \frac{1}{2} u_i u_i$

Table 1.1: *Enthalpy and energy variables used in conservation equations. c_p and c_v denote the specific heat capacity at constant pressure and constant volume respectively, while $\Delta h^0_{f,k}$ is the standard enthalpy of formation of the species k at the reference temperature T_0. The mixture-averaged thermodynamic properties $\psi = \{h, e, c_p, c_v\}$ are given by the mixing law: $\psi = \sum_{k=1}^{N_s} \psi_k Y_k$.*

Summary

The exact system of equations previously introduced may be simplified by neglecting terms having a low impact on the flow dynamics. The following assumptions will be used all along the thesis:

- Volume viscosity phenomena associated with relaxation effects between translational and other degrees of freedom of the molecule are neglected.
- External forces are supposed small compared to non-stationary, convective and diffusive terms.
- The diffusion of mass due to temperature gradients is non accounted for. However Soret effects may be important especially when light radicals such as H or H_2 play a major.
- Pressure induced species diffusion is neglected.
- The impact of concentration gradients on heat diffusion is considered negligible. Though its symmetric effect, the Soret effect can be non negligible in particular condition, the Dufour effect is generally reported as very low.

- The heat source term in the energy conservation equation is neglected as no external heat source is considered in this thesis.

The simplified set of equations recast as:

$$\begin{aligned}
&\frac{\partial \rho}{\partial t} + \frac{\partial}{\partial x_i}\left(\rho u_i\right) = 0 \\
&\frac{\partial \rho u_j}{\partial t} + \frac{\partial}{\partial x_i}\left(\rho u_i u_j\right) = -\frac{\partial P}{\partial x_j} + \frac{\partial \tau_{ij}}{\partial x_i} \\
&\frac{\partial \rho Y_k}{\partial t} + \frac{\partial}{\partial x_i}\left(\rho Y_k u_i\right) = -\frac{\partial}{\partial x_i}\left(\rho Y_k V_{k,i}\right) + \dot{\omega}_k \\
&\frac{\partial \rho e_t}{\partial t} + \frac{\partial}{\partial x_i}\left(\rho u_i e_t\right) = \frac{\partial}{\partial x_i}\left(\lambda \frac{\partial T}{\partial x_i} - \rho \sum_{k=1}^{N_s} Y_k V_{k,i} h_k\right) + \frac{\partial}{\partial x_i}\left(\sigma_{ij} u_j\right)
\end{aligned} \tag{1.11}$$

To close this system, an equation of state relating state variables is required. The mixture and its components are assumed to follow the perfect gas law. This equation of state relates temperature, pressure and density through the following expression:

$$P = \rho r T \tag{1.12}$$

where the specific gas constant of the mixture r is given by:

$$r = \frac{R}{W} = R \sum_{k=1}^{N_s} \frac{Y_k}{W_k} = \sum_{k=1}^{N_s} Y_k r_k \tag{1.13}$$

where $R = 8.314\,\mathrm{J.mol^{-1}.K^{-1}}$ is the universal gas constant, and r_k is the specific gas constant of species k.
In what follows, the modeling of transport properties (subsection 1.1.2), and kinetic effects (subsection 1.1.3) are described.

1.1.2 Transport properties modeling

Transport properties may be evaluated through four strategies featuring different level of complexity and accuracy. The multi-component approach based on the kinetic theory of gases is the most accurate and the most CPU demanding. The evaluation of the multi-component coefficients requires to solve a linear system of size $\propto (N_s \times N_s)$ in each direction, at each computational node and at each numerical iteration (Dixon-Lewis 1968; Coffee and Heimerl 1981). To decrease the computational cost associated with the direct resolution of this system of equations, Ern and Giovangigli (1994) proposed to iteratively solve a truncated system so as to identify approximate transport coefficients. This first order approximation of the multi-component transport coefficients allows an important reduction of the computational costs but is rarely used in simulation of practical configurations. Mixture-averaged approximations constitute the third category of transport model. This approach, based on mixing laws, is

often preferred to multi-component transport models for its relatively low cost, easy implementation and satisfactory predictive capabilities. Eventually, simplified low-cost models relying on empirical laws and dimensionless transport numbers are classically employed (Poinsot and Veynante 2012).
If the modeling of kinetic effects is of paramount importance to properly capture flame stabilization and the chemical flame structure, the transport properties also play a major role in combustion systems (Ern and Giovangigli 1998; Hilbert et al. 2004; Barlow et al. 2012). In this thesis both mixture-averaged and simplified models are considered to describe transport properties. Mixture-averaged assumptions will be used in combination with detailed reference kinetic schemes, while simplified approaches will be considered with reduced chemistry description strategies. These models are described in more details hereinafter.

1.1.2.1 Mixture-averaged properties

The mixture viscosity μ may be evaluated from individual species viscosities μ_k through the Wilke's formula (Wilke 1950):

$$\mu = \sum_{k=1}^{N_s} \frac{X_k \mu_k}{\sum_{l=1}^{N_s} X_l \tilde{\psi}_{kl}} \quad \text{with } \tilde{\psi}_{kl} = \frac{1}{\sqrt{8}} \frac{1}{\sqrt{1+\frac{W_k}{W_l}}} \left(1+\sqrt{\frac{\mu_k}{\mu_l}}\left(\frac{W_k}{W_l}\right)^{\frac{1}{4}}\right)^2 \tag{1.14}$$

or through a polynomial empirical approximation:

$$\mu = \frac{1}{2}\left[\sum_{k=1}^{N_s} X_k \mu_k + \frac{1}{\sum_{k=1}^{N_s} X_k/\mu_k}\right]. \tag{1.15}$$

If both formulations lead to a reasonable agreement with multi-component transport properties, the Wilke's law is more CPU demanding.
The mixture-averaged thermal conductivity λ is evaluated using the polynomial empirical approximation proposed by Mason and Saxena (1958):

$$\lambda = \frac{1}{2}\left[\sum_{k=1}^{N_s} X_k \lambda_k + \frac{1}{\sum_{k=1}^{N_s} X_k/\lambda_k}\right] \tag{1.16}$$

The zeroth-order approximation to the exact multi-component diffusion coefficients was proposed by Hirschfelder et al. (1954). This model uses an equivalent diffusion coefficient D_k describing the diffusion of the species k in the rest of the mixture. The diffusion velocity vector of the species k is then given by:

$$\mathbf{V}_k^* = -\frac{D_k}{X_k}\nabla X_k \quad \text{with} \quad D_k = \frac{1-Y_k}{\sum_{l\neq k}^{N_s} X_l/D_{lk}}. \tag{1.17}$$

Contrarily to the exact multi-component formulation, the Hirschfelder and Curtiss approximation does not ensure mass conservation. A correction velocity vector $\mathbf{V}^c$ is therefore introduced:

$$\mathbf{V}_k = \mathbf{V}_k^* + \mathbf{V}^c \quad \text{with } \mathbf{V}^c = -\sum_{k=1}^{N_s} Y_k \mathbf{V}_k^*. \tag{1.18}$$

An alternative to the Hirschfelder and Curtiss approach is the Fick's Law. This approximation assumes that the diffusion vector of the species k is directly proportional to its mass fraction gradient:

$$\mathbf{V}_k = -\frac{D_k}{Y_k}\nabla Y_k + \mathbf{V}^c \quad \text{with } \mathbf{V}^c = \sum_{k=1}^{N_s} D_k \nabla Y_k. \tag{1.19}$$

This model can be derived from Hirschfelder and Curtiss approximation by assuming that the mean molecular weight of the mixture is constant in space.

The single component properties μ_k, λ_k and binary diffusion coefficients D_{kl} are given by the standard kinetic theory. These transport coefficients depend on temperature and on molecular parameters such as the collision integrals, dipole moment or the Lennard-Jones potential well depth. The collision integrals are tabulated from the calculations of Monchick and Mason (1961), while the other molecular coefficients are given in reference databases (Kee et al. 1986).
Though the mixture-averaged is only a zeroth-order approximation of the exact equations, the computational cost required for the calculation of species diffusion coefficients is important, it scales with the number of species squared.

1.1.2.2 Simplified models

Simple analytic laws have been developed to evaluate the mixture viscosity at a very low computational cost. These models assume that the viscosity of the gaseous mixture does not depend on the gas composition, but only on the mixture temperature. The most common formulations are:

- The Sutherland (1893) law:

$$\mu = \mu_{ref} \left(\frac{T}{T_{ref}}\right)^{3/2} \left(\frac{T_{ref} + S}{T + S}\right) \tag{1.20}$$

  where μ_{ref} is the viscosity of the mixture at the reference temperature T_{ref} and S is the Sutherland temperature.

- The power law:

$$\mu = \mu_{ref} \left(\frac{T}{T_{ref}}\right)^{\beta} \tag{1.21}$$

  where μ_{ref} is the viscosity of the mixture at the reference temperature T_{ref}, and β stands for the power law constant.

In premixed fuel/air mixtures, as nitrogen is largely dominant, the use of such simple approximations induces very small errors. However important discrepancies are expected when dealing with non-premixed mixtures because the composition varies dramatically between pure fuel and pure oxidizer.
To alleviate the cost associated with thermal conductivity evaluation, simplified transport models assume that the molecular Prandtl number Pr is constant in space and time. Following this hypothesis, the heat conduction coefficient λ is computed as:

$$\lambda = \frac{\mu c_p}{\mathrm{Pr}} \qquad \text{with } \mathrm{Pr} = \mathrm{Pr}_0 = cst \tag{1.22}$$

This assumption is justified by the fact that the Prandtl number is almost constant through the flame front of a premixed flame. Figure 1.1, illustrating the evolution of the Prandtl number across a stoichiometric methane/air premixed flame front, shows that the Prandtl number varies by only a few percents between fresh (Pr_{FG}=0.705) and burnt gases (Pr_{BG}=0.689) states.

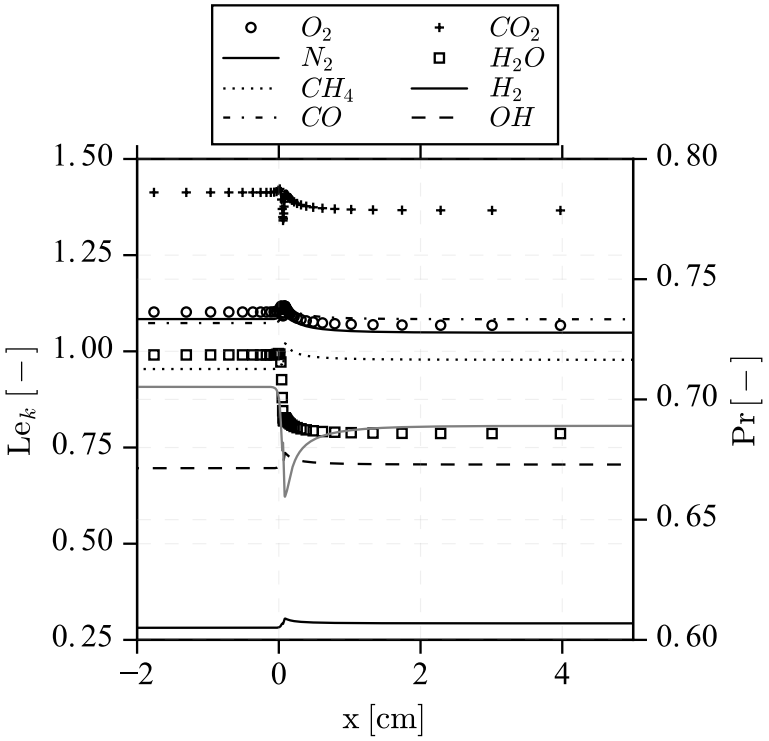

Figure 1.1: *Dimensionless transport coefficients evolution in a freely-propagating laminar premixed stoichiometric CH_4/air flame. The Lewis numbers of major species (black lines and symbols) and the Prandtl number (grey line) vary by small amounts through the flame front.*

Species Lewis numbers Le_k, comparing conductive and diffusive transport phe-

nomena, are also plotted in Fig. 1.1. Similarly as Prandtl number, it is observed that species Lewis numbers vary by small amount between fresh and burnt gases. If the Lewis numbers Le_k of the species k is assumed constant, the diffusion coefficient is given by:

$$D_k = \frac{\lambda}{\rho c_p \mathrm{Le}_k} = \frac{\mu}{\rho \mathrm{Pr} \mathrm{Le}_k} \tag{1.23}$$

As a consequence, the diffusion coefficients D_k are simply evaluated from the heat diffusion coefficient. As long as the constant species Lewis numbers are properly estimated and a sufficient numbers of species are involved in the mixture, this simple approach allows to take into account differential diffusion effects between species, at a reduced computational cost (Vié et al. 2015; Jaravel 2016).
Even simpler model assumes that the species diffusion coefficients are all equal to the thermal one.

1.1.3 Introduction to chemistry modeling

To finally close the system of equations (1.11), the species source terms $\dot{\omega}_k$ due to combustion need to be modeled. This *a priori* simple but fundamental term is in reality the outcome of a complex succession of chemical reactions involving a large number of species. Chemical kinetic studies, aiming at identifying the chemical reaction pathways transforming fuel and oxidizer into combustion products, allows the derivation of detailed kinetic models describing the processes of production and consumption of chemical species. These models rely on both the results of kinetic theory of gases and thermodynamics.
Before presenting general characteristics of hydrocarbon/air combustion, the main results of kinetic theory are first briefly described.

1.1.3.1 Chemical kinetics

A reactive system composed by N_s species interacting through N_r reactions is mathematically written as:

$$\sum_{k=1}^{N_s} \nu_{kj}^{'} \chi_k \leftrightarrow \sum_{k=1}^{N_s} \nu_{kj}^{''} \chi_k \qquad \text{for } j = 1, N_r \tag{1.24}$$

where $\nu_{kj}^{'}$ and $\nu_{kj}^{''}$ are respectively the forward and reverse stoechiometric coefficients of the species k in the reaction j and χ_k is the chemical symbol of the k^{th} species.
The mass net production rate $\dot{\omega}_k$ of species k is given by the sum of the contribution of all reactions involving the k^{th} species:

$$\dot{\omega}_k = W_k \sum_{j=1}^{N_r} \nu_{kj} Q_j \tag{1.25}$$

where $\nu_{kj} = \nu_{kj}^{'} - \nu_{kj}^{''}$ and Q_j is the rate of progress variable of the reaction j. The rate of progress of the j^{th} reversible reaction is given by the forward and reverse reaction rate:

$$Q_j = q_{fj} - q_{rj} \tag{1.26}$$

The forward and reverse reaction rates are closed using the law of mass action stating that the rate of progress of the reaction is proportional to the product of species molar concentrations:

$$Q_j = K_{fj} \prod_{k=1}^{N_s} [X_k]^{\nu_{kj}^{'}} - K_{rj} \prod_{k=1}^{N_s} [X_k]^{\nu_{kj}^{''}} \tag{1.27}$$

where $[X_k] = (\rho Y_k)/W_k$ is the species molar concentration or activity, while K_{fj} and K_{rj} are the forward and reverse rate constants of the j^{th} reaction. Numerous experimental studies were performed to identify empirical laws modeling the forward reaction rate K_{fj}. The theory proposed by Arrhenius (1889) and later validated by the kinetic gas theory is conventionally used in combustion for its simplicity. The modified Arrhenius law closes K_{fj} through the following temperature dependent empirical law:

$$K_{fj} = A_{fj} T^{\beta_j} \exp\left(-\frac{E_{aj}}{RT}\right) \tag{1.28}$$

where A_{fj} is the pre-exponential constant, β_j the temperature exponent and E_{aj} the activation energy of the reaction j. Using kinetic gas theory results, the product $A_{fj}T^{\beta_j}$ may be related to the steric factor that models the probability that a collision between two molecules effectively induces a reaction. A_{fj} models the collision frequency depending on the molecules geometry and orientation during the collision, while T^{β} expresses the impact of thermal agitation on collision success. An important parameter is the activation energy E_{aj} that accounts for the fact that a sufficient amount of energy must be provided to the system to initiate the reaction. These three kinetic parameters are generally identified empirically by fitting experimental data.
The reverse rate constant is evaluated from the forward rate constant and the equilibrium constant K_{cj} through the following relation:

$$K_{rj} = \frac{K_{fj}}{K_{cj}} \tag{1.29}$$

The equilibrium constant of the jth reaction is evaluated from the thermodynamic properties of the species involved in the reaction:

$$K_{cj} = \left(\frac{P_{atm}}{RT}\right)^{\sum_{k=1}^{N_s} \nu_{kj}} \exp\left(\frac{\Delta S_j^0}{R} - \frac{\Delta H_j^0}{RT}\right) \tag{1.30}$$

where P_{atm} is the atmospheric pressure, ΔS_j^0 and ΔH_j^0 are the change of entropy and enthalpy occurring through reaction j:

$$\Delta S_j^0 = \sum_{k=1}^{N_s} \nu_{kj} S_k^0 \qquad \text{and} \qquad \Delta H_j^0 = \sum_{k=1}^{N_s} \nu_{kj} H_k^0 \tag{1.31}$$

With these expressions, if a kinetic scheme describing the chemical pathways and their rate of progress (values of the kinetic rate parameters) is provided, the species net production rate can be evaluated. The next section introduces general concepts on hydrocarbon/air combustion.

1.1.3.2 Oxidation of hydrocarbon fuels

As previously mentioned, combustion is a complex process involving high degrees of freedom. A second complexity associated with combustion modeling is that the chemical paths strongly depend on the reactive mixture (type of fuel and oxidizer), the proportion of each reactant and the operating conditions (cold / intermediate / high temperature, low / high pressure). Figure 1.2 illustrates the main chemical reactions observed in a methane/air flame. The first column presents the chemical pathways related to lean mixtures, while the two second columns describe chemical reactions taking place in rich conditions.

The main steps of hydrocarbon/air combustion kinetics may be identified from this example:

- Free radicals such as H, O and OH attack the fuel through **chain-carrying reactions** promoting the production of additional free radicals and intermediate species.
- **Termination reactions** rapidly convert alkene radicals into intermediate and product species.
- Finally, intermediate species are finally transformed into combustion products through slow **recombination reactions**.

Though methane is a simple molecule Fig. 1.2 illustrates the complex chemical processes occurring during fuel oxidation. The description of combustion kinetics effects may be achieved through different level of details. Being the core of the thesis, this subject is discussed in more details in Chapter 2.

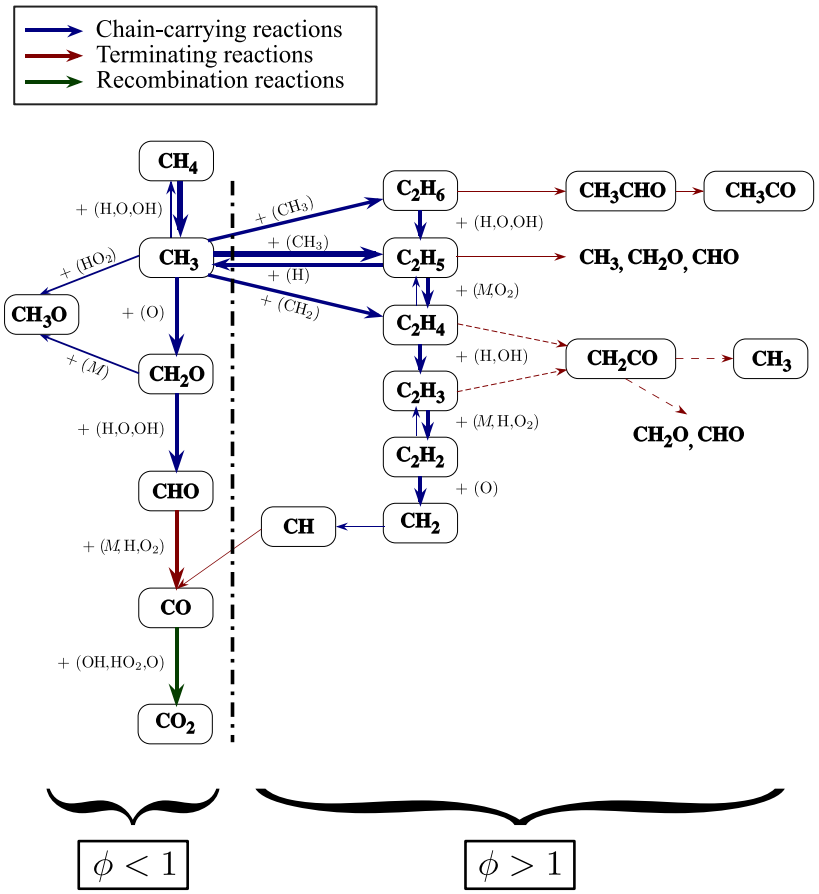

Figure 1.2: *Main chemical paths of the oxidation of methane by air. The thickness of the arrow indicate the relative importance of the reaction. Reproduced from (Warnatz 1981).*

1.2 Flame regimes for chemistry modeling

Before presenting in detail chemistry modeling approaches, general concepts on canonical flame problems and real flame structures are introduced. Elementary combustion problems such as laminar premixed and non-premixed flames constitute essential tools for the derivation of flame chemistry models. As it will be discussed in Chapter 2, chemical models generally distinct these two flame structures and are therefore often efficient on a unique combustion regime. However, in most real flame application it is not trivial to identify one single combustion mode.
The objective of this section is to identify the target flame configurations that will be used for the derivation of the proposed kinetic model. First, the main characteristics of both premixed and non-premixed canonical problems are described. Spatial flame structures, governing equations and key properties of these two flame archetypes are briefly introduced. Then, the relevance of these two canonical flame configurations to represent realistic combustion systems is discussed. Eventually, to illustrate the complexity of the chemical flame structures encountered in practical combustion chambers, the numerical simulation of an helicopter combustor is analyzed to identify the main combustion modes.

1.2.1 Canonical flame structures

Combustion regimes are usually divided into two categories: premixed and non-preximed. These two flame archetypes feature intrinsic differences in terms of internal chemical structure and global flame characteristics.

1.2.1.1 Unstretched laminar premixed flame

The premixed flame archetype is obtained when fuel and oxidizer are perfectly mixed prior to combustion. The fresh gases composed by fuel, oxidizer and dilutant are separated from burnt gases by the flame front. This thin interface, featuring high temperature gradient and strong chemical activity (see Fig. 1.3), freely propagates in the fresh gases and consumes reactants at a constant burning rate.

As illustrated in Fig. 1.3 the flame region can be split into three main regions:

- A pre-heat zone (I) dominated by temperature and molecular diffusion effects.
- A reaction zone (II), also called fuel oxidation layer, where fuel is converted into intermediate species that are then consumed to form secondary fuels. This reaction region is characterized by its thickness δ_r of the order of 10 micrometers.
- A post-flame zone (III) where major combustion products (H_2O and CO_2) are produced by the oxidation of secondary fuels (H_2 and CO).

The oxidation reactions being slow, the post-flame zone or oxidation layer is often very large (few tenth to few millimeters).

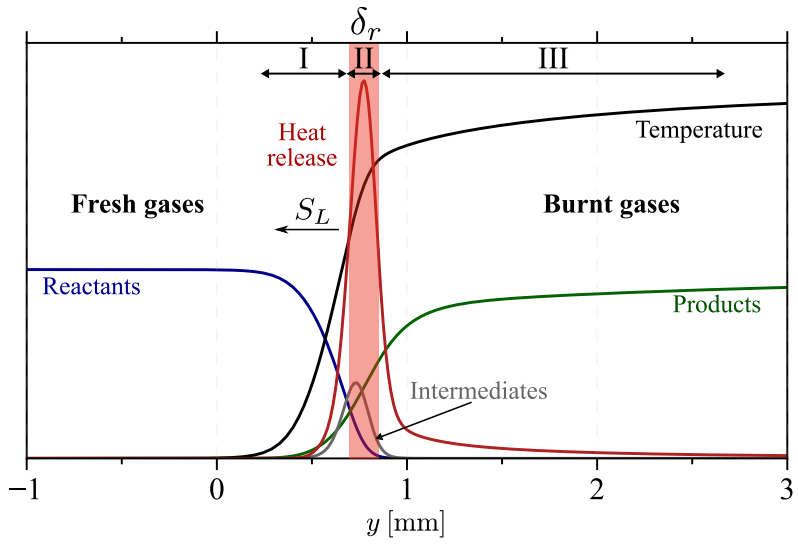

Figure 1.3: *Schematic of a 1-D premixed flame.*

Combination of both heat and species diffusion from the reactive region to the pre-heat zone promotes the flame front propagation towards the fresh gases. Thermal fluxes due to the flame locally increase the fresh gas temperature, while the back diffusion processes from the reaction zone feed the pre-heat zone with radicals ensuring the fuel consumption through chain-carrying reactions. The heat released by the chemical reactions amplifies the local temperature gradients enabling the flame propagation phenomenon to be maintained.
The numerical resolution of such a complex flame structure may be performed with dedicated codes such as REGATH (Darabiha and Candel 1992), CHEMKIN (Kee et al. 1996) or CANTERA (Goodwin 2002). These laminar flow solvers resolve the conservation equations describing laminar one-dimensional premixed flames. Under the assumption of steady flame, the system of equations (1.11) simplifies to:

$$\begin{aligned} \frac{\partial \rho u}{\partial x} &= 0 \;\rightarrow\; \rho u = \rho^f S_L = \dot{m} \\ \dot{m}\frac{\partial Y_k}{\partial x} &= -\frac{\partial}{\partial x}\left(\rho Y_k V_k\right) + \dot{\omega}_k \\ \dot{m} C_p \frac{\partial T}{\partial x} &= \frac{\partial}{\partial x}\left(\lambda \frac{\partial T}{\partial x}\right) - \frac{\partial T}{\partial x}\sum_{k=1}^{N_s} \rho Y_k V_k C_{pk} + \dot{\omega}_T \end{aligned} \tag{1.32}$$

where $\dot{m}$ is the mass flow rate per surface unit and constitutes the eigenvalue of the problem. The superscript f denotes the fresh gas state and S_L is the speed at which reactants are consumed. The last contribution in the right hand

side of the energy conservation equation is the heat release rate due to chemical reactions and is defined as:

$$\dot{\omega}_T = -\sum_{k=1}^{N_s} \dot{\omega}_k h_k \tag{1.33}$$

To fully close the system of equations (1.32), inlet and outlet boundary conditions must be prescribed. Inlet boundary conditions are defined by fresh gas properties, while zero gradient of the transported variables are prescribed at the outlet:

	Species mass fraction	Temperature
Inlet	$Y_k\|_{x=-\infty} = {Y_k}^f$	$T\|_{x=-\infty} = T^f$
Outlet	$\left.\frac{\partial Y_k}{\partial x}\right\|_{x=+\infty} = 0$	$\left.\frac{\partial T}{\partial x}\right\|_{x=+\infty} = 0$

where T_f is the fresh gas temperature and ϕ^f is the fresh gas equivalence ratio characterizing the proportion of each reactant in the reactive mixture. This controlling parameter is defined as the normalized ratio between fuel (F) and oxidizer (O) mass fraction:

$$\phi = \left(\frac{Y_F}{Y_O}\right) / \left(\frac{Y_F}{Y_O}\right)_{st} = s\left(\frac{Y_F}{Y_O}\right) \tag{1.34}$$

The subscript st corresponds to stoichiometric conditions where fuel and oxidizer are mixed in optimal proportions. The air/fuel stoichiometric mass ratio s is:

$$s = \frac{\nu_O W_O}{\nu_F W_F} \tag{1.35}$$

where ν_k are stoichiometric molar coefficients of the global reaction.
The numerical resolution of the system of equations (1.32) allows the evaluation of key quantities describing the premixed laminar flame. First, the laminar flame propagation speed S_L is evaluated by integrating the second equation of system (1.32) between fresh ($x = -\infty$) and burnt ($x = +\infty$) gas states:

$$S_L = \frac{1}{\rho^f \left(Y_k^b - Y_k^f\right)} \int_{x=-\infty}^{x=+\infty} \dot{\omega}_k \left(x'\right) dx' \tag{1.36}$$

The superscript b stands for the burnt gas state. The species k used to compute S_L is either a reactant or a product species.
Another important parameter characterizing the premixed flame structure is its thickness. Many definitions have been proposed including the thermal thickness

δ_L^0, the diffusive thickness δ_d or the Blint thickness δ_b. In this thesis, the thermal thickness evaluated from the temperature gradient is considered:

$$\delta_L^0 = \frac{T_b - T_f}{\max\left(\left|\frac{\partial T}{\partial x}\right|\right)}. \tag{1.37}$$

To account for the complexity of the chemical flame structure, the reactive thickness of the species k, noted $\delta_{r,k}^0$, is also considered in this study. It is defined as the full width at half maximum (FWHM) of the net production rate of species k.

1.2.1.2 Laminar non-premixed flame

The laminar non-premixed or diffusion flame constitutes the second canonical flame structure. In this flame configuration, fuel and oxidizer are not mixed before entering the flame region, but are separated by the flame front. Figure 1.4 illustrates the non-premixed flame in a counter-flow configuration, where fuel and oxidizer are injected in opposite directions. In zones I and III, the mixture is respectively too lean and too rich to burn. Oxidizer and fuel diffuse towards the reaction zone II where the local composition allows chemical reactions to occur. Contrarily to premixed combustion, the diffusion flame does not propagate and remains localized near the stoichiometric line.

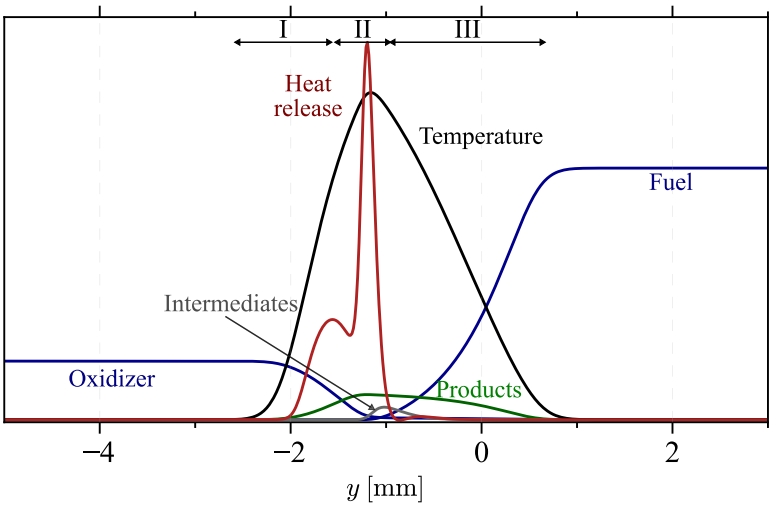

Figure 1.4: *Schematic of a counterflow non-premixed flame.*

The non-premixed flame structure strongly depends on mixing processes between fuel and oxidizer. Description of the diffusion flame structure is therefore generally based on a passive scalar called mixture fraction that accounts for the level of mixing between the reactants. By definition, the mixture fraction is not

affected by chemical reactions and obeys a generic advection-diffusion equation without source term:

$$\frac{\partial \rho Z}{\partial t} + \frac{\partial}{\partial x_i}\left(\rho u_i Z\right) = \frac{\partial}{\partial x_i}\left(\rho D_Z \frac{\partial Z}{\partial x_i}\right) \tag{1.38}$$

where the diffusivity of the mixture fraction D_z is equal to the thermal diffusivity $D_z = \lambda/(\rho c_p)$.
Using this new variable, the numerical study of non-premixed flames may be split up into two decoupled problems: i) a mixing problem and ii) a flame structure problem in the phase space. The equations governing this second combustion problem may be formally derived by a projection of the conservation equations onto the mixture fraction space. If unity Lewis numbers are considered and neglecting the iso-Z curvatures (i.e. the diffusion flame structure depends only on time and mixture fraction) the system (1.11) can be simplified by the so-called flamelet equations system:

$$\begin{aligned} \rho\frac{\partial Y_k}{\partial t} &= \frac{1}{2}\rho\chi\frac{\partial^2 Y_k}{\partial Z^2} + \dot{\omega}_k \\ \rho\frac{\partial T}{\partial t} &= \frac{1}{2}\rho\chi\frac{\partial^2 T}{\partial Z^2} + \dot{\omega}_T \end{aligned} \tag{1.39}$$

More general equations including the effect of non-unity Lewis numbers, curvature of mixture fraction iso-surfaces may be found (Pitsch and Peters 1998; Xuan et al. 2014). The system (1.39) can be directly solved in the Z-phase space providing that the scalar dissipation rate χ (Eq. (1.40)) describing the mixing processes is known:

$$\chi = 2D\left(\frac{\partial Z}{\partial x_i}\right)^2. \tag{1.40}$$

This parameter measuring the strength of molecular and heat diffusion effects is directly influenced by the external boundary conditions characterized by the strain rate a. From this key quantity, the Damköhler number Da comparing diffusion fluxes and chemical processes characteristic times τ_d and τ_c, may be defined:

$$\mathrm{Da} = \frac{\tau_d}{\tau_c} = \frac{1}{\chi\tau_c} \tag{1.41}$$

When high Damköhler numbers are encountered chemical processes are very fast compared to mixing processes. This regime is called infinitely fast chemistry. On the contrary when Damköhler numbers take finite values, the heat and mass diffusion affect the inner structure and the burning rate. This case is said finite-rate chemistry. When the scalar dissipation rate becomes very high ($\chi > \chi_{ext}$), combustion can not compensate the heat and mass transport through the stoichiometric surface and the flame extinguishes. Figure 1.5 illustrates the non-premixed flame structure in the Z-phase space for different level of scalar dissipation rate or strain rate.

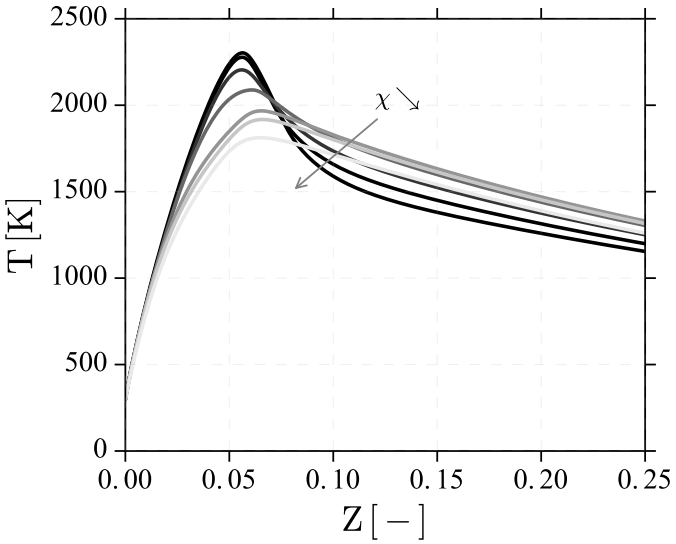

Figure 1.5: *Non-premixed flame structure evolution with scalar dissipation rate for CH_4/air combustion. Scalar dissipation rates are varied from 0.01 s^{-1} up to χ_{ext}.*

1.2.2 Flame structures in practical applications

1.2.2.1 Mutli-regime flames

Previous section introduces two canonical flame structures governed by substantially different combustion processes. In practical combustion chamber, fuel and oxidizer are injected separately promoting composition inhomogeneities. In this environment, multi-regime combustion flames, characterized by the co-existence of both premixed and non-premixed modes, are likely to be encountered. Figure 1.6 illustrates a multi-regime flame developing in an inhomogeneous composition mixture.

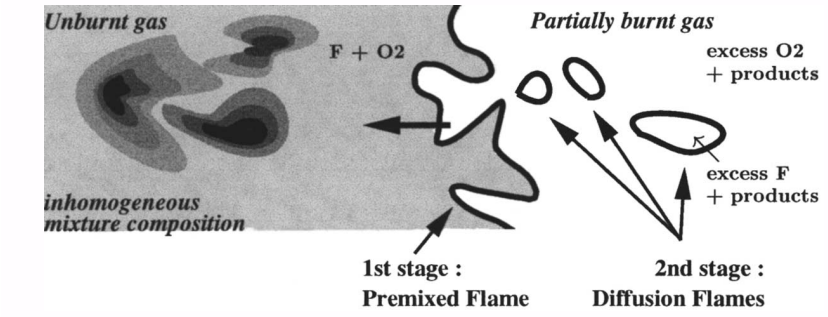

Figure 1.6: *Schematic representation of flame propagation in an heterogeneous mixture (Hélie and Trouvé 1998).*

First, a premixed flame front propagates towards unburnt gases. Then, in a secondary stage, burnt gases pockets composed by either oxidizer or fuel excess mix and burn in a diffusion-like flame front.
To gain better a understanding on these mixed combustion regimes numerous experimental (Masri 2015; Rosenberg et al. 2015) and numerical (Hélie and Trouvé 1998; Luo et al. 2011) studies have been performed. Interestingly, on the two last editions of the international workshop on measurement and computation of Turbulent (Non)premixed Flames (TNF Workshops 2018), a numerical comparative study was performed in order to asses combustion model capabilities to capture the complex and multiple flame structures of an inhomogeneous jet burner (Meares and Masri 2014).
To illustrate the variety of combustion regimes encountered in real application, the next section describes the flame structure identified in an aeronautical combustion chamber designed by Safran Helicopter Engine.

1.2.2.2 Flame structure analysis in an helicopter combustor

Flow topology and flame stabilization
A schematic of the investigated combustion chamber is presented in Fig. 1.7. This industrial combustor features a reverse flow architecture where the reactive mixture is injected in the motor axis opposite direction. The flow is then redirected through an elbow before exhaust.

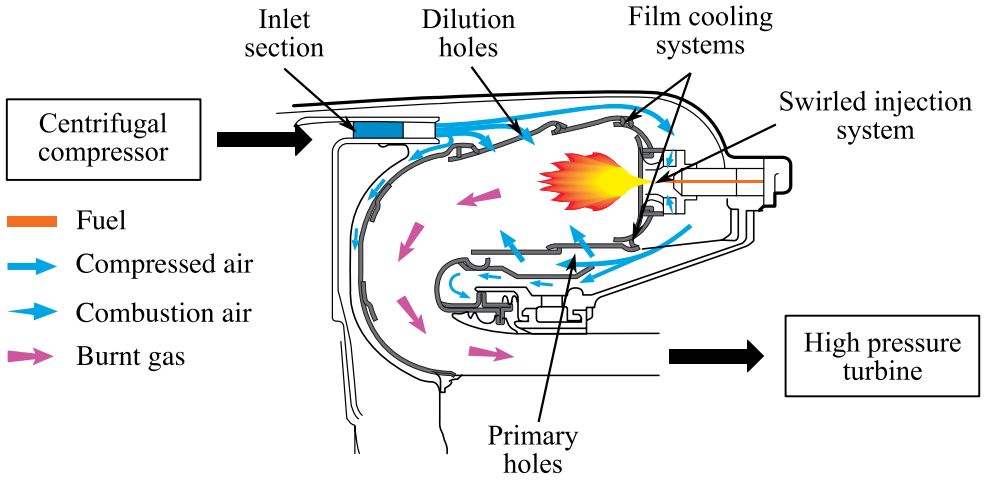

Figure 1.7: *2-D cut view of a reverse flow helicopter combustion chamber.*

The configuration is equipped with a swirled injection system in which air is injected radially through small tubes, and kerosene is axially injected under the form of a liquid spray. In the hot environment, the liquid kerosene is rapidly evaporated and partially mixes with the pre-heated air. As soon as mixture and thermal conditions are favorable, the flow reacts and is converted into

burnt gases. The combustion products are then exhausted from the combustion chamber to the high pressure turbine. A portion of the air flux coming from the compressor is injected through multiple cooling systems (primary holes, dilution holes, film cooling systems and multi-perforated walls) to reduce thermal and mechanical loads near the walls and decrease the burnt gases temperature levels before entering the high pressure turbine.

Figure 1.8 showing instantaneous fields of mixture fraction, heat release rate and temperature, illustrates the flow and flame topologies. For confidentiality reasons, only dimensionless quantities are displayed:

$$Z^+ = \frac{Z}{Z_{st}}; \quad HR^+ = \frac{HR}{HR_{\text{mean}}}; \quad T^+ = \frac{T}{T_3} \tag{1.42}$$

where the subscript 3 denotes thermodynamic conditions at the combustion chamber entrance.
Variables fields depicted in Fig. 1.8 are extracted from a Large Eddy Simulation solution obtained with the massively-parallel, compressible solver AVBP (Schönfeld and Rudgyard 1999) co-developed at CERFACS and IFPEN. In this calculation, chemistry effects are accounted for with a two-step global scheme devoted to kerosene/air combustion description (Franzelli et al. 2010). Underresolution of the species source terms on the LES grid is handled by the Thickened Flame model for LES (Colin et al. 2000), while impact of the sub-grid scale wrinkling is accounted for by the so-called efficiency function (Charlette et al. 2002a). Details on the kinetic scheme and turbulent combustion models are provided in Chapters 2 and 5 respectively. Kerosene is assumed to be perfectly evaporated before the flame front and is injected under gaseous form.
At the swirler exit on the outer recirculation zone, pure fuel mixes with fresh air and forms a rich stratified mixture. As the local equivalence ratio is well above the rich flammability limits, no flame can stabilize. However along the injector axis, a flame stabilizes on the stoichiometric line. In this region the recirculation zone brings unburnt combustion products that mix with air leading to a moderately lean stratified mixture. Further downstream, on both sides of the injection system the local rich flammable mixture conditions ($Z^+ \in [1, Z_r/Z_{st}]$), allows the stabilization of two flame fronts (see high heat release rate near the injection system Fig 1.8.b). This rich reaction zone is then followed by a pocket of burnt gases composed by unburnt hydrocarbon. The fresh air injected through primary holes, film cooling systems and multi-perforated walls mixes with the burnt gases leading to mixture fraction reduction. Along the stoichiometric line, identified by the white line in Fig 1.8.a, the hydrocarbon excess is completely consumed in a second reaction zone. Downstream the fresh gases injection through dilution holes dilutes burnt gases leading to temperature reduction.

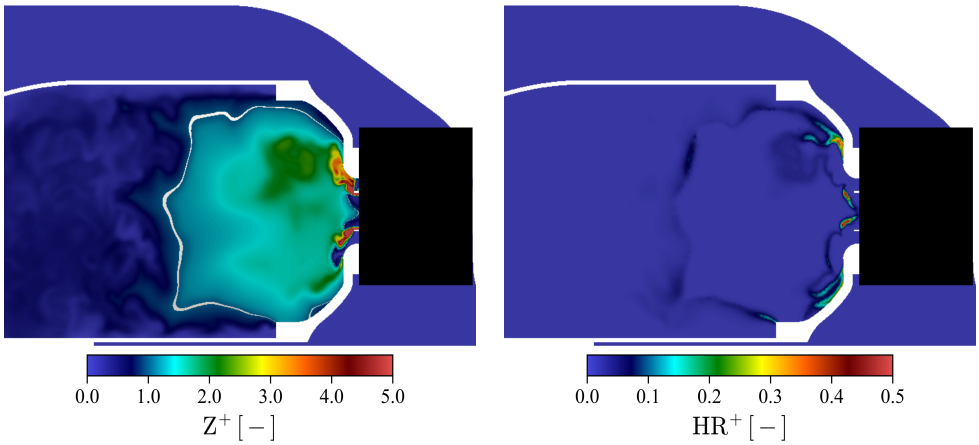

(a) Dimensionless mixture fraction field (b) Dimensionless heat release rate field

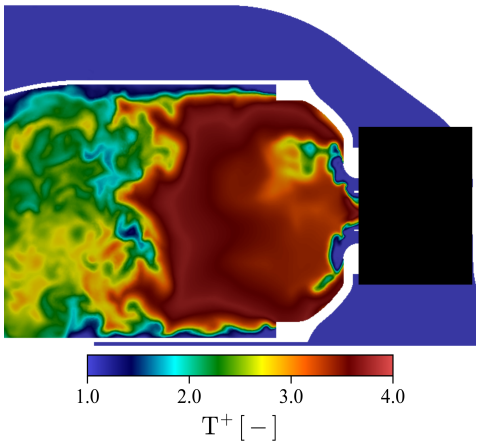

(c) Dimensionless temperature field

Figure 1.8: *Instantaneous fields of dimensionless resolved mixture fraction, heat release and temperature evaluated by Large-Eddy Simulation. The white line in Figure a) identifies the stoichiometric mixture fraction iso-surface.*

Scatter plots analysis

A simple method for the analysis of the flame structure consists in studying the chemical trajectories in the mixture fraction space. Figure 1.9 shows the repartitions of resolved temperature and heat release as a function of the resolved mixture fraction for different axial positions defined on Fig. 1.9. Normalized coordinates $x^* = x/L$ are used, where x denotes the distance to the injector exit and L is an arbitrary length.

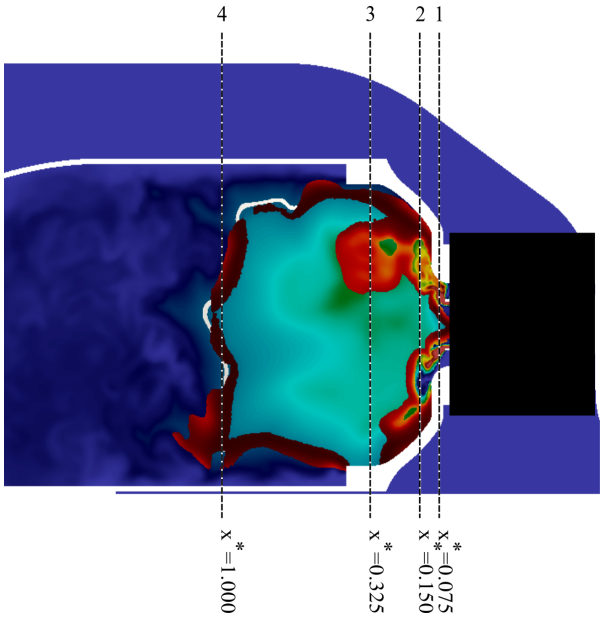

Figure 1.9: *Post-treatment planes positions and instantaneous resolved mixture fraction field. In red colors the iso-volume of resolved heat release rate identifies the reaction zone.*

Near the injection system exit, at $x^* = 0.075$, two main zones can be identified: i) a mixing zone between pre-heated fresh gases ($(Z^+, T^+) = (0, 1)$) and pure fuel ($(Z^+, T^+) = (1/Z_{st}, T_F^f/T_3)$) and ii) a lean/stoichiometric reaction zone. The Inner Recirculation Zone (IRZ) created by the swirled motion of the flow promotes the movement of rich burnt gases towards fresh air. The two counter-flow streams mix one towards the other and burn where the mixing is adequate. Further downstream, at $x^* = 0.15$, the scatter plots suggest a complex flame structure where both premixed and non-premixed combustion regimes co-exist. This double flame structure features i) a diffusion flame front, identified by the peak of heat release centered on stoichiometric mixture fraction, and ii) a rich partially premixed combustion regime, observed for $Z^+ \in [1, Z_r/Z_{st}]$. Moreover, mixing processes established between the different available gases (fresh air, fresh fuel and burnt gases) tend to reduce the mixture fraction space covered.
Along the third plane, located at $x^* = 0.325$, we retrieve a mixed regime with both a diffusion-like flame characterized by reduced heat released rate, and a rich partially premixed reaction zone. The lean intermediate temperature branch is representative of the progressive dilution of combustion products by fresh air coming from multi-perforated walls and film cooling systems.
For the last axial position investigated ($x^* = 1.0$), a diffusion flame may be observed. The burnt gases composed by unburnt hydrocarbon compounds and combustion products flows against fresh air injected through primary holes for dilution. Each reactant diffuses towards the reactive layer anchored to the

stoichiometric line.

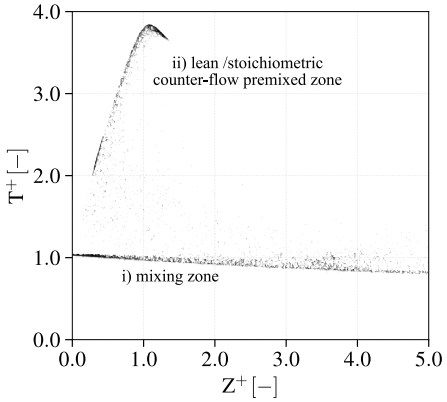

(a) $x^* = 0.075$

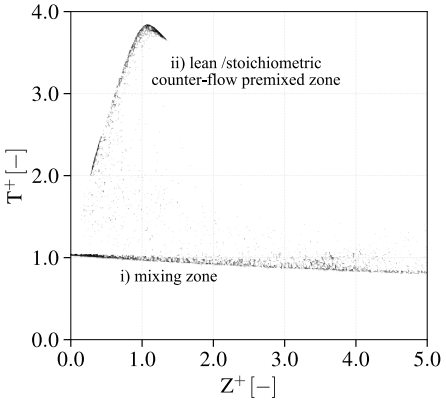

(b) $x^* = 0.075$

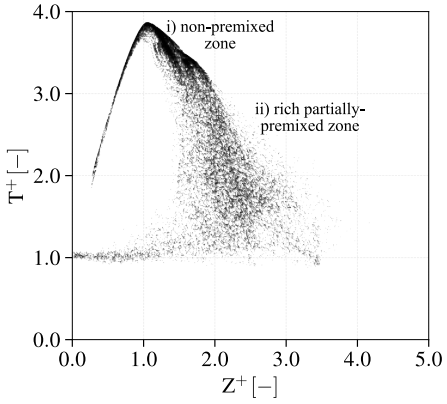

(c) $x^* = 0.150$

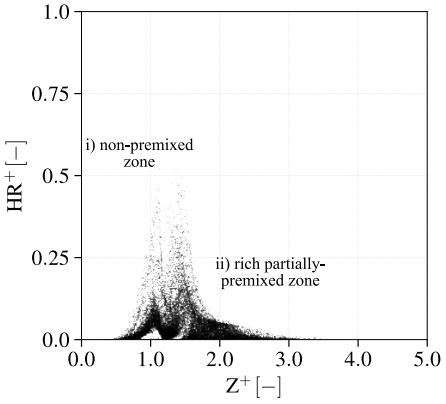

(d) $x^* = 0.150$

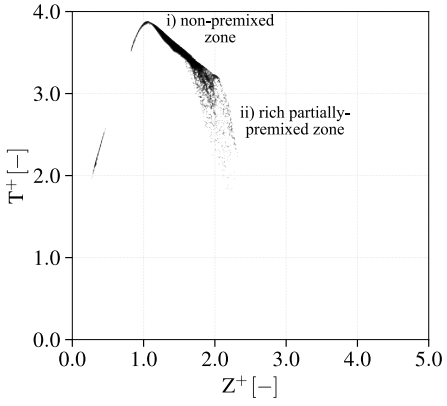

(e) $x^* = 0.325$

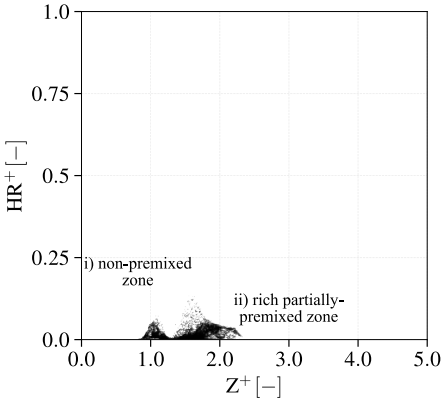

(f) $x^* = 0.325$

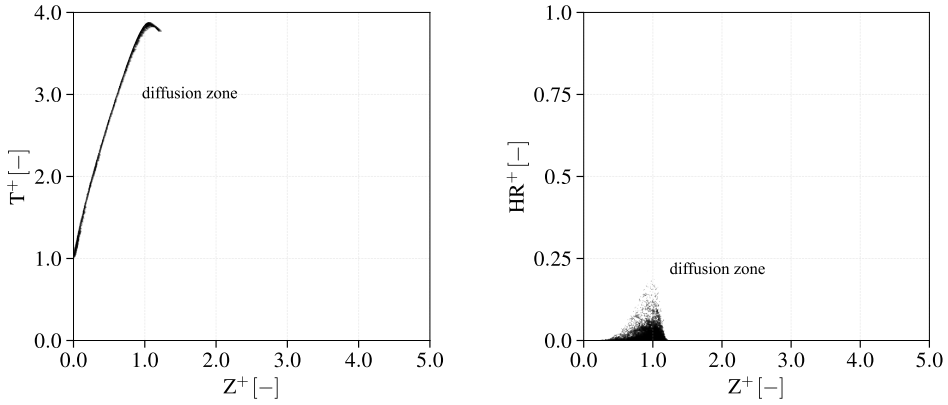

(g) $x^* = 1.00$ (h) $x^* = 1.00$

Figure 1.9: *Scatter plots of resolved temperature and heat release rate as a function of mixture fraction for different axial positions. Normalized coordinates $x^* = x/L$ where x denotes the distance to the injector exit and L is an arbitrary length. Plane positions are indicated in Fig. 1.9.*

Flame indicator analysis

Flame indicators have been proposed to identify the local flame structure. Yamashita et al. (1996) first introduced the Takeno index $\mathcal{I}_T$ analyzing the alignment between fuel and oxidizer mass fraction gradients:

$$\mathcal{I}_T = \left.\frac{\nabla Y_F.\nabla Y_O}{|\nabla Y_F.\nabla Y_O|}\right|_{HR>HR_{mean}} \tag{1.43}$$

The Takeno index is evaluated only if the heat release rate is above a threshold value (equal to the average heat release on the whole volume chamber) to ensure the analysis of reactive zones only. In a premixed flame, as fuel and oxidizer gradients are oriented in the same direction, the Takeno index equal unity. On the contrary, in a non-premixed flame as fuel and oxidizer diffuse one towards the other their gradients are opposed and the Takeno index is equal to -1. This simple flame index based on a one-dimensional view of flame archetypes, has been successfully applied in simulations of turbulent flames (Mizobuchi et al. 2005; Hannebique et al. 2013). However, when used with detailed chemistry, the Takeno index may fail in rich conditions where fuel is consumed through the flame front and converted into light intermediate fuels. To overcome this limitation, a more general definition based on the scalar product of mixture fraction and progress variable normals has been proposed (Domingo et al. 2002; Domingo et al. 2005). Recently, more complex flame regime indicators based on the study of explosive modes (CEMA) (Lu et al. 2010) or using drift term (Wu and Ihme 2016) were introduced.

As chemistry is described with a global two-step scheme, the Takeno index based on the scalar product of fuel and oxidizer mass fraction gradient is used.

Figure 1.10 displays an instantaneous field of the Takeno index extracted on the sector center plane.

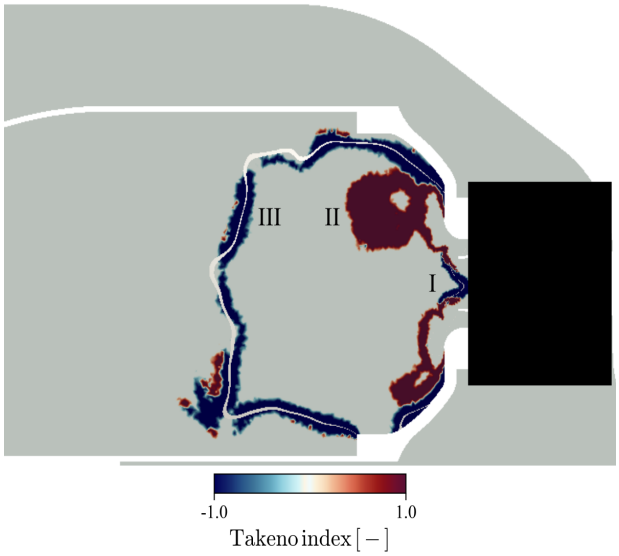

Figure 1.10: *Instantaneous resolved Takeno index field. The white line identifies the stoichiometric mixture fraction iso-surface.*

At the injector exit near the centerline, the negative value of the Takeno index suggests a non-premixed like combustion mode. On the outer region, few centimeter downstream the injector, a premixed like combustion mode dominates. Finally, the Takeno index identifies a second non-premixed flame front anchored to the stoichiometric line. Though qualitative this findings corroborate the scatter plot analysis, and confirm that three main combustion regimes are present in this combustion chamber:

- A lean partially premixed combustion mode (I) on the center region.
- A rich partially premixed combustion mode (II) on the outer region.
- A non-premixed combustion mode (III) downstream.

Summary

The flame structure analysis confirms that in practical applications the flame structure is neither perfectly premixed nor non-premixed. Indeed, real combustion chambers exhibit a high variability of flame structures changing from perfectly premixed to diffusion-like. The simple classification distinguishing premixed from non-premixed combustion regimes generally used to build chemical model may be questioned for its low representativity. To ensure reliability of the developed chemistry description models in practical combustors, a special care must be given to mixed combustion regimes where both premixed and non-premixed regimes are present.

This study performed in stabilized flame configuration, could be renewed in more complex combustion problems such as flame ignition and flame extinction. Moreover, it would be of great interest to perform a similar analysis in a two phase-flow environment where the spray dynamics and evaporation may have a strong impact on the local mixture composition and flame regimes.

Chapter 2

Chemistry modeling strategies

Contents

Combustion chemistry is a complex and high dimensionality phenomenon involving numerous competing processes that feature a high disparity of length and time scales. Reliable description of these chemistry effects is however of main importance to ensure a proper capture of pollutant formation, flame stabilization or ignition. Over the past 40 years intensive research has been carried out in order to both gain a better understanding on the underlying physics of flame chemistry and to provide kinetic models that can be used in numerical simulations. In this chapter, a review of the main modeling approaches aiming at describing combustion chemical effects is presented.

2.1 Detailed chemistry

2.1.1 Derivation and main characteristics of detailed schemes

The description of the governing chemical processes transforming fuel and oxidizer into products can be handled by detailed mechanisms. These kinetic models consist in a set of elementary reactions characterizing the interaction between species at the molecular level. Practically, detailed kinetic schemes are built through the following steps:

- Compilation of every possible reactions between every possible species,
- Evaluation of reaction rate parameters closing chemical reactions rates,
- Validation against a variety of experimental data.

The resulting detailed chemistry models contain an accurate and comprehensive description of kinetic effects over a wide range of operating conditions (initial pressure, temperature and composition) and canonical configurations (auto-ignition, premixed, non-premixed, ...).
Figure 2.1 shows the number of reactions and species involved in detailed kinetic schemes for fuels of different complexities.

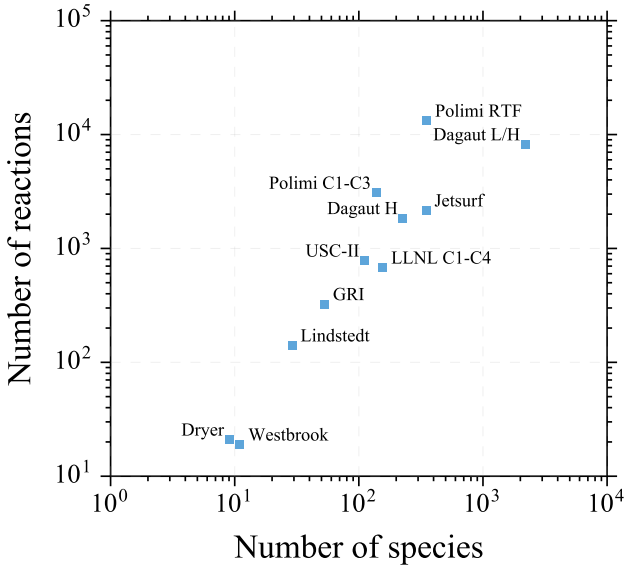

Figure 2.1: *Number of reactions versus number of species for selected detailed mechanisms. Adapted from (Lu and Law 2009).*

For simple fuels such as hydrogen, only ten species interacting through about twenty reactions are required to describe complex kinetic effects (Li et al. 2004). For hydrocarbon fuels, as the molecular size of the fuel increases, the number of species and reactions dramatically increases. Mechanisms for light hydro-

carbons involve hundreds of species (Marinov et al. 1998; Wang et al. 2007), whereas kinetic models for aeronautical fuels include about 300 species and few thousand reactions (Dagaut and Cathonnet 2006; Wang et al. 2010). When low temperature effects are included the number of species can reach more than one thousand (Dagaut et al. 2014).
Oxidation of practical fuels proceeds through numerous intermediate and radical species. These species, rapidly consumed after their production, feature very small characteristic chemical times and reactive thicknesses in comparison with final products. Figure 2.2 shows estimates of the species chemical times (τ_k) and reactive thicknesses (δ_{rk}) for a one-dimensional freely propagating laminar methane/air flame. The chemical time scale of species k is evaluated with the simple definition proposed by Hong et al. (1999):

$$\tau_k = \frac{\max\left(\rho Y_k\right)}{W_k \max\left(\dot{\omega}_k\right)} \tag{2.1}$$

Two reactive thicknesses characterizing the creation and destruction rates of the species are defined. Both reactive thicknesses are defined as the Full Width at Half Maximum of the source terms.

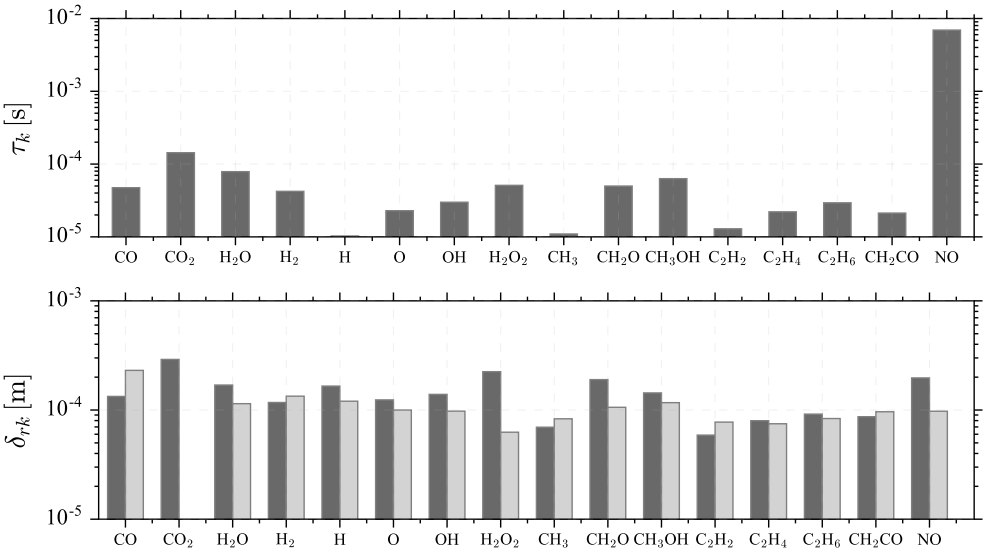

Figure 2.2: *Species chemical time (τ_k) and reactive thicknesses (δ_{rk}) associated with creation (dark gray) and destruction (light gray) rates. Quantities are evaluated from a methane/air 1-D premixed flame at $\phi = 1.0$ and atmospheric conditions.*

Intermediate species such as H, CH_3 or C_2H_2 present very low chemical times of the order of 10^{-5} s while the chemical time associated with CO_2 and H_2O is one order magnitude higher. NO_x species formation is characterized by very slow chemical time of few milliseconds. As regards with reactive thicknesses, one may observe that radicals species such as CH_3, C_2H_2 or C_2H_4 feature small

reactive thicknesses of about 70 μm, while reaction rate of major products occur on wider spatial region of the order of 300 μm.

2.1.2 Discussions

Despite the rapid increase in computational power, the use of detailed kinetic mechanisms for the simulations of practical configurations is still out of reach. Three main reasons can be invoked to explain this limitation:

- First, the high dimensionality of detailed models impose prohibitive CPU costs. Each species involved in the detailed kinetic scheme requires the solving of an additional balance equation. Also the time associated with species source term calculation is directly linked with the number of reactions included in the mechanism.
- Secondly, as shown in Fig. 2.2 intermediate and radical species feature very rapid timescale of production and destruction making the system of equations stiff. To ensure the proper resolution of such equations very small timesteps or specific integration algorithms are required.
- Finally, the coupling of detailed kinetic schemes and combustion models is theoretically complex. Indeed, the complexity of the coupling between turbulence and chemical combustion increases rapidly with the number of species and associated chemical time scales.

To include a description of kinetic effects in simulations of practical configurations, at a reduced computational cost, various strategies have been proposed (Fiorina et al. 2015). The following sections discuss these approaches.

2.2 Skeletal chemistry

2.2.1 Main characteristics of skeletal mechanisms

Skeletal mechanisms constitute the first level of reduction of a detailed scheme. These reduced schemes are built through a "chemistry driven reduction method" consisting in decreasing the number of reactions and species intervening in a detailed kinetic scheme. According to Turányi (1990), species can be classified into three classes: i) important species whose precise description is essential to represent combustion processes, ii) necessary species that are required for the prediction of important species and iii) redundant species that can be removed without affecting the reproduction of combustion phenomena. Considering a set of target flame properties, a range of applicability and a precision accuracy, skeletal reduction techniques aims at identifying and removing the redundant species and/or reactions that are considered as unimportant for the prediction of the targets. As the quantity of flame variables of interest, the variety of combustion elements and the degree of precision required increases, the number of

species and reactions included in the skeletal mechanism rises.
Skeletal reduction methods are oriented towards either species or reactions elimination. These two approaches are discussed in the following section.

2.2.2 Elimination of redundant species

The first step of skeletal reduction aims at discarding redundant species from the detailed kinetic scheme. This stage is often considered as the most important as it allows an important reduction of computational time. The identification of redundant species can be performed through a variety of strategies.

Reaction rates analysis
Turányi (1990) first suggested to perform a systematic analysis of the reaction rates. A species is considered as redundant if the elimination of the reactions where it is involved does not deteriorate the prediction of target quantities. Though very simple to set up this method is not used in practice because of the cost associated with the systematic evaluation of the kinetic mechanisms.

Jacobian sensitivity investigation
Alternative strategies based on the measure of the interactions between species have been proposed (Tomlin et al. 1992; Tomlin et al. 1997). The fundamental idea behind these approaches consists in keeping species strongly coupled to target species, while the species that are not coupled in a significant way are removed from the skeletal mechanism. Tomlin et al. (1992) suggested to use the analysis of Jacobian matrix to quantify the dependency relation between species. The Jacobian matrix element J_{AB} is defined as the change in the rate of production of species A caused by the change in concentration of species B. Its normalized definition is given by:

$$J_{AB} = \frac{\partial \ln \dot{\omega}_A}{\partial \ln [X_B]} \tag{2.2}$$

For a set of N_{target} species, a species B is considered as redundant if:

$$J_B = \sum_{k=1}^{N_{target}} \left(\frac{\partial \ln \dot{\omega}_k}{\partial \ln [X_B]} \right)^2 < \varepsilon \tag{2.3}$$

where ε is a threshold value allowing the distinction between redundant and necessary species. In situations where the coupling between necessary and important species is not direct, the criteria based on Eq. (2.3) does not perform well. To overcome this intrinsic lack of the method, an iterative procedure is used to identify the necessary species. Necessary species directly coupled to the important ones are identified on the basis of the sensitivity coefficient J_k and are added to the pool of targeted species, providing new estimates of $\mathbf{J}$. This strategy is repeated until no additional species is introduced in the set of important species.

Directed Relation Graph approaches

Lu and Law (2005) introduced an original method based on Directed Relation Graph (DRG). In this approach, the degree of coupling between species is mapped to a Directed Relation Graph so as to identify the dependency relation between species. In this graph, nodes represent species, and directed edges illustrate the direct influence of one species to another. The strength of the edge connecting species A to species B is given by the normalized interaction coefficient r_{AB}:

$$r_{AB} = \frac{\sum_{r=1}^{N_r} \nu_{Ar} q_r \delta_{Br}}{\sum_{r=1}^{N_r} \nu_{Ar} q_r} \tag{2.4}$$

where δ_{Br} equals 1 if the rth reaction involves species B, or 0 otherwise.
If the normalized contribution r_{AB} of species B to the net production of species A is sufficiently important (higher than a given tolerance ε), removing species B from the mechanism could lead to non negligible errors on the production rate of species A. Through a linear graph search, necessary species are identified as species strongly coupled to target species or its dependent set of species, while species presenting a weak coupling with important ones are detected as redundant.

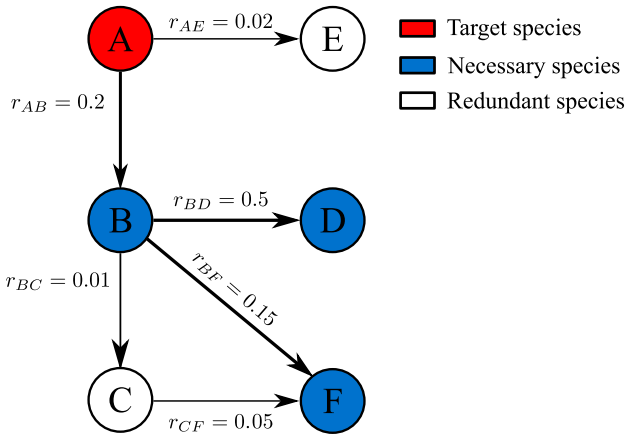

Figure 2.3: *Directed relation graph illustrating coupling between species. The interaction coefficient r_{AB} quantifies the degree of coupling between species A and B.*

Figure 2.3 shows a theoretical example of a graph obtained through the DRG method with a tolerance ε set to 0.10. The target species A is coupled with species B that is also strongly linked with species D and F. The species B, D and F form the set of dependent species and are considered as necessary species. On the contrary, species E and C featuring interaction coefficients lower than the tolerance are considered as redundant.
Contrarily to sensitivity analysis based methods DRG does not require the resolution of additional specific differential equation. Construction of the graph

mainly consists in analyzing a reference database composed by a selection of detailed chemistry solutions representative of the targeted combustion problems and operating conditions.
Capabilities of the DRG approach were demonstrated for the reduction of various detailed mechanisms (Lu and Law 2005; Lu and Law 2006a), however the reduction efficiency is limited by a number of deficiencies of the original method. First, as equal importance is given to all species some chemical compounds are kept in the mechanism though their influence on the target flame properties is low. To remedy this problem DRG with Error Propagation (DRGEP) method (Pepiot and Pitsch 2005), assuming damping of the error as it propagates along the graph, has been proposed. A second problem of the original DRG method concerns the treatment of systems with fast dynamics (QSS species or PEA reactions). Alternative definitions of the direct interaction coefficients based on different normalizing coefficients were therefore introduced (Lu and Law 2006b; Pepiot-Desjardins and Pitsch 2008). Finally, group-based interaction coefficients accounting for the effect of removing species on the target quantities were proposed (Pepiot-Desjardins and Pitsch 2008).
The DRG method along with its derived improvements is widely used for its efficiency, low cost and relatively easy implementation (Zheng et al. 2007; Pepiot 2008; Jaravel et al. 2017; Jaouen et al. 2017).

2.2.3 Identification of redundant reactions

The redundant species being identified, the second step of skeletal reduction consists in removing redundant reactions.

Sensitivity analysis

One major tool to detect unimportant reactions is based on sensitivity analysis. This method relies on the study of normalized sensitivity coefficients characterizing the effect of a reaction rate parameter change on the chemical system. A reaction is considered as unimportant if the perturbation of its rate has a small impact on the prediction of species concentrations. Either reaction rate or concentration sensitivity coefficients can be considered (Turányi and Bérces 1990), however reaction rate sensitivity coefficients are preferred as they can be expressed analytically from reaction rate expression. The element S_{kr} of the reaction rate sensitivity matrix, evaluating the impact of a perturbation in rate parameter k_r on the net production rate of species k, is given by:

$$S_{kr} = \frac{\partial \ln \dot{\omega}_k}{\partial \ln k_r} \tag{2.5}$$

An overall sensitivity coefficient S_r is then used to evaluate the impact of the reaction r on all the important species of the skeletal mechanism simultane-

ously:

$$S_r = \sum_{k=1}^{N_{target}} \left(\frac{\partial \ln \dot{\omega}_k}{\partial \ln k_r} \right)^2 \tag{2.6}$$

Sensitivity coefficients contain high quality information on the chemical system. However, as the size of the detailed scheme increases deriving meaningful information from the large amount of matrices elements becomes a difficult task.

Principal Component Analysis

To extract the most information from the sensitivity analysis, Vajda et al. (1985) suggested to analyze the eigenvalues of the sensitivity matrix. This method, called Principal Component Analysis (PCA), identifies the more important and strongly coupled reactions as those featuring the largest eigenvalues and the largest eigenvector elements respectively. PCA has been successfully applied to the reduction of a H_2/air mechanism (Vlachos 1996) and CH_4/air scheme (Brown et al. 1997).

Methods based on Directed Relation Graph previously discussed may also be used to identify reactions having a low impact on the targets.

2.2.4 Optimization-based skeletal reduction

Elimination of redundant species and reactions can also be performed through optimization-based techniques. These strategies aim at identifying the minimal set of species and their associated reactions that best reproduce the target flame quantities. This objective is expressed mathematically into a minimization problem represented as:

$$\min \left(\sum_{k=1}^{N} \lambda_k + \sum_{i=1}^{N_t} \mathcal{E} \left(\psi_i^d - \psi_i^{red} \right) \right) \tag{2.7}$$

where λ_k is a binary variable equal to 0 if the k^{th} species (or reaction) is removed from the detailed mechanism, or 1 if the species k (or reaction) is kept. The function $\mathcal{E}$ evaluates the capabilities of the reduced scheme to reproduce the N_t targets ψ. This non-convex minimization problem, featuring local optima, is generally solved using evolutionary algorithms such as Genetic Algorithms (GA). Edwards et al. (1998) first used GA to derive reduced model with controlled error on quantities of interest. Fixing the number of species in the reduced mechanism N_s^{red}, Elliott et al. (2006) identified through a binary encoded GA the $N_s^d - N_s^{red}$ redundant species and in a second stage originally suggested to optimize the reaction rate parameters to fit a set of experimental data. More recently, Sikalo et al. (2014) suggested to include the computational time associated to the integration of the chemical system in the minimization

problem. With such an approach one may expect to obtain an optimal kinetic scheme involving a minimal number of species featuring a reduced chemical stiffness.

2.2.5 Discussions

Though redundant species and reactions are removed, skeletal mechanisms preserve high predictive capabilities. Skeletal mechanisms can indeed be seen as a subset of the detailed mechanism which is valid for the prediction of the target quantities and on a specified application domain. Figure 2.4 shows a comparison of iso-octane ignition times obtained with detailed chemistry and skeletal mechanisms derived from DRGEP application (Pepiot-Desjardins and Pitsch 2008). Independently of the reduced scheme size, the low and high temperature regions are accurately reproduced. However, the description of the complex kinetic phenomena occurring in the negative temperature coefficient region is achieved only if a sufficient number of species is considered.

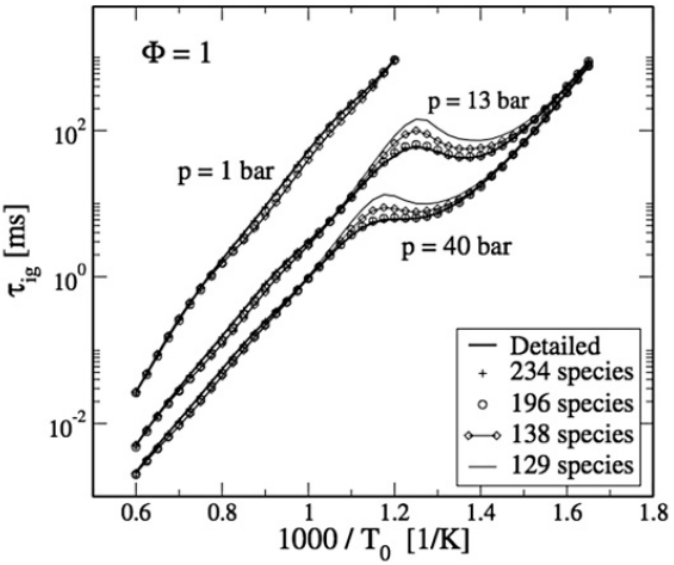

Figure 2.4: *Comparison of auto-ignition delay times predicted by a detailed kinetic scheme and skeletal mechanisms of different sizes (Pepiot-Desjardins and Pitsch 2008).*

As illustrated in Table 2.1, the reduction rate obtained through skeletal reduction can be high, especially if heavy fuels are considered. It is also noticeable that the reduction factor varies strongly from one study to another. As the efficiency of the reduction is mainly dependent on the targets (variables of interest and canonical combustion problems) and required precision, it is difficult to control it without compromising the predictive capabilities of the skeletal scheme. Unfortunately, the final number of species involved in the reduced mechanism is still too high and prevents the use of skeletal schemes for the

simulation of practical configurations. In addition, radical species featuring low characteristic time and small reactive thickness are kept in the reduced mechanism and require small integration time and high spatial resolution that are prohibitive. Finally, as previously explained, the coupling of such heavy mechanisms with turbulent combustion models is not straightforward.

Authors	Fuel	Reduction method	Initial mechanism	Final mechanism
Lu and Law (2008)	Methane	DRG DRGASA	53 species 325 reactions	36 species 222 reactions
Luche et al. (2004)	Kerosene	Atomic flux analysis and PCA	225 species 3493 reactions	134 species 1220 reactions
Pepiot (2008)	Iso-octane	DRGEP	850 species 7212 reactions	195 species 802 reactions
Jaravel (2016)	Dodecane	DRGEP	137 species 1222 reactions	47 species 452 reactions

Table 2.1: *Exemple of skeletal mechanisms for selected hydrocarbon/air mixtures.*

2.3 Analytic chemistry

2.3.1 Main characteristics of analytic schemes

As skeletal mechanisms cannot be used in simulations of real combustion chambers, these high-fidelity kinetic models are further reduced to obtain the so-called analytic schemes. Analytically-reduced mechanisms are derived through a chemistry-driven reduction approach aiming at i) decreasing the number of transported species and ii) lessening the stiffness of the chemical system. The key ingredient of the reduction method is to decouple the fast species and reactions from the controlling slow ones. Two main strategies are reported in the literature to remove short chemical time scales. The first one called, Partial-Equilibrium Approximation (PEA), assumes that some very fast reversible reactions, featuring high nearly balanced forward and backward reaction rates, are in partial-equilibrium. In this condition, algebraic relations between reactant and product concentrations are obtained. As an example, if the rth reaction is in partial-equilibrium, its reaction rate is assumed to be null $q_r = 0$, leading to:

$$K_{f,r} \prod_{k=1}^{N_s} [X_k]^{\nu''_{kr}} = \frac{K_{f,r}}{K_{eq,r}} \prod_{k=1}^{N_s} [X_k]^{\nu'_{kr}} \tag{2.8}$$

$$\prod_{k=1}^{N_s} [X_k]^{\nu_{kr}} = K_{eq,r} \tag{2.9}$$

The second approach referred to as Quasi-Steady State Approximation (QSSA) assumes that some fast species, featuring very low concentration and net pro-

duction rate, are in an equilibrium state. This supposition allows to shift these fast species, also called Quasi-Steady State (QSS) species, to an algebraic equations sub-system. According to Goussis and Maas (2011) and Lu and Law (2006c), a species k may be considered as QSS, if its production rate is rapidly balanced by its destruction rate, leading to low species concentration and negligible net production rate. With this assumption, algebraic equation may be derived for species concentration:

$$\dot{\omega}_k = 0 \tag{2.10}$$

$$K_{f,r} \prod_{k'=1}^{N_s} [X_{k'}]^{\nu''_{k'r}} = \frac{K_{f,r}}{K_{eq,r}} \prod_{k'=1}^{N_s} [X_{k'}]^{\nu'_{k'r}} \tag{2.11}$$

The use of QSSA and PEA can lead to an important reduction of the computational time. First, the elimination of some fast species from the set of transported equations reduces the stiffness of the system and allows an increase in the timestep. Secondly, the replacement of some transport equations by an algebraic system of equations may result in a speed-up of the computational process.

2.3.2 Selection of QSS species

To automate the derivation of analytically-reduced mechanisms various strategies have been proposed. These approaches mainly oriented towards QSS species identification rely on the study of species production rates, time-scale analysis and optimization algorithms. These methods are briefly presented hereinafter.

Analysis of species production rates

Considering QSS species characteristics, some criteria based on the comparison of production and destruction rates have been proposed (Chen 1997; Lepage 2000; Zambon and Chelliah 2007). For instance, Lepage (2000) suggested that a species k is in Quasi-Steady State if the following constraint is respected:

$$K_k = [X_k] \left(\frac{\dot{\omega}_k^c}{\dot{\omega}_k^d} - 1 \right) < \varepsilon \tag{2.12}$$

where $\dot{\omega}_k^c$ and $\dot{\omega}_k^d$ are the creation and destruction rate of species k. To improve the representativity of the methodology, K_k is integrated over the flame front and evaluated for different parametric conditions.

Very simple to use, these methods suffer however from various lacks (Montgomery et al. 2006). Though consistent with the definition of a QSS species, the criteria based on species production rates do not guarantee that the stiffness of the reduced mechanism is reduced. Moreover, these simple criteria do not account for the sensibility of the targeted quantities to the error induced by

assuming a species in QSS. Indeed, as some species are strongly coupled a small error introduced by the QSS approximation may lead to important deviations of the quantities of interest.

Time-scale analysis

Time-scale analysis is considered as a key ingredient for QSS species identification. The Computational Singular Perturbation (CSP) first introduced by Lam (1985) exploits the eigenvalue analysis of the Jacobian matrix to decouple slow and fast subspaces. Species featuring small chemical timescales are considered as QSS, while species with large time scales are considered as slow and are transported in the system. Chemical timescales of the species τ_k are evaluated as the inverse of the eigenvalues of the Jacobian matrix $\mathbf{J}$. Providing a chemical time scale separating fast and slow sub-spaces therefore enables to identify the QSS species. As the Jacobian matrix is time dependent, the evaluation and diagonalization of the Jacobian matrix is complex and CPU demanding. To overcome these drawbacks some refinement procedures have been proposed (Lam and Goussis 1994; Lu and Law 2008), but the CSP strategy remains costly.

An alternative criterion combining lifetime and species sensitivity has been proposed by Løvås et al. (2002). This method called Level Of Importance (LOI) considers a species k as QSS if:

$$LOI_k = [X_k]\,\tau_k S_k^Q < \varepsilon \tag{2.13}$$

where τ_k is the lifetime of species k assumed equal to the inverse of the diagonal element of the Jacobian matrix. S_k^Q is the species sensitivity of the relevant variable Q on species k, and ε is a tolerance parameter discriminating rapidly exhausted species from slow ones.

This method simpler and less costly than CSP approach has been successfully used in a number of flame configurations (Løvås et al. 2002; Felden et al. 2018).

Optimization algorithms

Due to the difficulties related to QSS species identification, Montgomery et al. (2006) used Genetic Algorithm to optimally detect the species that can be viewed as QSS. As previously described for skeletal reduction, this brute force approach seeks the set of QSS species that minimizes the error between the reduced and the detailed mechanism regarding the capture of selected flame properties on a defined range of operating conditions. This method has proven to be efficient for the development of accurate reduced mechanisms. It must however be pointed out that it is costly as it requires to solve the system of differential equations for each reduced scheme considered.

2.3.3 Discussions

Provided that QSS species are properly identified, the application of QSS approximation does not affect much the predictive capabilities of the initial complex kinetic mechanism. A posteriori validation of analytically-reduced mechanisms shows that the flame structure and pollutant species are well recovered. As analytic schemes retain important chemical pathways and chemical compounds they also conserve a physical representation of the chemical phenomena. Predictive capabilities of analytic schemes are illustrated in Fig. 2.5. This figure compares the evolution of species mass fraction predicted by detailed and analytically-reduced schemes during constant pressure auto-ignition. It is observed that only small chemical information is lost during chemistry reduction since intermediate species are well captured.

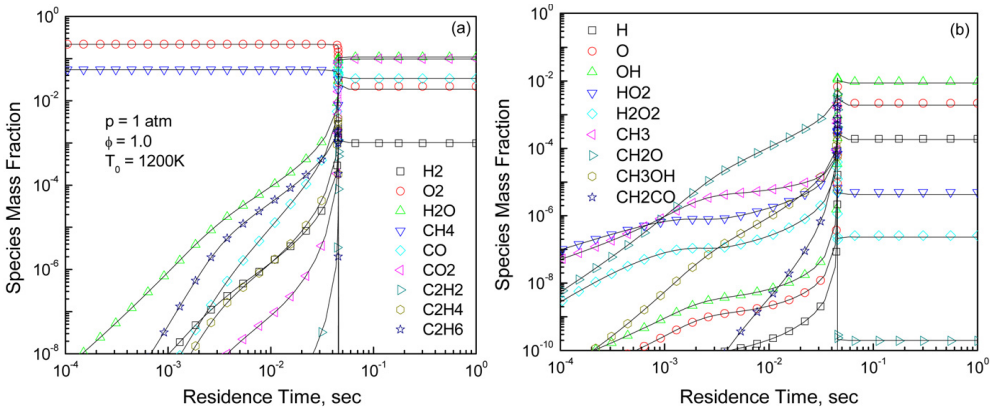

Figure 2.5: *Mass fraction profiles for major species (left) and minor species (right) during constant pressure auto-ignitions (Lu and Law 2008). Detailed chemistry solution (lines) is compared with analytically reduced chemistry (symbols).*

Until recently the use of analytic mechanisms was limited to the study of academic configurations (Sankaran et al. 2007; Yoo et al. 2011; Vié et al. 2015; Miguel-Brebion et al. 2016). This may be explained by various disadvantages associated with the method. First, as shown in Table 2.2, the number of transported species may be important, especially for heavy multi-components hydrocarbon fuels. Then, when the system of algebraic equations is complex and non-linear, the resolution of the system can be more expensive than solving the differential equations leading to important computational times. Thirdly, though QSS species are eliminated from the system of equation, analytically reduced mechanisms still contain intermediate species that may impose small timesteps in an explicit framework.

With the progresses in computational hardware, analytic mechanisms have recently gained considerable interest for the simulations of practical combustion chambers (Jaravel et al. 2017; Jaouen et al. 2017; Franzelli et al. 2017; Felden

et al. 2018; Felden et al. 2018). However, it must be underlined that the cost associated with these simulations is more important than with classical strategies. If heavy hydrocarbon molecules such as soot precursors are targeted, we expect that more chemical paths and species will be required, increasing even more the CPU costs. Additionally, derivation of analytic kinetic schemes describing the combustion of complex and heavy fuels such as alternative fuels may results in high dimensionality mechanisms.

Authors	Fuel	QSS species identification method	Initial mechanism	Final mechanism
Lu and Law (2008)	Methane	CSP	36 species 222 reactions	21 species 222 reactions
Luche (2003)	Kerosene	Lepage (2000) criterion	134 species 1220 reactions	94 species 1220 reactions
Pepiot (2008)	Iso-octane	LOI	195 species 802 reactions	100 species 802 reactions
Jaravel (2016)	Dodecane	DRGEP	47 species 452 reactions	27 species 452 reactions

Table 2.2: *Exemple of analytic mechanisms for selected hydrocarbon/air mixtures.*

2.4 Global and semi-global chemistry

2.4.1 Main features of global mechanisms

Global mechanisms are composed by few major species interacting through a reduced number of global reactions. These mechanisms are built to reproduce global flame quantities such as: adiabatic temperature, laminar premixed flame speed or auto-ignition delay times (Westbrook and Dryer 1981; Jones and Lindstedt 1988; Martin 2005; Fernandez-Tarrazo et al. 2006). A wide variety of strategies has been proposed to build reduced global mechanisms. Two main stages are however common for most global scheme derivation approaches:

- **Selection of species and reactions.** First, a set of species and associated reactions are proposed to describe the chemical processes. The choice of the species (number and nature) intervening in the global scheme results from a compromise between the computational cost and the level of accuracy. The number of species considered directly impacts the prediction of the adiabatic temperature and the description of the flame structure. Regarding the definition of the global reactions, most strategies rely on kinetic intuition and flame structure analysis and rarely on more refined techniques such as Partial-Equilibrium Approximation or Quasi-Steady State Approximation (Jones and Lindstedt 1988).

- **Selection of reaction rate parameters.** Once the reduced mechanism is chosen, the second step consists in selecting the kinetic rate parameters so that the target quantities are well reproduced. Kinetic rate parameters might be evaluated through experimental measurement fitting, asymptotic analysis or optimization. As low order mechanisms are naturally unable to predict the laminar flame speed evolution over the whole flammability range, equivalence ratio dependent kinetic rate parameters may be introduced to improve predictive capabilities (Fernandez-Tarrazo et al. 2006; Franzelli et al. 2010).

During the last 40 years, numerous global kinetic schemes were developed. To illustrate the different strategies previously introduced some examples of reduced schemes are presented.
In the pioneering work of Westbrook and Dryer (1981) a method to build two-step schemes for the oxidation of hydrocarbon fuels was proposed. The structure of the reduced mechanisms was defined exploiting the two layers flame structure of premixed hydrocarbon/air flames characterized by a rapid oxidation of the fuel and a slow consumption of intermediate species. Reaction rate parameters were optimized by hand to capture the evolution of the flame speed and equilibrium CO concentrations on a wide range of equivalence ratios and pressures. With non-unity reaction orders for reactants, the global scheme accurately retrieves the global quantities targeted, but it suffers from an unstable numerical behavior.
Jones and Lindstedt (1988) used flame structure analysis and results from sensitivity analysis and PEA to derive a generic four-step mechanism. The kinetic rate parameters of the two reactions zone model were manually tuned to capture the flame structure of both premixed and non-premixed flames. Unfortunately, if the agreement with experimental data is satisfactory for counterflow and lean premixed flames, predictive capabilities of the reduced scheme deteriorate for stoichiometric and rich mixtures.
Another major contribution was made by Franzelli et al. (2010) who developed an empirical method to build two-step mechanisms valid on a wide range of operating conditions. In this work, pre-exponential factors of the two reactions are expressed as equivalence ratio dependent functions whose values are optimized to fit laminar flame speeds and obtain a rapid reach of the equilibrium. Selection of the reaction orders of the first reaction is made to model the impact of pressure on laminar flame speed. Global kinetic schemes built with this strategy have shown capacity to adequately reproduce the laminar flame speed for the whole flammable region, and the burnt gas temperature for lean and moderately rich mixtures (Franzelli et al. 2012; Paulhiac 2015).
An original approach based on genetic optimization was introduced by Polifke et al. (1998). Instead of selecting the chemical rate parameters by hand or by kinetic intuition, an evolutionary optimization algorithm is used to automatically identify the best set of unknown kinetic coefficients. Moreover, contrarily

to classical global reduction methods that target global flame properties, the optimization procedure aims at capturing species production or heat release rate. This strategy provides a satisfactory description of flame temperature and major species, but intermediate species (CO and H_2) profiles do not match the reference solution. In addition, the optimization is performed for a unique equivalence ratio limiting the overall representativity of the procedure.
Following the work of Polifke et al. (1998), many reduced schemes were developed using genetic algorithms (Martin 2005; Abou-Taouk et al. 2013; Farcy et al. 2014).

2.4.2 Discussions

As they are cost-effective and easily coupled with turbulent motions, low-order kinetic schemes are widely used for LES of large scale combustion systems (Hermeth et al. 2014; Abou-Taouk et al. 2016; Volpiani et al. 2017). However as discussed hereinbefore, reduced schemes only reproduce global flame properties, and are not able to capture complex chemistry phenomena such as flame ignition or extinction. Generally built to describe premixed flame structure, reduced-order schemes do not account for strain effects and fail to predict non-premixed combustion mode. Finally, as few intermediate species are included pollutant formation processes are not described.

2.5 Tabulated chemistry

2.5.1 Main features of tabulated chemistry approaches

A widely used approach to account for complex chemistry effects at a low computational cost is the tabulated chemistry strategy. This method relies on the fact that the chemical trajectories accessed during the combustion process are confined to a sub-space of low dimension N_c called manifold. Thermochemical properties $\psi = \{Y_1, ..., Y_{N_s}, \dot{\omega}_1, ..., \dot{\omega}_{N_s}, T\}$ are then parametrized as a function of a reduced number of coordinates φ:

$$\psi = F\left(\varphi_1, ..., \varphi_{N_c}\right) \tag{2.14}$$

The function F does not have an analytical expression but is defined in a discrete form through a chemical look-up table evaluated along the manifold with detailed chemistry. As a consequence, tabulated chemistry approaches not only allow a reduction of the number of equations to solve but also enable a decrease of the CPU time associated with chemical source term evaluation.

The identification of the low-dimensional manifold and its control parameters φ is a key challenge of the strategy. Maas and Pope (1992b) first suggested that the manifold is composed by the slow time scales determined by examining the eigenvalues of the chemical system. This methodology has been successfully

applied to syngas/air 0-D reactors where the solution is near the equilibrium state (Maas and Pope 1992b; Maas and Pope 1992a). However, shortcomings arise when low temperature effects are to be captured (Gicquel et al. 2000). Other strategies based on physical considerations assume that combustion can be described by a collection of 1-D laminar flame elements called flamelets. Depending on the turbulent flame studied different flame prototypes and control parameters are used to be representative of the dominant combustion regime:

- For premixed and weakly stratified configurations, Gicquel et al. (2000) and Van Oijen et al. (2001) independently suggested to build the manifold from 1-D laminar premixed flames. Chemical trajectories are mapped as a function of two coordinates: the progress variable Y_c describing the progress of the reaction and the mixture fraction Z characterizing the fresh gas equivalence ratio. Flame Prolongation of ILDM (FPI) and Flamelet Generated Manifold (FGM) have shown great capabilities to reproduce premixed and weakly stratified flame structures (Fiorina et al. 2015).

- Diffusion flames have been first modeled using chemical look-up tables made of steady counterflow diffusion flames parametrized by both the mixture fraction Z and the scalar dissipation rate χ (Peters 1984). Then, to account for flame extinction or re-ignition phenomena, Pierce and Moin (2004) proposed to tabulate unsteady counterflow flames with the progress variable as a new control parameter. This tabulated chemistry method called Flame-Progress Variable (FPV) was applied successfully in a number of configurations (Pitsch and Ihme 2005; Mueller and Pitsch 2012).

- Autoignition phenomena may be accounted for through the tabulation of homogeneous autoignition calculations. As in FPI or FGM models, thermochemical properties are expressed as a function of a progress variable and a mixture fraction (Embouazza 2005). Perfectly or partially stirred reactors simulations can also be used to map the chemical trajectories of autoignition processes. In this case, the residence time is used as a new coordinate (Fichet 2008).

2.5.2 Discussions

Tabulated chemistry strategies are widely used for the simulation of various turbulent flame configurations (Kuenne et al. 2011; Mercier et al. 2014; Perry et al. 2017). However, when applied in real configurations these approaches show some limitations. As described in section 1.2.2 industrial devices exhibit complex chemical flame structure where both premixed and non-premixed regimes may be encountered. To treat these mixed combustion regimes specific tabulation strategies are required to capture pollutant species such as CO (Fiorina et al. 2005; Franzelli et al. 2013). Bykov and Maas (2007) first proposed

to identify the slow dimension manifolds accessed in real flames through an iterative method. A similar approach introduced by Nguyen et al. (2010) assumes that the chemical sub-space of complex flames is well described in the (Z,Y_c) subspace parametrized by: Z, Y_c and their scalar dissipation rates. All these studies concluded that to recover the flame structures observed in practical combustion systems various flame archetypes must be included in the manifold and the number of control parameters must be increased. If the computation of individual flame element is possible, the tabulation of these different types of flames in one unique table raises several issues. Among them we can mention coordinates identification difficulties (Ihme et al. 2012; Niu et al. 2013), storage issues on massively parallel machines (Ribert et al. 2006; Ihme et al. 2009) and theoretical difficulties to close the balance equations for the coordinates in both laminar and turbulent context (Fiorina et al. 2015). Another difficulty associated with tabulated chemistry is the simultaneous treatment of complex phenomena such as: heat losses, multiple fuel inlets or dilution by hot gases. Taking into account all these mechanisms can also lead to storage issue due to the high dimension of the look-up table and theoretical difficulties to identify flame prototypes combining these effects. Finally, as some chemical phenomena, such as thermal NO_x or soot precursors formation, are very slow in comparison with carbon chemistry, classical tabulated chemistry approaches must be refined. To properly account for slow chemistry processes, additional modeling efforts relying on additional control variables (Ihme and Pitsch 2008; Pecquery et al. 2014) are required.

2.6 Optimized Reduced Chemistry

A new chemistry reduction approach, called Optimized Reduced Chemistry (ORCh), has been recently developed (Jaouen et al. 2017). This hybrid strategy allows the derivation of optimized analytic mechanisms through three main steps:

- First, the chemical trajectories accessed in a given problem configuration are identified. A priori analysis of the chemical trajectories is performed using a stochastic approach. Particles representative of both the inlet boundary condition and the burnt gases state (to secure flame ignition) are tracked in a Lagrangian framework. A deterministic micro-mixing model is then used to evaluate a reduced set of representative chemical trajectories.
- Classical chemistry-driven reduction techniques are then applied to the one-dimensional deterministic trajectories in order to generate an analytic mechanism. Skeletal reduction is performed with the DRGEP approach, while QSS species are identified through reaction rate analysis.
- Kinetic rate coefficients of the analytically-reduced mechanism are finally optimized to ensure a proper reproduction of the reference chemical tra-

jectories. To extend the domain of validity of the reduced scheme additional flame archetypes such as premixed flames can be included.

The resulting optimized reduced mechanisms are smaller than classical analytic mechanism, leading to a reduction of the computational cost. This increase of the reduction efficiency may be attributed to two main reasons. First, as genetic optimization is used as a corrective step after reduction the limits of traditional DRGEP and QSS approximation are extended to allow higher reduction factor. Secondly, as the reduction and optimization target a reduced set of chemical trajectories fewer chemical paths and species are required.
This approach has been successfully applied to the reduction of the RAMEC mechanism dedicated to methane oxy-combustion in auto-thermal reforming conditions (Jaouen et al. 2017). Recently, optimized reduced mechanism devoted to kerosene air combustion has been derived for aeronautical operating conditions (Jaouen 2017).

2.7 Hybrid tabulated/transported chemistry

Combined methods based on tabulated and global kinetic schemes have been developed to make the most of both strategies. As previously discussed, tabulated chemistry allows to include complex chemistry by transporting only few control variables. However, as the look-up table restrain the chemical trajectories to a unique canonical combustion regime and set of boundary conditions, tabulated chemistry models fails when used in real configurations. Finite rate chemistry methods, on the contrary, naturally accounts for a wider range of phenomena such as : heat losses, dilution or multiple inlet compositions. The combined use of these two methods is then expected to improve the predictive capabilities.
In the context of soot modeling, Lecocq et al. (2013) proposed a hybrid technique relying on a reduced global kinetic scheme to describe the flame structure and a tabulated chemistry model to account for the soot precursors formation. The hybrid model was compared against fully tabulated strategy showing very small differences for the flame structure, and more important departures for soot precursors (Franzelli et al. 2015). Jaravel (2016) recently extended this approach to the prediction of NO_x by coupling a global two-step mechanism with the tabulated chemistry model for NO_x called NOMANI (Pecquery et al. 2014).
An interesting combination between tabulated and detailed transport chemistry was proposed by Ribert et al. (2014). The approach called Hybrid Tabulated-Transported Chemistry (HTTC) conserves the full detailed mechanism, but transports only major species featuring non zero concentration in fresh an burnt gases. Intermediate species exhibiting a self-similar behavior are efficiently tabulated as a function of a reduced set of control parameters, namely a mixture fraction and an optimized progress variable. By removing intermediate species

from the set of transported equations, HTTC model allows both a reduction of computational time and a diminution of the stiffness of the chemical system. This method has been successfully applied to 1-D laminar unstrained and strained premixed methane/air flames (Ribert et al. 2014). Unfortunately, for more complex fuels such as kerosene heavy intermediate species do not share a generic behavior (Duboc et al. 2015), leading to a more complex and costly implementation of the HTTC approach.

2.8 Summary

Figure 2.6 summarizes the main chemistry modeling routes as long as their respective advantages and drawbacks. Transported chemistry approaches rely either on the definition of a few global reactions modeling the macroscopic characteristic of combustion, or on the successive elimination of species and reactions that are unimportant or too fast. Alternative approaches based on the tabulation of flame solutions evolving on a reduced chemical subspace have been proposed. Hybrid methods using optimization or combining transported and tabulated chemistry approaches have also been introduced to improve the classical chemistry modeling strategies.
In this thesis, an alternative approach consisting in building virtual reaction mechanisms capable of describing user-defined flame properties on both premixed and non-premixed flame archetypes is proposed. This new flame chemistry model is presented and validated both in laminar and turbulent environments in the next Chapters.

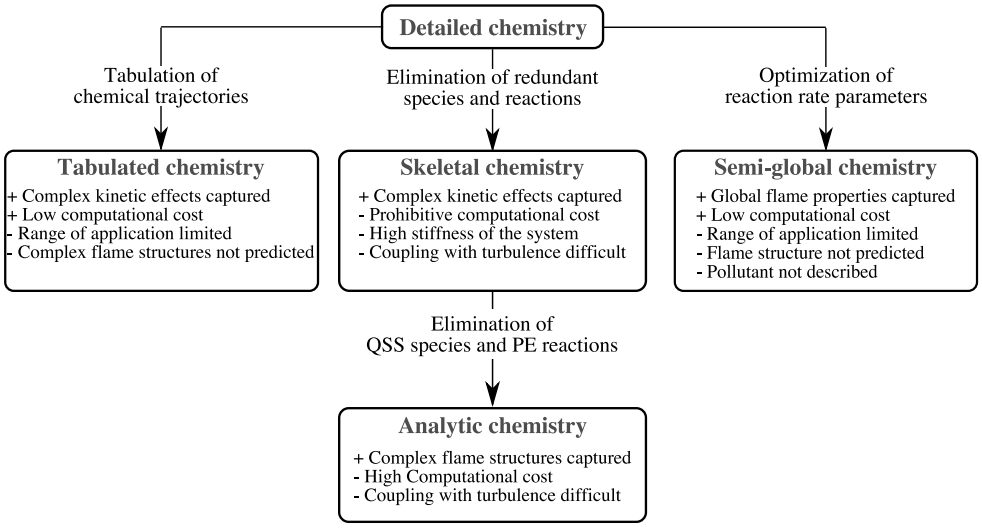

Figure 2.6: *Main chemistry description strategies.*

Part II

Virtual optimized chemistry approach

Chapter 3

Methodology for building-up virtual kinetic schemes

Contents

In this chapter, a new chemistry modeling strategy called virtual optimized chemistry is introduced. First, the concept of virtual species and reactions is presented and the general architecture of virtual optimized mechanisms is described. Then the general approach for the derivation of the main virtual scheme devoted to the prediction of flame/flow field interaction is discussed. Finally, the concept of virtual satellite scheme for the prediction of pollutant species is illustrated for CO.

3.1 Objectives

As discussed in Chapter 1, the proper description of complex and multiple combustion regimes is essential in simulations of industrial combustion chambers. To account for mixed combustion modes while keeping low CPU costs, a new and original approach, called virtual optimized chemistry, has been developed and is presented in this Chapter. First, the concept of virtual optimized mechanism is introduced in section 3.2. The procedure employed for the optimization of virtual kinetic schemes is then presented. Thirdly, section 3.4 details the derivation of the so-called main mechanism dedicated to the capture of the flame/flow field interaction. Finally, the concept of satellite sub-mechanisms devoted to the prediction of pollutant species formation mechanisms is applied to CO prediction in section 3.5.

3.2 Virtual chemistry concept

The virtual reaction mechanism is optimized to predict specific flame properties requested by a Research and Development engineer on an ensemble of user-defined flame configurations. The properties of interest may be for instance the flame temperature, the consumption speed and the formation of a given pollutant (CO, NO_x, soot precursors, etc.). The target flame prototypes must be representative of the variety of combustion elements encountered in practical applications. In the present work, the optimized scheme targets both premixed and non-premixed adiabatic flame archetypes so that complex flame structures are captured. The reference database could however be enlarged by adding other reactive configurations such as 0-D homogenous reactors or non-adiabatic cases, if these combustion events occur in the targeted application.

The virtual mechanisms are generated through an original method relying on:

- Building-up a reduced chemical mechanism from scratch instead of reducing a detailed scheme. Contrarily to classical reduction methods whose principle is to reduce the number of species and reactions to achieve a certain agreement with the reference mechanism, we suggest to gradually increase the dimensionality of the kinetic scheme so that the quantities of interest are properly described.
- Using virtual global reactions that do not model real kinetic paths between species. Virtual optimized mechanism may be seen as a mathematical architecture designed to retrieve a set of user-defined physical targets.
- Using virtual species whose physical properties (thermodynamic and transport) are optimized to capture real mixture-averaged properties. In opposition with classical reduction methods (Westbrook and Dryer 1981; Jones and Lindstedt 1988) that use real species, in this approach, species

do not represent real chemical entities but are considered as degrees of freedom of the model. It must however be underlined that when pollutant species are targeted the virtual mechanism involves virtual species that model the real chemical compound of interest.

The virtual optimized mechanisms architecture is illustrated in Fig. 3.1. The proposed strategy consists in building and optimizing independent blocks of virtual kinetic schemes dedicated to the capture of a given flame property. The main mechanism models the mixture-averaged thermodynamic and transport properties as well as the heat released by combustion. As a consequence, this chemical scheme also governs the temperature profiles as well as the flame front consumption speed. The main virtual kinetic block is coupled with the flow governing equations through species and energy conservation equations. It therefore impacts the mixture density and temperature fields, and as such describes the flame/flow field interactions.

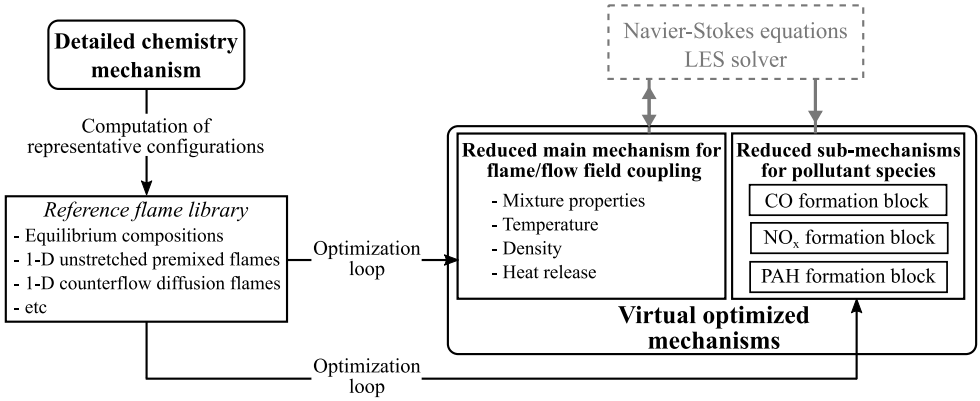

Figure 3.1: *Virtual optimized mechanisms architecture.*

As pointed out in Chapter 2, species production and consumption involve multiple chemical pathways interacting over a high variability of time scales, leading to important numerical stiffness. The temporal integration of such stiff chemical system therefore requires the use of either prohibitively small timesteps or costly algorithms. To simplify this issue independent satellite sub-mechanisms have been introduced. Unlike the main mechanism, the satellite sub-mechanisms are not involved in the closure of mass, momentum and energy equations but are only devoted to the description of pollutant formation. To limit the interactions between slow and fast chemical species, each sub-mechanism is dedicated to the prediction of a given species such as for instance CO, NO_x or soot precursors. Both main and sub-mechanisms are trained through genetic optimization to recover a target database composed of reference solutions representative of different canonical combustion problems. The choice of the flamelet library used during the optimization process is of importance as it will be discussed in section 4.2.2.

Virtual schemes (including main mechanism and sub-mechanisms) have a structure similar to conventional mechanisms. Hereafter, the superscript v will refer to quantities associated to virtual species and reactions whereas the superscript d will denote detailed chemistry formalism. Consequently, a detailed mechanism involving N_s^d species of chemical symbols $\mathcal{V}_k^d$ interacting through N_r^d reactions is formulated as follows:

$$\sum_{k=1}^{N_s^d} \alpha_{k,r}^{'d} \mathcal{V}_k^d \rightarrow \sum_{k=1}^{N_s^d} \alpha_{k,r}^{''d} \mathcal{V}_k^d \quad \text{for } r = 1, ..., N_r^d \tag{3.1}$$

where $\alpha_{k,r}^d$ are the stoichiometric coefficients per mass unit. Similarly, the virtual mechanism reads:

$$\sum_{k=1}^{N_s^{v_j}} \alpha_{k,r}^{'v_j} \mathcal{V}_k^{v_j} \rightarrow \sum_{k=1}^{N_s^{v_j}} \alpha_{k,r}^{''v_j} \mathcal{V}_k^{v_j} \quad \text{for } r = 1, ..., N_r^{v_j} \tag{3.2}$$

where the superscripts v_j identify the j^{th} virtual mechanism (main and sub-mechanisms for CO, PAH, NO_x, ...).

With these definitions, the final systems of conservation equations associated to both main and satellite sub-mechanisms may be written as:

Main mechanism:

$$\begin{aligned}
\frac{\partial \rho^v}{\partial t} + \frac{\partial}{\partial x_i}\left(\rho^v u_i^v\right) &= 0 \\
\frac{\partial \rho^v u_j^v}{\partial t} + \frac{\partial}{\partial x_i}\left(\rho^v u_i^v u_j^v\right) &= -\frac{\partial P^v}{\partial x_j} + \frac{\partial \tau_{ij}^v}{\partial x_i} \\
\frac{\partial \rho^v Y_k^{v_m}}{\partial t} + \frac{\partial}{\partial x_i}\left(\rho^v Y_k^{v_m} u_i^v\right) &= -\frac{\partial}{\partial x_i}\left(\rho^v Y_k^{v_m} V_{k,i}^{v_m}\right) + \dot{\omega}_k^{v_m} \\
\frac{\partial \rho^v e_t^v}{\partial t} + \frac{\partial\left(\rho^v u_i^v e_t^v\right)}{\partial x_i} &= \frac{\partial}{\partial x_i}\left(\lambda^v \frac{\partial T^v}{\partial x_i} - \rho^v \sum_{k=1}^{N_s^{v_m}} Y_k^{v_m} V_{k,i}^{v_m} h_k^{v_m}\right) \\
&\quad + \frac{\partial}{\partial x_i}\left(\sigma_{ij}^v u_j^v\right)
\end{aligned} \tag{3.3}$$

Satellite-mechanism:

$$\frac{\partial \rho^v Y_k^{v_{sj}}}{\partial t} + \frac{\partial}{\partial x_i}\left(\rho^v Y_k^{v_{sj}} u_i^v\right) = -\frac{\partial}{\partial x_i}\left(\rho^v Y_k^{v_{sj}} V_{k,i}^{v_{sj}}\right) + \dot{\omega}_k^{v_{sj}} \tag{3.4}$$

where the virtual properties of the mixture, evaluated by integration of the system 3.3, are identified by the superscripts v. The superscripts v_m and v_{sj} denote the quantities associated with the main mechanism and the j^{th} virtual satellite scheme respectively.

3.3 Virtual scheme optimization procedure

This section aims at presenting the optimization method used for virtual chemistry mechanism building. The optimization problem is first introduced. A short description of minimization technique is then provided. The evolutionary algorithm implemented is further described.

3.3.1 Problem definition

One major ingredient of the strategy is the optimization of species physical properties and reaction rate parameters to accurately recover a set of target flame properties. This inverse problem expresses as a constraint minimization problem:

$$\begin{cases} \text{minimize} \quad \mathcal{E}\left(\mathbf{w}^v\left(\mathcal{X}^v\right), \mathbf{w}^d\left(\mathcal{X}^d\right)\right) \\ \text{submitted to} \quad \mathcal{S}\left(\mathbf{w}^v\left(\mathcal{X}^v\right)\right) \end{cases} \tag{3.5}$$

where $\mathcal{E}$ is the function comparing the virtual and detailed reference solutions, often called fitness or cost function. Though the optimization problem is formally multi-objective (multiple flame and mixture variables are targeted) a unique cost function expressed as a linear combination of the various objectives is used. The vector $\mathcal{X}$ refers to the set of free parameters describing the thermodynamic, transport and kinetic rate properties and $\mathbf{w} = (\rho u, \rho v, \rho w, \rho Y_k, \rho E)$ is the state vector. Detailed state vector $\mathbf{w}^d$ and virtual state vector $\mathbf{w}^v$ are constrained by $\mathcal{S}$ referring to the set of conservation equations introduced in Chapter 1 and expressed here in vectorial notation:

$$\frac{\partial \mathbf{w}}{\partial t} + \nabla.\mathbf{F}\left(\mathbf{w}, \mathcal{X}\right) = \mathbf{s}\left(\mathbf{w}, \mathcal{X}\right) \tag{3.6}$$

where $\mathbf{F}$ is the flux tensor and $\mathbf{s}$ the source term vector.
Following the work of Polifke et al. (1998), the identification of the best set of free parameters $\mathcal{X}^v$ is performed through an efficient and automated procedure. The following section briefly presents the main classes of optimization methods that may be used to build the virtual kinetic schemes.

3.3.2 Optimization methods

Two main classes of minimization approaches may be identified in the literature: deterministic and stochastic methods. The two following paragraphs present fundamental principles of these two optimization approaches and discuss their applicability to handle the problem of interest.

3.3.2.1 Deterministic optimization algorithms

Deterministic optimization methods include all optimization algorithms using a specific rule to guide the evolution from one set of candidate parameters to

another (Cavazzuti 2013). With the advent of computer power, a wide variety of deterministic methods have been proposed. A non-exhaustive list of these methods is here discussed.

Classical gradient-based approaches use the cost function and its gradient to iteratively identify a new set of optimum parameters. The first order gradient-based method, called gradient descent, assumes that the function to minimize decreases fastest in the direction of its gradients. Starting from an initial guess $\mathcal{X}^0$, the optimum set of parameters is evaluated as:

$$\mathcal{X}^{k+1} = \mathcal{X}^k - \alpha^k \nabla \mathcal{E}\left(\mathcal{X}\right) \tag{3.7}$$

where α^k is the step length. To improve the convergence speed, a higher order approach named Newton's algorithm has been introduced. This method uses both the gradient and the hessian of the cost-function:

$$\mathcal{X}^{k+1} = \mathcal{X}^k - \alpha^k H\left(\mathcal{E}\left(\mathcal{X}\right)\right)^{-1} \nabla \mathcal{E}\left(\mathcal{X}\right) \tag{3.8}$$

If these approaches feature very high quality in terms of convergence speed or low dependence on the dimensionality of the problem, their use for the optimization of complex problems is limited. This may be first explained by the fact these optimization algorithms require high quality cost function such as continuity, and derivability. Then, as gradient-based methods tend to converge to the nearest local minimum the result of the optimization strongly depends on the initial guess.

Surface mapping approach aims at approximating the surface of the objective function by a simple algebraic expression (polynomials, spline functions ...) obtained within a subspace χ of the parameter space $\mathcal{X}$. In this method, optimization of the cost function no longer requires costly evaluation of cost function Jacobian or Hessian but rather the simple evaluation of algebraic expressions. However, when the function to optimize feature highly structured shape the approximation of the cost function by an analytic expression is likely to produce large errors and affect the optimization procedure.

3.3.2.2 Stochastic methods

A wide variety of stochastic search methods may be identified in the literature going from simulated annealing to particle swarm or genetic algorithm. The main ingredient of these approaches is the introduction of randomness or probability rules during the search process. If deterministic algorithms may easily converge towards local optimum, stochastic approaches overcome this problem by injecting randomness in the search direction (Gentle et al. 2012). By balancing exploration of the search space (through randomness) and exploitation of the information contained in the cost function, stochastic approaches are

able to identify global optima. Another characteristic of these optimization algorithms concerns their domain of application. As stochastic methods do not require the evaluation of the gradient of the cost function, they can be used to minimize any kind of function going from high quality functions to highly structured and noisy cost-function. Unfortunately, stochastic approaches feature low convergence rate and require numerous cost function evaluations in comparison with deterministic methods.

3.3.2.3 Discussions

Depending on the problem treated, the two techniques can feature very different behaviors. In this study, as the cost function is evaluated through the resolution of a non-linear system of differential equations, it can features multiple ridges and valleys (Elliott et al. 2004) as well as discontinuities (because of calculations non convergence). This is illustrated in Fig. 3.2 showing the evolution of a fitness function observed during optimization of a unique kinetic parameter. One may notices that the function is not defined on the whole domain and exhibits high frequency oscillations that may be accounted for the non-linearity of the system to solve. From these observations, stochastic methods appear as particularly adapted to handle the optimization of virtual mechanisms. As Genetic Algorithms have been used with success for the reduction of kinetic schemes (Polifke et al. 1998; Martin 2005; Farcy et al. 2014) this specific family of search optimization method is considered.

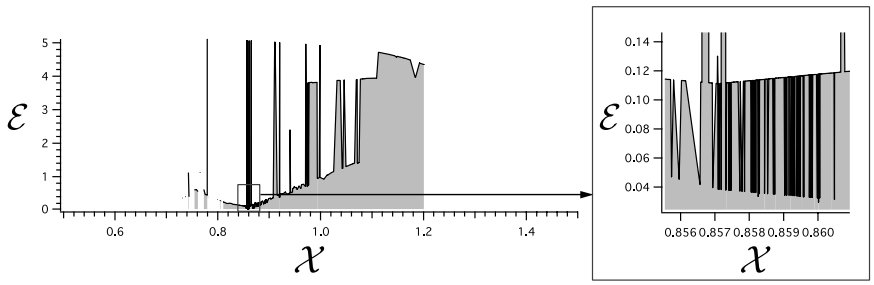

Figure 3.2: *Typical evolution of the fitness function for kinetic parameter optimization problem. Reproduced from (Martin 2005)*

3.3.3 Evolutionary algorithms principle

Evolutionary algorithms explore the domain by modeling biological evolution principles and hereditary laws. Following the evolutionary theory proposed by Darwin (1872), a number of optimization algorithms based on this concept were introduced. In this work, optimization of species thermodynamic properties and reaction rate parameters is performed using the genetic algorithm proposed by Holland et al. (1975) and later modified by Goldberg (1989). The evolutionary

algorithm principle implemented in the in-house optimization code is described in Fig. 3.3.

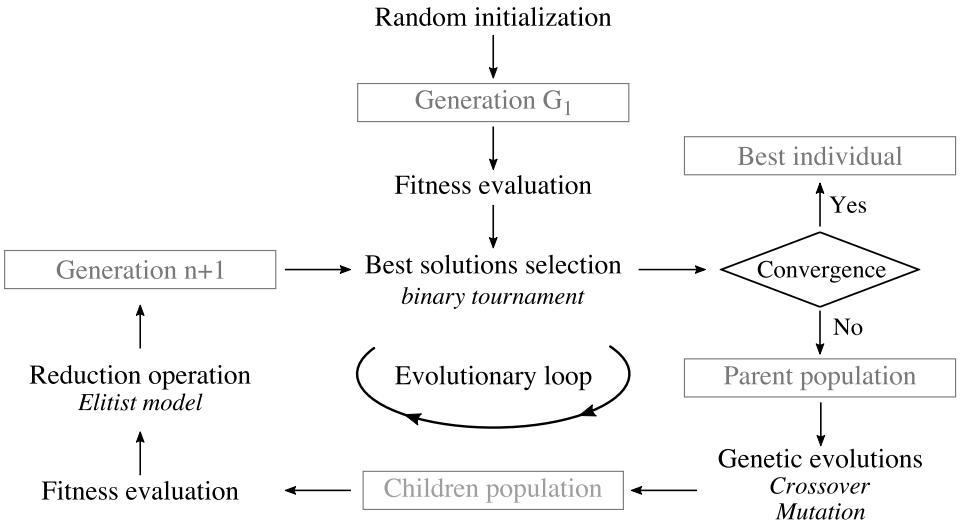

Figure 3.3: *Evolutionary algorithm principle.*

The main steps of the evolutionary algorithm may be summarized as follows:

1. In a first stage, the initial generation composed of a set of individuals, representing potential solutions, is randomly generated. Each individual is represented by a real vector also called chromosome whose values called gene correspond to the unknown parameters. Definition of the chromosomes for the calibration of the species thermodynamic properties and the kinetic parameters are given in Sec. 3.6.
2. Each individual (potential solution) of the first generation is then evaluated through the fitness function $\mathcal{E}$ that discriminates good solution candidates from the others.
3. The next step relies on population evolution through the application of three genetic operators:
   (i) A selection procedure is used to choose couples of fittest solutions that define the survivor parents. The selection operator is based on a k-tournament algorithm.
   (ii) A crossover operation is then applied on a couple of randomly chosen parents. This genetic operator imitates the hereditary process that mixes parental qualities towards potential improvement of the offspring. This operation is performed with a crossover probability $\mathcal{P}_c$.
   (iii) Eventually, mutation operation is randomly applied on children solutions to increase diversity. Every solution may undergo mutation

with a probability $\mathcal{P}_m$.

4. The predictive capabilities of every individual of the children population is then evaluated by comparing reference solutions to those obtained with the corresponding virtual models.
5. Finally, a reduction or filtering operation relying on tournament selection is applied to the total population formed by the merging between the parents' population and the children' population. To ensure a constant improvement of the generations an elitist model is used.

This evolutionary algorithm has been implemented in an in-house optimization code called MelOptim. Details about genetic operators, selection procedure and elitism model are given in Appendix A. The optimization code is coupled to the REGATH thermochemistry package (Darabiha and Candel 1992) developed at the EM2C laboratory to ensure the evaluation of the virtual kinetic models.

3.4 Virtual main scheme for flame structure prediction

The general methodology to build-up the main mechanism devoted to the description of flame/flow field interaction is presented. The structure of the virtual schemes is first introduced. Then, the optimization of virtual species properties and reaction rate parameters is discussed.

3.4.1 Main virtual mechanisms generation principles

We assume that the reactive mixture, composed of fuel (F), oxidizer (Ox) and an inert dilutant (D), is transformed into combustion products through a virtual mechanism. Products are modeled by a combination of $N_p^{v_m}$ virtual species P_k. Two virtual mechanism structures are investigated in this work:

- A one-step irreversible mechanism named M_1 transforming fuel and oxidizer in a set of $N_p^{v_m}$ virtual products:

$$\alpha_F^{v_m} F + \alpha_{Ox}^{v_m} Ox + \alpha_D^{v_m} D \rightarrow \sum_{k=1}^{N_p^{v_m}} \alpha_{P_k}^{v_m} P_k + \alpha_D^{v_m} D \qquad \text{(M1-1)}$$

- A two-step mechanism called M_2 composed of two consecutive reactions. It converts first the reactants into an intermediate species I, which is then transformed into virtual products P_k:

$$\alpha_F^{v_m} F + \alpha_{Ox}^{v_m} Ox + \alpha_D^{v_m} D \rightarrow \alpha_I^{v_m} I + \alpha_D^{v_m} D \qquad \text{(M2-1)}$$

$$\alpha_I^{v_m} I \rightarrow \sum_{k=1}^{N_p^{v_m}} \alpha_{P_k}^{v_m} P_k \qquad \text{(M2-2)}$$

Figure 3.4 illustrates the two consecutive stages required to build-up the main virtual scheme. First, the thermo-chemical and transport properties of the virtual species are optimized to mimic real mixture properties such as heat capacity, heat conductivity and mixture-averaged molecular weight. Table a) in Fig. 3.4 summarizes the physical properties optimized during the first stage of the procedure. The second step of the optimization aims at evaluating the kinetic rate constants of the virtual reactions detailed in Table b (Fig 3.4). The unknown parameters are fitted so that solutions obtained with the virtual scheme are as close as possible to a set of reference solutions obtained with a detailed chemistry mechanism. In the present study, the reference database is made of 1-D adiabatic laminar freely-propagating flames and 1-D non-premixed counterflow flames.

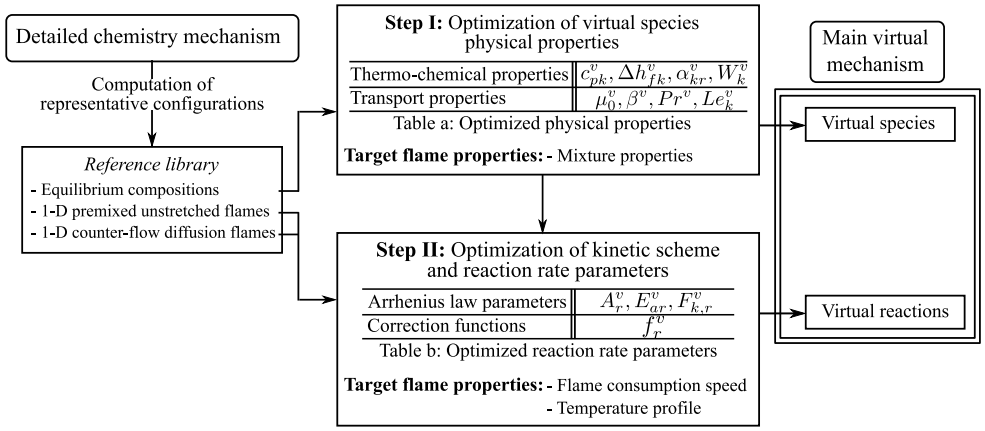

Figure 3.4: *Main virtual optimized mechanism generation procedure.*

The calibration of the main virtual scheme is performed step-by-step to minimize the total number of unknown that is identified at each step. The performance of the overall optimization procedure is therefore improved.

The optimization of virtual species physical properties and kinetic rate constants are discussed in section 3.4.2 and 3.4.3 respectively.

3.4.2 Optimization of virtual species properties

In a first step, the thermo-chemical and transport properties of the virtual species are optimized to recover averaged properties of the multi-component real mixture.

3.4.2.1 Thermodynamic properties

For both detailed and virtual formalisms, the quantity ψ is introduced to represent the mixture-averaged thermodynamic properties:

$$\psi^d = \sum_{k=1}^{N_s^d} \psi_k^d Y_k^d \tag{3.9}$$

$$\psi^{v_m} = \sum_{k=1}^{N_s^{v_m}} \psi_k^{v_m} Y_k^{v_m} \tag{3.10}$$

where the vector $\psi_k = \{h_k, c_{pk}\}$ gathers the enthalpy and the heat capacity at constant pressure of the k^{th} species. Following the NASA parametrization (McBride et al. 1993), c_{pk} and h_k are modeled by temperature dependent polynomial functions:

$$\frac{c_{pk}}{R} = a_{1k} + a_{2k}T + a_{3k}T^2 + a_{4k}T^3 + a_{5k}T^4 \tag{3.11}$$

$$\frac{h_k}{RT} = a_{1k} + \frac{a_{2k}}{2}T + \frac{a_{3k}}{3}T^2 + \frac{a_{4k}}{4}T^3 + \frac{a_{5k}}{5}T^4 + \frac{a_{6k}}{T} \tag{3.12}$$

The coefficients a_{lk} of species k corresponds to thermodynamic coefficients. Classically, these coefficients are given in thermodynamic database built to retrieve the evolution of species properties with the temperature. In this work, for any virtual species k, the $N_T = 6$ coefficients a_{lk} are optimized so that the properties of the real mixture are correctly described in both fresh and burnt gases:

$$\psi^{v_m}|^f = \psi^d|^f \tag{3.13}$$

$$\psi^{v_m}|^{eq} = \psi^d|^{eq} \tag{3.14}$$

where superscripts f and eq denote respectively fresh and equilibrium states. At this stage, evolution of the mixture thermodynamic properties (heat capacity and enthalpy) across the flame front is not explicitly targeted during the optimization process as the only local property considered is temperature. However, capability of the virtual scheme to capture mixture-averaged thermodynamic properties variation along the flame is *a-posteriori* verified

The description of mixture-averaged properties in the fresh gases is achieved by attributing real properties to reactants (F and Ox) and dilutant (D) species of the virtual mixture:

$$\psi_A^{v_m} = \psi_A^d \quad \text{for } A = \{F, Ox, D\} \tag{3.15}$$

In practice, this condition is fulfilled by imposing real thermodynamic coefficients to virtual species:

$$a_{lA}^{v_m} = a_{lA}^d \quad \text{for } A = \{F, Ox, D\} \quad \text{and} \quad l \in [1; N_T] \tag{3.16}$$

For instance, for CH_4/air combustion, F, Ox and D have the thermo-chemical properties of CH_4, O_2 and N_2 respectively. In the following, the subset of species composed by fuel, oxidizer and dilutant species is referred as A.

The modeling of burnt gases thermodynamic properties is more complex as for hydrocarbon/air mixtures the equilibrium composition may involve hundreds of real species. To overcome this difficulty, the in-house genetic algorithm presented in subsection 3.3.3 is used to identify both the minimal number of virtual products $N_p^{v_m}$ and their associated thermodynamic properties $a_{lP_k}^{v_m}$ that describe the most reliably the burnt gases state. This is achieved through the minimization of the fitness function $\mathcal{E}_{\text{thermo}}^{\text{main}}$ defined as:

$$\mathcal{E}_{\text{thermo}}^{\text{main}}(\mathcal{X}) = \sum_{i=1}^{N_c} \left[\psi^{v_m}|^{eq}(\phi_i) - \psi^{d}|^{eq}(\phi_i) \right] \tag{3.17}$$

where $\mathcal{X}$ corresponds to the set of parameters to optimize and N_c is the number of equivalence ratio conditions targeted in the flammability range $[\phi_L; \phi_R]$. Referring to reactions M2-1 and M2-2 and to Eqs. (3.10) and (3.9), mixture-averaged thermodynamic properties ψ^d and ψ^{v_m} can be expressed by:

$$\psi^{d} = \sum_{k=1}^{N_s^d} \psi_k^d Y_k^d \tag{3.18}$$

$$\psi^{v_m} = \sum_{k\in A} \psi_k^{v_m} Y_k^{v_m} + \psi_I^{v_m} Y_I^{v_m} + \sum_{k=1}^{N_p^{v_m}} \psi_{P_k}^{v_m} Y_{P_k}^{v_m} \tag{3.19}$$

By combining Eqs. (3.17), (3.18) and (3.19), the fitness function $\mathcal{E}_{\text{thermo}}^{\text{main}}$ reads:

$$\mathcal{E}_{\text{thermo}}^{\text{main}}(\mathcal{X}) = \sum_{i=1}^{N_c} \left[\sum_{k\in A} \psi_k^{v_m} Y_k^{v_m}|^{eq}(\phi_i) + \sum_{k=1}^{N_p^{v_m}} \psi_{P_k}^{v_m} Y_{P_k}^{v_m}|^{eq}(\phi_i) - \sum_{k=1}^{N_s^d} \psi_k^d Y_k^d|^{eq}(\phi_i) \right] \tag{3.20}$$

Accordingly to the structure of the two-step virtual mechanism, given by reactions M2-1 and M2-2, intermediate species fractions is null at equilibrium. Intermediate species contribution to the fitness function is therefore null.

Under equilibrium conditions, species mass fractions of virtual products are related to mass stoichiometric coefficients $\alpha_{P_k}^{v}$:

$$Y_{P_k}^{v_m}|^{eq} = \alpha_{P_k}^{v_m} Y_P^{v_m}|^{eq} \tag{3.21}$$

where $Y_P^{v_m}|^{eq} = \sum_{k=1}^{N_p^{v_m}} Y_{P_k}^{v_m}|^{eq}$ is the total mass fraction of virtual products in fully burnt gases. At equilibrium state, mass balance equation gives:

$$Y_P^{v_m}|^{eq} = 1 - \sum_{k \in A} Y_k^{v_m}|^{eq} \tag{3.22}$$

In real mixture, the equilibrium concentrations of product species depends on the initial temperature, pressure and composition of the fresh gases. To reduce the number of degrees of freedom, only equivalence ratio dependency is considered in the following. However, the formulation can be extended to pressure and fresh gases temperature dependency in a straightforward manner. To mimic equilibrium composition variations with equivalence ratio, the stoichiometric coefficients $\alpha_{P_k}^{v_m}$ are expressed as a function of the fresh gases composition. As a consequence, the set of parameters $\mathcal{X}$ to be optimized is defined as:

$$\mathcal{X} = \left\{ N_p^{v_m}, \alpha_{P_k}^{v_m}(\phi_i), a_{lP_k}^{v_m} \right\} \quad \text{for} \quad \begin{cases} k \in [1; N_p^{v_m}] \\ i \in [1; N_c] \\ l \in [1; N_T] \end{cases} \tag{3.23}$$

Considering thermodynamic properties closure given in Eqs. (3.11) and (3.12) and identifying polynomial coefficients, one may express the fitness function given in Eq. (3.20) as follows:

$$\mathcal{E}_{\text{thermo}}^{\text{main}} \left(N_p^{v_m}, \alpha_{P_k}^{v_m}(\phi_i), a_{lP_k}^{v_m} \right) = \sum_{i=1}^{N_c} \sum_{l=1}^{N_T} \left[\overline{a}_{lA}^{v_m}|^{eq}(\phi_i) + \overline{a}_{lP}^{v_m}|^{eq}(\phi_i) - \overline{a}_l^d|^{eq}(\phi_i) \right] \tag{3.24}$$

The mixture-averaged coefficients $\overline{a}_l$ refer to the linear combination of the thermodynamic coefficients a_{lk} for each group of species:

$$\overline{a}_{lA}^{v_m}|^{eq}(\phi_i) = \sum_{k \in A} a_{lk}^{v_m} Y_k^{v_m}|^{eq}(\phi_i) \tag{3.25}$$

$$\overline{a}_{lP}^{v_m}|^{eq}(\phi_i) = \sum_{k=1}^{N_p^{v_m}} a_{lP_k}^{v_m} \alpha_{P_k}^{v_m} Y_P^{v_m}|^{eq}(\phi_i) \tag{3.26}$$

$$\overline{a}_l^d|^{eq}(\phi_i) = \sum_{k=1}^{N_s^d} a_{lk}^d Y_k^d|^{eq}(\phi_i) \tag{3.27}$$

The practical resolution of the optimization problem is detailed in Appendix B.

Primary optimization tests

The optimization procedure has been first applied to model the equilibrium of a methane/air flame under atmospheric conditions. Figure 3.5 shows the adiabatic flame temperature predicted with different virtual mixtures composed of the subset of species A= $\{F, Ox, D\}$ as well as two, three or four products with optimized thermodynamic properties. A reference computation has been performed including the 53 species present in the detailed GRI3.0 mechanism (Smith et al. 2011) and the corresponding thermodynamic database. For comparison purposes, the equilibrium temperature obtained with real mixtures made up with : reactant species (CH_4, O_2 and N_2) and two (H_2O; CO_2), three (H_2O; CO_2; CO) or four (H_2O; CO_2; CO; H_2) combustion products is shown in Fig. 3.5 right.

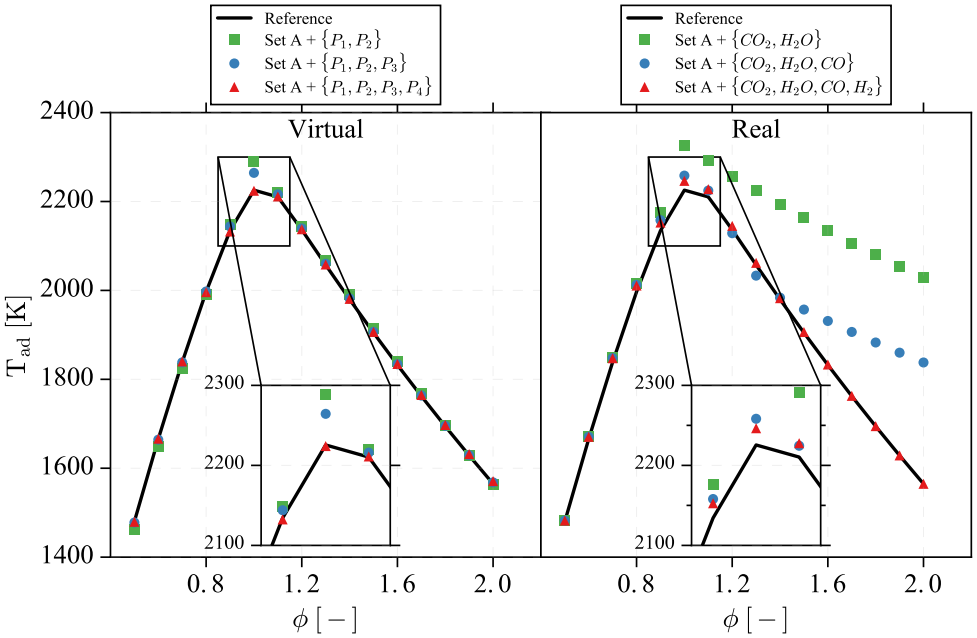

Figure 3.5: *Adiabatic flame temperature versus equivalence ratio for premixed methane/air mixtures at fresh gas temperature* $T_f = 300\,\mathrm{K}$ *and pressure* $P = 1\,\mathrm{atm}$. *Equilibrium calculations performed with virtual mixtures (left) and real mixtures (right) are compared. The subset of species noted A is composed by the fuel, the oxidizer and the nitrogen.*

For low number of species, the proposed strategy, based on optimization of virtual species thermodynamic properties, outperforms the classical methods that use real species. Indeed, the equilibrium calculations performed with the set of optimized virtual species are in close agreement with the reference case (Fig. 3.5 left). On the contrary, real mixtures including only two and three product species do not properly describe the equilibrium state for rich mixtures (Fig. 3.5 right). When four product species are involved, the virtual optimized

method recovers the burnt gases temperature over the whole range of equivalence ratio. However, the mixture characterized by a limited selection of real species slightly over-predicts the adiabatic temperature at near stoichiometry conditions. The mixture composed by four virtual products and the set of reactant species A is retained for the next optimization calculations.

The same optimization test is performed to model the equilibrium state of kerosene oxidation in the conditions of the HERON configuration studied in Chapter 8. Figure 3.6 left shows the dimensionless adiabatic flame temperature obtained for different virtual mixtures of increasing dimensionality.

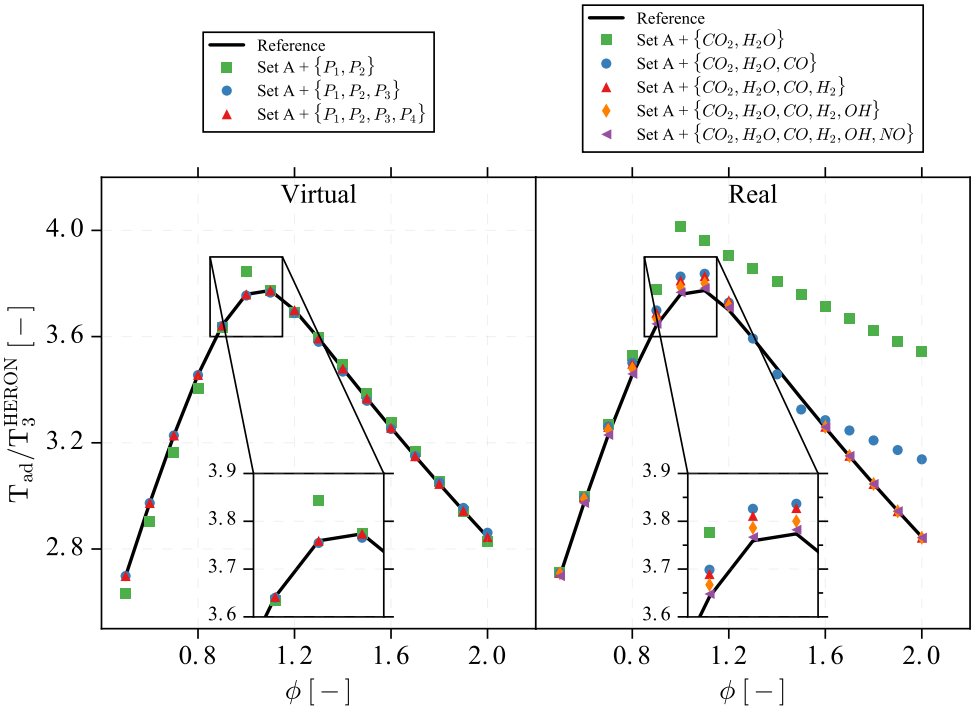

Figure 3.6: *Dimensionless adiabatic flame temperature versus equivalence ratio for premixed kerosene/air mixtures at fresh gas temperature* $T_f = T_3^{HERON}$ *and pressure* $P = P_3^{HERON}$. *Equilibrium calculations performed with virtual mixtures (left) and real mixtures (right) are compared. The subset of species noted A is composed by the fuel, the oxidizer and the nitrogen.*

The conclusions established for methane/air combustion are retrieved for kerosene oxidation. For a small number of species, the use of virtual species with optimized thermodynamic properties and stoichiometric coefficients is more efficient to recover the burnt gas temperature than using real species. A minimum number of three virtual products is required to obtain a fair description of the equilibrium temperature on the whole flammability range. However, as far as real mixtures are concerned, the equilibrium state is correctly described if at

least six real species are included. In case of heavy fuel combustion, the use of virtual species with optimized properties allows an important reduction of the number of transported species for equal predictive capabilities regarding equilibrium state description.

Thermodynamic properties of intermediate species

As previously stated, the thermodynamic properties of the intermediate species have no impact on the equilibrium gas state. However, as the intermediate species I may feature high concentrations in the flame front the value of the NASA coefficients $a_{Il}^{v_m}$, modeling the species sensible and chemical energy, can strongly influence the description of the inner flame structure. As a consequence, thermodynamic properties of the intermediate species must be carefully modeled. To reach a proper description of the temperature profiles, the coefficients a_{lI} may be included in the set of coefficients to optimize, similarly as reaction rate parameters (see subsection 3.4.3).

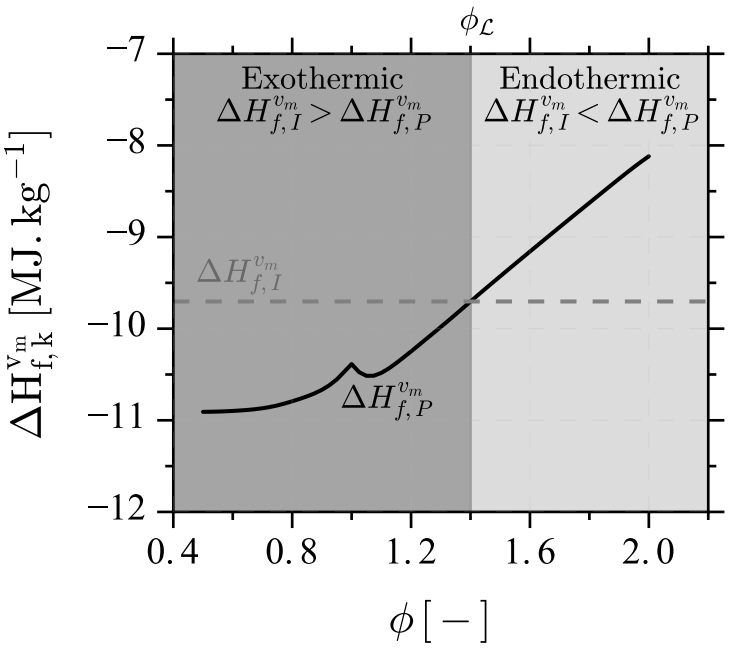

Figure 3.7: *Evolution of the standard enthalpy of formation of the burnt gases virtual mixture with the equivalence ratio for methane/air mixtures at fresh gas temperature* $T_f = 300\,\mathrm{K}$ *and pressure* $P = 1\,\mathrm{atm}$. *The dotted grey line represents the standard enthalpy of formation of the virtual intermediate species I.*

Interestingly, the typical endothermic behavior observed in rich premixed flame front may be considered to reduce the number of parameters to optimize. Detailed chemistry simulations show that in hydrocarbon/air rich premixed flames

(typically for $\phi > \phi_{\mathcal{L}}$) the maximum flame temperature reached in the flame front is higher than the equilibrium temperature T_{ad} obtained in fully burnt gases. To properly capture this phenomenon, the standard enthalpy of formation of species I is chosen so that reaction M2-2 is exothermic for $\phi < \phi_{\mathcal{L}}$ and endothermic for $\phi > \phi_{\mathcal{L}}$. Figure 3.7 shows the evolution of the standard enthalpy of formation of the virtual products in burnt gases with the equivalence ratio. The dotted grey line corresponds to the standard enthalpy of formation of the intermediate species. For $\phi < \phi_{\mathcal{L}}$, the condition $\Delta H_{f,I}^{v_m} > \Delta H_{f,P}^{v}$ ensures an exothermic behavior of the reaction M2-2, while for $\phi > \phi_{\mathcal{L}}$ the relation $\Delta H_{f,I}^{v_m} < \Delta H_{f,P}^{v_m}$ implies that reaction M2-2 is endothermic. This condition allows to express the NASA coefficient $a_{6,I}$ as a function of the targeted standard enthalpy of formation and the coefficients modeling the sensible part of the energy:

$$a_{6I}^{v_m} = \frac{\Delta H_{f,I}^{v_m}}{R} - \left(a_{1I}^{v_m} T_0 + \frac{a_{2I}^{v_m}}{2} T_0^2 + \frac{a_{3I}^{v_m}}{3} T_0^3 + \frac{a_{4I}^{v_m}}{4} T_0^4 + \frac{a_{5I}^{v_m}}{5} T_0^5 \right) \tag{3.28}$$

3.4.2.2 Specific gas constants

As the main virtual mechanism aims at describing the density profiles across a flame, the specific gas constant $r_k^{v_m}$ (or equivalently the molecular weight $W_k^{v_m}$) of the virtual species k must be identified so as to reproduce the reference mixture-averaged specific gas constant r^{v_m} (or equivalently the molecular weight W^{v_m}) in both fresh and burnt gases:

$$r^{v_m}|^f = r^d|^f \Rightarrow \sum_{k=1}^{N_s^{v_m}} r_k^{v_m} Y_k^{v_m}|^f = \sum_{k=1}^{N_s^d} r_k^d Y_k^d|^f \tag{3.29}$$

$$r^{v_m}|^{eq} = r^d|^{eq} \Rightarrow \sum_{k=1}^{N_s^{v_m}} r_k^{v_m} Y_k^{v_m}|^{eq} = \sum_{k=1}^{N_s^d} r_k^d Y_k^d|^{eq} \tag{3.30}$$

Fresh gases specific gas constant is naturally obtained by assigning real properties to the reactant subset of species A:

$$r_A^{v_m} = r_A^d \quad \text{for } A = \{F, Ox, D\} \tag{3.31}$$

Virtual product specific gas constant $r_{P_k}^{v}$ are determined by minimizing the cost function $\mathcal{E}_{\text{chemistry}}^{\text{main}}$ given by:

$$\mathcal{E}_{\text{chemistry}}^{\text{main}}\left(r_{P_k}^{v_m}\right) = \sum_{i=1}^{N_c} \left[\sum_{k \in A} r_k^{v_m} \alpha_{P_k}^{v_m} Y_P^{v_m}|^{eq}(\phi_i) + \sum_{k=1}^{N_p^{v_m}} r_{P_k}^{v_m} Y_{P_k}^{v_m}|^{eq}(\phi_i) - \sum_{k=1}^{N_s^d} r_k^d Y_k^d|^{eq}(\phi_i) \right] \tag{3.32}$$

3.4.2.3 Transport properties

Virtual mixture-averaged transport properties are closed with simplified models. The mean dynamic viscosity μ^v is given by:

$$\mu^v = \mu_0^v \left(\frac{T^v}{T_0^v} \right)^{\beta^v} \tag{3.33}$$

where μ_0^v is the dynamic viscosity at the reference temperature T_0^v. The coefficient β^v is optimized to retrieve the dynamic viscosity dependence on temperature. In this work, the reference viscosity μ_0^v value is optimized to reproduce the mixture viscosity at stoichiometry. As discussed in Chapter 1, such simple assumption may lead to important errors in non-premixed flames. Keeping the same simple power law, a possible improvement would be to express μ_0^v as dependent on the local composition.
The gas mixture thermal conductivity λ^v reads:

$$\lambda^v = \frac{\mu^v c_p^v}{\mathrm{Pr}_0^v} \tag{3.34}$$

where Pr_0^v is the Prandtl number, assumed constant and equal to the Prandtl number in the burnt gases of a premixed flame at stoichiometry.
The molecular diffusion velocities $V_k^{v_m}$ are closed using a unity Lewis number assumption:

$$Y_k^{v_m} V_k^{v_m} = -D^{v_m} \frac{\partial Y_k^{v_m}}{\partial x_i} = -\frac{\lambda^v}{\rho^v c_p^v} \frac{\partial Y_k^{v_m}}{\partial x_i} \tag{3.35}$$

Molecular diffusion coefficients D^{v_m} of virtual species are here assumed equal. As discussed in Section 4.2.1.2, this assumption does not limit the prediction of the laminar flame consumption speed, as long as targeted flame solutions include differential diffusion effects. Nevertheless, to handle changes in elemental composition and displacement of equilibrium properties induced by preferential diffusion, as observed experimentally in (Sweeney et al. 2012a), transport coefficients of virtual species may be included in the optimization procedure.

3.4.3 Optimization of virtual reaction rate parameters

During the second step of the main virtual mechanism generation (Fig. 3.4), the kinetic rate parameters are optimized so that the virtual optimized scheme reproduces as best as possible a set of flame properties characterizing the interaction between the flame and the flow field. The target quantities retained for the optimization are the laminar flame consumption speed and temperature profiles of 1-D premixed flames.

Global kinetic schemes composed by 1 to 4 reactions have shown capabilities

to describe the laminar flame speed for moderately lean and stoichiometric injection conditions (Martin 2005). However, beyond this narrow range of equivalence ratio, reduced low-order schemes tend to overestimate this key quantity. To remedy this shortcoming, authors suggested to correct kinetic rate coefficients with fresh gas equivalence ratio dependent functions. As an example, Fernandez-Tarrazo et al. (2006) expressed the activation temperature T_a as a function of the equivalence ratio. Liñán and Williams (1993) imposed a functional dependency of the pre-exponential factor on the equivalence ratio. In the present work, a similar strategy has been retained. Rates of progress q_1 and q_2 respectively read:

$$q_1 = A_1^v f_1^v\left(Z\right) \exp\left(\frac{-E_{a,1}^v}{RT^v}\right) \left([F]^{v_m}\right)^{F_{F,1}^v} \left([Ox]^{v_m}\right)^{F_{Ox,1}^v}, \tag{3.36}$$

$$q_2 = A_2^v \exp\left(\frac{-E_{a,2}^v}{RT^v}\right) \left([I]^{v_m}\right)^{F_{I,2}^v f_2^v(Z)}, \tag{3.37}$$

where A_r^v and $E_{a,r}^v$ are the pre-exponential factor and activation energy of the rth reaction. The exponent $F_{k,r}^v$ corresponds to the forward reaction order of the species k in reaction r. The quantity $[X_k]^{v_m}$ refers to the molar concentration of the virtual species k. Z denotes the mixture fraction characterizing the fresh gases composition. As unity Lewis numbers are considered here, the mixture fraction is directly related to the normalized dilutant mass fraction defined as:

$$Z = \frac{Y_d^{v_m} - Y_d^{v_m}|^{Ox}}{Y_d^{v_m}|^{F} - Y_d^{v_m}|^{Ox}} \tag{3.38}$$

where the superscripts F and Ox denote conditions in the pure oxidizer and pure fuel respectively. The pre-exponential factor of the first reaction A_1^v is corrected by a function f_1^v depending on the mixture fraction Z. The correction function f_1^v is optimized to match the laminar flame speed within the flammability limits. Also, the reaction exponent of the intermediate $F_{I,2}^v$ is corrected by a mixture fraction dependent function f_2^v to control the thickness of the post-flame zone and to improve the flame structure prediction (Cailler et al. 2017). The genetic algorithm used to optimize species properties is employed to determine the set of reaction rate parameters (A_r^v, $E_{a,r}^v$, $F_{k,r}^v$) and correction functions f_1^v and f_2^v that best reproduce the temperature profiles and laminar flame speed. The fitness function $\mathcal{E}_{\text{kinetic}}^{\text{main}}$ comparing solutions obtained by the virtual mechanism and the reference flamelet is defined by:

$$\mathcal{E}_{\text{kinetic}}^{\text{main}}\left(A_r^v, E_{a,r}^v, F_{k,r}^v, f_r^v\left(Z_i\right)\right) = \sum_{i=1}^{N_c} w_{S_L} \frac{|S_{L_i}^v - S_{L_i}^d|}{S_{L_i}^d} + w_T \frac{\|T_i^v\left(x\right) - T_i^d\left(x\right)\|_{L_2}}{\|T_i^d\left(x\right)\|_{L_2}}, \tag{3.39}$$

where S_{L_i} and $T_i\left(x\right)$ respectively represent the laminar flame speed and the temperature profile of the i^{th} set of operating conditions ϕ_i. The factors w_1

and w_2 are weights attributed to each objective to give appropriate influence to each targeted quantity. Here, w_{S_L} equals 0.01, while w_T is set to 0.99. The operator $\|.\|_{L_2}$ represents the L^2 norm given by:

$$\|f\|_{L_2} = \left(\int_{x=-\infty}^{x=+\infty} f\left(x\right) dx \right)^{\frac{1}{2}} \tag{3.40}$$

3.5 Virtual sub-mechanism for pollutant prediction

3.5.1 Virtual sub-mechanisms generation principles

As indicated previously, pollutants are predicted by specific sub-schemes. Virtual sub-mechanisms do not retroact on the flow field (see equation systems (3.3) and (3.4)), but use quantities predicted by the main virtual mechanism. More precisely, the temperature, density and mixture properties (heat capacity, enthalpy, conductivity, *etc*) evaluated from the main virtual mechanism are used as input in satellite kinetic models. Similarly to the optimization of the main virtual mechanism for temperature prediction, the sub-schemes are optimized to capture profiles of a given pollutant species. The optimization consists in evaluating both:

- the minimal number of species and reactions constituting the virtual sub-block,
- the best set of kinetic rate parameters so as to reproduce the pollutant concentration on the collection of targeted flame configurations.

Contrarily to main scheme generation procedure, evaluation of the thermodynamic properties of the species included in the satellite scheme is not required. The study focusses on the description of CO, but the methodology can be transposed to any chemical species. The next section details the optimization of the sub-mechanism for CO prediction.

3.5.2 Virtual sub-scheme for CO formation prediction

CO is an intermediate species featuring two characteristic times. In the fuel oxidation layer, CO is rapidly produced through reactions promoted by highly active radicals. Then in the post-flame zone, CO slowly recombines into CO_2. The following set of virtual reactions is proposed to describe these processes:

$$\alpha_F^{v_{CO}} F + \alpha_{Ox}^{v_{CO}} Ox + \alpha_D^{v_{CO}} D \rightarrow \alpha^{v_{CO}} CO + \left(1 - \alpha^{v_{CO}}\right) V_1 + \alpha_D^{v_{CO}} D \tag{R3}$$

$$F + V_1 \rightarrow F + CO \tag{R4}$$

$$CO \leftrightarrow V_2 \tag{R5}$$

where F, Ox and D are the fuel, oxidizer and dilutant transported in the main mechanism while V_1 and V_2 are virtual species. The first reaction R3 describes

the fast CO production from fuel oxidation. The second reaction converting V_1 into CO mimics the slow CO formation processes occurring in rich conditions (see Figure 4.11). Finally, the reversible reaction R5 between CO and V_2 models the slow recombination processes observed in the post-flame zone.
The rate of progress of the virtual reactions R3, R4 and R5 are closed with Arrhenius type laws:

$$q_3 = A_3^v f_3^v\left(Z\right) \exp\left(\frac{-E_{a,3}^v}{RT^v}\right) \left([F]^{v_{CO}}\right)^{F_{F,3}^v} \left([Ox]^{v_{CO}}\right)^{F_{Ox,3}^v} \tag{3.41}$$

$$q_4 = A_4^v f_4^v\left(Z\right) \exp\left(\frac{-E_{a,4}^v}{RT^v}\right) \left([F]^{v_{CO}}\right)^{F_{F,4}^v} \left([V_1]^{v_{CO}}\right)^{F_{V_1,4}^v} \tag{3.42}$$

$$\begin{aligned} q_5 = A_5^v f_5^v\left(Z\right) \exp\left(\frac{-E_{a,5}^v}{RT^v}\right) \Bigg(&\left([CO]^{v_{CO}}\right)^{F_{CO,5}^v} \left([V_2]^{v_{CO}}\right)^{F_{V_2,5}^v} \\ &- \frac{\left([CO]^{v_{CO}}\right)^{R_{CO,5}^v} \left([V_2]^{v_{CO}}\right)^{R_{V_2,5}^v}}{K_{c,5}^v}\Bigg) \end{aligned} \tag{3.43}$$

where $F_{k,r}^v$ and $R_{k,r}^v$ are respectively the forward and reverse reaction orders of the species k in the reaction r. Functions $f_r^v\left(Z\right)$ are correction functions applied to the pre-exponential factors to improve the predictive capabilities of the virtual sub-mechanism on the whole flammability range. Details about these functions are given in the next session. The closure of the equilibrium constant $K_{c,5}^v$ of the reversible reaction R5 is presented hereinafter.

To decrease the computational cost related to the integration of the CO subscheme, the species F, Ox and D intervening in reaction R3 are not transported. Instead, we assume that:

$$Y_A^{v_{CO}} = Y_A^{v_m} \quad \text{for } A = \{F, Ox, D\} \tag{3.44}$$

This assumption is realized only if the kinetic rate parameters defining the reaction rate of reaction R3 are identical to these of the fuel consumption reaction M2-1 in the main virtual scheme i.e. if $A_3^v = A_1^v$, $f_3^v = f_1^v$, $E_{a,3}^v = E_{a,1}^v$, $F_{F,3}^v = F_{F,1}^v$ and $F_{Ox,3}^v = F_{Ox,1}^v$. Thus, the coefficients A_3^v, f_3^v, $E_{a,3}^v$, $F_{F,3}^v$ and $F_{Ox,3}^v$ are not calibrated but their values are fixed by the optimization of the main mechanism.
Imposing the kinetic rate parameters of reaction R3 tends to constrain the optimization problem. Typically, the set of kinetic coefficients of reactions R4 and R5 leading to calculation convergence evolve in a reduced domain. This restriction of the parameter domain evolution may lead the calibration procedure to converge towards unwanted kinetic parameters values such as negative reaction orders.

3.5.3 Prediction of the CO equilibrium concentration

The equilibrium constant in concentration unit of the rth reaction is by definition given by:

$$K_{c,r}^{v_{CO}} = \prod_{k=1}^{N_s^{v_{CO}}} \left([X_k]^{v_{CO}}|^{eq}\right)^{\alpha_{k,r}^{v_{CO}}} \tag{3.45}$$

For the reverse reaction R5, the equilibrium constant $K_{c,5}^{v_{CO}}$ reads:

$$K_{c,5}^{v_{CO}} = \frac{[V_2]^{v_{sCO}}|^{eq}}{[CO]^{v_{sCO}}|^{eq}} \tag{3.46}$$

Although sub-mechanisms are not involved in mass balance conservation equation, the kinetic schemes for pollutant prediction are built so that the sum of virtual species mass fractions equals one:

$$\sum_{k=1}^{N_s^{v_{sj}}} Y_k^{v_{sj}} = 1 \tag{3.47}$$

Considering that the virtual species V_1 is completely consumed through reaction R4, and as species F, Ox in reaction R3 are the same as in reaction M2-1 the equilibrium mass fraction of the virtual species V_2 expresses as:

$$Y_{V_2}^{v_{CO}}|^{eq} = 1 - \left(\sum_{k\in A} Y_k^{v_m}|^{eq} + Y_{CO}^{d}|^{eq}\right) \tag{3.48}$$

where the equilibrium composition of reactants F, Ox and dilutant species D are determined by the main mechanism, while the equilibrium mass fraction of CO is the reference quantity given by complex thermo-equilibrium calculations (Kee et al. 1996).
The equilibrium constant $K_{c,5}^{v_{CO}}$ is pre-tabulated versus the mixture fraction Z to properly describe the equilibrium state within the flammability limits:

$$K_{c,5}^{v_{CO}}(Z) = \frac{[V_2]^{v_{CO}}|^{eq}(Z)}{[CO]^{d}|^{eq}(Z)} \tag{3.49}$$

As for the main virtual kinetic scheme, the reaction orders are included in the set of optimized parameters to increase the degrees of freedom and enhance the predictivity of the virtual scheme. However, the modification of the reaction orders of the reversible reaction R5 must be consistent with the rule conditioning the chemical equilibrium. In fact, elementary kinetics ensures that at equilibrium the reaction rate of reaction R5 is null $q_5|^{eq} = 0$. This condition is expressed using Eqs. (3.43) and (3.46) as:

$$\left([CO]^{v_{CO}}|^{eq}\right)^{F_{CO,5}^{v}} \left([V_2]^{v_{CO}}|^{eq}\right)^{F_{V_2,5}^{v}} = \frac{\left([CO]^{v_{CO}}|^{eq}\right)^{R_{CO,5}^{v}} \left([V_2]^{v_{CO}}|^{eq}\right)^{R_{V_2,5}^{v}}}{\left([CO]^{v_{CO}}|^{eq}\right)^{-1} [V_2]^{v_{CO}}|^{eq}} \tag{3.50}$$

The equilibrium behavior is therefore retrieved if the following conditions are satisfied:

$$F^v_{CO,5} - R^v_{CO,5} = 1 \tag{3.51}$$

$$F^v_{V_2,5} - R^v_{V_2,5} = -1 \tag{3.52}$$

3.5.4 Prediction of the CO mass fraction profiles

The virtual sub-scheme is designed so that enough flexibility is given to capture a large variety of CO evolutions. For instance, to match the CO mass fraction peak evolution with the equivalence ratio, the pre-exponential factor A^v_5 of reaction R5 is adjusted through a correction function f^v_5 tabulated as function of the mixture fraction. In addition, for very rich conditions, detailed chemistry calculations show that CO produced by the combustion of classical hydrocarbon fuels features a slow increase in the oxidation layer. At the opposite for lean and moderately rich mixtures, CO mass fraction profiles exhibit a decrease or constant evolution in the post-flame zone. To account for the different CO mass fraction behaviors in the post-flame zone, the stoichiometric coefficient α^{vCO} of reaction R3 is tabulated versus the fresh gas equivalence ratio. For lean and moderately rich mixtures, $\alpha^{vCO}(Z)$ is set to unity so that CO is first rapidly produced in the reaction zone and then slowly converted into V_2 in the post-flame zone through the equilibrium reaction R5. For rich injection conditions, $\alpha^{vCO}(Z)$ is set lower than unity to model the slow production of CO in the post-flame zone, through reaction R4. Finally, to fit the thickness of the CO oxidation layer, a correction function f^v_4 depending on the mixture fraction is applied on the pre-exponential factor A^v_4 of reaction R4.
The set of reaction rate parameters and tabulated functions are identified using the optimization algorithm previously introduced. The fitness function $\mathcal{E}^{\mathrm{CO}}_{\mathrm{kinetic}}$ minimized through the genetic optimization procedure is given by:

$$\mathcal{E}^{\mathrm{CO}}_{\mathrm{kinetic}}\left(A^v_r, E^v_{a,r}, F^v_{k,r}, f^v_r(Z_i)\right) = \sum_{i=1}^{N_c} \frac{\| Y^{vCO}_{CO_i}(x) - Y^d_{CO_i}(x) \|_{L_2}}{\| Y^d_{CO_i}(x) \|_{L_2}} \tag{3.53}$$

3.6 Summary

A summary of the different stages required for the design of the main and satellite sub-mechanisms is illustrated in Fig. 3.8. For each step of the virtual mechanisms generation process, the set of unknown parameters or chromosome that must be calibrated are also provided.

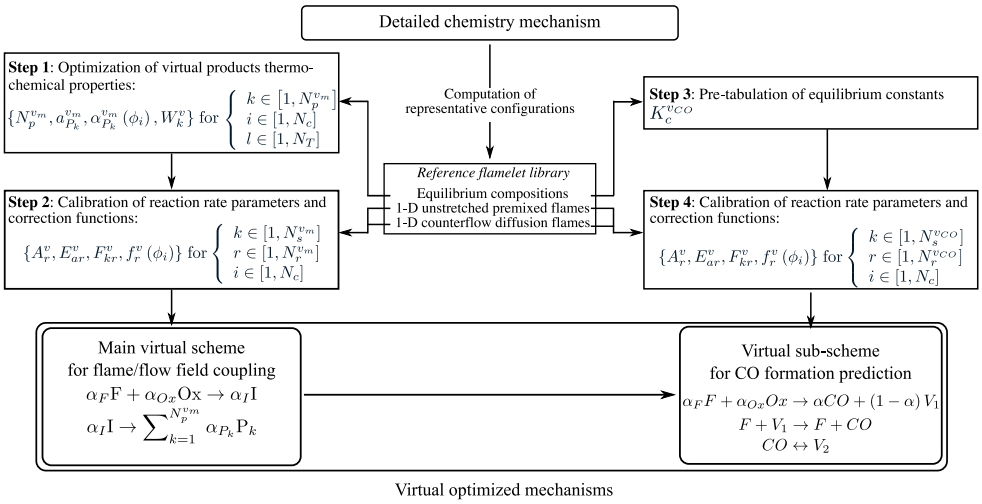

Figure 3.8: *Summary of the procedure to build virtual optimized mechanisms.*

Chapter 4

Application of the virtual optimized chemistry approach to laminar premixed and non-premixed flames

Contents

This chapter focuses on the application of the virtual optimized chemistry approach introduced in Chapter 3. The new chemistry description method is first used to derive virtual reduced schemes dedicated to the prediction of the flame temperature and CO concentration in methane/air flames. The subsequent virtual mechanisms are compared against main chemistry description approaches in terms of predictive capabilities, computational costs and numerical stiffness. In a second part, fully resolved simulations of two-dimensional laminar methane/air burners are performed to assess virtual optimized schemes capabilities in a multi-dimensional context. Finally, virtual optimized kinetic schemes devoted to the description of heavy fuels oxidation are built-up and compared to detailed chemistry solutions.

4.1 Objectives

The proposed virtual optimized chemistry approach is first applied to the derivation of methane/air reduced kinetic schemes. This light fuel, intensely studied experimentally (Vagelopoulos and Egolfopoulos 1998; Yu et al. 1995) and theoretically (Sánchez et al. 2000), constitutes a first good candidate for the validation of the strategy. Moreover, numerous chemical models including detailed (Smith et al. 2011; Ranzi et al. 2012), analytic (Lu and Law 2008; Jaravel 2016) as well as global (Westbrook and Dryer 1981; Jones and Lindstedt 1988) mechanisms have been proposed and may be used for reference flamelet library generation or comparison purposes. As described in Chapter 3, two virtual optimized schemes dedicated to temperature and CO formation prediction are built-up. The virtual optimized mechanisms are then tested on one-dimensional laminar canonical cases, and compared against tabulated, global, analytically-reduced and detailed complex schemes. In section 4.3, Direct Numerical Simulations of simple two-dimensional partially-premixed burner configuration are performed to evaluate the capabilities of the virtual optimized approach in a stratified environment. Finally, section 4.4 presents the application of the virtual chemistry approach for the derivation of reduced virtual schemes describing aeronautical hydrocarbons oxidation. In particular, the methodology is employed for the generation of two virtual optimized mechanisms that will be used for the numerical study of an industrial two-phase combustion chamber.

4.2 Modeling of 1-D laminar methane/air flames

In this section, the strategy presented in Chapter 3 is applied to the description of the flame/flow field interactions and CO formation in methane/air flames. As described in Fig. 3.8, a prerequisite to the optimization procedure is the generation of a flamelet library that serves as a reference for the evaluation of the virtual scheme predictive capabilities. The target database, used for the methane/air virtual scheme optimization, is composed by flamelets computed with the detailed chemistry mechanism GRI3.0 (Smith et al. 2011) and with mixture-averaged transport models (Hirschfelder et al. 1954). The influence of the flamelet archetypes retained to generate the reference database is discussed in sub-sections 4.2.1 and 4.2.2.

The performances of the virtual schemes in terms of prediction, computational cost and chemical stiffness are compared against analytically-reduced chemistry, global mechanisms and tabulated chemistry strategy. Table 4.1 summarizes the chemical models considered for the comparative study.

Case	Chemistry description strategy
Reference	Detailed chemistry GRI3.0 (Smith et al. 2011)
Global 1	Semi-global scheme BFER (Franzelli et al. 2012)
Global 2	Semi-global scheme Jones (Jones and Lindstedt 1988)
Analytic	Analytically-reduced chemistry LU19 (Lu and Law 2008)
Tabulated	Premixed based tabulated chemistry FPI (Gicquel et al. 2000)
Virtual	Virtual optimized chemistry

Table 4.1: *Chemistry description approaches considered for the comparative study.*

Main characteristics of these chemistry description methods are summarized hereinafter:

- **Global chemistry method oriented towards global flame properties capture:** The two-step mechanism BFER developed for methane/air combustion (Franzelli et al. 2012) is used in the comparative study. It is composed of two global reactions, the first one (G1-BFER) describes the fuel oxidation, while the second one (G2-BFER) represents the CO-CO_2 equilibrium.

$$CH_4 + \frac{3}{2}O_2 \rightarrow 2H_2O + CO \qquad \text{(G1-BFER)}$$

$$CO + \frac{1}{2}O_2 \leftrightarrow CO_2 \qquad \text{(G2-BFER)}$$

  The reaction rate parameters of the Arrhenius laws are fitted to reproduce a set of flame characteristics such as the laminar flame speed and the auto-ignition delay time over a wide range of initial pressures, temperatures and equivalence ratios. Though composed of a reduced number of reactions and species, this kinetic scheme has been successfully applied in LES of different burners (Hernández et al. 2013; Hermeth et al. 2014).

- **Global chemistry approach oriented towards local flame properties description:** The four-step Jones mechanism developed by Jones and Lindstedt (1988) is also considered in this work. This reduced scheme is composed of seven species interacting through four pseudo-global reactions:

$$CH_4 + {}^1\!/_2 O_2 \rightarrow CO + 2H_2 \qquad \text{(G1-JONES)}$$

$$CH_4 + H_2O \rightarrow CO + 3H_2 \qquad \text{(G2-JONES)}$$

$$CO + H_2O \leftrightarrow CO_2 + H_2 \qquad \text{(G3-JONES)}$$

$$H_2 + {}^1\!/_2 O_2 \leftrightarrow H_2O \qquad \text{(G4-JONES)}$$

  This kinetic scheme architecture is derived exploiting the so-called two layers flame structure of premixed and non-premixed hydrocarbon/air

flames. In this simplified view of the flame, the reactive zones may be divided into two basic regions: a primary reaction zone where fuel is converted into intermediate species, and a secondary reaction zone where intermediate species are partially converted in final combustion products. In their work, Jones and Linsdtedt proposed to describe the thin fuel oxidation layer, through two global competing fuel breakdown reactions given in G1-JONES and G2-JONES. Regarding the post-flame reaction zone, two global equilibrium reactions (G3-JONES and G4-JONES) were derived from partial equilibrium and quasi steady-state assumptions. The reaction rate parameters of the Arrhenius laws are fitted to account for the structure of both premixed and counterflow flames.

- **Premixed-based tabulated strategy:** A tabulated chemistry approach based on the FPI formalism, proposed by Gicquel et al. (2000), is also considered to describe complex chemistry effects. The FPI strategy assumes that the chemical subspace accessed in a stratified flame can be described by a collection of 1-D premixed flamelets computed for different initial compositions. All flame quantities (temperature, density, mass fraction, ...) are assumed to depend on a reduced number of control variables: the mixture fraction Z and the progress variable Y_c. The mixture fraction, equal to 0 in pure air and 1 in pure fuel, is a passive scalar characterizing the fuel/air mixture. Its normalized definition is given by:

$$Z = \frac{Y_{N_2} - Y_{N_2}|^F}{Y_{N_2}|^O - Y_{N_2}|^F} \tag{4.1}$$

where the superscripts F and O denote conditions in the pure oxidizer and pure fuel respectively.
The second coordinate is the progress variable describing the progress of the reaction. For methane/air combustion, the progress variable can be efficiently defined by (Fiorina et al. 2003):

$$Y_c = Y_{CO_2} + Y_{CO}. \tag{4.2}$$

With this strategy, the chemical effects are described by transporting only two variables instead of N_s for all species composing the detailed mechanism.

$$\frac{\partial \rho Z}{\partial t} + \frac{\partial}{\partial x_i}\left(\rho u_i Z\right) = \frac{\partial}{\partial x_i}\left(\frac{\mu}{Sc}\frac{\partial Z}{\partial x_i}\right) \tag{4.3}$$

$$\frac{\partial \rho Y_c}{\partial t} + \frac{\partial}{\partial x_i}\left(\rho u_i Y_c\right) = \frac{\partial}{\partial x_i}\left(\alpha_{Y_c}\frac{\mu}{Sc}\frac{\partial Y_c}{\partial x_i}\right) + \dot{\omega}_{Y_c} \tag{4.4}$$

To take into account differential diffusion effects, the parameter α_{Y_c} (Eq. 4.5) proposed by Mercier et al. (2014) and Nambully et al. (2014a) is

introduced. This term, comparing the molecular diffusive fluxes evaluated from mixture-averaged and simplified transport model, is tabulated from 1-D premixed flames computed with complex diffusive transport model:

$$\alpha_{Y_c}[Y_c, Z] = -\frac{\sum_{k=1}^{N_s} n_k \rho^* Y_k^* V_k^*}{\frac{\mu}{Sc}\frac{\partial Y_c^*}{\partial x_i^*}} \tag{4.5}$$

where the superscript * denotes values extracted from the 1-D laminar flames.

- **Analytically-reduced chemistry:** The analytic mechanism developed by Lu and Law (2008) for the description of methane/ air flames is considered in this work. The kinetic scheme is reduced from the GRI3.0 scheme using the Directed Relation Graph (DRG) method (Lu and Law 2005; Lu and Law 2006b) and Quasi Steady State (QSS) approximation. A criterion based on Computational Singular Perturbation (CSP) (Lam 1993; Lam and Goussis 1994) is used to identify the QSS species. The kinetic scheme is composed of 19 transported species and 11 species in Quasi Stationary State interacting through 184 elementary reactions. The computational time related to the time-integration of the equations is reduced using analytic solutions for QSS species concentrations.

Section 4.2.1 shows results obtained with the main virtual mechanism whereas performances of the virtual sub-mechanism for CO are discussed in section 4.2.2. The computational time and stiffness associated with each chemistry description strategy is discussed in sections 4.2.3 and 4.2.4.

4.2.1 Main virtual mechanism for flame/flow field interaction description

4.2.1.1 Evolutionary optimization settings

Identification of the fittest reaction rate parameters and correction functions closing the main virtual mechanism is performed with the in-house genetic algorithm described in Chapter 3 and Appendix A. The target reference database, used to calibrate the unknown parameters, is made up with $N_c = 31$ one-dimensional unstretched premixed flamelets with fresh gas equivalence ratio varying from lean (ϕ_L=0.5) to rich (ϕ_R=2.0) flammability limit. As correction functions $f_r^v(Z)$ are not expressed analytically but tabulated for N_c points of the flammable zone, the simultaneous optimization of the all set of kinetic rate parameters and individual values of $f_r^v(Z)$ is computationally costly. For example, optimization of the one-step mechanism requires the identification of 31 unknowns, while optimization of the two-step scheme involves the evaluation of 69 kinetic rate parameters. To improve the optimization efficiency a two-stage strategy allowing a reduction of the problem dimensionality is used. Figure 4.1 illustrates this optimization procedure.

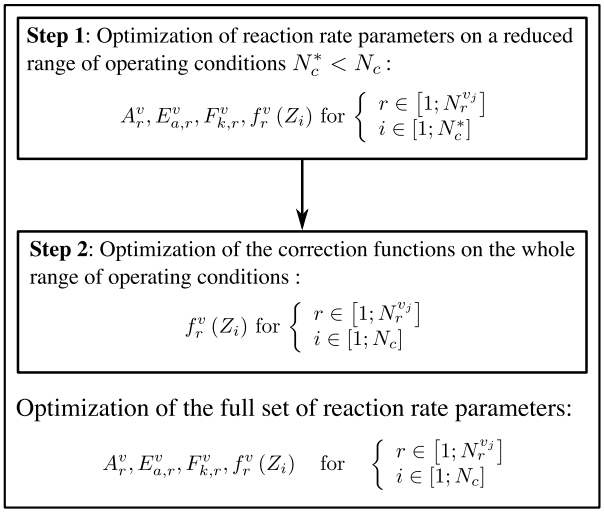

Figure 4.1: *Procedure for the optimization of the virtual reaction rate parameters.*

In a first step, a reduced number $N_c^* < N_c$ of operating conditions are used for both the optimization of constant kinetic rate parameters ($A_{r,k}^v$, $E_{a,r}^v$ and $F_{k,r}^v$) and N_c^* points of the mixture fraction dependent correction functions $f_r^v(Z)$. Then, a second optimization step is performed to independently identify the correction function values in the N_c points discretizing the whole flammable domain. During this second stage, the constant parameters ($A_{r,k}^v$, $E_{a,r}^v$ and $F_{k,r}^v$) issued from the first optimization step are used. To ensure that the fixed parameters identified during the first optimization step are sufficiently representative of the variety of laminar premixed flame structures, the N_c^* targeted operating points are carefully chosen. In this work, $N_c^* = 3$ premixed flames representative of the typical hydrocarbon/air flame temperature profiles are selected:

- a lean flame featuring a one-layer flame structure,
- a near-stoichiometric flame exhibiting a two-layers structure,
- a rich flame for which endothermic behavior occurs.

To ensure physical values of the optimized coefficients, kinetic rate coefficients are bounded between user-defined values. Table 4.2 presents the domain of definitions of the reaction rate parameters used during the optimization. This definition intervals have been chosen to be large enough to enable diversity of the solutions and sufficiently restrictive to limit the convergence time of the algorithm. Tests have been performed to check the optimized coefficients sensitivity to the definition intervals.

Parameter	Interval of definition
A_r^v	$[1.0 \times 10^{15}, 5.0 \times 10^{18}]$
$E_{a,r}^v$	$[2.0 \times 10^{04}, 1.0 \times 10^{05}]$
$F_{r,k}^v$	$[1.0, 3.0]$

Table 4.2: *Intervals of definition of the kinetic rate parameters defining the main virtual scheme.*

For all optimization calculations, the crossover probability $\mathcal{P}_c$ is fixed to 0.7, while non-uniform mutation probability is set to $\mathcal{P}_m = 0.1$. For the first genetic optimization calculation the population is made of 70 individuals simultaneously evaluated on $N_c^* = 3$ operating conditions. Convergence of the first optimization step is obtained after 4h on an Intel Xeon E5-2670 Haswell machine using 210 processors. As the evaluation part of the genetic algorithm is fully parallel, the 210 ($N_c^* \times 70$) flames to compute are evaluated on 210 processors. The second optimization stage is performed on the same machine using $48 \times N_c$ processors during 0.5 h. To ensure convergence of the calculation a systematic verification of the temporal evolution of both the best and average fitness is performed.

The resulting optimized kinetic rate parameters are given in Table 4.3 while the evolutions of the correction functions f_1^v (for reaction M1-1 and M2-1) and f_2^v (for reaction M2-2) are displayed in Fig. 4.2. Contrarily to previous works (Fernandez-Tarrazo et al. 2006; Franzelli et al. 2010) the correction function f_1^v has been applied on whole flammability domain to perfectly match the laminar flame speed evolution.

Reaction	A_r^v	$E_{a,r}^v$	$F_{k,r}^v$	
M1-1	6.3×10^{17}	35.6×10^3	$F_{F,1}^v$	1.64
			$F_{Ox,1}^v$	0.92
M2-1	1.5×10^{18}	35.6×10^3	$F_{F,1}^v$	1.70
			$F_{Ox,1}^v$	0.86
M2-2	3.9×10^{18}	85.7×10^3	$F_{I,2}^v$	2.34

Table 4.3: *Kinetic rate constants of the main virtual mechanisms (Units: cm, s, cal and mol)*

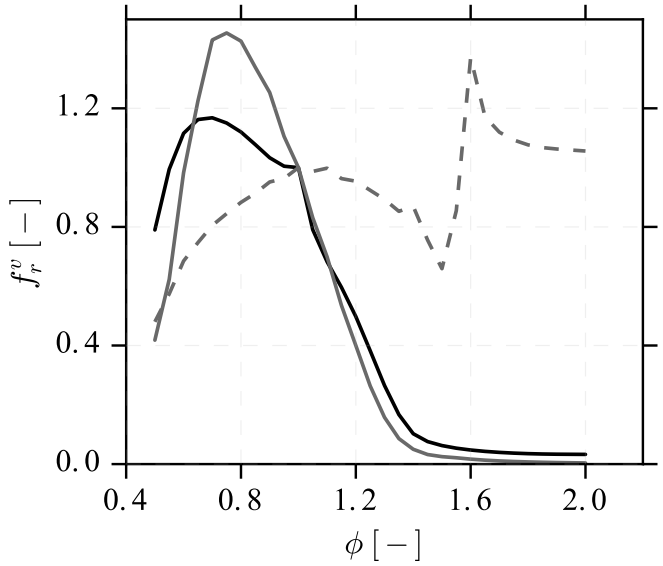

Figure 4.2: *Evolution of the correction function f_r^v with the equivalence ratio. Function f_1^v for reaction M1-1 (—), f_1^v for reaction M2-1 (—) and f_2^v for reaction M2-2 (--).*

4.2.1.2 Unstretched laminar premixed flames

A series of 1-D premixed laminar methane-air flames is simulated with the chemical combustion models shown in Table. 4.1. Predicted laminar consumptions speeds S_L are plotted in Fig. 4.3. Both virtual and BFER global schemes reproduce well the laminar flame speed evolution in comparison with the detailed mechanism. The optimization of the correction function applied on the pre-exponential factor of the fuel oxidation reaction enables a very good agreement between the low-order mechanisms and the reference detailed chemistry. Interestingly, as long as the main virtual scheme is trained to reproduce a reference database including differential diffusion effects, the molecular diffusive fluxes may be modeled with a unity Lewis number assumption without impacting the capture of the laminar speed. The tabulated chemistry approach with correction of differential diffusion effects matches very well the reference curve. The analytically-reduced chemistry method recovers successfully the evolution of the laminar flame consumption speed with the equivalence ratio. Finally, the global scheme proposed by Jones and Lindstedt gives an overall good description of the bell-shaped curve, but overestimates the laminar flame speed for lean and especially rich flames.

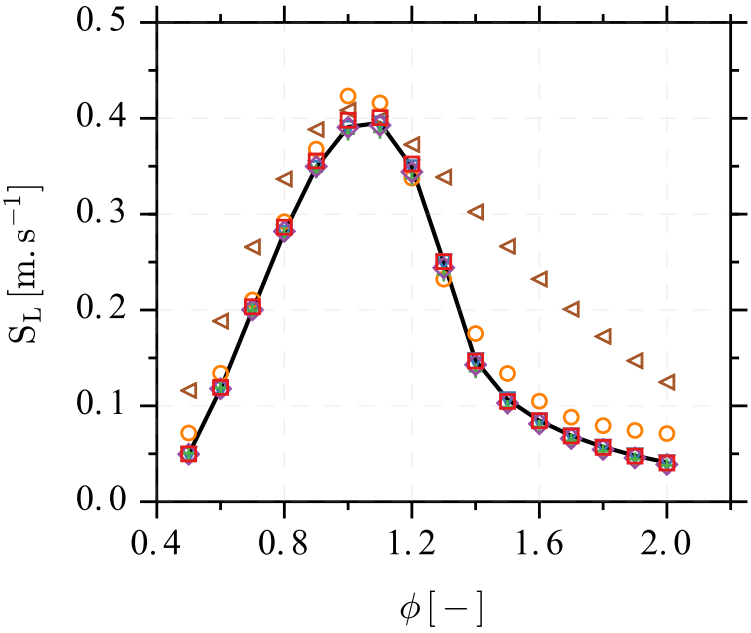

Figure 4.3: *Evolution of the laminar flame speed S_L with the equivalence ratio for a premixed methane/air flame at fresh gas temperature T_f = 300 K and pressure P = 1 atm. Legends: (—) Reference, (○) Global 1, (◁) Global 2, (+) Analytic, (▽) Tabulated, (◇) Virtual M1, (□) Virtual M2.*

Figure 4.4 shows the temperature profiles of a selection of 1-D laminar premixed methane/air flames computed for four values of equivalence ratio, namely ϕ = 0.6, 1.0, 1.4 and 1.8. For lean condition at $\phi = 0.6$, the two virtual mechanisms provide a correct description of the spatial temperature evolution. When increasing the fresh gas equivalence ratio, discrepancies arise between the two virtual optimized models. In stoichiometric conditions, contrarily to the M2 scheme the optimized one-step mechanism M1 fails to predict the two layers flame structure composed of a thin fuel oxidation layer followed by a thicker oxidation layer (Bui-Pham et al. 1992). The one-step virtual scheme featuring a unique characteristic time scale is indeed not able to predict both the two layers flame structure observed for $\phi \in [0.7, 1.3]$, and the single-layer structure taking place for very lean ($\phi \in [0.5, 0.7]$) and rich ($\phi \in [1.3, 2.0]$) mixtures. In the M2 scheme, the tabulation of the intermediate reaction order $F^v_{I,2}$ with the mixture fraction enables the adjustment of the characteristic thickness of the post-flame zone and a proper description of both flame structure types. Regarding global chemistry, the BFER scheme built to reproduce global flame quantities fails to retrieve the local flame structure and predicts a very rapid reach of the equilibrium. For all equivalence ratios investigated, the global mechanism shows a very thin post-flame region where the temperature is overestimated. Though the Jones and Lindsedt scheme was derived to retrieve the

local flame structure of a stoichiometric laminar premixed flame, the global scheme lacks of predictive capabilities for all initial compositions investigated. Similarly to BFER mechanism, the four-step model predicts a very rapid reach of the equilibrium, and underestimates the thickness of the recombination zone. Finally, the analytic mechanism and the tabulated chemistry strategy provide a correct description of the temperature profiles.

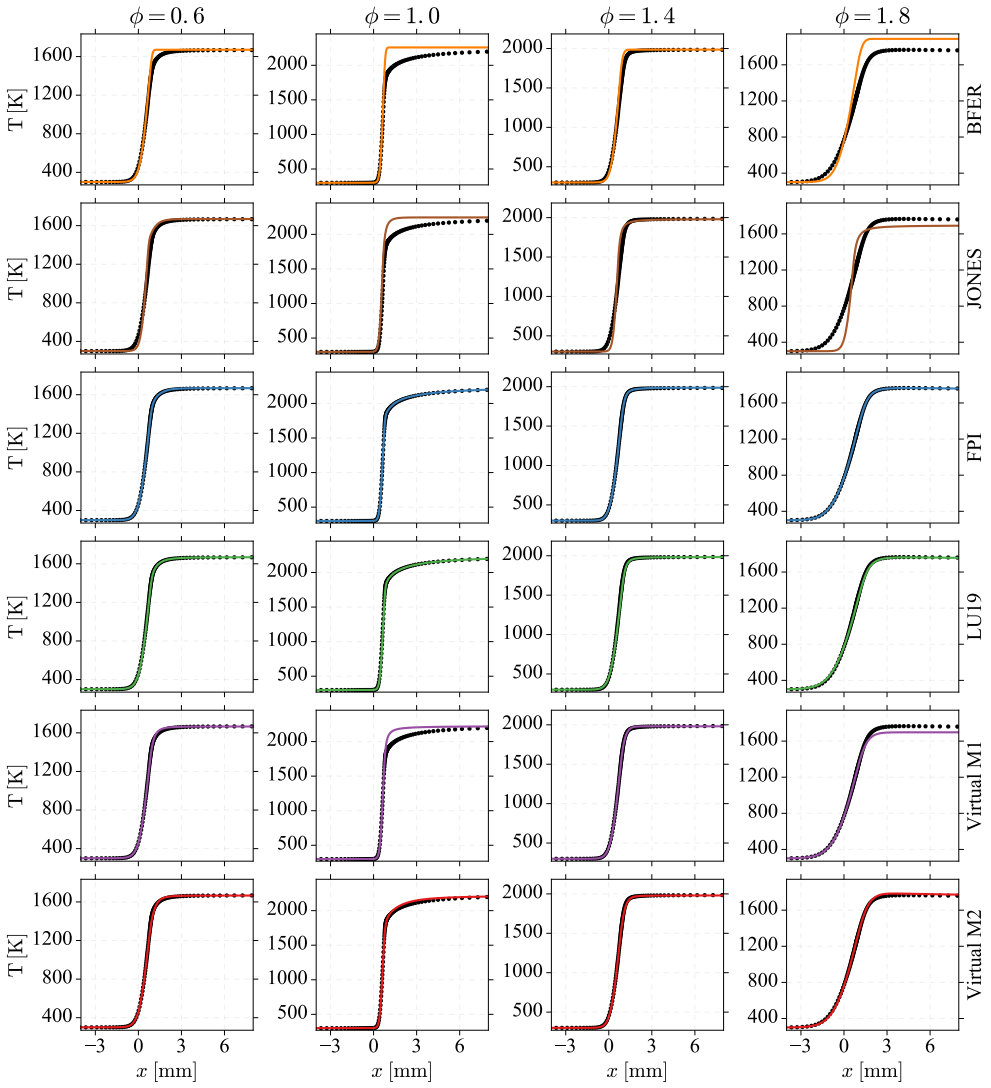

Figure 4.4: *Spatial evolution of temperature for premixed methane/air flames at fresh gas temperature* $T_f = 300$ K *and pressure* $P = 1$ atm. *Legends: (• •) Reference, (—) Global scheme 1, (—) Global scheme 2, (—) Tabulated, (—) Analytic, (—) Virtual M1, (—) Virtual M2.*

Detailed chemistry calculations show that for rich injection conditions (for $\phi > 1.4$), the maximum flame temperature reached in a premixed flame front is

higher than the equilibrium temperature T_{eq} obtained in fully burnt gases. This behavior, characterized as endothermic, is clearly visible on Fig. 4.5 showing the temperature evolution across the rich premixed flame of Fig. 4.4 (fourth column) with a different spatial scale. As the second reaction M2-2 of the two-step virtual mechanism is designed to predict endothermic behavior for $\phi > 1.4$, the asymptotic temperature decrease from its maximum value to the equilibrium is well captured. The two semi-global schemes are not optimized to capture this effect and predicts a rapid reach of the equilibrium. The M1 mechanism, being in essence not able to reproduce such temperature decrease, also reaches directly the equilibrium temperature.

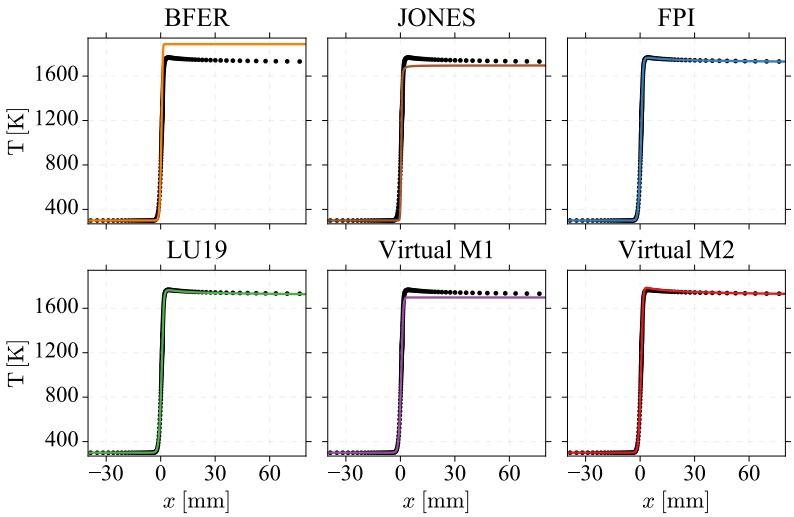

Figure 4.5: *Spatial evolution of temperature for premixed methane/air flames at fresh gas temperature* $T_f = 300$ K*, initial pressure* $P = 1$ atm *and initial equivalence ratio* $\phi = 1.8$*. Legends: (• •) Reference, (—) Global scheme 1, (—) Global scheme 2, (—) Tabulated, (—) Analytic, (—) Virtual M1, (—) Virtual M2.*

Even though the heat release rate is not an explicit target of the optimization process, it is mandatory to evaluate the capabilities of the virtual mechanism to describe this key quantity. Figure 4.6 illustrates the heat release rate evolution along the flame for the six reduced mechanisms. Both BFER and Jones mechanisms importantly overestimate the heat release rate amplitude. This observation is consistent with the fact that the global-step schemes predict a very rapid reach of the asymptotic equilibrium temperature. For stoichiometric and rich conditions, the optimized virtual mechanisms correctly predict the heat release profiles in terms of both amplitude and thickness. For lean injection conditions, the amplitude of the maximum heat release is under-estimated. Eventually, analytic and tabulated chemistry heat release rate profiles are in excellent agreement with the reference complex kinetic solutions.

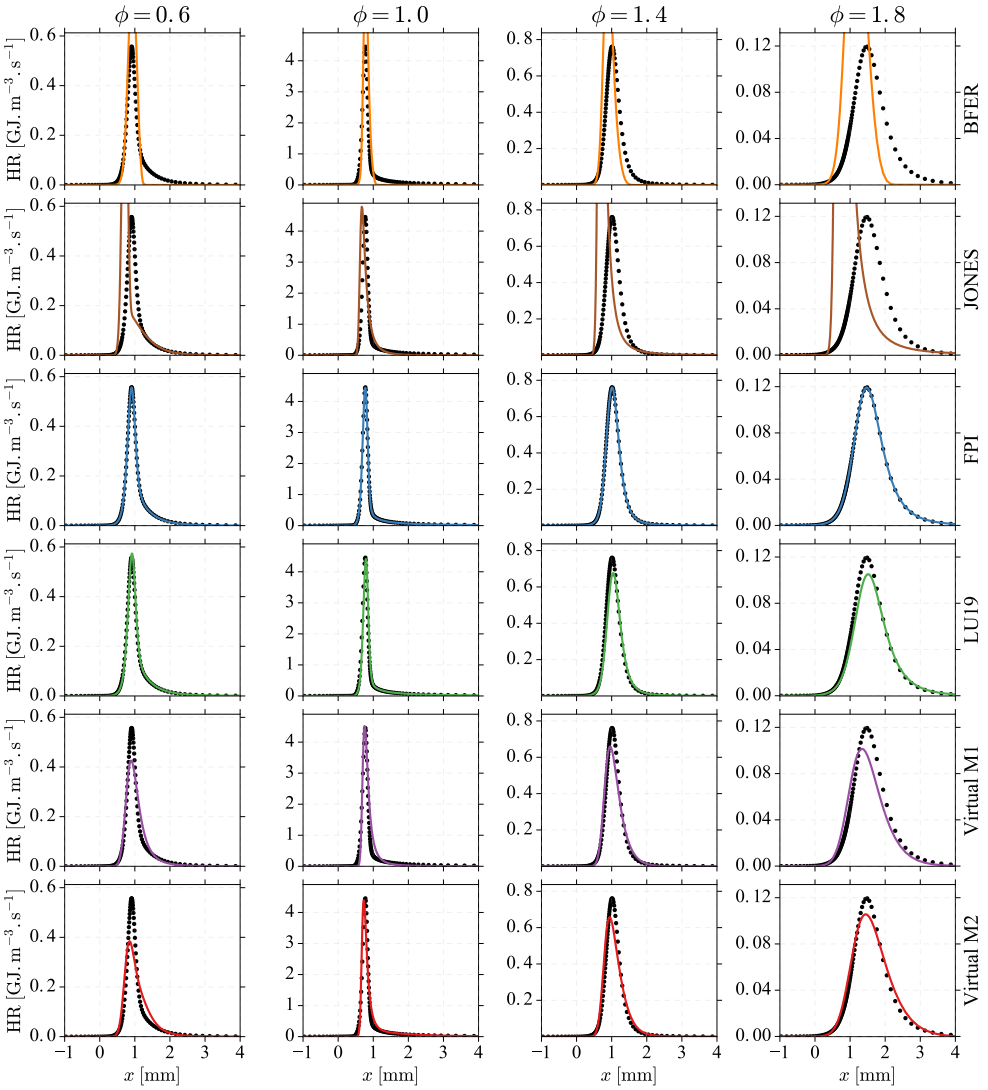

Figure 4.6: *Spatial evolution of heat release rate for premixed methane/air flames at fresh gas temperature* $T_f = 300$ K *and pressure* $P = 1$ atm. *Legends: (• •) Reference, (—) Global scheme 1, (—) Global scheme 2, (—) Tabulated, (—) Analytic, (—) Virtual M1, (—) Virtual M2.*

4.2.1.3 Counterflow laminar flames

The virtual mechanism trained to capture the premixed flame structure is *a posteriori* tested on non-premixed counterflow flames. A set of counterflow flames have been simulated for strain rates varying from $a = 15$ s^{-1} to a_c, the strain rate at which the diffusion flame is close to quenching. The variation with the strain rate of the peak temperature obtained in the flame front is presented in Fig. 4.7.

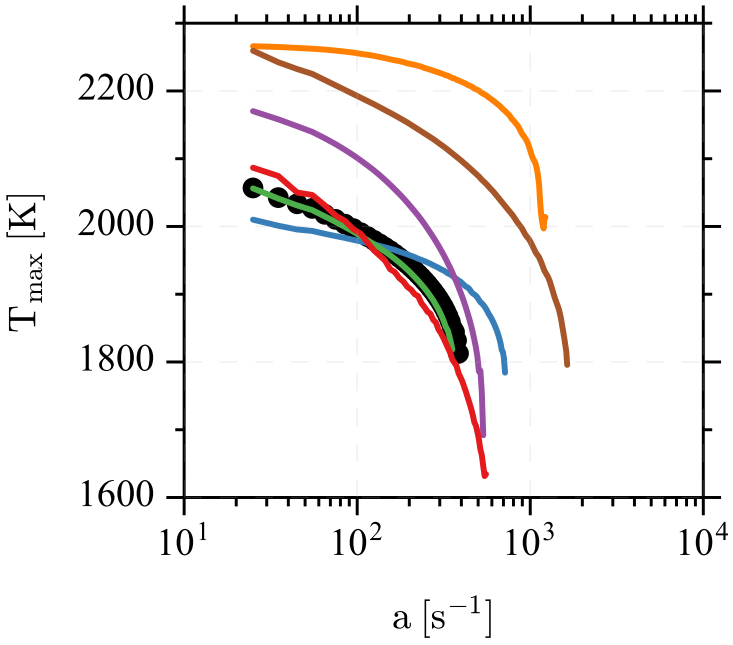

Figure 4.7: *Evolution with the strain rate of the peak temperature obtained in 1-D counterflow methane/air flames at fresh gas temperature $T_f = 300$ K and pressure $P = 1$ atm. Legends: (• •) Reference, (—) Global scheme 1, (—) Global scheme 2, (—) Tabulated, (—) Analytic, (—) Virtual M1, (—) Virtual M2.*

The optimized one-step mechanism M1 over-predicts the maximum temperature on the whole range of strain rates. On the contrary, the two-step virtual mechanism captures well the maximum temperature obtained in diffusion flame fronts. However, a slight overestimation of the extinction strain rate is observed. The detailed kinetic model GRI3.0 predicts extinction of the counter-flow diffusion flame for a strain rate a_c^d of 385 s^{-1}, while with the two-step virtual scheme the diffusion flame front persists up to 535 s^{-1}. Regarding the two semi-global schemes, important overestimation of the peak temperature is noticed for all strain rates. BFER and Jones mechanism are almost not affected by the mechanical effects and over-predict the quenching strain limit by almost one order of magnitude. The FPI approach tends to under-estimates the temperature levels for low strain rates, while over-estimation of the peak temperature is found

for high strain rates. The quenching limit predicted by the premixed-based tabulated approach is twice higher than the reference value. Analytically-reduced chemistry reproduces very well the maximum temperature levels and the occurence of flame extinction.

Figure 4.8 compares spatial temperature profiles predicted by the different kinetic models. Pure methane is injected from the right side and air flows from the left.

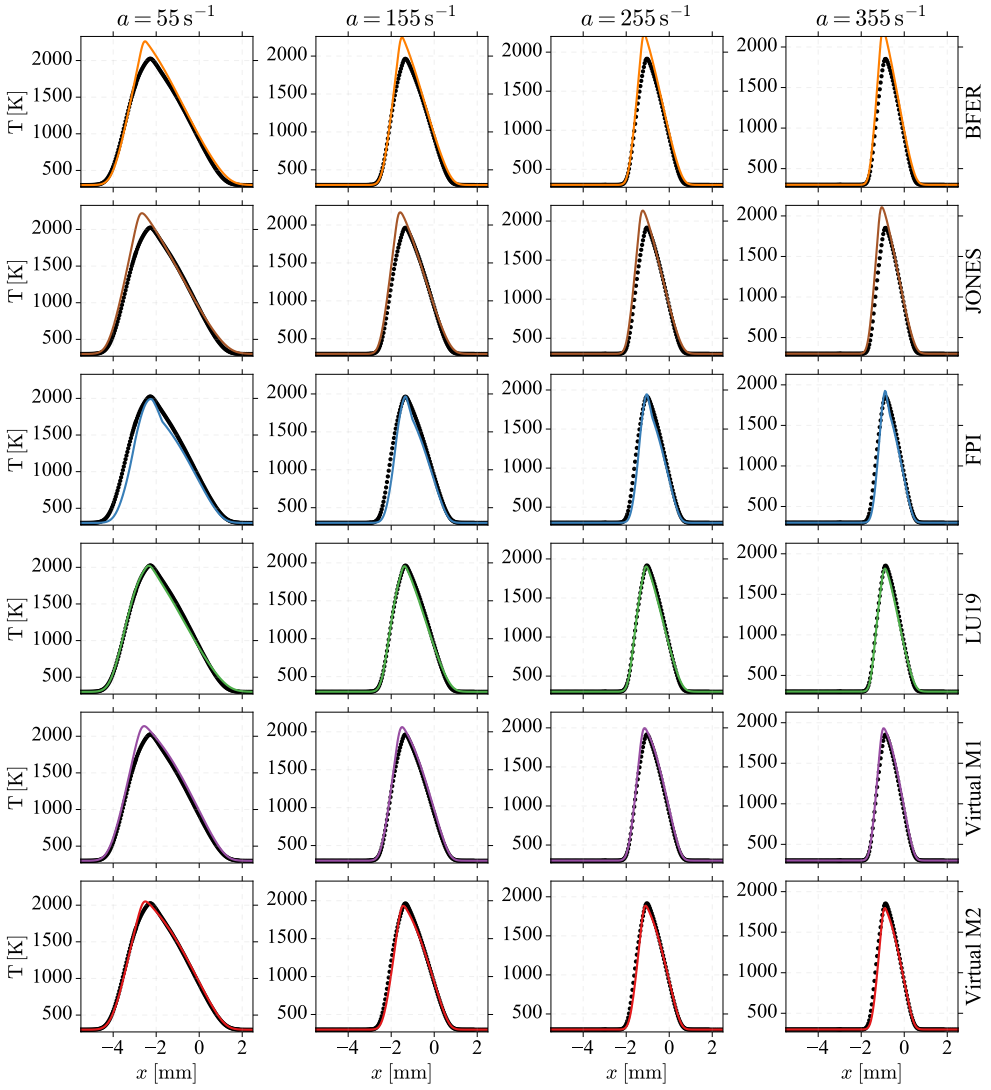

Figure 4.8: *Spatial evolution of the temperature for counterflow methane/air flames at fresh gas temperature $T_f = 300\ K$ and pressure $P = 1\ atm$. Legends: (• •) Reference, (—) Global scheme 1, (—) Global scheme 2, (—) Tabulated, (—) Analytic, (—) Virtual M1, (—) Virtual M2.*

Comparison between the reference temperature profiles and the solutions provided by the M1 virtual scheme shows that the reduced one-step mechanism tends to overestimate the maximum temperature. Increasing the dimensionality of the virtual scheme improves greatly the agreement between detailed chemistry and the virtual optimized approach. Indeed, the temperature profiles predicted by the two-step virtual optimized mechanism match well the reference database for all strain rates investigated. The position of the maximum temperature is nevertheless slightly shifted towards the oxidizer side. This discrepancy, especially present for low strain rates, may be explained by the unity Lewis number assumptions. As the diffusion flame archetype is not included in the reference flame library, the effects of differential diffusion under strain rate are not fully captured. Improvements would be i) to add the counterflow flames in the reference database, and ii) identify the virtual species transport properties (Le_k) that best capture differential diffusion effects under both strained and unstrained configurations. For the whole range of strain rates, the global mechanisms predict a quasi constant maximum temperature. This suggests that the reduced global schemes have difficulties to retrieve the impact of strain rate on the counterflow flame structure. The tabulated chemistry strategy provides a reasonable reproduction of the temperature profiles. The temperature departs however from the reference solution in the lean side of the flame. This observation is in accordance with the *a posteriori* test of the premixed tabulated method on diffusion flames performed in (Fiorina et al. 2005). Regarding the analytic scheme, a very good agreement is obtained with detailed chemistry calculations.

4.2.2 Virtual sub-mechanism for CO emission prediction

The concept of virtual satellite scheme dedicated to the capture of a pollutant species formation is here tested for CO. As discussed in Chapter 3, the sub-mechanism for CO prediction is coupled with the main virtual scheme for temperature prediction. Regarding the results of the comparative study, the two-step main virtual scheme, providing a better description of the flame temperature profiles, is retained.

4.2.2.1 Optimization of the kinetic rate parameters

The influence of the reference database used to train the virtual mechanism for CO is discussed. A first optimization procedure is performed using a target database composed of a collection of 1-D premixed laminar flames only. While a second optimization calculation uses a reference flame library made up of both 1-D premixed and non-premixed laminar flamelets. Table 4.4 summarizes the different optimization calculations carried out.

Virtual scheme	Reference database
CO-PREM	Premixed flames for $\phi \in [\phi_L; \phi_R]$
CO-PREM-DIFF	Two premixed flames for $\phi = \{1.0, 1.6\}$ Non-premixed strained flame for $a = 50\ s^{-1}$

Table 4.4: *Target database used for the CO satellite mechanism optimization calculations.*

For the first optimization calculation, the two-stage optimization procedure presented in sub-section 4.2.1.1 is used. As the second optimization calculation targets a non-premixed counterflow flame, experiencing variation of the mixture fraction from 0 to 1, this strategy is not relevant. To allow an efficient optimization, mixture fraction dependent correction functions are expressed analytically. Consequently, only a reduced set of parameters closing the analytic functions must be optimized instead of the individual values of the correction functions. Expressions of the analytic functions are deduced by fitting the tabulated correction functions optimized in the first optimization.

Kinetic rate parameters associated with the two virtual mechanisms are reported in Table 4.5, while evolution of the correction functions are depicted in Fig. 4.9. For both CO-PREM and CO-PREM-DIFF, the optimization calculations converge towards negative values for the forward reaction orders of the virtual species V_2. To prevent numerical difficulties clipping of the virtual species concentration is therefore required when evaluating species source terms.

Reaction	A_r^v	$E_{a,r}^v$	$F_{k,r}^v$	
CO-PREM R4	7.9×10^{18}	62.1×10^3	$F_{F,4}^v$	1.52
			$F_{V_1,4}$	1.23
CO-PREM R5	2.8×10^{17}	53.7×10^3	$F_{CO,5}^v$	2.88
			$F_{V_2,5}$	-0.88
CO-PREM-DIFF R4	7.9×10^{18}	74.8×10^3	$F_{F,4}^v$	1.17
			$F_{V_1,4}$	1.34
CO-PREM-DIFF R5	2.8×10^{17}	37.9×10^3	$F_{CO,5}^v$	3.71
			$F_{V_2,5}$	-1.09

Table 4.5: *Kinetic rate constants of the CO sub-mechanisms (Units: cm, s, cal and mol)*

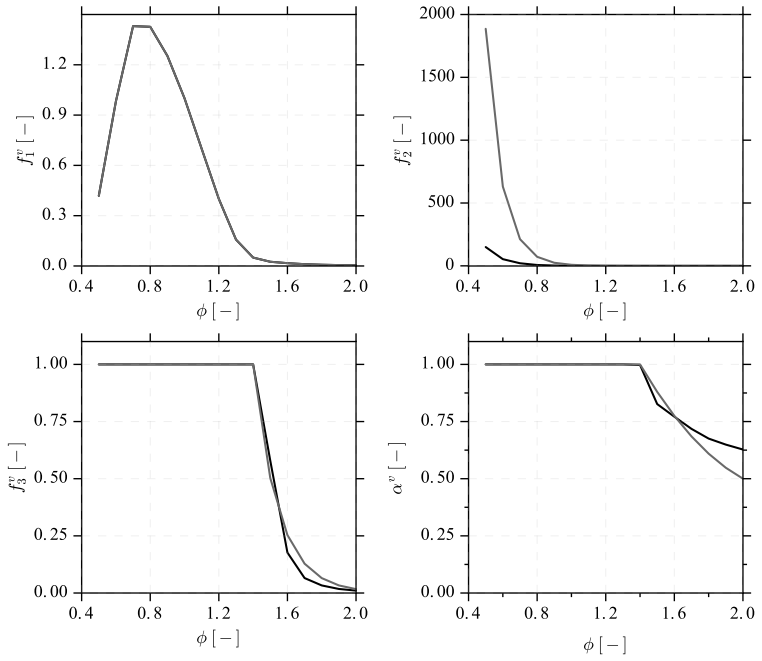

Figure 4.9: *Evolution of the correction function f_r^v and stoichiometric coefficient α^v with the equivalence ratio. Legends : (▬) CO-PREM scheme, (▬) CO-PREM-DIFF scheme.*

4.2.2.2 Unstretched laminar premixed flames

1-D laminar premixed flames are computed for various equivalence ratios with the different chemistry reduction methods. The ability of reduced chemical schemes to retrieve thermo-chemical equilibrium state is first challenged. For that purpose, compositions of burnt gases is extracted from the steady state

solutions of premixed laminar flames. Figure 4.10 compares the CO mass fractions in burnt gases of premixed flames predicted by reduced chemistry and detailed mechanisms. Both virtual mechanisms reproduce well the equilibrium values thanks to the tabulation of the equilibrium constant in reaction R5. The global scheme, composed by only 6 species, does not capture the CO mass fraction at equilibrium for rich mixtures. In these conditions, the exclusion of H_2 does not make possible a proper description of the equilibrium state. Eventually, the Jones and Lindstedt scheme, the FPI tabulated approach and the analytic model provide a correct description of CO equilibrium mass fractions.

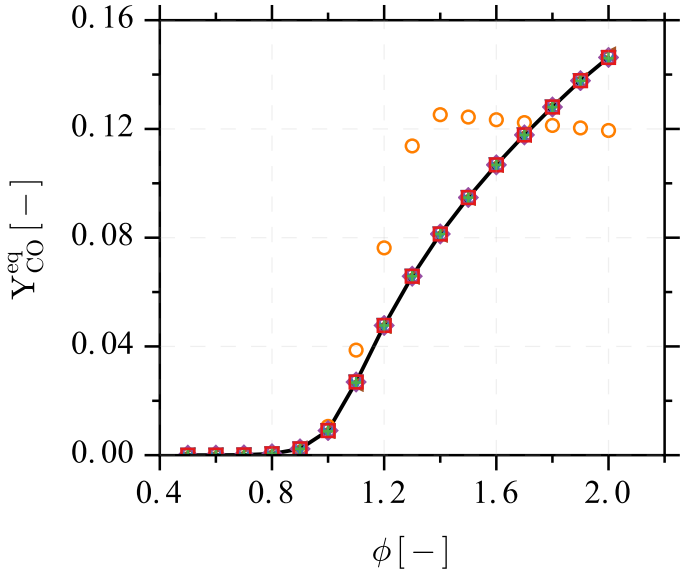

Figure 4.10: *CO equilibrium mass fraction versus equivalence ratio for a premixed methane/air flame at fresh gas temperature $T_f = 300\ K$ and pressure $P = 1\ atm$. Legends: (—) Reference, (○) Global 1, (◁) Global 2, (+) Analytic, (▽) Tabulated, (◇) Virtual CO-PREM, (□) Virtual CO-PREM-DIFF.*

Spatial CO mass fraction profiles predicted by different reduced and tabulated approaches are compared to detailed chemistry solutions in Fig. 4.11. The virtual optimized sub-schemes for CO formation matches reasonably well the complex chemistry profiles. For lean and stoichiometric injection conditions, the characteristic time to reach the equilibrium value is however either slightly too slow (lean conditions) or too fast (stoichiometry). In very rich flames, the optimized virtual mechanisms reproduce well the slow increase of CO mass fraction profile in the post-flame zone. It should be noted that CO-PREM and CO-PREM-DIFF sub-mechanisms feature similar predictive capabilities with an overall good prediction of CO mass fraction profiles. It means that the addition of the non-premixed flame in the reference database does not alter the

prediction of CO profiles in premixed combustion regime.

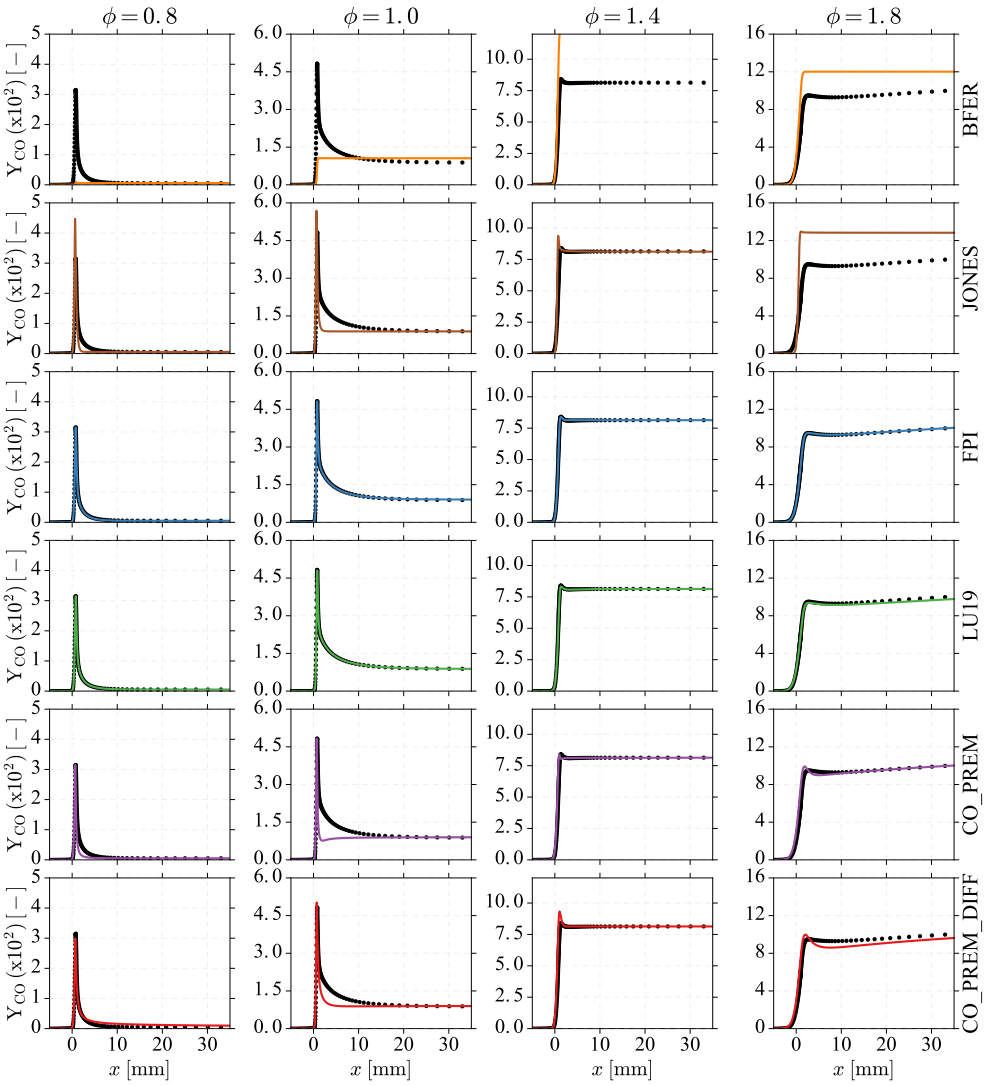

Figure 4.11: *Spatial evolution of the CO mass fraction for a 1-D premixed methane/air flame at fresh gas temperature T_f = 300 K and pressure P = 1 atm. Legends: (• •) Reference, (—) Global scheme 1, (—) Global scheme 2, (—) Analytic, (—) Tabulated, (—) Virtual CO-PREM, (—) Virtual CO-PREM-DIFF.*

On the whole range of equivalence ratio investigated, the seven species global mechanism tends to overestimate the CO mass fraction peaks and predict a rapid reach to of asymptotic equilibrium value. As demonstrated by Franzelli (2011), the two-step global scheme BFER predicts a monotonous evolution of CO mass fraction profile toward the equilibrium value. As a consequence, the semi-global scheme tends to underestimate CO formation in lean and moderately rich flames, and over-predicts CO emissions in very rich conditions. The

premixed based tabulated strategy FPI and the analytically-reduced mechanism LU19 are in very good agreement with detailed chemistry solutions.

4.2.2.3 Diffusion flames

Both CO-PREM and CO-PREM-DIFF virtual blocks are tested on counterflow flames for different values of strain rates. Figure 4.12 compares the CO mass fraction profiles obtained with the different chemistry description strategies of Tables 4.1 and 4.4.

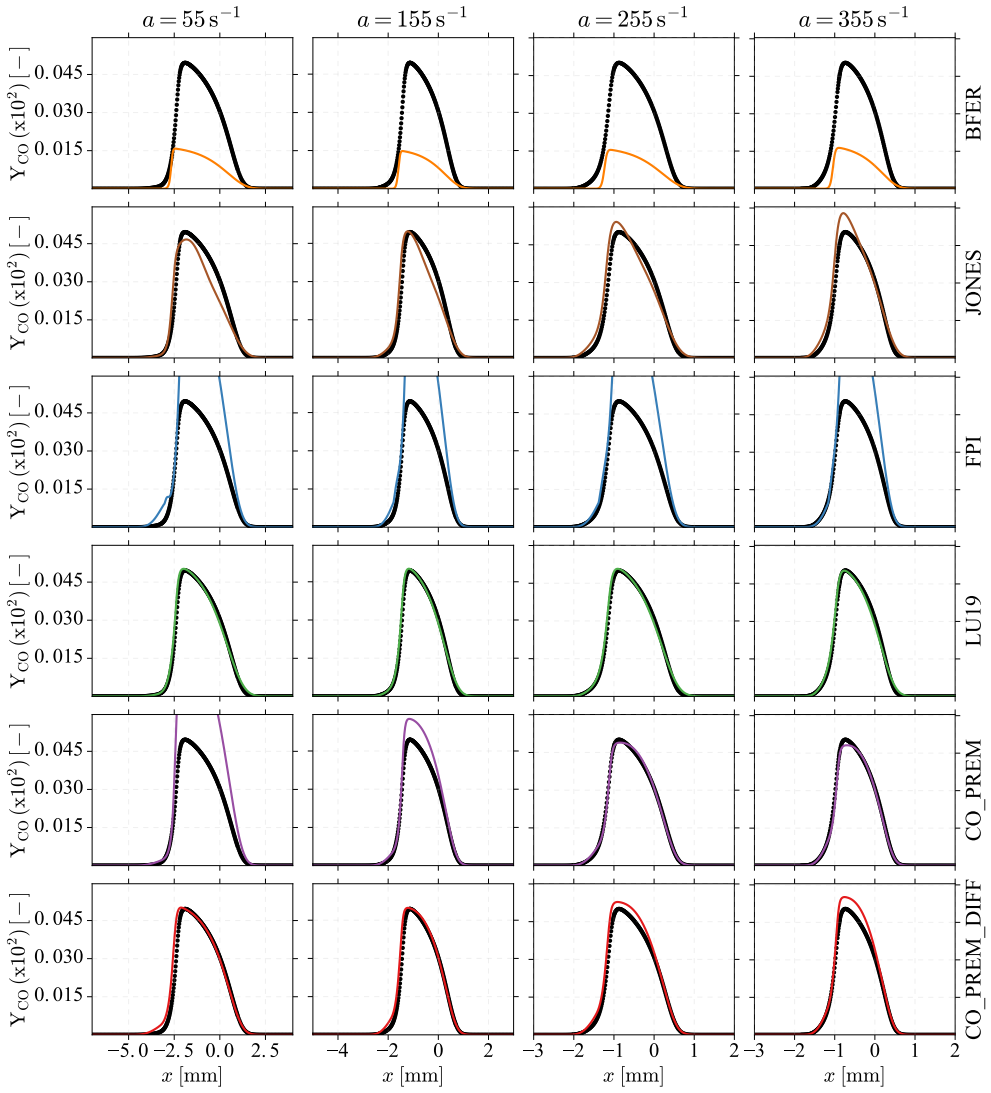

Figure 4.12: *Spatial evolution of the CO mass fraction for 1-D counterflow methane/air flames at fresh gas temperature* $T_f = 300$ K *and pressure* $P = 1$ atm. *Legends: (• •) Reference, (—) Global scheme 1, (—) Global scheme 2, (—) Analytic, (—) Tabulated, (—) Virtual CO-PREM, (—) Virtual CO-PREM-DIFF.*

The Jones global scheme solutions are in overall good agreement with detailed chemistry for all strain rates. Some slight discrepancies regarding the CO mass fraction peak positions and values are however noticeable. The BFER global scheme underestimates the CO mass fraction for all strain rates. These discrepancies can be related to the fact that in premixed configuration (see Fig. 4.11), the global model underestimates the level of CO in the fuel oxidation layer from lean to moderately rich mixtures. Regarding results obtained with the analytically-reduced mechanism, Fig. 4.12 shows that a very good agreement is obtained for the all range of strain rates investigated. If the two virtual blocks CO-PREM and CO-PREM-DIFF give similar responses in premixed configurations, this is not the case in non-premixed mode. For low strain rates, the CO-PREM sub-mechanism built from a premixed database highly overestimates the CO levels. On the contrary, the mass fraction profiles are well captured with the CO-PREM-DIFF virtual scheme for low strain rates. The addition of the non-premixed strained flame archetype at $a = 50\,s^{-1}$ in the reference library greatly improves the predictive capabilities not only for $a = 55\,s^{-1}$ but also for higher strain rates. Therefore to properly predict CO levels the kinetic model must be optimized on both premixed and non premixed flame. This conclusion is consistent with tabulated chemistry solutions, where the premixed-based tabulated approach does not capture the CO profiles. Unlike to heat release and temperature, it appears mandatory to account for the co-existence of different combustion regimes to capture pollutant species such as CO.

4.2.3 Computational costs and model errors

The computational time associated with the calculation of mono-dimensional laminar premixed flames is discussed. The resolution of such canonical problem is performed with the REGATH flame solver (Darabiha and Candel 1992) based on a Newton-type algorithm whose cost is mainly dependent on the evaluation of the Jacobian matrix and the inversion of the system. It can be shown that this cost is proportional to the number of reactions and scales with the squared number of equations to solve (Pepiot 2008). When complex transport models are used, a non-negligeable additional cost is associated with the evaluation of binary diffusion coefficients. As discussed in Chapter 1, this overcost scales with N_s^2. Finally, the computational cost also depends on the stiffness of the numerical system.

Table 4.6 presents the relative CPU time $\mathcal{C}_r$ of the different chemical strategies with virtual chemistry taken as reference. The cost of an iteration T is averaged over 50 iterations to ensure representativity of the comparison. The normalized cost $\mathcal{C}_n$, whose definition is given in Table 4.6, is added to highlight the overcosts associated with transport modeling and chemical stiffness. Compared to the detailed scheme, virtual chemistry allows a reduction of computational time by a factor of 135. As the normalized cost is not close to unity, this high

difference is not only due to the size of the kinetic scheme. Indeed, the chemical stiffness of the detailed mechanism and the complex transport model used to close the molecular diffusive fluxes contribute importantly to the overall cost of the simulation. With identical transport models, virtual chemistry is about 10 times less expensive than analytic mechanism. The computational gain offered by virtual mechanisms is first related with the low numbers of species and reactions involved in the scheme in comparison with analytic chemistry. Secondly, the residual stiffness of the analytically-reduced mechanism tends to increase the computational time associated with the resolution of species transport equations (see stiffness analysis hereinafter). Comparing the proposed strategy to global chemistry shows that virtual chemistry is about 40% more expensive. This 40% difference, explained by the additional number of transported species involved in virtual mechanisms, is acceptable. Finally tabulated chemistry strategy is more than ten times cheaper than virtual chemistry. However, as the normalized cost is almost unity, we can conclude that the extra cost associated with virtual chemistry is due to the number of transported variables.

Case	Transport model	Number of eq. N_{eq}	Relative CPU time $\mathcal{C}_r = T/T^v$	Normalized CPU time $\mathcal{C}_n = (TN_{eq}^{v\,2})/(T^v N_{eq}^2)$
Reference	Complex	55	135	7.58
Global 1	$Sc_k = cst$	9	0.76	1.57
Global 2	$Sc_k = cst$	8	0.65	1.70
Analytic	$Sc_k = cst$	21	9.55	3.66
Tabulated	$Sc_k = cst$	3	0.07	1.30
Virtual	$Sc_k = cst$	13	1.00	1.00

Table 4.6: *Relative costs of chemical strategies compared to virtual chemistry approach for 1-D methane/air premixed flame calculations with REGATH*

The deviation between reduced chemistry models and the reference complex kinetic scheme is quantified by adding error criteria for each quantity of interest. The relative error between the reduced model r and the detailed model d associated with the target quantity s is given by:

$$\mathcal{E}_s = \sum_{i=1}^{N_{op}} \frac{\| s_i^r(x) - s_i^d(x) \|_{L_2}}{\| s_i^d(x) \|_{L_2}} \tag{4.6}$$

where N_{op} is the number of operating conditions tested (i.e. equivalence ratio in premixed flames or strain rates in diffusion flames). Table 4.7 summarizes the level of errors in both premixed and non-premixed flames. Relative errors for the quantities considered during the optimization procedure (laminar flame speed $\mathcal{E}_{S_L}$, temperature $\mathcal{E}_T$ and CO mass fraction $\mathcal{E}_{CO}$) are presented. The relative error norms associated with the capture of density profiles ($\mathcal{E}_\rho$), which are not directly targeted when deriving the virtual mechanism, are also given.

	Premixed flames				Diffusion flames		
Case	$\mathcal{E}_{S_L}$ [%]	$\mathcal{E}_T$ [%]	$\mathcal{E}_\rho$ [%]	$\mathcal{E}_{CO}$ [%]	$\mathcal{E}_T$ [%]	$\mathcal{E}_\rho$ [%]	$\mathcal{E}_{CO}$ [%]
Global 1	14.34	2.72	0.49	37.32	10.01	1.28	69.57
Global 2	77.95	0.43	0.55	8.70	11.44	2.26	16.24
Analytic	4.38	0.16	0.08	0.89	2.59	0.71	5.78
Tabulated	0.19	0.03	0.04	0.35	8.58	3.42	84.81
Virtual P	1.11	0.15	0.10	6.34	5.65	1.96	23.00
Virtual P-D	1.11	0.15	0.10	7.18	5.65	1.96	11.75

Table 4.7: *Relative errors of chemical strategies compared to virtual chemistry approach for 1-D methane/air premixed and diffusion flame calculations with REGATH*

As expected, in premixed combustion mode, the FPI tabulated chemistry approach yields negligible error levels (lower than 1%) mainly associated with the choice of the progress variable. However, as noticed in Fig. 4.12 when the premixed tabulated method is applied in counterflow non-premixed flame configuration, it fails to capture CO emission levels. Regarding analytically-reduced chemistry scheme, small deviation levels are obtained for both premixed and non-premixed conditions. In premixed combustion mode, the four-step global mechanism features important error levels for all flame variables of interest. These high discrepancies are the results of i) the overestimation of laminar flame speed in rich conditions leading to shorter thermal thicknesses, and ii) an underestimation of the chemical time scales in the post-flame region leading to temperature and CO mass fraction over-prediction. In non-premixed flame configurations, the Jones and Lindstedt kinetic scheme is associated with acceptable error levels for the CO mass fraction prediction, but lacks of predictive capabilities for temperature description compared to other models. As previously discussed the BFER semi-global scheme built to reproduce global flame properties features important error levels for temperature and CO profiles in both premixed and counterflow flames. Finally, for premixed flames virtual optimized chemistry approach provides acceptable error level for all quantities investigated. In non-premixed conditions, the virtual optimized schemes dedicated to the prediction of the flame/flow field interaction produces acceptable overall error levels of about 5 %. As regards with CO formation, the CO-P virtual block associated with the main virtual scheme produces a deviation of 23 % in comparison with the detailed GRI mechanism. This discrepancy is reduced to 12 % with the virtual P-D sub-scheme built by using both premixed and non-premixed flames in the learning database.

4.2.4 Stiffness analysis

One key feature of a kinetic scheme is its chemical stiffness. This parameter characterizes the degree of disparity of the chemical time scales involved in the

system, and may be defined as follows:

$$\mathcal{S} = \frac{\max(\tau_k)}{\min(\tau_k)} \tag{4.7}$$

Where τ_k^{max} and τ_k^{min} refers to the maximum and minimum times scales. Various definitions of the chemical time scale τ_k can be identified in the literature. The simplest one assumes that convective and diffusive contributions are negligible in the flame front region (Hong et al. 1999). With this assumption, the chemical response of the kth species to a perturbation can be estimated as:

$$\tau_k = \frac{\max(\rho Y_k)}{W_k \max(\dot{\omega}_k)} \tag{4.8}$$

where max is the maximum value over the domain.
As discussed in the chemistry modeling review, more refined definitions based on the eigenvalues of the Jacobian matrix of the system could also be used to quantify chemical stiffness (Lam 1985). However, as the objective is to compare different kinetic mechanisms, estimation of Eq. 4.8 is sufficient as long as the different diffusive times do not induce important deviations between methods. Table 4.8 presents the minimum and maximum of chemical characteristic time scale for each kinetic scheme. The relative stiffness $\mathcal{S}^* = S^i/S^v$ comparing the stiffness of each method i to the main virtual mechanism stiffness is considered. Since flame structure and CO predictions are treated independently in the virtual chemistry formalism, two stiffnesses must be evaluated.

Case	$\tau_k^{min}[s]$	$\tau_k^{max}[s]$	$\mathcal{S}^* = \frac{\mathcal{S}^i}{\mathcal{S}^v}$
Reference	3.32×10^{-6}	6.93×10^{-3}	229.38
Global 1	4.17×10^{-5}	4.46×10^{-4}	1.17
Global 2	4.17×10^{-5}	4.46×10^{-4}	1.17
Analytic	1.05×10^{-5}	6.66×10^{-4}	6.70
Tabulated	7.95×10^{-5}	7.95×10^{-5}	/
Virtual TS	7.83×10^{-5}	7.13×10^{-4}	1.00
Virtual CO	4.13×10^{-5}	5.89×10^{-4}	1.57

Table 4.8: *Species chemical characteristic times of chemical strategies compared to virtual chemistry approach for 1-D methane/air premixed flame calculations with REGATH*

As expected, the detailed kinetic mechanism features a wide range of chemical time scales, leading to a very stiff behavior compared to other methods. Regarding analytically-reduced scheme, one may observe that the smallest chemical time associated to highly reactive species (H and CH_3) is lower than those exhibited by reduced mechanisms, confirming the hypothesis of residual stiffness.

Global reduced mechanisms and virtual mechanism show similar chemical time scales and level of stiffness. As tabulated chemistry involves only one transported variable, stiffness is meaningless. However, it is interesting to note that the chemical time scale of the progress variable is similar to the minimum time scale of global and virtual chemistry strategies.

The virtual optimized mechanisms for methane/air combustion have been successfully validated on 1-D premixed and non-premixed flames. The predictive capabilities of virtual chemistry are now evaluated on a 2-D laminar configuration.

4.3 Modeling of 2-D laminar methane/air burners

In most practical applications, the fuel/air mixture issuing the injection system exhibits composition inhomogeneities leading to stratified combustion regimes. To assess the virtual chemistry abilities to describe such combustion mode, a two-dimensional partially premixed burner is simulated. This simple laminar configuration has been chosen for two main reasons. First, laminar flow configuration eliminates the impact of turbulent combustion modeling, enabling a focus on combustion kinetics effects only. Secondly, the small dimensions of the burner make Direct Numerical Simulation (DNS) accessible in terms of CPU time even with complex chemistry model. The objective is to compare and analyze DNS of a partially premixed burner performed with the chemistry description strategies investigated in section 4.2.

4.3.1 Numerical set-up

The 2-D burner studied in this work has been previously investigated by (Fiorina et al. 2003) in non-adiabatic conditions. The burner geometry and its dimensions are illustrated in Fig. 4.13. A lean methane-air mixture, featuring a fresh gas equivalence of ratio of $\phi_P = 0.8$, is injected through a central injector. The primary stream is surrounded by air co-flow to isolate the flame from ambient perturbations. For both streams, the inlet velocity profile prescribed is a plug flow with characteristic velocity $U_{cf} = 0.05$ m.s^{-1} for the co-flow, and $U_P = 0.8$ m.s^{-1} (Re$_P$=125) for the primary inlet. The fresh gases temperature and pressure correspond to atmospheric conditions with $T_0 = 300$ K and $P = 1$ atm. As virtual chemistry mechanisms have been built to capture adiabatic flame configurations, injector walls are treated with adiabatic conditions. The transverse size of the computational domain being large enough to avoid interactions between premixed branches and the side boundaries, symmetry boundary conditions are considered for lateral walls. The computational domain is discretized into 1.03 million cells featuring a characteristic size Δ_x of 0.020 mm. With a laminar flame thickness $\delta_L^0|$ of 0.5 mm, the thermal flame front is resolved on about 25 points.

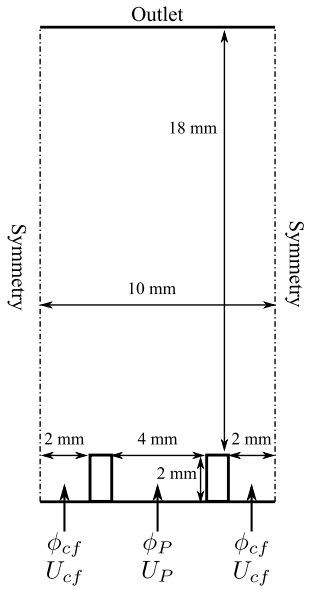

Figure 4.13: *Schematic view of the partially burner configuration.*

Direct Numerical Simulations have been performed with the low-Mach number, unstructured finite volume flow YALES2 solver (Moureau et al. 2011a). A centered fourth-order scheme is used for spatial discretization, while temporal integration is performed explicitly using a fourth-order TRK4 scheme (Kraushaar 2011).

4.3.2 Results analysis

4.3.2.1 Temperature and flame stabilization

Figures 4.14 and 4.15 display the temperature and heat release rate fields predicted by detailed, analytic, semi-global, tabulated and virtual chemical models. The direct comparison of the temperature 2-D fields demonstrates a qualitative good agreement between all chemistry modeling approaches. All reduced chemical models provide a good reproduction of the temperature levels. A small difference is however noticeable for the global BFER scheme that over-predicts the temperature in the post-flame zone.
Regarding the heat release prediction, except the two-step global scheme that strongly overestimates its peak value, the agreement between the detailed and reduced chemical models is satisfactory. If the flame lengths evaluated by the different models are compared some slight differences may be observed. Table 4.9, presenting the distance between the combustion chamber wall and the flame tip, shows that both BFER and the virtual optimized schemes underestimate the flame length by about 13 %, while the premixed tabulated strategy predicts a flame 7.5 % shorter than detailed chemistry solution.

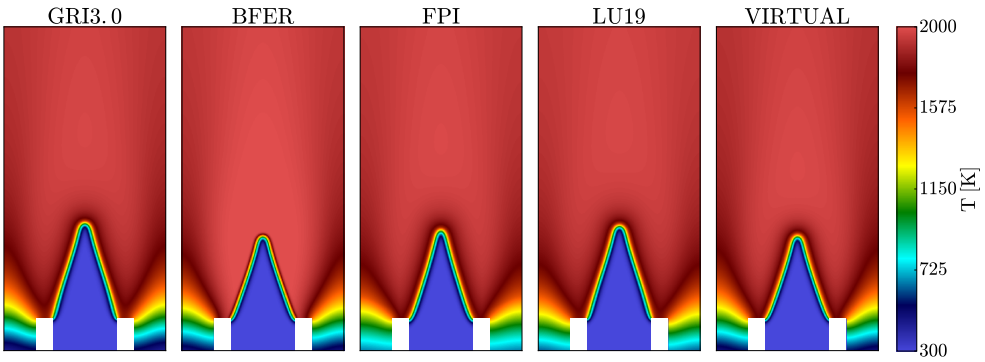

Figure 4.14: *Temperature field in the laminar partially premixed burner.*

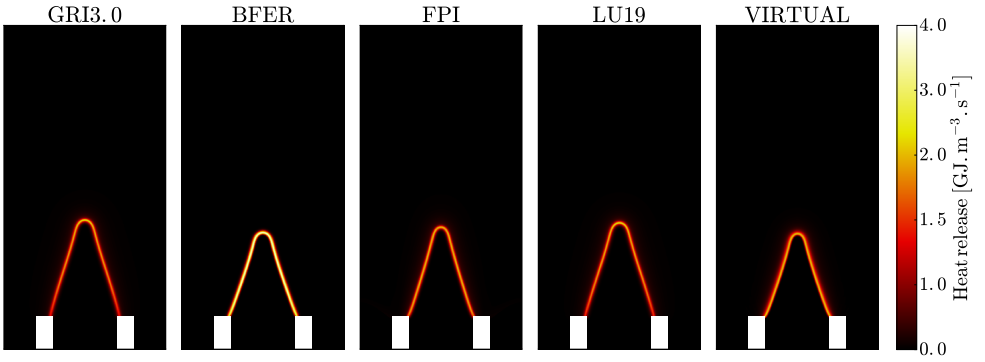

Figure 4.15: *Heat release field in the laminar partially premixed burner.*

Not only the flame length varies between the kinetic models, but the flame front shape and thickness depend on the chemistry modeling approach and transport models. Reduced global schemes and the tabulated model predict a straight and thick flame front, while with complex and analytic chemistry models the flame front features curved shapes with thickness variation along the axial direction. Finally, it may be noted that simulations performed with simplified transport models show a constant value of the heat release rate along the flame, whereas LU19 and GRI3.0 schemes show a variation of the heat release magnitude with the axial position. On the flame foot, near the injector wall, low values of heat release rate are encountered, and in the curved region at the flame top the levels of heat release are slightly higher than in the flat region. The reasons for these discrepancies may be attributed mainly to transport modeling. Tabulated, global and virtual chemistry close the diffusion fluxes with a unity Lewis number assumption. While, the analytic scheme evaluates species diffusivities assuming a constant Schmidt number for each species. The phenomena combining flame curvature and preferential diffusion effects, occurring in the direction tangential to the flame front, are not properly captured by the two reduced mechanisms due to too simple transport models.

	Reference	Global	Tabulated	Analytic	Virtual
Flame length [mm]	5.95	5.2	5.5	5.80	5.2

Table 4.9: *2-D partially premixed flame lengths estimated by the different chemistry description strategies*

Quantitative comparisons are provided in Fig. 4.16 and 4.17 where radial profiles of temperature and heat release are plotted for different axial positions from the burner entrance. The virtual optimized mechanism captures well the temperature and heat release profiles. Very good agreement is also observed between detailed, analytic and FPI models. However, the BFER scheme is not able to reproduce the temperature evolution in the flame front. Temperature profiles exhibit a sharp increase that can be related to the high amplitudes of heat release rate.

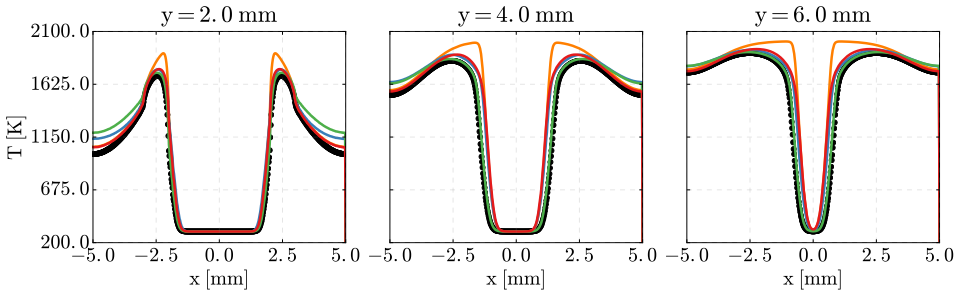

Figure 4.16: *Radial profile of temperature for different axial positions. (• •) Detailed mechanism, (—) BFER global scheme, (—) premixed tabulated method, (—) LU19 analytic scheme and (—) virtual mechanisms are compared.*

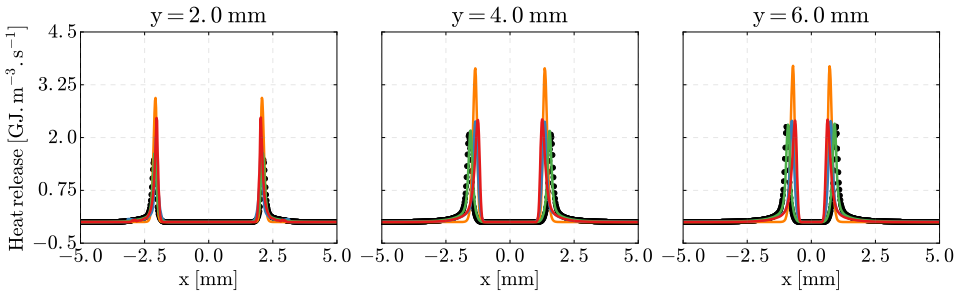

Figure 4.17: *Radial profile of heat release rate for different axial positions. (• •) Detailed mechanism, (—) BFER global scheme, (—) premixed tabulated method, (—) LU19 analytic scheme and (—) virtual mechanisms are compared.*

4.3.2.2 Carbone monoxide formation

A comparison of CO mass fraction fields is provided in Fig. 4.18. As expected from 1-D premixed laminar comparisons, the BFER global scheme largely under-predicts the CO concentration in the flame region. The satellite sub-scheme dedicated to CO formation matches well the detailed solution. Except a slight overestimation of the CO peak concentration the premixed-based tabulated approach reproduces well the CO field. Eventually, analytically-reduced chemistry is in excellent agreement with the complex GRI3.0 mechanism.

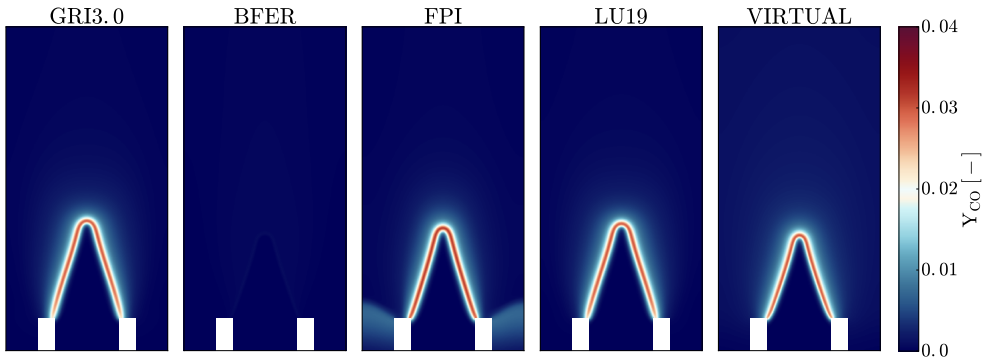

Figure 4.18: *CO mass fraction field in the laminar partially premixed burner.*

Qualitative comparisons from 2-D fields are complemented with the radial profiles of CO mass fraction displayed in Fig. 4.19. Except some slight discrepancies in the post-flame zone, the CO mass fraction predicted by the virtual chemistry approach fits well the detailed reference solution.

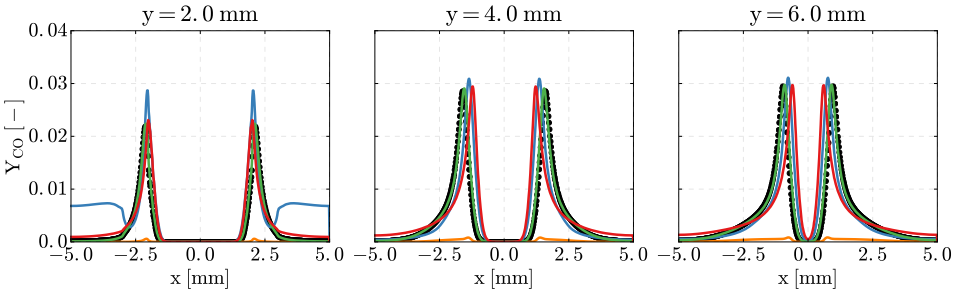

Figure 4.19: *Radial profile of CO mass fraction for different axial positions. (• •) Detailed mechanism, (—) BFER global scheme, (—) premixed tabulated method, (—) LU19 analytic scheme and (—) virtual mechanisms are compared.*

4.4 Modeling of aeronautical fuel oxidation

The virtual optimized strategy presented in Chapter 3 is used for the derivation of a reduced virtual scheme dedicated to the prediction of kerosene/air combustion. Particularly, two virtual optimized mechanisms are designed to capture the flame/flow field interaction and CO formation in high pressure and high temperature kerosene/air flames. Before presenting the virtual optimized models, a focus is made on the kerosene surrogate and associated complex kinetic scheme used for the generation of the reference flamelet database.

Virtual optimized chemistry approach has also been applied to the description of the oxidation of fuels of varying complexity. Appendix C discusses the predictive capabilities of three virtual optimized kinetic schemes devoted to the capture of ethylene, propane and n-heptane oxidation.

4.4.1 Kerosene surrogate and reference kinetic scheme

Kinetic modeling of jet fuel combustion is a challenging task. As aeronautical fuels are complex mixture of hundreds of chemical components, the comprehensive description of the fuel oxidation phenomena would require the merging of each individual detailed kinetic scheme, which is impractical. Moreover, jet fuels production is only constrained by the reproduction of a number of physical and chemical properties, and not by a defined chemical composition. Depending on the feedstock and refining processes, the resulting jet fuel composition may strongly vary. To circumvent these difficulties model fuels or surrogates composed by a reduced number of representative chemical molecules have been developed. The components intervening in the definition of the surrogate are chosen so as to emulate the physical (density, heat capacity, thermal conductivity, viscosity, boiling temperature, *etc*) and/or chemical (proportion of chemical classes, hydrogen content, *etc*) properties of the real aeronautical fuel. A number of surrogates and associated kinetic mechanisms were proposed to model kerosene/air combustion. Simplest models including a unique linear alkane provide a good reproduction of the oxidation kinetics of kerosene but fail to capture benzene and PAH concentrations (Dagaut et al. 1994). More complex surrogates are generally composed of alkanes, aromatics and naphthenes, and their size may vary from 2 to 6 chemical components (Lindstedt and Maurice 2000; Violi et al. 2002; Agosta et al. 2004). Detailed reviews of surrogates and available kinetic data describing aviation fuel oxidation can be found in (Edwards and Maurice 2001; Dagaut and Cathonnet 2006).

In this study the three-component surrogate model proposed by Dagaut (2002), along with the skeletal mechanism derived by Luche (2003) are used. Following the recommendations from Edwards and Maurice (2001), the choice of a multi-component surrogate was made to reproduce fuel vaporization, main flame

properties and pollutant emissions of the real fuel. Table 4.10 summarizes information on the surrogate composition.

Family	Species name	Composition	Mass fraction
Linear alkane	n-decane	$C_{10}H_{22}$	0.767
Aromatic	n-propylbenzene	C_9H_{12}	0.132
Naphtene	n-cyclohexane	C_9H_{18}	0.101
	surrogate	$C_{9.7396}H_{20.0542}$	1.000

Table 4.10: *Composition of the surrogate model for kerosene.*

The Luche skeletal scheme, composed by 91 species and 694 reactions, was obtained through reduction of the complex detailed mechanism (225 species and 1800 reactions) including NO and PAH formation processes (El Bakali et al. 1999). The reduced model, validated on a wide range of operating conditions in terms of initial pressures, temperatures and equivalence ratios constitutes an excellent reference kinetic scheme for the high pressure application targeted.

4.4.2 Derivation of reduced virtual optimized schemes

The global procedure summarized in Fig. 3.8 is used to derive virtual optimized schemes dedicated to the description of kerosene/air combustion in the condition of the HERON experiment. First, the main virtual mechanism targeted towards the capture of the flame/flow field interaction is presented. Then, a virtual satellite scheme devoted to CO formation description is discussed.

4.4.2.1 Main virtual scheme

Virtual species properties optimization

The first step consists in identifying the thermodynamic properties and molecular weights of the virtual product species so as to reproduce the physical properties of the real mixture at equilibrium. The set of four virtual optimized products identified in Chapter 3 is used in the following.

Kinetic rate parameters optimization

The physical properties of the species being identified, the characterization of the reaction rates is now required. Following the conclusions of section 4.2, the two-step virtual mechanism, allowing a better description of temperature profiles, is retained. Its expression is given by

$$\alpha_K^{v_m} K + \alpha_{O_2}^{v_m} O_2 + \alpha_{N_2}^{v_m} N_2 \rightarrow \alpha_I^{v_m} I + \alpha_{N_2}^{v_m} N_2 \qquad \text{(Kero-R1)}$$

$$I \rightarrow \sum_{k=1}^{N_P^{v_m}} \alpha_{P_k}^{v_m} P_k \qquad \text{(Kero-R2)}$$

In the context of virtual optimized chemistry, the surrogate kerosene is viewed as a unique chemical species noted K whose properties are defined as mixture-averaged properties of the three components model fuel.

The set of kinetic parameters and associated correction functions allowing the best description of laminar flame speed and temperature profiles is identified using evolutionary optimization. The cost function $\mathcal{E}^{\text{main}}_{\text{kinetic}}$ that discriminates fittest virtual schemes from other is written as

$$\mathcal{E}^{\text{main}}_{\text{kinetic}}\left(A_r, E_{a,r}, F_{k,r}, f_r\right) = \begin{cases} \mathcal{P} & \text{if} \quad \text{auto-ignition} \\ \sum_{i=1}^{N_c} w_{S_L}\mathcal{E}_{SL,i} + w_T\mathcal{E}_{T,i} & \text{else} \end{cases} \tag{4.9}$$

where:

- $\mathcal{P}$ is an arbitrary high penalty value applied if auto-ignition is detected. As initial temperature is high, auto-ignition events are likely to occur during the optimization procedure. To overcome this problem, a simple criteria comparing the temperature between two points in the fresh gases is used to identify mixture auto-ignition and reject the corresponding set of kinetic parameters.
- $\mathcal{E}_{SL}$ and $\mathcal{E}_T$ are respectively the relative error on the laminar flame speed and the L_2 relative error norm on the temperature profile.
- w_{S_L} and w_T are the weights associated to each objective.

First, capabilities of the virtual scheme to predict global flame properties are investigated. Figure 4.20 compares the dimensionless laminar flame speed S_L^+ and thermal thickness ${\delta_L}^{0^+}$ predicted by the two-step virtual scheme and the reference Luche skeletal mechanism. For the whole flammability range, a very good agreement is obtained between the detailed solution and the reduced virtual mechanism.
Capabilities of the virtual two-step mechanism to capture local flame properties are assessed in Fig. 4.21 and 4.22. As noticed for methane-air combustion, the one-layer flame structure typical of lean conditions and the two-layer flame regime observed in moderately rich injection condition are well recovered by the two-step scheme. The endothermic behavior experienced in very rich flame condition is also well captured. The characteristic time to reach the equilibrium temperature is nonetheless overestimated. Heat release rate profiles predicted by the global virtual scheme are in fair agreement with the skeletal complex mechanism. Especially, the profiles thickness as well as amplitudes and positions of the heat release peaks are correctly reproduced. Slight discrepancies may be noticed near the lean and rich flammability limits.

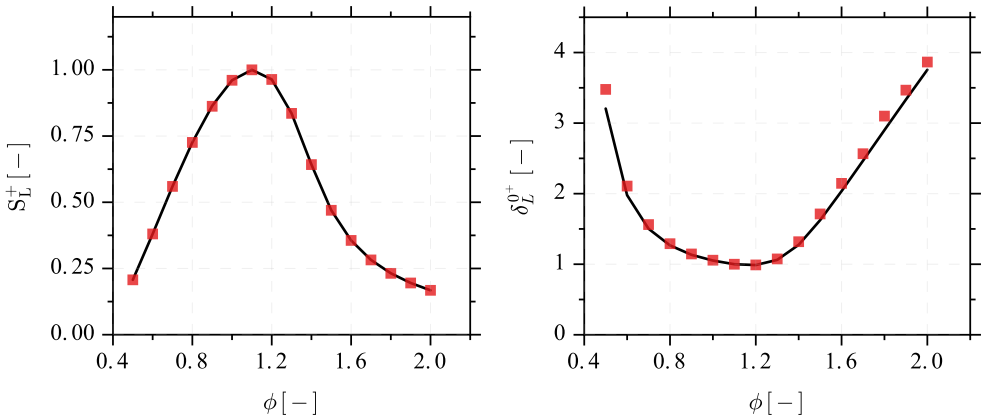

Figure 4.20: *Dimensionless laminar flame speed* $S_L^+ = S_L/S_L^d|_{st}$ *and thermal thickness* ${\delta_L}^{0^+} = \delta_L^0/{\delta_L}^{0^d}|_{st}$ *versus equivalence ratio for premixed kerosene/air flames at fresh gas temperature* $T_f = T_3^{HERON}$ *and pressure* $P = P_3^{HERON}$. *Legends: (—) Reference, (■) Two-step main virtual scheme.*

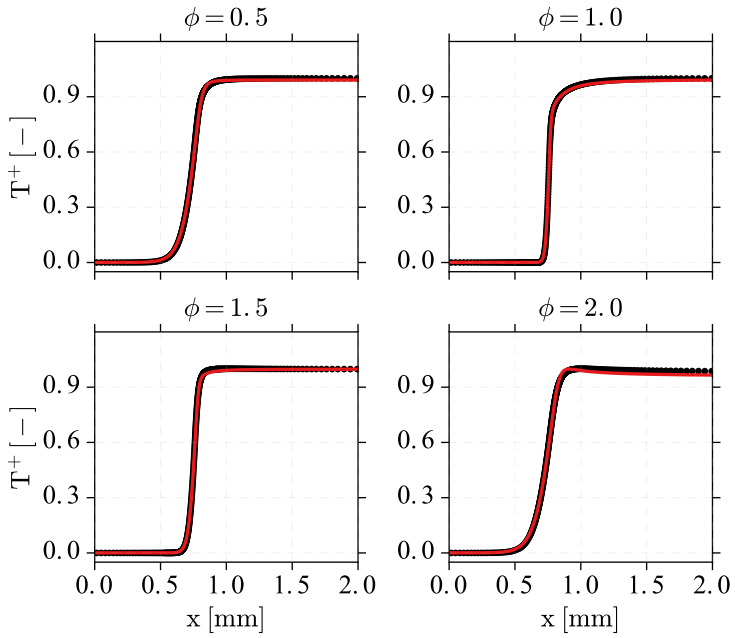

Figure 4.21: *Spatial evolution of the dimensionless temperature* $T^+ = (T - T_f)/(\max(T^d) - T_f)$ *for premixed kerosene/air flames at fresh gas temperature* $T_f = T_3^{HERON}$ *and pressure* $P = P_3^{HERON}$. *Legends: (• •) Reference, (—) Two-step main virtual scheme.*

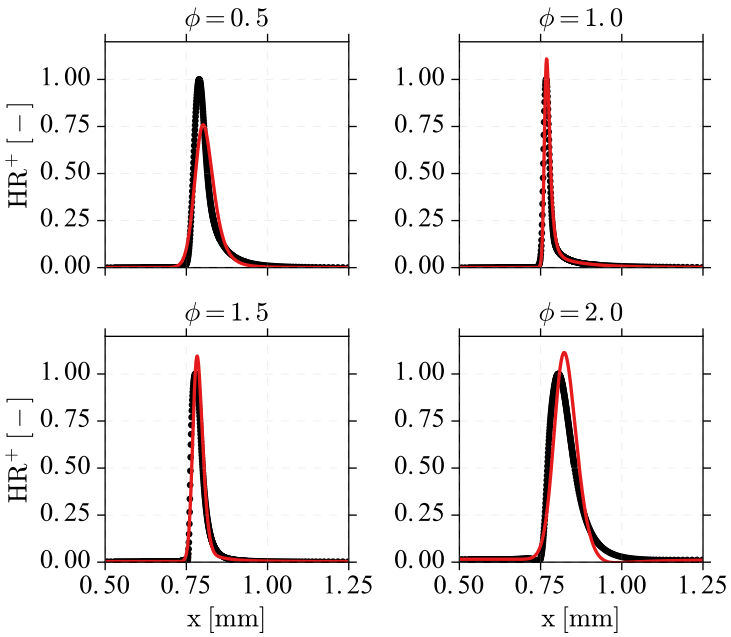

Figure 4.22: *Spatial evolution of the dimensionless heat release rate* $HR^+ = HR/\max(HR^d)$ *for premixed kerosene/air flames at fresh gas temperature* $T_f = T_3^{HERON}$ *and pressure* $P = P_3^{HERON}$. *Legends: (• •) Reference, (—) Two-step main virtual scheme.*

Satellite sub-scheme for CO prediction

In conjunction with the main mechanism, a satellite sub-mechanism dedicated to the capture of CO formation processes is used. The three-step scheme structure proposed for methane/air combustion is also considered for kerosene/air combustion

$$\alpha_K^v K + \alpha_{O_2}^v O_2 + \alpha_{N_2}^v N_2 \rightarrow \alpha^v CO + (1-\alpha^v)\, V_1 + \alpha_{N_2}^v N_2 \qquad \text{(Kero-R3)}$$

$$K + V_1 \rightarrow K + CO \qquad \text{(Kero-R4)}$$

$$CO \leftrightarrow V_2 \qquad \text{(Kero-R5)}$$

Pre-exponential factors, activation energy and reaction orders closing the rates of reactions of the CO mechanism are identified through genetic optimization.

Dimensionless equilibrium CO mass fractions predicted by the virtual mechanism are compared with reference equilibrium computations performed with the set of 91 species included in the Luche skeletal scheme (Fig. 4.23). For the whole flammability range, a good agreement is obtained between the virtual optimized model and the reference equilibrium calculations.
Figure 4.24 shows the CO mass fractions profiles predicted by the virtual satel-

lite scheme and the skeletal mechanism. For the four equivalence ratio investigated, a good agreement is obtained between the reduced virtual scheme and the detailed one.

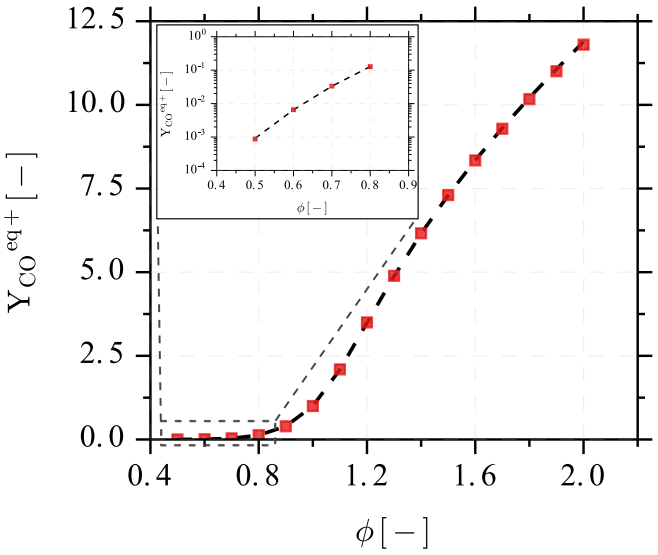

Figure 4.23: *Dimensionless equilibrium CO mass fraction* $Y_{CO}{}^{eq+} = Y_{CO}^{eq}/Y_{CO}{}^{eqd}|_{st}$ *versus equivalence ratio for a kerosene/air mixture at fresh gas temperature* $T_f = T_3^{HERON}$ *and pressure* $P = P_3^{HERON}$. *Legends: (—) Reference, (■) Two-step main virtual scheme.*

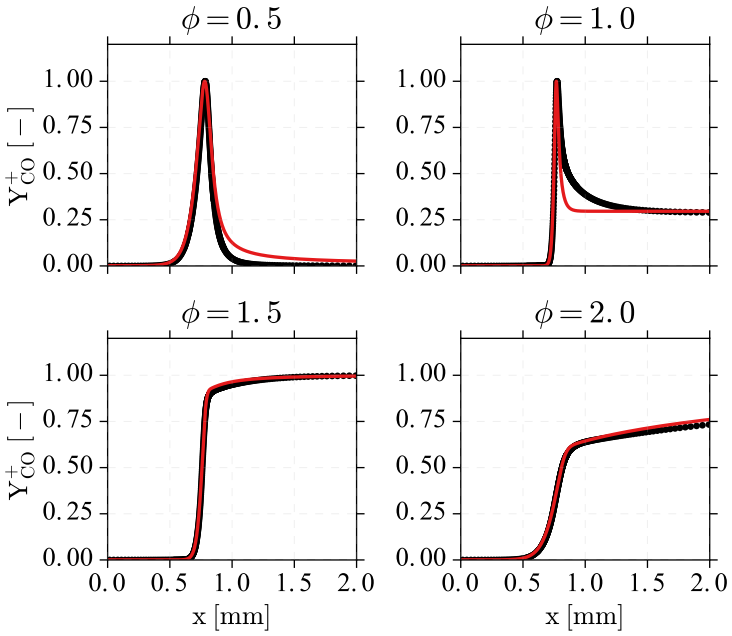

Figure 4.24: *Spatial evolution of the dimensionless CO mass fraction* $Y^+_{CO} = Y_{CO}/\max(Y^d_{CO})$ *for a premixed kerosene/air flame at fresh gas temperature* $T_f = T_3^{HERON}$ *and pressure* $P = P_3^{HERON}$. *Legends: (• •) Reference, (—) Two-step main virtual scheme.*

4.5 Summary

A new reduced chemical model based on virtual optimized mechanisms has been developed for the prediction of heat release and CO formation. This methodology relies on the use of virtual reactions and virtual species optimized in order to reproduce a reference flamelet database calculated with detailed chemistry. Using genetic algorithm two sub-mechanisms are optimized, one dedicated to the prediction of heat release and the other to the capture of CO emission. The resulting virtual schemes are compared to different chemistry description strategies on 1-D laminar premixed and non-premixed flames. For both targeted quantities and flame archetypes analyzed, virtual chemistry is in good agreement with detailed chemistry, and shows good predictive capabilities in comparison with classical chemistry reduction approaches.
The influence of the reference database used to design the virtual mechanism has been studied. It has been shown that contrarily to heat release prediction, CO emissions modeling is importantly impacted by the choice of the reference database used to optimize the virtual kinetic scheme. When both premixed and non-premixed flame elements are included in the reference flamelet library the predictive capabilities of the virtual sub-mechanism are greatly improved.

The first application of the virtual optimized chemistry in a multi-dimensional context was performed. Comparison between the reference flame solution and the virtual optimized calculation validates the predictive capabilities of the approach to capture temperature, heat release rate and CO formation in a laminar stratified flame. Coupled effects between preferential diffusion and flame curvature are however not well captured leading a slight underestimation of the flame length.

Eventually, the strategy developed for methane/air flame was applied for the derivation of a reduced virtual scheme devoted to the prediction of kerosene oxidation in representative conditions. Interestingly, the virtual optimized architecture developed for methane, involving a two-step mechanism for temperature prediction and a three-step scheme for CO, reproduces very well the reference solutions calculated with the skeletal mechanism. Unlike classical "chemistry driven" reduction approaches, the size of the virtual optimized mechanism does not depend on the size of the complex kinetic scheme used to generate the reference library.

Part III

Application of virtual chemistry in laboratory scale turbulent configuration

Chapter 5

Turbulent Combustion Modeling

Contents

This chapter introduces the main challenges associated with the modeling of turbulent reacting flows. After a presentation of the different computational approaches used to describe turbulent combustion processes, a focus is made on the Large-Eddy Simulation formalism. This simulation technique, based on an explicit representation of the largest structures and on modeling of the smallest one, makes use of dedicated closures to account for the interaction between unresolved turbulent motions and the flame front. These models of critical importance to properly describe the flame dynamics and pollutant formation are summarily introduced. Eventually, the coupling between virtual optimized mechanisms and turbulence through the TFLES model is discussed.

5.1 Computational methods for turbulent reacting flows

As briefly discussed in the introduction, turbulent flows encountered in industrial combustion chambers are characterized by a wide range of spatial scales ranging from the largest eddies at the integral length scale $l_t \approx 0.1\,\mathrm{m}$, to the smallest dissipative eddies at the Kolmogorov scale $\eta_k \approx 10\,\mu\mathrm{m}$. The explicit resolution of all these turbulent length scales through Direct Numerical Simulations (DNS) is out of reach for the configurations of interest. It would indeed require to use mesh resolution Δ_x of the order of the Kolmogorov scale η_k (Pope 2000) leading to a prohibitive number of computational cells and extremely high computational costs. To allow the simulations of turbulent flows at a reduced computational cost, two alternatives were proposed. The first one, called Reynolds Averaged Navier Stokes (RANS) approach, relies on the separation of the flow variables into temporally-averaged and fluctuating components. In this method the turbulent eddies are not solved, but their impacts on the resolved mean quantities is accounted for through turbulence models. The second modeling technique, named Large Eddy Simulation (LES), consists in explicitly solving the large structures of the flow field, whereas the effect of the smallest ones is modeled. Differences between RANS, LES and DNS methods are illustrated in both physical and spectral spaces in Fig. 5.1.

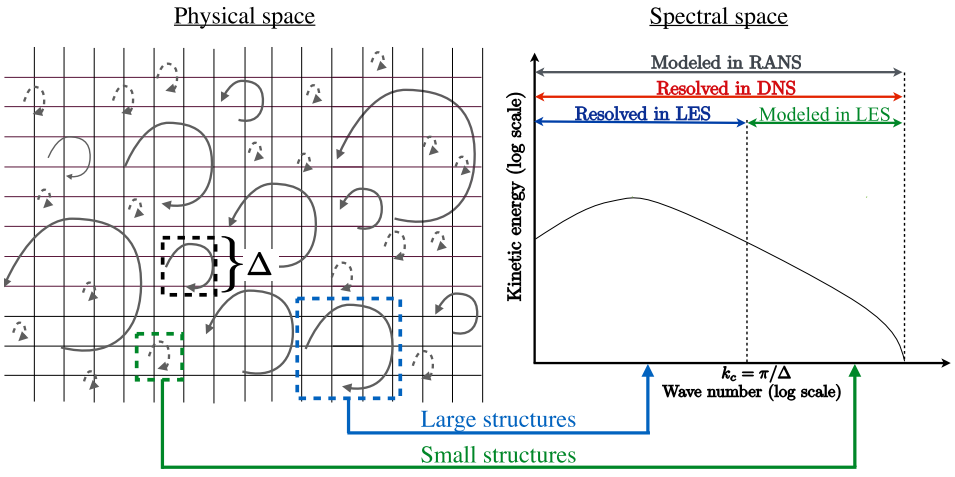

Figure 5.1: *Simulation techniques for an idealized isotropic non reacting turbulent flow (Mercier 2015). Δ denotes the LES filter size expressed in terms of cut-off wave number in spectral space. Differences between DNS, LES and RANS are depicted both in the physical space (left) and spectral space (right). All turbulent eddies are resolved in DNS, whereas in RANS only mean flow fields are resolved and no turbulent motion is explicitly captured. In LES turbulent structures larger than the filter size are resolved, while the effects of the smallest motions is modeled.*

RANS and LES were first proposed to describe non reacting flows but were rapidly extended to account for unresolved chemical reactions. Although LES is more expensive than RANS simulation, the use of LES in the turbulent combustion framework has considerably grown during the last years. This may be explained by the following reasons:

- Larger-scale motions generally contain most of the energy allowing LES to capture most of the kinetic energy of the flow (Pope 2000).
- Large turbulent structures are strongly dependent on the configuration geometry. As a result, LES formalism based on an explicit representation of large eddies is expected to provide higher predictive capabilities than RANS simulations relying on models of limited validity (Pope 2000). On the contrary, small-scales turbulent motions feature quasi-universal and isotropic properties. LES therefore appears as an efficient strategy to provide a reliable and comprehensive description of the small structures.
- Unlike RANS approach, Large-Eddy Simulations may use the knowledge of the resolved scales to model the effects of the smaller one. Based on the assumption of similarity between large and small scales, this concept allows the derivation of local turbulent model valid in both space and time.
- As LES provides an unsteady representation of the most energetic structures it allows a better description of turbulent mixing processes (Pitsch 2006) and turbulence/combustion interactions (Poinsot and Veynante 2012).
- Contrarily to RANS computations, grid refinement of a Large-Eddy Simulation allows to increase the resolved energy spectrum and relaxes the impact of sub-grid scale models. Theoretically when the LES mesh size tends to the Kolmogorov scale, resolution of a Large-Eddy Simulation degenerates towards DNS.

5.2 Large-Eddy Simulation formalism

As mentioned hereinbefore, the LES strategy consists in explicitly solving the large structures of the flow field, whereas the effects of the smallest ones are modeled. The separation between calculated and modeled scales is performed by filtering the exact equations. With G the LES filter associated with the cut-off scale Δ, the filtered quantity ψ is defined as :

$$\overline{\psi}\left(\mathbf{x},t\right) = \int \psi\left(\mathbf{x}',t\right) G_{\Delta}\left(\mathbf{x}-\mathbf{x}'\right) d\mathbf{x}'. \tag{5.1}$$

In reacting mixtures, a mass weighted Favre filtering operator is introduced:

$$\widetilde{\psi}\left(\mathbf{x},t\right) = \frac{\overline{\rho\psi}}{\overline{\rho}} \tag{5.2}$$

Any quantity ψ is defined as the sum of a resolved filtered part $\widetilde{\psi}$ and an unresolved sub-filter contribution $\psi'' = \psi - \widetilde{\psi}$ associated with unresolved flow motions. In practice, the separation between resolved and unresolved scales is implicitly performed through the mesh. Typically, turbulent eddies larger than twice the mesh size Δ_x are resolved while the effect of the smaller structures is accounted for through models.
The filtered conservation equations resolved in LES context are obtained by filtering the instantaneous balance system of equations (1.11):

$$\frac{\partial \overline{\rho}}{\partial t} + \frac{\partial}{\partial x_i}\left(\overline{\rho}\widetilde{u_i}\right) = 0 \tag{5.3}$$

$$\frac{\partial \overline{\rho}\widetilde{u_j}}{\partial t} + \frac{\partial}{\partial x_i}\left(\overline{\rho}\widetilde{u_i}\widetilde{u_j}\right) = -\frac{\partial \overline{P}}{\partial x_j} + \frac{\partial}{\partial x_i}\left(\overline{\tau}_{ij} - \overline{\rho}\left(\widetilde{u_i u_j} - \widetilde{u_i}\widetilde{u_j}\right)\right) \tag{5.4}$$

$$\frac{\partial \overline{\rho}\widetilde{Y_k}}{\partial t} + \frac{\partial}{\partial x_i}\left(\overline{\rho}\widetilde{u_i}\widetilde{Y_k}\right) = \frac{\partial}{\partial x_i}\left(\overline{\rho V_{k,i} Y_k} - \overline{\rho}\left(\widetilde{u_i Y_k} - \widetilde{u_i}\widetilde{Y_k}\right)\right) + \overline{\dot{\omega}_k} \tag{5.5}$$

$$\begin{aligned}\frac{\partial \overline{\rho}\widetilde{e_t}}{\partial t} + \frac{\partial}{\partial x_i}\left(\overline{\rho}\widetilde{u_i}\widetilde{e_t}\right) = &\frac{\partial}{\partial x_i}\left(\overline{\lambda\frac{\partial T}{\partial x_i} - \rho\sum_{k=1}^{N_s} Y_k V_k h_k}\right) \\ &+ \frac{\partial}{\partial x_i}\left(\overline{\sigma_{ij}u_j} - \overline{\rho}\left(\widetilde{u_i e_t} - \widetilde{u_i}\widetilde{e_t}\right)\right)\end{aligned} \tag{5.6}$$

Due to the non-linear nature of the governing equations, spatial filtering yields a system of equations featuring unclosed terms that need to be modeled. These different unknown contributions may be classified as follow (Poinsot and Veynante 2012):

- The **unresolved Reynolds stress tensor** $\overline{\tau}_{ij}^{sgs} = -\overline{\rho}(\widetilde{u_i u_j} - \widetilde{u_i}\widetilde{u_j})$ represents the effects of sub-grid scale motions on the resolved momentum. This unknown term is commonly closed using the Boussinesq assumption stating that the effect of the sub-grid scale field on the resolved flow motion is purely diffusive. This model, valid within the cascade theory framework, expresses the turbulent fluxes as a function of the resolved rate of stress tensor $\widetilde{S}_{ij}$:

$$\overline{\tau}_{ij}^{sgs} = 2\overline{\rho}\nu^{sgs}\left(\widetilde{S}_{ij} - \frac{1}{3}\delta_{ij}\widetilde{S}_{kk}\right) \tag{5.7}$$

$$\overline{\tau}_{ij}^{sgs} = \overline{\rho}\nu^{sgs}\left[\left(\frac{\partial \widetilde{u}_i}{\partial x_j} + \frac{\partial \widetilde{u}_j}{\partial x_i}\right) - \frac{2}{3}\delta_{ij}\frac{\partial \widetilde{u}_k}{\partial x_k}\right] \tag{5.8}$$

  where ν^{sgs} is the sub-grid scale kinematic viscosity. The sub-filter diffusive viscosity can be closed by a variety of turbulence models (Smagorinsky 1963; Germano et al. 1991; Nicoud and Ducros 1999; Nicoud et al. 2011).

- The **unresolved species fluxes** $\overline{J}_{i,k}^{sgs} = \overline{\rho}(\widetilde{u_i Y_k} - \widetilde{u}_i \widetilde{Y}_k)$ and **energy fluxes** $\overline{q}_i^{sgs} = \overline{\rho}(\widetilde{u_i e_t} - \widetilde{u}_i \widetilde{e}_t)$ are usually closed using a gradient assumption:

$$\overline{J}_{i,k}^{sgs} = \overline{\rho}\left(\frac{\nu^{sgs}}{\mathrm{Sc}_k^{sgs}}\frac{W_k}{W}\frac{\partial \widetilde{X}_k}{\partial x_i} - \widetilde{Y}_k \widetilde{V}_i^{c,sgs}\right) \tag{5.9}$$

$$\overline{q}_i^{sgs} = -\frac{\mu^{sgs}\overline{c_p}(\overline{T},\overline{Y}_k)}{\mathrm{Pr}^{sgs}}\frac{\partial \widetilde{T}}{\partial x_i} + \sum_{k=1}^{N_s} \overline{J}_{i,k}^{sgs}\tilde{h}_k \tag{5.10}$$

where Sc_k^{sgs} and Pr^{sgs} are respectively the turbulent Schmidt number of species k and the turbulent Prandtl number of the mixture. These numbers are either set to a constant value over the entire domain, or are dynamically evaluated (Moin et al. 1991). Constant turbulent Schmidt and Prandtl numbers equal to 0.6 (Sagaut 2006) are considered in this thesis.

- The **laminar filtered diffusion fluxes for momentum** $\overline{\tau}_{ij}$, **for species** $\overline{J}_{i,k} = \overline{\rho V_{k,i} Y_k}$ and **for energy** $\overline{q}_i = \overline{\lambda\frac{\partial T}{\partial x_i} - \rho\sum_{k=1}^{N_s} Y_k V_k h_k}$ are closed with a gradient assumption:

$$\overline{\tau}_{ij} = \overline{\rho\nu}\left[\left(\frac{\partial \widetilde{u}_i}{\partial x_j} + \frac{\partial \widetilde{u}_j}{\partial x_i}\right) - \frac{2}{3}\delta_{ij}\frac{\partial \widetilde{u}_k}{\partial x_k}\right] \tag{5.11}$$

$$\overline{J}_{i,k} = \overline{\rho}\left(-\overline{D}_k\frac{W_k}{W}\frac{\partial \widetilde{X}_k}{\partial x_i} + \widetilde{Y}_k\widetilde{V}_i^c\right) \tag{5.12}$$

$$\overline{q}_i = -\overline{\lambda}\frac{\partial \widetilde{T}}{\partial x_i} + \sum_{k=1}^{N_s}\overline{J_{i,k}}\widetilde{h}_{sk} \tag{5.13}$$

The filtered transport coefficients $\overline{\nu}$, $\overline{D}_k$ and $\overline{\lambda}$ are computed neglecting correlations between density, species and temperature. With this assumption, transport coefficients may be evaluated directly from the resolved field.
When dealing with highly turbulent flows, the laminar diffusion fluxes are negligible compared to unresolved turbulent fluxes $\overline{\tau}_{ij}^{sgs}$, $\overline{J}_{i,k}^{sgs}$ and $\overline{q}_i^{sgs}$.

- The **filtered chemical reaction rate** $\overline{\dot{\omega}_k}$ may be considered as the main challenging term to model in turbulent combustion. As such, most turbulent combustion models aim at providing a closure for these filtered quantities. A brief presentation of the main combustion models is provided in section 5.3.

5.3 Turbulence/chemistry interaction closures

Within the Large-Eddy Simulation context, turbulent combustion models aims at coupling combustion chemistry and turbulent flows motions. More particularly, the objective is to model the interactions between the sub-filter scale turbulent eddies and the flame front. In practice turbulence/chemistry interaction closures should also face two modeling difficulties (Fiorina et al. 2015). First, as instantaneous chemical source terms feature characteristic length scales smaller that the typical LES filter size ($\delta_{r,k} \approx 0.05\,\text{mm} < \Delta_x \approx 0.5\,\text{mm}$), models should be able to account for combustion at the sub-grid scale. Secondly, turbulent combustion models must properly degenerate when sub-grid scale wrinkling of the flame is fully resolved.
In the following, main turbulent combustion modeling approaches are briefly introduced.

5.3.1 Three formalisms to model turbulent combustion

Detailed reviews on turbulent combustion modeling (Veynante and Vervisch 2002; Poinsot and Veynante 2012; Fiorina et al. 2015) identify three different physical formalisms to achieve coupling between turbulence and combustion:

- The first strategy, called **Turbulent Mixing**, assumes that chemical time scales are shorter than turbulent time scales and that the chemical reaction rates are mainly limited by turbulent mixing processes. Several turbulent combustion models based on this concept have been derived such as the Eddy Dissipation Model (Magnussen and Hjertager 1977) or the Linear-Eddy Model (Menon and Calhoon Jr 1996). However, their use in LES is limited.

- The second approach is based on a **statistical** representation of the turbulent flame front. Unresolved sub-filter fluctuations of the thermochemical variables ψ lost by the filtering procedure are accounted for through Probability Density Functions (PDF). With this formalism, any filtered source term $\overline{\dot{\omega}_k}$ may be directly estimated from the flow field thermochemical quantities $\mathbf{\Phi} = (Y_1, ..., Y_{N_s}, T, P)$ as:

$$\overline{\dot{\omega}_k} = \int_{\mathbf{\Phi}} \dot{\omega}_k \left(\mathbf{\Phi^*}\right) \overline{\mathcal{P}} \left(\mathbf{\Phi^*}\right) d\mathbf{\Phi^*} \tag{5.14}$$

  where $\overline{\mathcal{P}} \left(\mathbf{\Phi^*}\right)$ is the joint filtered probability function (FDF), and $\dot{\omega}_k \left(\mathbf{\Phi^*}\right)$ is the species source terms given by the chemistry description approach. The joint FDF may be either evaluated by the resolution of a dedicated transport equation (Gao and O'Brien 1993) or presumed from the first moments of the resolved quantities (Galpin et al. 2008). This last strategy is well adapted for methods involving a small number of control variables such as tabulated chemistry approaches. As long as transported

chemistry is considered, the shape of the statistical distribution is difficult to presume, and methods based on the transport of FDF balance equation are generally preferred. However, due to its high dimensionality, the exact balance equation for the joint FDF cannot be solved. Instead, Lagrangian Monte Carlo (Pope 1994) or Eulerian stochastic field (Valiño 1998) methods are used. Providing a correct closure for the micro-mixing term, transported PDF methods coupled with a reliable chemical model can handle complex flame structures where premixed and non-premixed flames are encountered. However, both Lagrangian and Eulerian strategy impose high computational costs, complex implementation, and important modeling efforts.

- Finally, **geometrical strategies** consider the flame front as a propagating interface in the turbulent field. Based on this physical approach a wide range of turbulent combustion models were proposed. Among them we can mention the G-equation model (Kerstein et al. 1988), the flame surface density approach (Boger et al. 1998), the Thickened Flame model for LES (Colin et al. 2000) and the Filtered-Tabulated Chemistry for LES approach (Fiorina et al. 2010). The TFLES model, compatible with transported chemistry strategies, is considered in this thesis for its easy implementation and robustness. Detailed description of this model is provided in the next section.

5.3.2 Thickened flame model for LES (TFLES)

To ensure a proper description of chemical source terms on typical LES grids, the TFLES model artificially thickens the reaction zone so that a sufficient resolution of the flame front is obtained. This combustion model, initially proposed by Butler and O'Rourke (1977) in the RANS context, consists in modifying the diffusion and source terms in the species balance equation so as to ensure flame thickening and conservation of the consumption speed. Following simple theories of laminar premixed flame (Williams 1985) the laminar flame speed S_L^0 and thermal flame thickness δ_L^0 may be expressed as:

$$S_L^0 = \sqrt{D\bar{\dot{\omega}}} \tag{5.15}$$

$$\delta_L^0 = \frac{D}{S_L^0} \tag{5.16}$$

where D and $\bar{\dot{\omega}}$ respectively represent the thermal diffusivity and mean reaction rate. If the diffusion terms are multiplied by a thickening factor F, and the species source terms are divided by F, the flame thickness is multiplied by F, while the laminar flame speed is unaltered. For sufficiently high thickening factor, the TFLES model therefore allows to propagate a thickened flame front at the desired flame speed.

In turbulent flow configurations, the thickening of the flame affects the chemistry/turbulence interactions by reducing the flame wrinkling and the local turbulent consumption speed S_T. Typically, turbulent eddies smaller than $F\delta_L^0$ that would theoretically wrinkle the flame front do not interact with it anymore. Additionally, if turbulent structures larger than $F\delta_L^0$ still affect the flame front their impact on flame wrinkling is decreased (Angelberger et al. 1998). To account for the flame sensitivity reduction to turbulent flow motions Colin et al. (2000) introduced a model for the sub-grid scale wrinkling factor $\Xi_\Delta = S_T/S_L$. The balance equation for Favre-filtered species mass fraction $\widetilde{Y}_k$ is therefore given by:

$$\begin{aligned}\frac{\partial \overline{\rho}\widetilde{Y}_k}{\partial t} + \frac{\partial}{\partial x_i}\left(\overline{\rho}\widetilde{u}_i\widetilde{Y}_k\right) = \frac{\partial}{\partial x_i}\left[\overline{\rho}\left(F\Xi_\Delta \overline{D}_k \frac{W_k}{W}\frac{\partial \widetilde{X}_k}{\partial x_i} - \widetilde{Y}_k\widetilde{V_i^c}\right)\right] \\ + \frac{\Xi_\Delta}{F}\overline{\dot{\omega}_k}\end{aligned} \tag{5.17}$$

Numerous formulations of the sub-grid wrinkling factor Ξ_Δ have been proposed in the literature. Most simple models are based on analytic expressions assuming equilibrium between flame wrinkling and turbulence (Colin et al. 2000; Charlette et al. 2002a; Pitsch and Duchamp De Lageneste 2002; Fureby 2005). Unfortunately, these expressions may fail especially when transition from laminar to highly wrinkle flames occurs (Richard et al. 2007). To overcome this problem, dynamic formulations making use of the knowledge of the resolved scales have then been proposed (Charlette et al. 2002b; Knudsen and Pitsch 2008; Veynante and Moureau 2015).

To avoid an increase of the diffusive fluxes in mixing controlled regions, a dynamic formulation of the TFLES model, referred as DTFLES was proposed by Legier et al. (2000). In this model, the thickening is only applied in the flame reactive layer detected by the flame sensor $\mathcal{S}$, which equals 1 in the flame front, and 0 elsewhere. With this new formulation, the species balance equation 5.17 is rewritten as:

$$\begin{aligned}\frac{\partial \overline{\rho}\widetilde{Y}_k}{\partial t} + \frac{\partial}{\partial x_i}\left(\overline{\rho}\widetilde{u}_i\widetilde{Y}_k\right) = &\frac{\partial}{\partial x_i}\left[\overline{\rho}\left(F\Xi_\Delta \overline{D}_k + (1-\mathcal{S})\frac{\nu_{sgs}}{\mathrm{Sc}_k^{sgs}}\right)\right. \\ &\left.\frac{W_k}{W}\frac{\partial \widetilde{X}_k}{\partial x_i} - \overline{\rho}\widetilde{Y}_k\left(\widetilde{V}_i^c + \widetilde{V}_i^{c,sgs}\right)\right] + \frac{\Xi_\Delta}{F}\overline{\dot{\omega}_k}\end{aligned} \tag{5.18}$$

where the local thickening factor reads:

$$F = 1 + \mathcal{S}\left(F_{\max} - 1\right). \tag{5.19}$$

The maximum value of the thickening factor $F_{\max}$ is defined locally so as to ensure the resolution of the thermal flame thickness δ_L^0 on n grid points of the

LES grid:

$$F_{\max} = \frac{n\Delta_x}{\delta_L^0} \tag{5.20}$$

where Δ_x denotes the local cell size. To guarantee a proper description of the flame speed typical value of $n = 5$ are used.
Equation (5.18) applies the TFLES model in the reactive zone, while outside of the flame front only unresolved species fluxes $\overline{J}_{i,k}^{sgs}$ closed with a classical gradient assumption (Eq. (5.9)) are accounted for.

As very simple to implement and robust, the Thickened Flame model for LES has been successfully used in a number of turbulent premixed (De and Acharya 2009; Kuenne et al. 2011), stratified (Franzelli et al. 2012; Proch and Kempf 2014) and partially-premixed (Jaravel 2016) flame configurations.

5.4 Coupling between virtual schemes and the TFLES model

In this section, a novel formulation of the flame sensor and associated thickening factor adapted to virtual chemistry is introduced. Theoretically, the TFLES model can be coupled with any size of chemical mechanism going from global to detailed mechanisms. However, the difficulty to set-up the turbulent combustion model increases importantly with the number of chemical species and reactions involved in the kinetic mechanism.
Various definitions of flame sensor were proposed depending on the model used to describe chemistry. With irreversible one-step mechanism Legier et al. (2000) first suggested to use an Arrhenius-like expression based on the reactants concentration and temperature. In multi-step chemistry, an alternative formulation based on the net production rate of an intermediate species was introduced by Franzelli (2011). The recent work of Jaravel (2016) showed that efficient coupling between TFLES and an analytically-reduced mechanism was obtained by defining the flame sensor on the source term of the fuel.
All these definitions are limited to the description of a unique chemical time scale and length scale. However, in practice the flame features a complex structure covering a wide range of time scales. Typically, the fuel oxidation occurs rapidly in a thin reaction layer, while the CO oxidation into CO_2 is a slow process. In this work, a new expression of the flame sensor is proposed to enable an efficient thickening when species feature different time scales. For that purpose, species flame sensors $\mathcal{S}_k$ are first introduced as:

$$\mathcal{S}_k = \min\left(\left|\frac{\overline{\dot{\omega}_k}}{p_k \dot{\omega}_k^{\max}}\right|, 1\right) \tag{5.21}$$

where $\overline{\dot{\omega}_k}$ is the net production rate of species k evaluated from filtered quantities, $\dot{\omega}_k^{\max}$ stands for the maximum value of the species source term evaluated from a laminar 1-D premixed computation in representative conditions. The parameter p_k refers to a threshold percentage enabling the control of the species sensor thickness. Typical values of p_k varies between 5% and 20%.
Each flame sensor $\mathcal{S}_k$ captures the thickness of production and/or consumption zones of its associated species. A thickening factor per species F_k is then defined as:

$$F_k = \max\left(1 + (F_k^{\max} - 1)\mathcal{S}_k, 1\right) \tag{5.22}$$

where $F_k^{\max}$ is the maximum value of the species thickening factor evaluated from the local mesh resolution:

$$F_k^{\max} = \frac{n\Delta x}{\delta_{rk}} \tag{5.23}$$

where δ_{rk} is the reactive thickness of the species k defined as the full width at half maximum of the k^{th} creation and/or destruction species source term. n is the number of grid points needed in the reaction rate thickness δ_{rk} to ensure its proper resolution.
Eventually, the global flame sensor S and the thickening factor F applied in the transport equations for filtered species mass fractions (Eq. (5.18)) are written as the envelops of their N_s components:

$$\mathcal{S} = \max\left(0, \mathcal{S}_k\right) \qquad \text{for} \quad k \in [1, N_s] \tag{5.24}$$

$$F = \max\left(1, F_k\right) \qquad \text{for} \quad k \in [1, N_s] \tag{5.25}$$

To avoid spurious oscillations in the pre-heat zone due to a too narrow thickened zone, multiple filtering operations are applied to both the global flame sensor $\mathcal{S}$ and global thickening factor F, as suggested by (Franzelli 2011; Jaravel 2016).

The proposed formalism is tested on a 1-D laminar premixed flame at an equivalence ratio $\phi = 0.85$. The unstretched laminar flame is simulated with the methane/air virtual mechanisms presented in Chapter 4 on a grid of constant cell size $\Delta_x = 0.5\,\text{mm}$.
Figure 5.2 illustrates the thickened reaction rates $\overline{\dot{\omega}_k}$ and associated flame sensors $\mathcal{S}_k$ for a selection of species (CH_4, P_2, CO, V_2). For each species, the species sensors $\mathcal{S}_k$ encompass the highly reactive zone with maximum reaction rate, allowing a subsequent thickening in the region where it is numerically required. In the post-flame region, however, the species sensors rapidly tend towards zero to avoid unnecessary and unphysical thickening of sufficiently resolved flame regions. This behavior is controlled by adjusting the values of the threshold percentages p_k characterizing the thicknesses of the sensors.

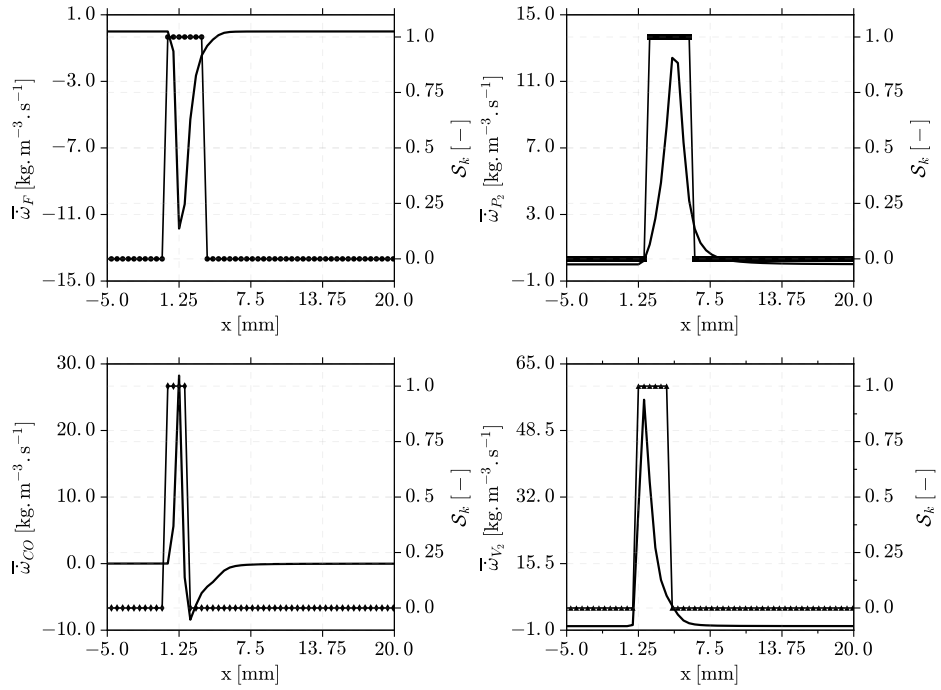

Figure 5.2: *Thickened Flame model applied to a 1-D premixed methane/air flame at an equivalence ratio of* $\phi = 0.85$ *and for a mesh size* $\Delta_x = 0.5\,\text{mm}$ *. Thickened species reaction rates* $\overline{\dot{\omega}_k}$ *(full line) and their associated flame sensors* S_k *(symbols). Legend: (● ●)* CH_4*; (■ ■) P2; (◆ ◆) CO; (▲ ▲) V1.*

Figure 5.3 (left) presents the location of the flame sensors associated to each species. The effective flame sensor is the envelop of all species flame sensors and corresponds to the full line. Figure 5.3 (right) shows the different values of species thickening factor F_k. The value of thickening needed to resolve one species reaction rate on n grid points strongly differs depending on their characteristic thickness. In particular, the largest thickening $F_{CO} = 5.8$ is required for CO source term while $F_{V_2} = 2.5$ is sufficient to resolve the production layer of the V_2 virtual species in the post flame zone on the $\Delta_x = 0.5$ mm mesh grid. Figure 5.4 illustrates the spatial evolution of temperature and CO mass fraction resulting from the thickening factor F built from each species thickening F_k as detailed previously. These profiles can be compared with the thickened temperature and CO profile in dashed line resulting from a constant thickening. To ensure a proper comparison between the new formulation and the constant thickening simulation, the value of the constant thickening factor is chosen so that the smallest reactive thickness is equal in both cases (Auzillon et al. 2011). As regards with temperature, the main difference between the two approaches lies in the high temperature layer where the constant thickening generates a very large post flame zone which is not the case for the new strategy. The thermal flame thickness obtained with the constant thickening approach $\delta_L^{\text{F=cst}} = 3\,\text{mm}$,

while a smaller thermal flame front of $\delta_L^{F=f(F_k)} = 2.6\,\text{mm}$ is observed with the proposed flame sensor. For CO mass fraction profiles, similar observations are made. The CO mass fraction profile evaluated with the new formulation is thinner than the CO profile resulting from constant thickening.

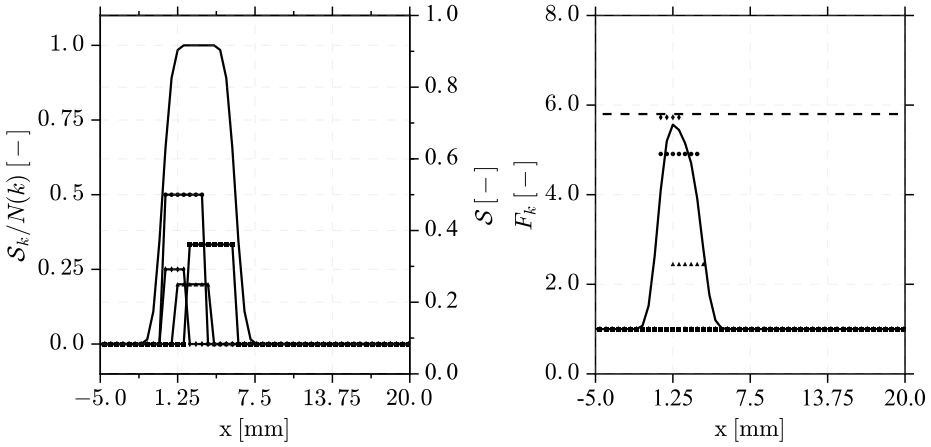

Figure 5.3: *Thickened Flame model applied to a 1-D premixed methane/air flame at an equivalence ratio of $\phi = 0.85$ and for a mesh size $\Delta_x = 0.5$ mm. Left: Species sensors S_k (symbols) and global flame sensor S (full line). For clarity, species flames sensors are divided by arbitrary values $N(k)$. Right: Species thickening factors F_k (symbols), global thickening factor (full line) and constant thickening factor (dashed line). Details about the symbols are indicated in Fig. 5.2*

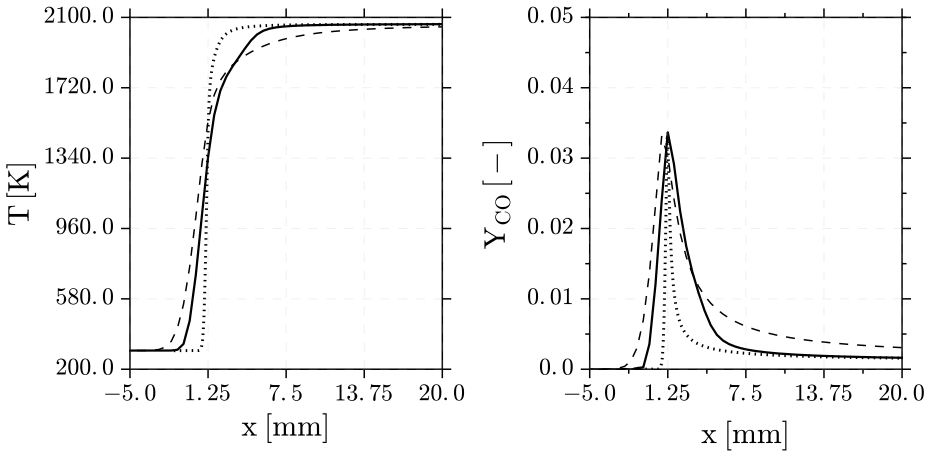

Figure 5.4: *Thickened flame model applied to a 1-D premixed methane/air flames at an equivalence ratio of $\phi = 0.85$ and for a mesh size $\Delta_x = 0.5$ mm. Temperature profiles for different thickening methodologies: No thickening (dotted line); constant thickening (dashed line); species associated thickening (full line). Details about the symbols are indicated in Fig. 5.2*

Stratified and partially-premixed combustion

This flame sensor formulation is valid in perfectly premixed combustion regime. When stratified or partially premixed combustion modes are encountered, a dependency to the local equivalence ratio is added to composition dependent parameters. Typically, the species flame sensor and maximum value thickening factor are modified as:

$$\mathcal{S}_k = \min\left(\left|\frac{\overline{\dot{\omega}_k}}{p_k \dot{\omega}_k^{max}(\phi)}\right|, 1\right) \tag{5.26}$$

$$F_k^{\max} = \frac{n\Delta x}{\delta_{rk}(\phi)} \tag{5.27}$$

Chapter 6

LES of a Turbulent Premixed burner and Stratified jet flame using Virtual Optimized Chemistry

Contents

The aim of this Chapter is to assess the predictive capabilities of the virtual optimized chemistry approach on a turbulent context. The virtual kinetic schemes derived in Chapter 4 are combined with the Thickened Flame model for LES (TFLES) presented in Chapter 5. This modeling strategy is tested on two laboratory-scale turbulent burners. First, the premixed swirled burner PRECCINSTA, widely used for turbulent combustion model validation, is investigated. The stratified non-swirling Cambridge flame is then simulated with the virtual optimized chemistry approach. Capabilities of the virtual kinetic schemes to predict the flame position and to capture the CO formation in a turbulent environment are assessed.

6.1 Introduction

Predictive capabilities of the virtual optimized chemistry description approach have been successfully validated in laminar 1-D and 2-D flame configurations. The objective of this Chapter is to assess the performances of the newly proposed reduced schemes in a turbulent context.
Two gaseous flame configurations are considered in this work. First the lean premixed swirled burner PRECCINSTA, experimentally investigated at DLR (Weigand et al. 2005; Weigand et al. 2007; Meier et al. 2007) within the Prediction and Control of Combustion Instabilities in Industrial Gas Turbines (PRECCINSTA) project, is selected. This model combustor, equipped with an aeronautical injector, is representative of an industrial gas turbine combustion chamber. Moreover, the PRECCINSTA burner is particularly well suited for model validation as an important database of experimental measurements is available. The second investigated turbulent test case is the Cambridge non-swirling stratified burner (SwB). This jet flame, widely studied experimentally (Sweeney et al. 2011; Sweeney et al. 2011; Barlow et al. 2012; Sweeney et al. 2013; Zhou et al. 2013) and numerically (Nambully et al. 2014a; Proch and Kempf 2014; Mercier et al. 2015; Proch et al. 2017), constitutes a relevant and complementary test case for virtual optimized chemistry validation.
Large-Eddy Simulations of the premixed swirled burner and of the stratified jet flame SwB are presented in sections 6.2 and 6.3. In the following sections, a particular attention is given to the evaluation of :

- the main virtual mechanism capabilities to capture the flame flow/field interactions (temperature and velocity fields),
- the virtual satellite scheme capacity to describe CO formation processes.

6.2 LES of the premixed PRECCINSTA burner

This section focuses on the validation of the virtual optimized chemistry strategy in the lean-premixed combustion chamber PRECCINSTA. After a brief state of the art of previous numerical studies a presentation of the experimental set-up is provided. Then, adiabatic simulations using the virtual optimized mechanisms derived in Chapter 4 are compared with experimental measurements. Eventually, capabilities of the virtual optimized approach to capture heat losses effects are validated on non-adiabatic LES of the PRECCINSTA configuration.

6.2.1 State of the art of previous numerical studies

The PRECCINSTA burner specifically designed to study combustion instabilities and turbulence/chemistry interaction phenomena has been widely numerically investigated. First, Roux et al. (2005) assessed Large-Eddy Simulation and acoustic analysis potential to capture thermo-acoustic instabilities in cold

flow and reacting cases. The premixed swirled burner was then numerically studied to validate chemistry modeling approaches and turbulent combustion models. Table 6.1 summarizing the numerical works dealing with model validation on the PRECCINSTA test rig, suggests that a wide variety of chemistry description strategies and turbulent combustion models have been tested. The ghost-fluid method, representing the flame front as an interface of finite thickness, was first tested on the PRECCINSTA burner (Moureau et al. 2007). Comparison between velocity measurements and the numerical solution shows excellent agreement, demonstrating the ability of the approach to capture the flame/flow field interactions. Premixed tabulated strategies associated with presumed probability density functions (top-hat and clipped Gaussian) have also been used (Galpin et al. 2008; Wang et al. 2014). In both studies, an overall good agreement was obtained for temperature and main species. It may however be mentioned that numerical simulations tend to underestimate the flame length, while CO mass fraction profiles present important discrepancies in comparison with experimental measurements. Similar results were obtained in numerical simulations using semi-global (Franzelli et al. 2012; Volpiani et al. 2017) or analytic (Franzelli 2011) schemes coupled with the TFLES model. Improvement of flame length description was obtained in numerical works based on filtered-tabulated chemistry approaches (Fiorina et al. 2010; Mercier et al. 2015)

Numerical work	Chemistry model	Turbulent combustion model
(Moureau et al. 2007)	/	Ghost fluid method
(Galpin et al. 2008)	Premixed tabulated	Presumed FDF
(Fiorina et al. 2010)	Premixed tabulated	F-TACLES
(Franzelli 2011)	Analytic scheme	TFLES
(Franzelli et al. 2012)	Semi-global scheme	TFLES
(Wang et al. 2014)	Tabulated (REDIM)	Presumed FDF
(Mercier et al. 2015)	Premixed tabulated	F2-TACLES
(Volpiani et al. 2017)	Semi-global scheme	TFLES

Table 6.1: *Large-Eddy Simulations of the PRECCINSTA burner for turbulent combustion model validation.*

Quasi Direct Numerical Simulation of the premixed swirled combustor was performed by Moureau et al. (2011b) to evaluate the validity of turbulent combustion models based on presumed probability density function.

6.2.2 Experimental set-up

The PRECCINSTA burner is derived from a low emissions industrial gas turbine injector designed by Safran Helicopter Engine. A schematic of the nozzle

mounted on the combustion chamber is presented in Fig. 6.1. The laboratory scale combustor is composed by three main parts, namely; a plenum, a swirled aeronautical injector and a squared combustion chamber provided with large optical access. In the original design, plenum is fed with dry air at ambient temperature, while pure gaseous fuel is tangentially injected in the swirler through twelve small holes of 1 mm diameter. The intense mixing between fuel and air in the swirler forms an assumed perfectly premixed fuel/air mixture at the combustion chamber entrance. At the nozzle tip, a turbulent flame with the typical characteristics of a swirled flame stabilizes. Finally, burnt gases are released in the atmosphere through a central exhaust pipe connected to the chamber through a convergent nozzle.

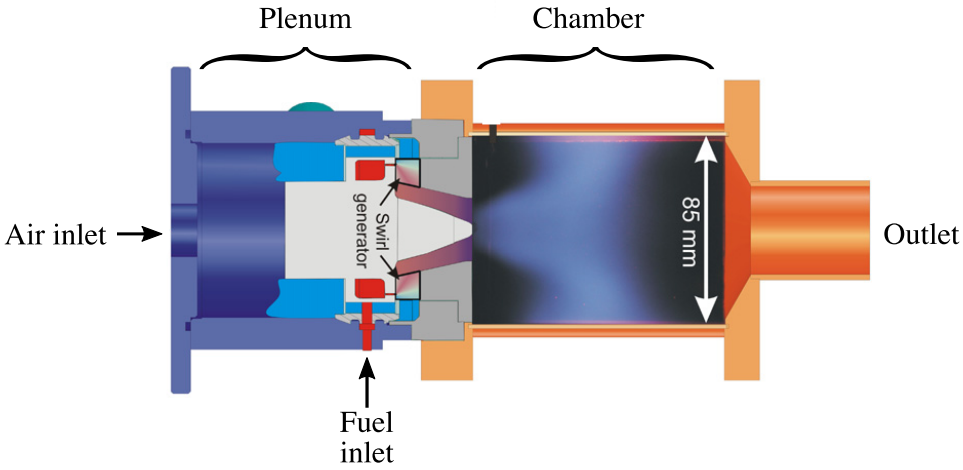

Figure 6.1: *Sketch of the PRECCINSTA burner and Mean OH-LIF image. Adapted from (Meier et al. 2007).*

Two reacting operating points have been studied experimentally varying the fuel mass flow rate. The richer flame with a global equivalence of $\phi_g = 0.83$ exhibits a stable and quite behavior. Conversely, the leaner case featuring a global equivalence ratio of $\phi_g = 0.75$ presents a strong self-excited thermo-acoustic instability. In the following, the stable flame configuration is considered.

Laser-based diagnostics were performed to characterize the model-burner. Raman scattering measurements are used to evaluate flame temperature and main species mass fractions (CH_4, O_2, CO_2, H_2O, CO and H_2). Planar-Laser-Induced-Fluorescence and chemiluminescence measurements of OH^* were performed to identify the instantaneous flame structure. As regards with aerodynamic, the three velocity components were evaluated with Laser-Doppler Velocimetry measurements.

6.2.3 Adiabatic Large-Eddy Simulations

6.2.3.1 Numerical set-up

A global view of the computational domain is illustrated in Fig. 6.2. Though fuel and air are injected separately, experimental scatter plots of temperature versus mixture fraction show that at the nozzle tip stratification levels are low and most reacting points burn at the global equivalence ratio $\phi_g = 0.83$ (Meier et al. 2007). From this observation, most numerical studies were performed assuming the injection of a perfectly premixed mixture (Roux et al. 2005; Moureau et al. 2007; Galpin et al. 2008; Mercier et al. 2015). Impact of this simplification was shown to be reduced for the stable flame configuration (Franzelli et al. 2012). As a consequence, to alleviate the computational efforts associated with the resolution of the fuel/air mixing occurring in the swirler, a fully premixed hypothesis is retained. The atmosphere inlet is fed with a low velocity co-flow ($U_{co} = 0.5\,m.s^{-1}$) of inert N_2 to avoid any recombination reaction with burnt gases. Regarding wall boundary conditions, adiabatic no-slip boundary conditions are considered for this first numerical study.

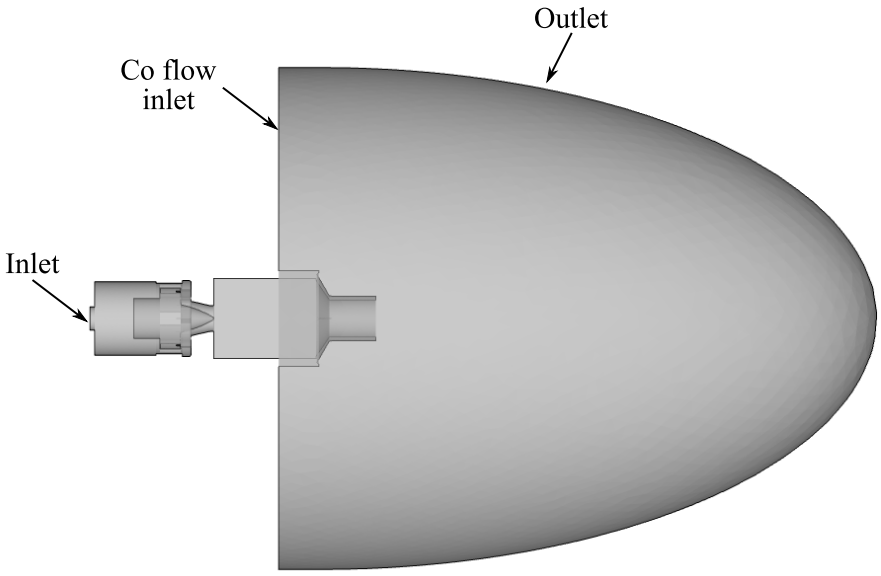

Figure 6.2: *PRECCINSTA computational domain for the adiabatic LES performed with AVBP.*

Figure 6.3 (bottom) presents a view of the mesh in the region of interest. To ensure a sufficient description of the flow in the small canals a typical cell size of $\Delta_x = 0.2\,mm$ is used. In the swirler and flame region, the mesh features a characteristic cell size of $\Delta_x = 0.5\,mm$. The tetrahedral mesh is composed by about 22.5 M cells and 4.0 M nodes.

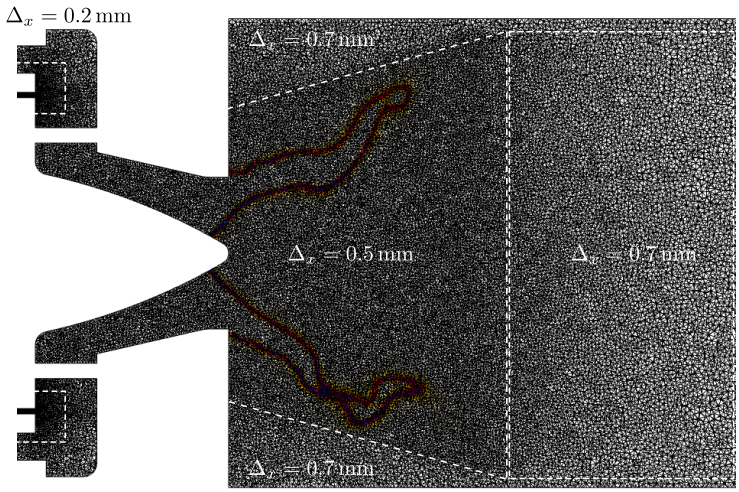

Figure 6.3: *View of the mesh colored by instantaneous fuel source term.*

Adiabatic Large-Eddy Simulations of the PRECCINSTA burner were performed with the compressible solver AVBP (Schönfeld and Rudgyard 1999) developed at CERFACS and IFPEN. In the present computations, solution variables (density, momentum, species mass fraction and energy) are numerically integrated with the finite element Two-step Taylor-Galerkin C (TTGC) scheme (Colin and Rudgyard 2000), which is third-order in space and time. The sub-grid stress tensor $\overline{\tau}_{ij}^{sgs}$ is closed using a Boussinesq assumption, with the turbulent viscosity given by the Wall Adapting Linear Eddy model WALE (Nicoud and Ducros 1999).

Regarding turbulent combustion modeling, the virtual optimized mechanisms validated on laminar configurations in Chapter 4 are coupled with the DTFLES model (Colin et al. 2000) and flame sensor introduced in Chapter 5. With a characteristic cell size of $\Delta_x = 0.5\,\text{mm}$ in the flame front region a global thickening factor F of 5 is required to resolve fuel and CO source terms. Impact of the sub-grid flame wrinkling is modeled with the algebraic formulation of the efficiency function proposed by (Charlette et al. 2002a) and later modified by Wang et al. (2011). The model parameter β is set to its classical constant value of 0.5.

For comparison purposes, results obtained with the two-step global scheme BFER are also provided. Under-resolution of chemical sources is also accounted for with the DTLES model, and turbulence/chemistry interactions are modeled through the same efficiency function (Wang et al. 2011). The local flame thickening is evaluated from the flame sensor based on the envelop of species flame sensors introduced in Chapter 5.

6.2.3.2 Simulations results analysis

Flame structure and CO formation

Figure 6.4 compares instantaneous fields of resolved temperature evaluated by the main virtual mechanism and the semi-global model BFER. No major difference in terms of flame shape, stabilization and position is noticeable. The two reduced mechanism capture a typical V-shape flame with an inner reaction zone and an outer flame front near the outer recirculation zone. Both kinetic schemes predict anchoring of the inner flame front on the nozzle tip, while the second flame front is attached to the combustion chamber wall. Regarding temperature levels, slight differences may be observed on post-flame zones. The LES based on virtual optimized schemes predicts large post-flame regions characterized by intermediate temperature levels of about 1800 K. On the contrary, with the BFER semi-global mechanism temperature directly reach its adiabatic value (T$\approx$ 2040 K), and post-flame thickness is almost zero. These observations can be correlated with premixed comparisons performed in Chapter 4.

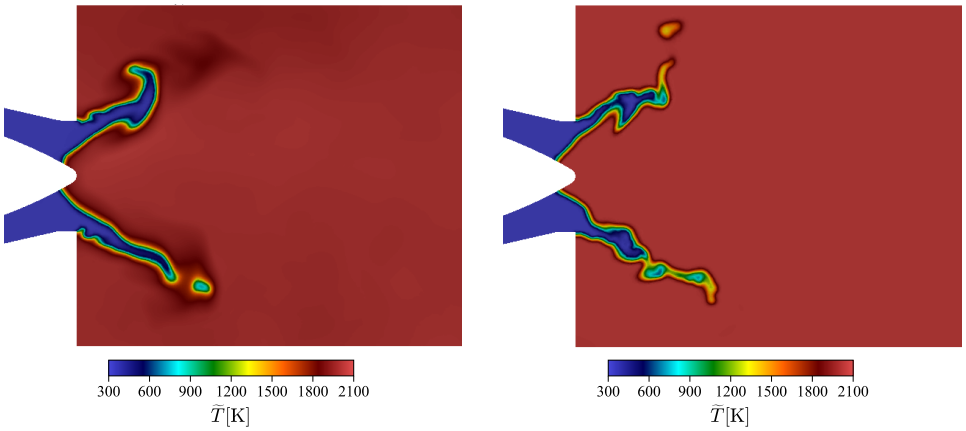

(a) Virtual optimized chemistry (b) BFER semi-global chemistry

Figure 6.4: *Instantaneous fields of resolved temperature predicted by the virtual optimized chemistry approach and the semi-global kinetic scheme BFER are compared.*

Instantaneous field of CO mass fraction predicted by the two reduced kinetic mechanisms are compared in Fig. 6.5. The virtual optimized scheme captures a strong peak of CO mass fraction in the flame front that rapidly decreases towards its quasi-null equilibrium value. In agreement with results presented in Chapter 4, the BFER mechanism predicts very low concentrations of CO in the flame front that are almost ten times lower that what observed in the virtual scheme simulation.

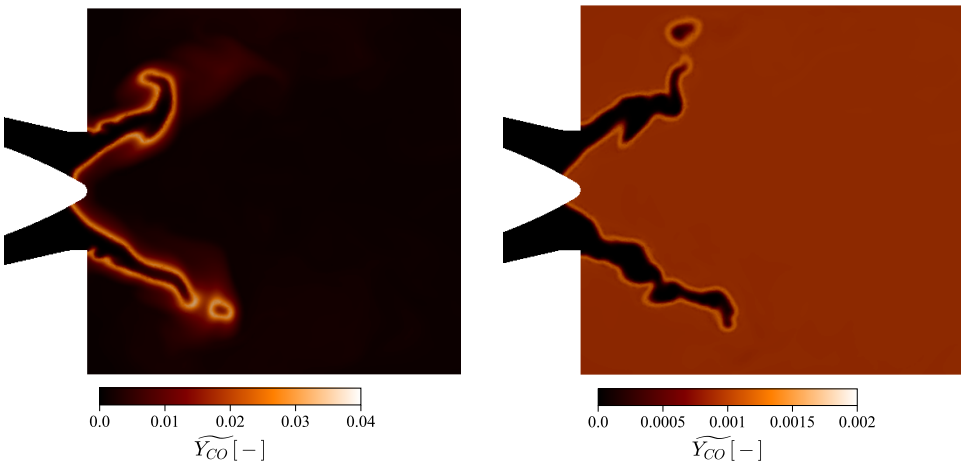

(a) Virtual optimized chemistry

(b) BFER global chemistry

Figure 6.5: *Instantaneous fields of resolved CO mass fraction predicted by the virtual optimized chemistry approach and the semi-global kinetic scheme BFER are compared. Attention must be paid to legend scalings that are different between the two figures.*

Quantitative comparisons between experiments and numerical simulations in terms of statistics are now presented.

Temperature statistics

Figure 6.6 shows the mean and RMS temperature profiles in eight axial locations from the burner exit plane. Main observations from the comparison between experimental measurements and numerical results obtained with the virtual mechanism may be summarized as follow:

- For the first section investigated ($Z = 6\,\text{mm}$), and near the centerline ($r < 15\,\text{mm}$), comparison between virtual chemistry solution and Raman scattering measurements shows that the main virtual scheme retrieves well the temperature profile, demonstrating a proper description of the first reactive branch. However, in the near wall region the virtual kinetic model overestimates temperature levels by about 400 K. This important discrepancy already reported in previous numerical simulations (Galpin et al. 2008; Volpiani et al. 2017) may be attributed to the use of adiabatic wall boundary conditions. Experimentally, combustion chamber walls are cool down by air or water circulation to maintain acceptable temperature levels in the quartz. Subsequently, in the corner region the enthalpy of the burnt gases is decreased, leading to local temperature reduction.
- For $Z = 10\,\text{mm}$, similar observations may be put forward: the overall agreement between virtual chemistry and measurement is good in the inner flame front region, but temperature is importantly overestimated in

the near wall zone.

- Further downstream, $Z = 15, 20$ and $30\,\text{mm}$, the main virtual scheme tends to overestimate temperature levels for all radial positions $r > 20\,\text{mm}$. Differences between numerical solution and experimental measurements may be accounted for the treatment of wall boundary condition. Recently, Bénard et al. (2019) performed a parametric study aiming at identifying the impact of non-adiabatic effects and mesh resolution on the flame structure. One of the main conclusions of this numerical study is that when thermal losses are taken into account the flame structure evolves from an M-shape to a V-shape flame. Simulations using adiabatic walls therefore predict a non-physical second flame front consuming prematurely fresh gases and leading to a too short flame.
- Near the combustion chamber exit plane, for $Z = 40$, 60 and $80\,\text{mm}$, virtual chemistry approach retrieves well the equilibrium temperature levels.

Comparisons between the semi-global scheme and experimental measurements show that BFER underestimates the mean flame brush thickness. This observation is to relate with the results obtained in laminar premixed flames (Chapitre 4) demonstrating that the BFER scheme predicts a too rapid reach of the equilibrium associated with laminar flame thickness under-prediction. Additionally, mean temperature radial profiles evaluated at $Z = 30$ and $40\,\text{mm}$ suggest that the two-step global mechanism predicts a shorter flame than the main virtual scheme.
As regards with resolved RMS temperature, both chemistry description approach are in good agreement with Raman measurements in the flame front region. However, temperature fluctuations are under-estimated in the inner and outer recirculation zones due to adiabatic wall boundary conditions.

Reactant species statistics

Figure 6.7 and 6.8 compare the time-averaged fuel and oxidizer mass fraction profiles measured experimentally and obtained with reduced schemes. Global and virtual schemes provide very similar mean solutions which match well with experimental measurements. Small discrepancies observed on the peak of CH_4 mass fraction profile are due to the simplified injection boundary conditions. As numerical solutions are obtained assuming a perfect mixing between fuel and air, fuel stratification due to imperfect mixing are not captured. Regarding the description of reactants RMS profiles both chemical descriptions are in good agreement with the experiments.

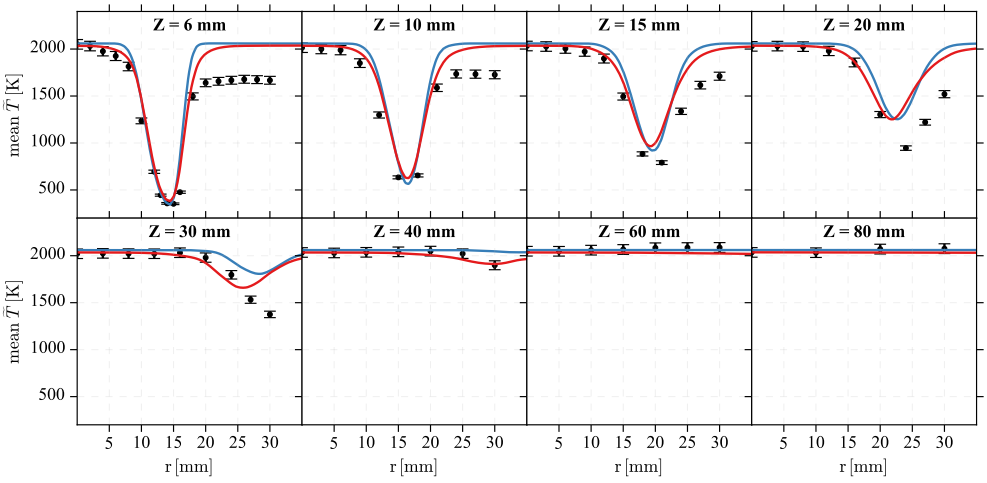

(a) Mean temperature profiles

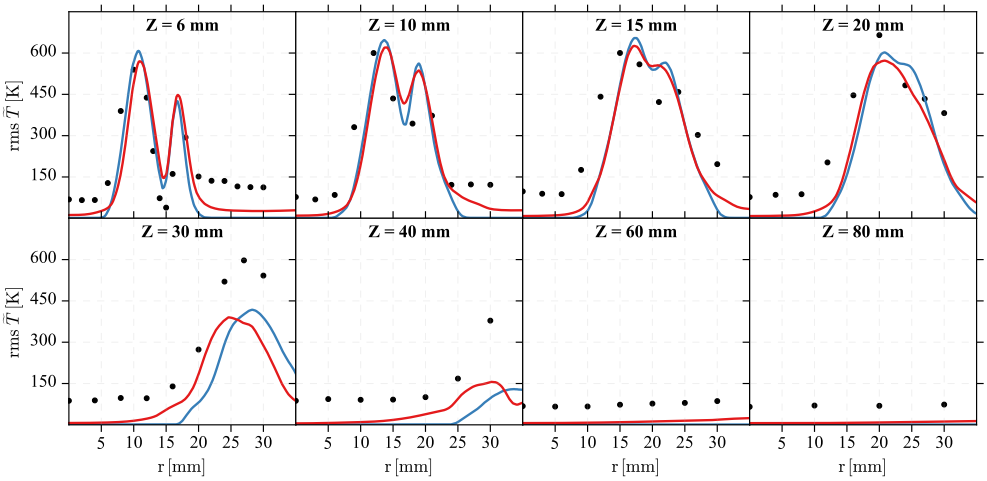

(b) RMS temperature profiles

Figure 6.6: *Mean and RMS temperature profiles for different distance from the burner exit. Error bars associated with experimental data correspond to a standard deviation $(-\sigma;\sigma)$. Symbols: Experimental data. Lines: Numerical simulations: (—) Virtual optimized mechanisms, (—) BFER semi-global scheme.*

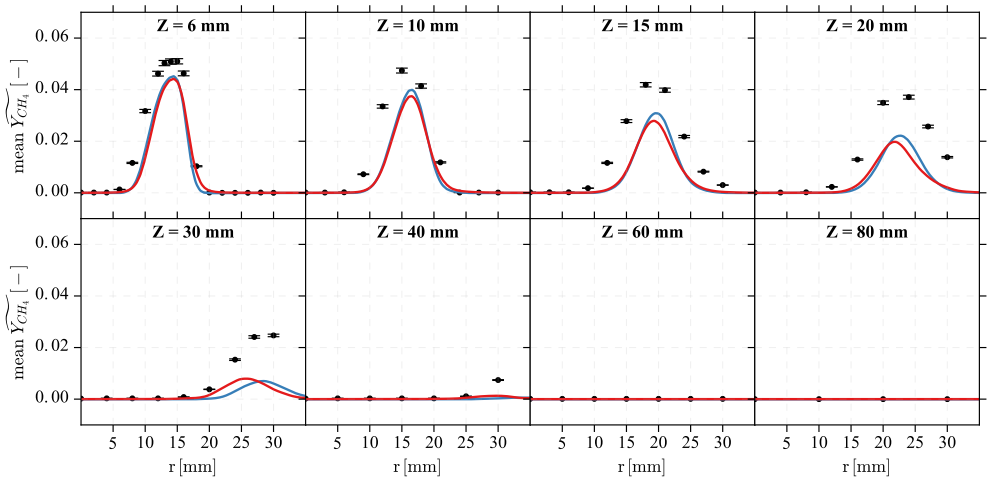

(a) Mean CH_4 mass fraction profiles

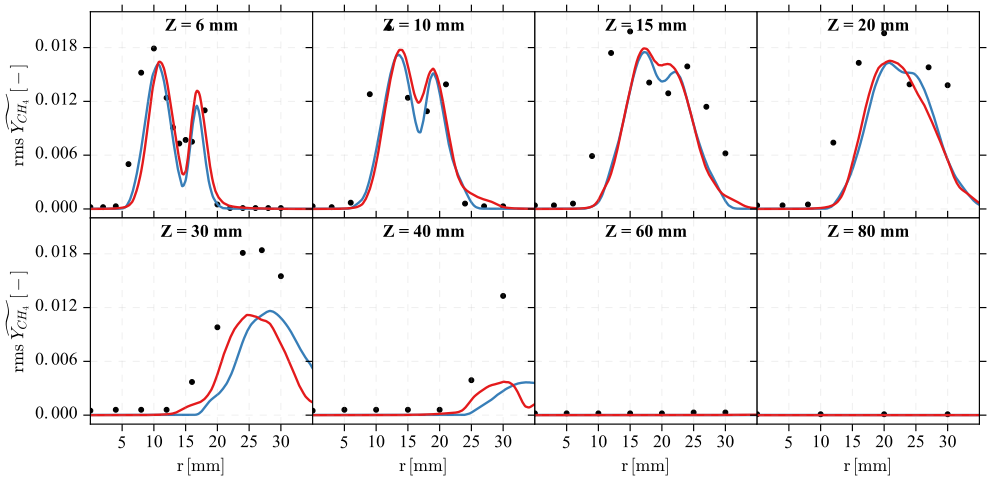

(b) RMS CH_4 mass fraction profiles

Figure 6.7: *Mean and RMS CH_4 mass fraction profiles for different distance from the burner exit. Error bars associated with experimental data correspond to a standard deviation $(-\sigma;\sigma)$. Symbols: Experimental data. Lines: Numerical simulations: (—) Virtual optimized mechanisms, (—) BFER semi-global scheme.*

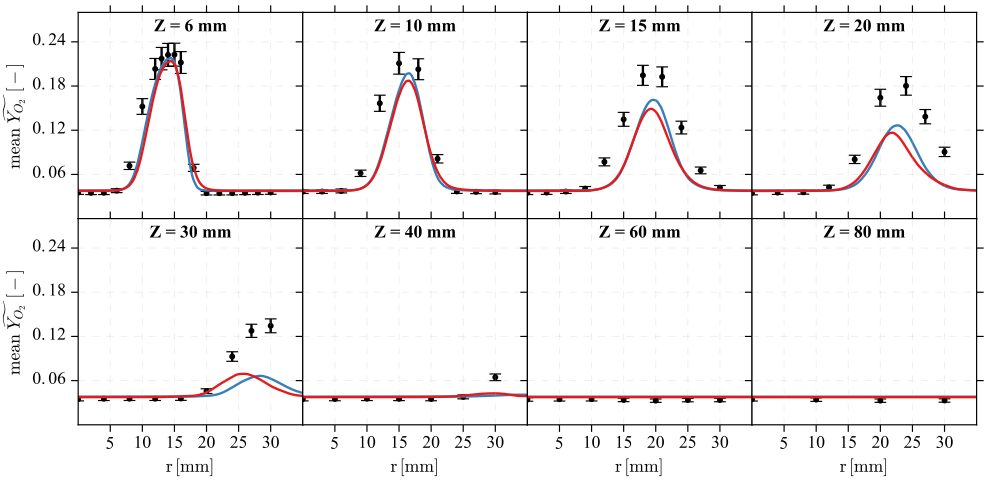

(a) Mean O_2 mass fraction profiles

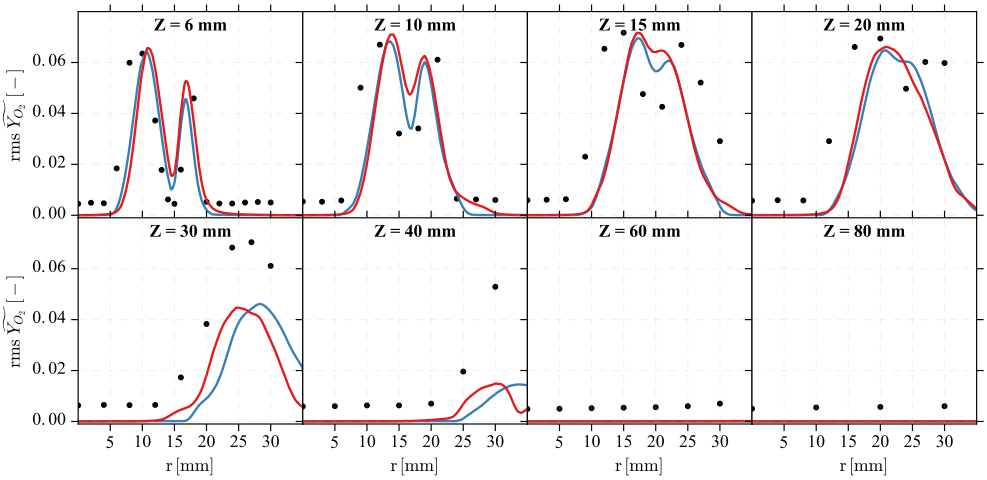

(b) RMS O_2 mass fraction profiles

Figure 6.8: *Mean and RMS O_2 mass fraction profiles for different distance from the burner exit. Error bars associated with experimental data correspond to a standard deviation $(-\sigma;\sigma)$. Symbols: Experimental data. Lines: Numerical simulations: (—) Virtual optimized mechanisms, (—) BFER semi-global scheme.*

CO concentration statistics

Figure 6.9 compares Reynolds mean and RMS of CO mass fraction profiles. Though experimental measurements exhibit high level of uncertainties, none of the considered kinetic model provides a satisfactory description of measured mean CO mass fraction profiles. As observed in laminar freely propagating flames, the BFER mechanism underestimates the CO mass fraction, in the flame fronts region, for mean and fluctuations components. On the contrary, the virtual sub-mechanism dedicated to CO formation description strongly overestimates the species production processes. Similar discrepancies between numerical results and experimental data were already reported in the literature with different chemical models going from global kinetic schemes (Volpiani et al. 2017) to premixed-based tabulated approach (Galpin et al. 2008), or analytically-reduced mechanisms (Franzelli 2011). Differences between Raman scattering measurements and virtual optimized chemistry solution may be accounted for the following reasons:

- As already discussed, the outer recirculation zone is submitted to important thermal losses due to wall cooling. In this region, the mixture enthalpy decrease produces both CO-CO_2 equilibrium shifts leading to CO conversion into CO_2, and local flame extinction. As thermal losses are not accounted for, the virtual chemistry simulation is not able to describe these two contributions.
- In the first flame front zone, the overestimation of CO mass fraction is assumed to be associated with the use of the TFLES model. The model based on flame thickening intrinsically tends to over-predict the concentration of intermediates species such as CO. This possible explanation has been recently supported by numerous authors (Mehl 2018; Maio et al. 2019; Bénard et al. 2019), and is discussed in more details in section 6.3.

As non-adiabatic effects are of primarily importance in this configuration, non-adiabatic simulations are performed with virtual optimized schemes designed to capture the effects of heat losses on the flame structure. Next section presents the results of this complementary numerical study.

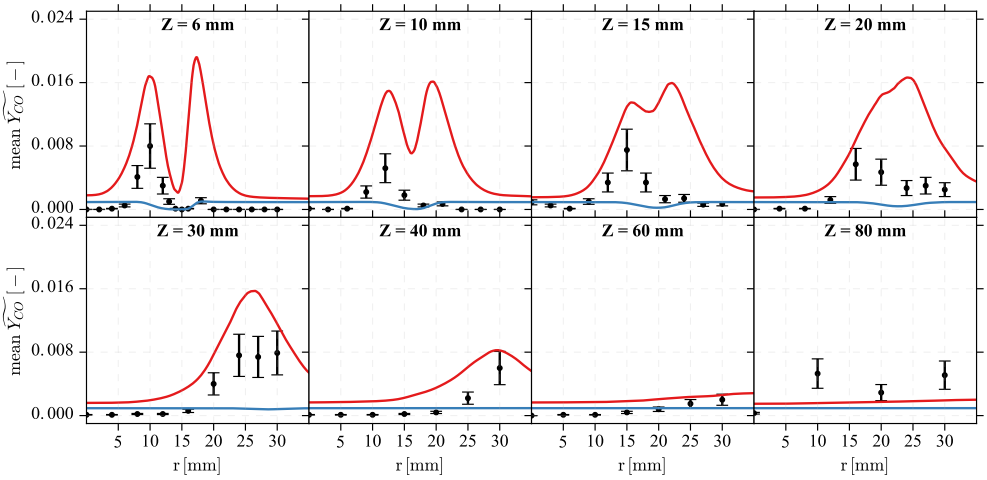

(a) Mean CO mass fraction profiles

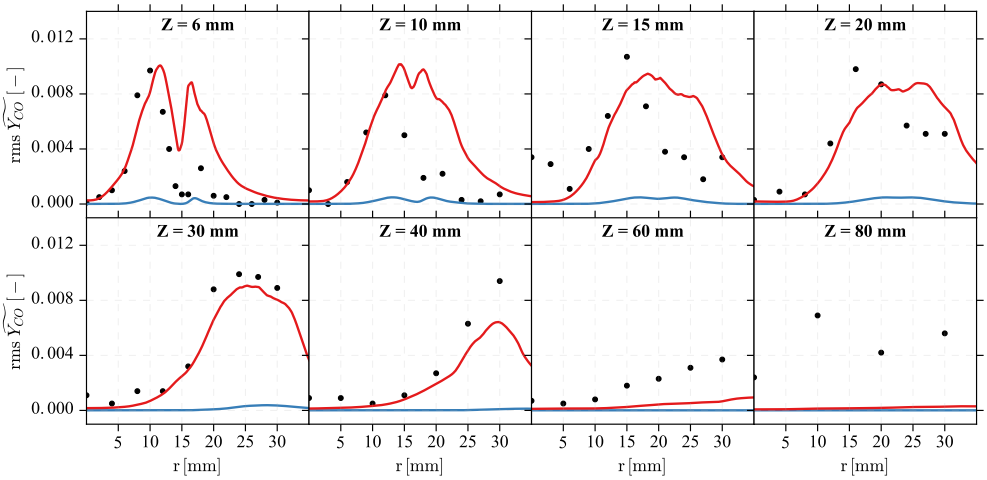

(b) RMS CO mass fraction profiles

Figure 6.9: *Mean and RMS CO mass fraction profiles for different distance from the burner exit. Error bars associated with experimental data correspond to a standard deviation ($-\sigma;\sigma$). Symbols: Experimental data. Lines: Numerical simulations: (—) Virtual optimized mechanisms, (—) BFER semi-global scheme.*

6.2.4 Accounting for heat losses with the virtual chemistry strategy.

Extension of virtual optimized chemistry approach to non-adiabatic flame configurations was performed in the PhD. Thesis of Giampaolo Maio (Maio et al. 2019). Influence of thermal losses is accounted for by adding burner stabilized flamelets in the training database, while keeping the kinetic scheme architecture presented in Chapter 3. Modification of equilibrium thermodynamic state due to non-adiabaticity is obtained by changing the repartition of virtual species products in the composition space. Impact of enthalpy defect on the flame structure is taken into account by expressing correction functions introduced in Chapter 3 as dependent on the enthalpy defect $\Delta h = h^{ad} - h$. This approach was successfully validated on 1-D laminar burner stabilized flames and freely propagating flames submitted to radiative heat losses. The application of non-adiabatic virtual chemistry to the PRECCINSTA configuration is shown in this section. Simulations have been conducted with the YALES2 solver at CORIA laboratory (Moureau et al. 2011a).

The chemical flame structure predicted by both adiabatic and non-adiabatic simulations is illustrated in Fig. 6.10. Instantaneous fields of resolved heat release rate suggest a strong impact of the heat losses in the outer recirculation zone. In the non-adiabatic calculation, local flame extinctions are observed near the wall corners due to heat losses and enthalpy decrease. On the contrary, a thick outer flame front characterized by high heat release rates is observed in the adiabatic simulation.

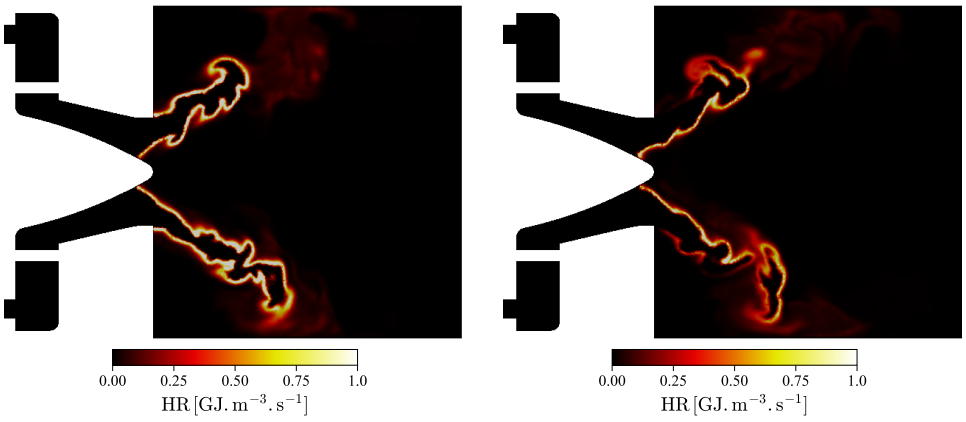

(a) Adiabatic simulation (b) Non-adiabatic simulation

Figure 6.10: *Instantaneous fields of resolved heat release rate predicted by the adiabatic and non-adiabatic Large-Eddy Simulations.*

Figure 6.11 displays mean and resolved RMS temperature profiles predicted by the non-adiabatic main virtual mechanism using both adiabatic and non-adiabatic walls. Results obtained with the LU17 skeletal scheme Sankaran et al. (2007) for lean premixed methane/air combustion are also presented (Bénard et al. 2019) for comparison purposes. The main virtual mechanism modified for the description of non-adiabatic combustion retrieves well the mean temperature profiles in the outer recirculation zone. Temperature fluctuations associated with local flame extinction are also well captured. Interestingly, a very good agreement may be observed between virtual and skeletal schemes.

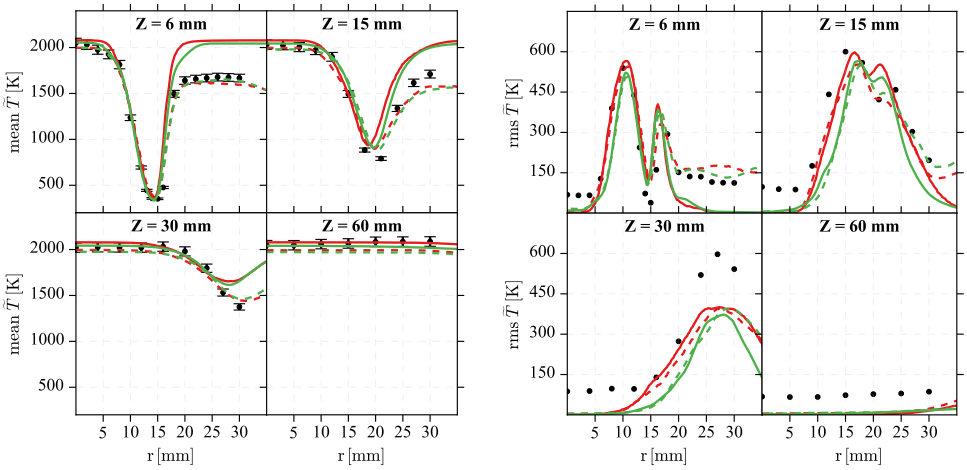

(a) Mean temperature profiles

(b) RMS temperature profiles

Figure 6.11: *Mean and RMS temperature profiles for different distance from the burner exit. Error bars associated with experimental data correspond to a standard deviation ($-\sigma;\sigma$). Symbols: Experimental data. Lines: Numerical simulations: (—) Virtual optimized schemes adiabatic conditions, (- -) Virtual optimized schemes non-adiabatic conditions, (—) Skeletal LU17 scheme adiabatic conditions and (- -), Skeletal LU17 scheme non adiabatic conditions (Bénard et al. 2019).*

Figure 6.12 presenting mean and RMS of CO mass fraction profiles, demonstrates the impact of the heat losses on the CO production in the outer recirculation zone. The non-adiabatic simulation shows an important reduction of the amplitude of the second peak of CO. It means that the shift of CO-CO_2 equilibrium due to temperature reduction is well captured by the new virtual optimized chemistry mechanism. Further improvement on the prediction of CO concentration level is expected by refining the mesh so as to reduce the impact of the TFLES model.

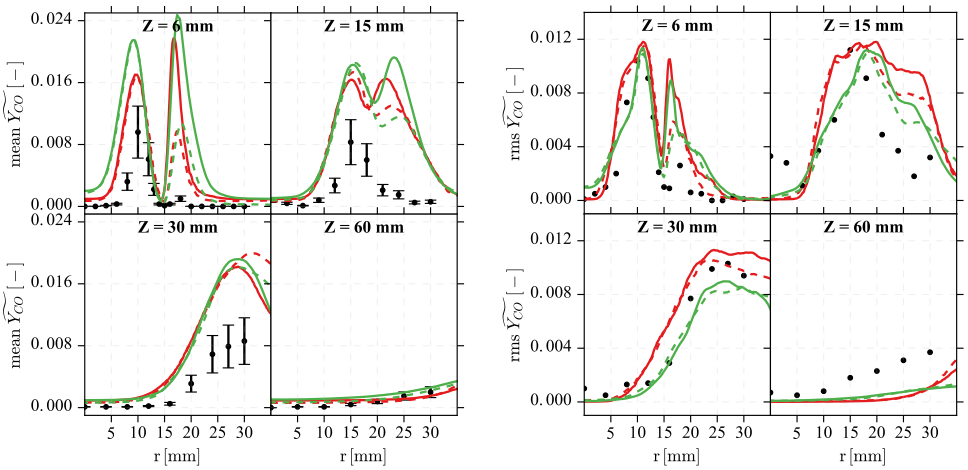

(a) Mean CO mass fraction profiles

(b) RMS CO mass fraction profiles

Figure 6.12: *Mean (left) and RMS (right) CO mass fraction profiles for different distance from the burner exit. Error bars associated with experimental data correspond to a standard deviation ($-\sigma;\sigma$). Symbols: Experimental data. Lines: Numerical simulations: (—) Virtual optimized schemes adiabatic conditions, (- -) Virtual optimized schemes non-adiabatic conditions, (—) Skeletal LU17 scheme adiabatic conditions and (- -), Skeletal LU17 scheme non adiabatic conditions (Bénard et al. 2019).*

6.2.5 Summary

In this section the first validation of the virtual chemistry concept in a turbulent swirled premixed burner was performed. In adiabatic conditions, the main virtual optimized mechanism shows capabilities to account for flame dynamics and mean flame position. The flame shape and CO concentration levels were however mispredicted due to the use of adiabatic wall conditions. Additional non-adiabatic Large-Eddy Simulation, using a virtual scheme tailored to account for non-adiabatic effects, finally demonstrates the ability of virtual optimized chemistry to account for the correct flame shape, and CO emissions in the outer recirculation zone.

Validation of the virtual optimized chemistry approach in a gaseous turbulent context is complemented with the Large-Eddy Simulation of the stratified jet flame Cambridge.

6.3 LES of the stratified jet flame Cambridge

The objective of this section is to evaluate the virtual optimized chemistry approach in a stratified context. The Cambridge burner experimented both at Cambridge University (Sweeney et al. 2011; Sweeney et al. 2012a; Zhou et al. 2013; Euler et al. 2014) and at Sandia National Laboratories (Barlow et al. 2012) is considered here. This configuration is especially challenging since recent numerical simulations using unstretched premixed flame tabulation models (Nambully et al. 2014b; Proch and Kempf 2014; Mercier et al. 2015) failed to capture the CO formation.
The experimental set-up and available experimental measurements are first described. Capabilities of the virtual schemes to capture flame stabilization and CO concentration are assessed by comparing numerical simulation against experimental measurements
This work was performed in strong collaboration with Dr. R. Mercier in the context of the "Grand Challenge" on the Cobalt machine. Results of this numerical study were presented at the AIAA SciTech Forum 2017, and published in the conference proceedings (Cailler et al. 2017).

6.3.1 Experimental set-up

The geometry and dimensions of the stratified Cambridge burner are illustrated in Fig. 6.13. This laboratory-scale configuration is composed of two concentric tubes surrounding a central bluff-body ensuring flame stabilization. Both inner (i) and outer (o) tubes are fed with premixed methane-air streams whose equivalence ratio ϕ and bulk velocity $\overline{U}$ are controlled independently. A surrounding air co-flow isolates the flame from ambient perturbations.
A wide range of operating conditions have been experimentally investigated by varying the levels of fuel/air stratification and swirl of the outer stream. The numerical work focuses here on the non-swirling and stratified case SwB5 featuring a Stratification Ratio SR of 2.0. Table 6.2 summarizes the inflow conditions in terms of equivalence ratio, bulk velocities and corresponding Reynolds numbers. All streams are injected at the ambient temperature $T_0 = 298.0$ K.

Stream	ϕ [-]	$\overline{U}$ [m/s]	Re [-]
inner	1.0	8.31	5960
outer	0.5	18.7	11540
co-flow	0.0	0.4	0

Table 6.2: *Inlet boundary conditions for the SwB5 flame configuration.*

Available experimental data include velocity (Zhou et al. 2013) and thermochemical quantities (Sweeney et al. 2011; Sweeney et al. 2013; Sweeney et al.

2012a; Sweeney et al. 2012b) such as temperature, equivalence ratio and species mass fraction profiles (CH_4, CO_2, CO, H_2O, O_2).

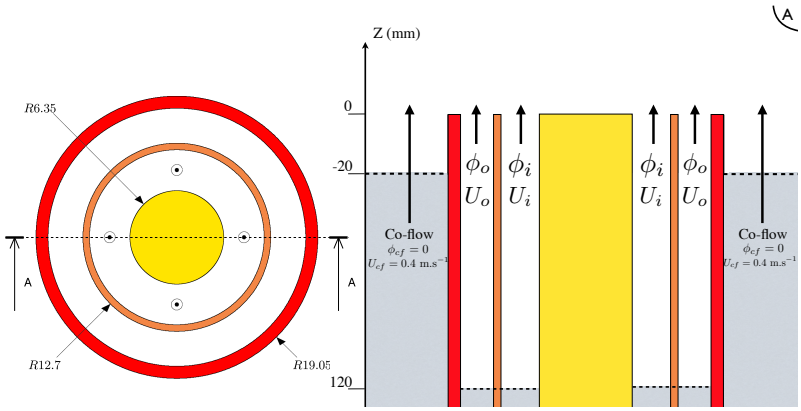

Figure 6.13: *Longitudinal cut of the SwB burner. The white area indicates the computational domain. Dimensions are in mm. SwB5 inlet equivalence ratio:* $\phi_i = 1.0$*;* $\phi_o = 0.5$*;* $\phi_{cf} = 0.0$*. SwB5 inlet bulk velocities:* $\overline{U_i} = 8.31\ m.s^{-1}$ *;* $\overline{U_o} = 18.7\ m.s^{-1}$ *;* $\overline{U_{cf}} = 0.4\ m.s^{-1}$*.*

6.3.2 Numerical set-up

Computational domain definition, boundary conditions and cold flow analysis are based on the numerical study performed by Mercier et al. (2015). Figure 6.13 shows the computational domain delineated by the grey area. For both inner and outer tubes, Homogeneous and Isotropic Turbulence is injected. Burner walls are considered as adiabatic and are treated with classical log-law. LES are performed using the YALES2 low-Mach number, unstructured finite volume flow solver (Moureau et al. 2011a). Fourth-order schemes are used for both spatial discretization and time integration (Kraushaar 2011). The impact of sub-grid scale turbulent motions on the resolved momentum is described by the σ-model (Nicoud et al. 2011) as suggested by (Proch et al. 2013).

Case #	Turbulent combustion model	Chemical model	Mesh size Δ_x [mm]	max $\overline{F}$ [-]
bfer-c	TFLES	Semi-global	0.5	7.2
virtual-c	TFLES	Optimized virtual	0.5	6.3
virtual-f	TFLES	Optimized virtual	0.25	3.2

Table 6.3: *Simulated cases*

Two different chemical models are considered to simulate the SwB configuration as shown in Tab. 6.3. Case 1 is based on the semi-global mechanism BFER

(Franzelli et al. 2012) while cases 2 and 3 use the virtual optimized mechanisms derived in Chapter 4. Semi-global and virtual schemes are coupled with the DTFLES model (Legier 2001) and sub-grid scale turbulence/chemistry interactions are accounted for with the Charlette model (Charlette et al. 2002a). For virtual optimized mechanisms, the flame sensor is based on the envelop of species flame sensors as introduced in Chapter 5.
Impact of the mesh resolution on the target flame properties is investigated with two different computational grids. The first and coarser mesh is composed of 30 millions of tetrahedral elements with a characteristic cell size of $\Delta_x = 0.5$ mm in the flame region. The finer mesh, obtained via homogeneous grid refinement is made of 240 million elements with $\Delta_x = 0.25$ mm in the flame region. The maximum value of the thickening factor for each simulation are provided in Tab. 6.3.

6.3.3 Simulations results analysis

This section presents the comparison between simulation results and experimental data. The capabilities of the reduced mechanisms to capture the flame stabilization are first discussed. Then, virtual and global mechanisms are compared against experimental measurements in terms of CO prediction. Finally, the impact of differential diffusion in the CO prediction previously observed experimentally (Barlow et al. 2012) and numerically (Nambully et al. 2014a) is discussed.

6.3.3.1 Instantaneous flame shape

Flame structure is illustrated in Fig. 6.14 showing an instantaneous iso-surface of the resolved heat release rate colored by the filtered nitrogen mass fraction. As described in (Mercier 2015), the SwB5 flame structure exhibits three different parts. Near the burner exit, as the inner tube is fed with a low Reynolds number flow, a very low flame wrinkling is observed. Moreover, as the incoming flow only comes from tube i, the low-wrinkled flame front is fully premixed. When the flame front crosses the turbulent shear layer holding between tubes i and o, the the reactive region starts to wrinkle and high levels of stratification occur. Further downstream, when the injected stream i and o mix with the air co-flow, the flame wrinkling and stratification increase. This jet flame configuration exhibits a well identified fully premixed zone near the burner exit and a highly stratified zone further downstream.

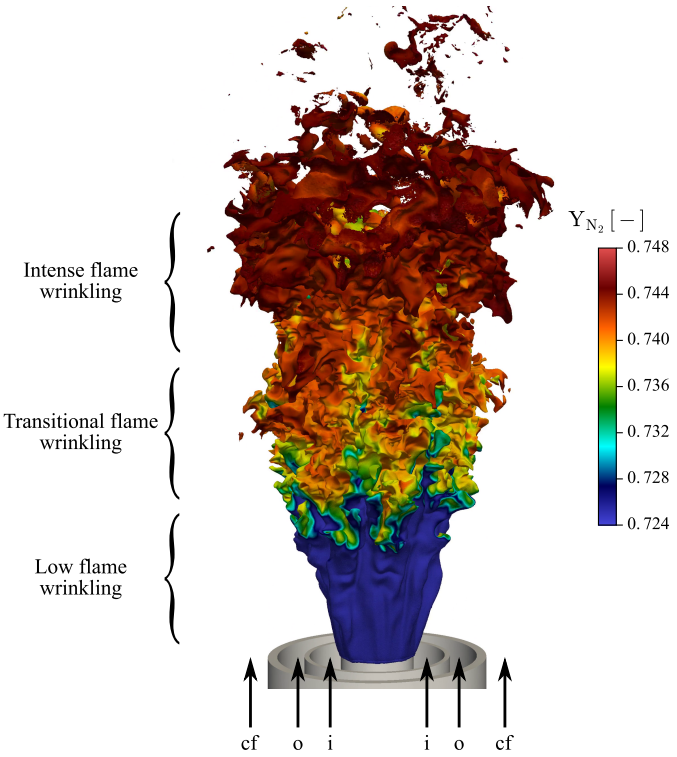

Figure 6.14: *Instantaneous iso-surface of the resolved heat release rate* $\widetilde{HR}$ *colored by the resolved nitrogen mass fraction* $\widetilde{Y}_{N_2}$ *for the LES of the SwB5 flame with virtual optimized chemistry on the fine grid.*

6.3.3.2 Flame stabilization and temperature field

Mean and RMS of axial velocity profiles are compared to Laser Doppler Anemometry (LDA) and Particle Image Velocimetry (PIV) measurements in Fig. 6.15. A very good agreement is found for the first profiles, which validates the velocity boundary conditions prescribed at the inlet. The mean axial velocity is however mispredicted by all the simulations in the inner recirculation zone (IRZ) located behind the bluff-body ($Z < 10$ mm and $r < 5$ mm). This discrepancy already investigated in (Mercier et al. 2015) is due to the sub-grid scale wrinkling modeling (Charlette et al. 2002a) which assumes equilibrium between turbulence and flame wrinkling. This assumption is not verified at the flame basis located near the recirculation zone where low levels of turbulence and flame wrinkling are encountered. A slight underestimation of mean axial velocity is also observed for $r < 10$ mm and $Z > 30$ mm for all simulated cases. This error, also visible on mean temperature and CH_4 mass fraction at $Z = 50$ mm (see Figs. 6.16 and 6.17), is due to a misprediction of the mean flame opening angle.

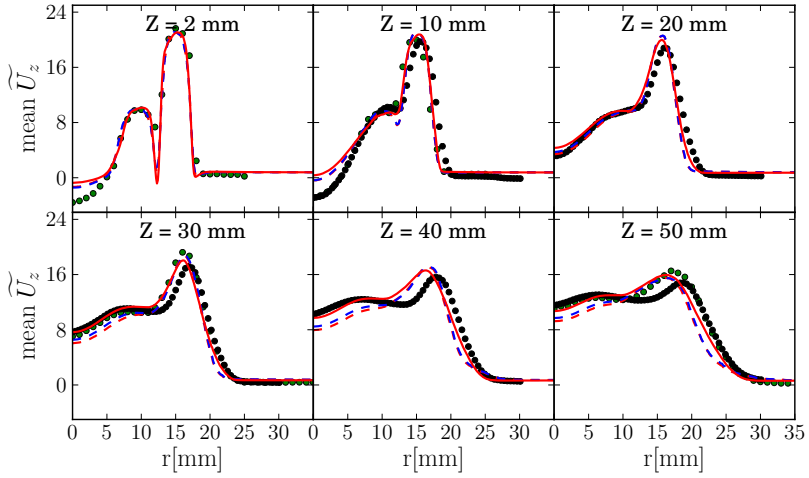

(a) Mean axial velocity profiles

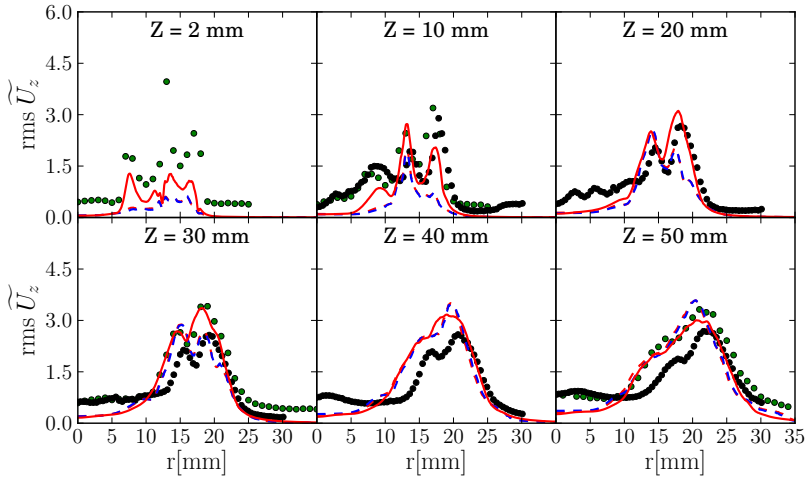

(b) RMS axial velocity profiles

Figure 6.15: *Mean and RMS axial velocity profiles for different distances from the burner exit. Symbols: Experimental data (● ●) PIV measurements, (● ●) LDA measurements. Lines: Numerical simulations (- - -) case bfer-c, (- - -) case virtual-c, (——) case virtual-f*

Axial velocity RMS plotted in Fig.6.15 (bottom), less sensitive to the chemistry modeling, are well predicted by both simulations bfer-c and virtual-c. As expected, an increase in RMS level is obtained when the mesh is refined (simulation virtual-f). Small scale turbulence is not fully resolved within the injection tubes which explains the defect of fluctuations at the injection tube exits ($Z = 2$ mm). However, large scales turbulence generated in shear layers between *i*) the recirculation zone and the inner injection; *ii*) the inner and outer injections and *iii*) the outer injection and the co-flow are well reproduced.

Figure 6.16 displays radial profiles of mean and RMS of temperature at different axial positions from the burner exit plane. Main observations from the comparison between numerical results and Rayleigh scattering measurements may be summarized as follow:

- For all axial positions, both reduced kinetic models over-predict the temperature in the IRZ. This behavior was expected since the burner is considered as adiabatic. As a consequence, heat losses at the bluff-body wall surface are not taken into account and the flow enthalpy is overestimated.
- The recirculating burnt gases temperature predicted by the two kinetic schemes differs by about 30 K. The BFER global scheme, which involves 6 species with real thermodynamic properties, overestimates the adiabatic flame temperature in stoichiometric conditions. On the contrary, the virtual mechanism made up of virtual species with optimized properties predicts accurately the adiabatic temperature.
- At the flame basis, where the flame is fully premixed, both global and virtual mechanisms predict the flame brush position. It can be however noticed that the temperature profile predicted by case virtual-c deviates from experimental data in the high temperature zone of the mean flame brush (for instance at $r = 5$ mm and $Z = 10$ mm). On the coarse mesh, the flame thickening strongly affects the burnout zone as seen in Fig. 5.4 (right). On the fine grid, the application of a reduced thickening factor leads to a finer post-flame region and better capture of temperature profile. Since the BFER scheme under-predicts the post-flame zone thickness (see Fig. 4.4) the impact of flame thickening is not observed on the burnout zone.
- For high axial positions ($Z = 50$ mm), departure is observed between numerical results and experimental data. The mean flame position predicted by virtual and global schemes is shifted towards the burner axis. Previous investigation (Proch and Kempf 2014) suggests that a damping of the flame dynamics due to thickening of the flame front causes a misprediction of the mean flame angle at high axial positions. This explanation agrees with the fact the finer mesh simulation allows a better capture of flame opening.

For both reduced mechanisms (simulations bfer-c and virtual-c), the temperature fluctuations are underestimated on the coarse mesh. As expected, the mesh refinement (simulation virtual-f) increases the level of resolved flame-turbulence interactions and therefore the level of temperature RMS within the mean flame brush. However, the fine mesh resolution is not sufficiently fine to capture all the flame wrinkling scales.

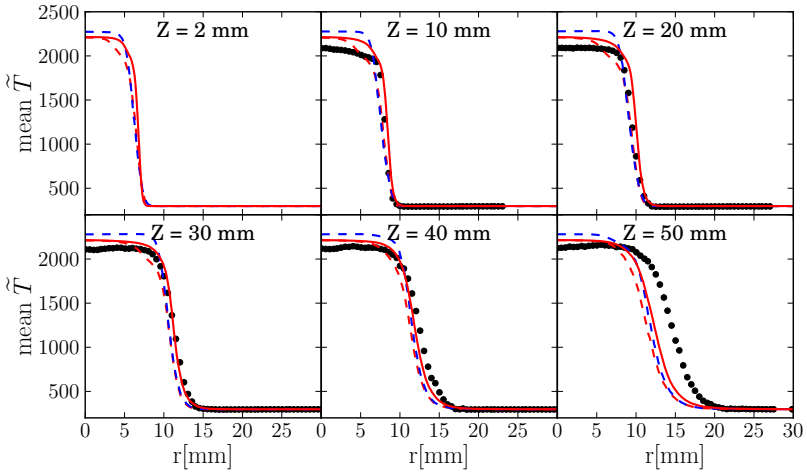

(a) Mean temperature profiles

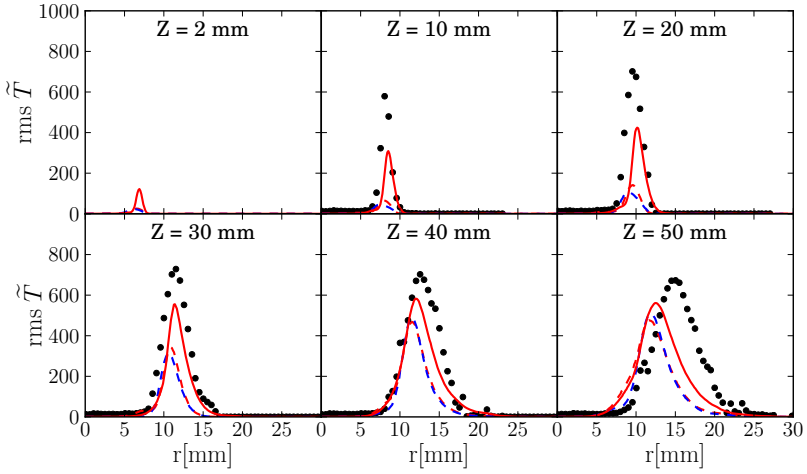

(b) RMS temperature profiles

Figure 6.16: *Mean and RMS temperature profiles for different distances from the burner exit. Symbols: (● ●) Experimental data. Lines: Numerical simulations (- -) case bfer-c, (- -) case virtual-c, (—) case virtual-f*

Figures 6.17 and 6.18 show radial profiles of mean and RMS of CH_4 and O_2 mass fraction profiles, respectively. A very good agreement is found on the mean profiles of fuel and oxidizer evaluated by both global and virtual chemistry. A misprediction of the mean flame brush position at $Z = 50$ mm is also noted and corroborates the analysis proposed for the mean temperature profiles at $Z = 50$ mm (see Fig. 6.16). As expected, the levels of RMS are importantly under-predicted for both chemical models, especially at the interface between the inner stream and the IRZ. As previously pointed out, the fine mesh simulation allows a net improvement of fluctuations prediction.

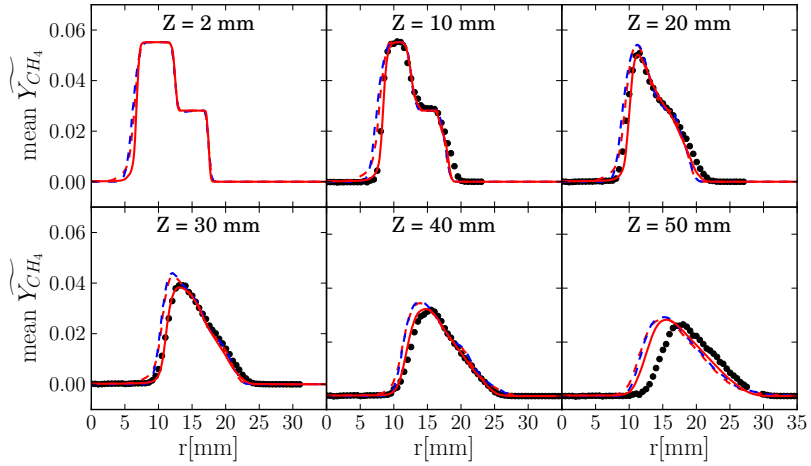

(a) Mean CH_4 mass fraction profiles

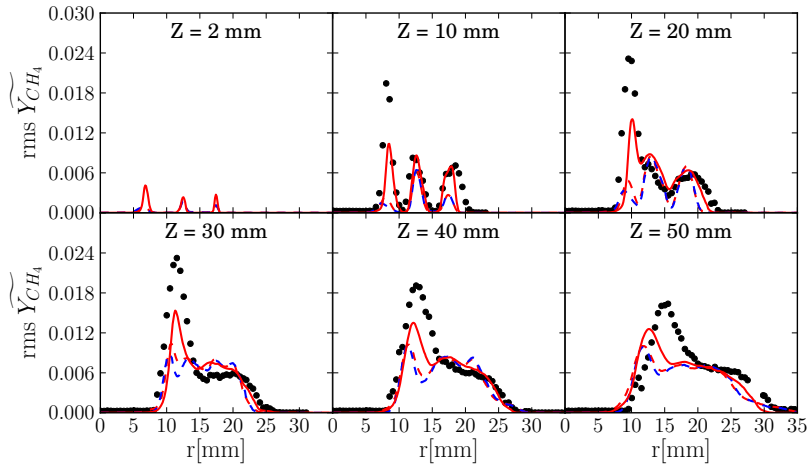

(b) RMS CH_4 mass fraction profiles

Figure 6.17: *Mean and RMS profiles of CH_4 mass fraction for different distances from the burner exit. Symbols: (● ●) Experimental data. Lines: Numerical simulations (– –) case bfer-c, (– –) case virtual-c, (——) case virtual-f*

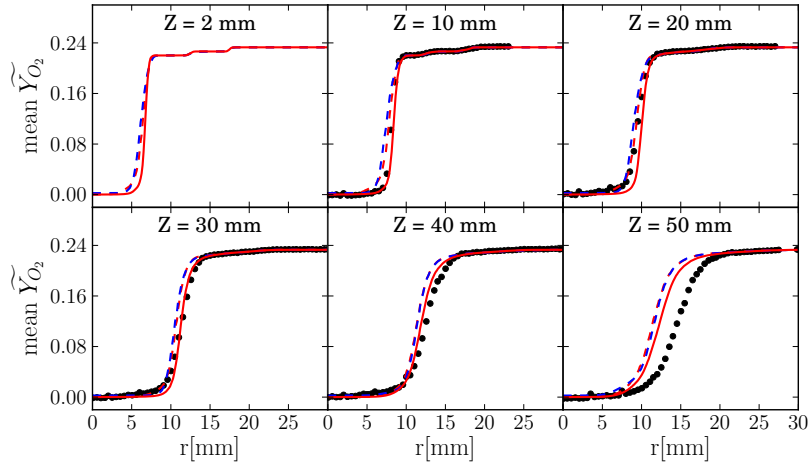

(a) Mean O_2 mass fraction profiles

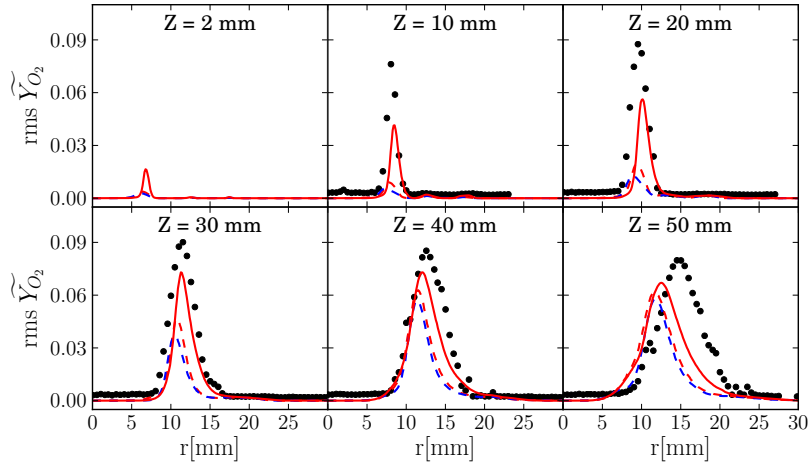

(b) RMS O_2 mass fraction profiles

Figure 6.18: *Mean and RMS profiles of O_2 mass fraction for different distances from the burner exit. Symbols: (● ●) Experimental data. Lines: Numerical simulations (- -) case bfer-c, (- - -) case virtual-c, (——) case virtual-f*

6.3.3.3 CO prediction

Capability of the virtual mechanism to provide a correct prediction of CO formation is evaluated by comparing mean and RMS CO profiles against experimental data in Fig. 6.19. The standard deviation associated to the CO Laser Induced Fluorescence (LIF) measurements, indicated by error bars, is estimated to $\sigma = 5.9\%$ (Sweeney et al. 2013).

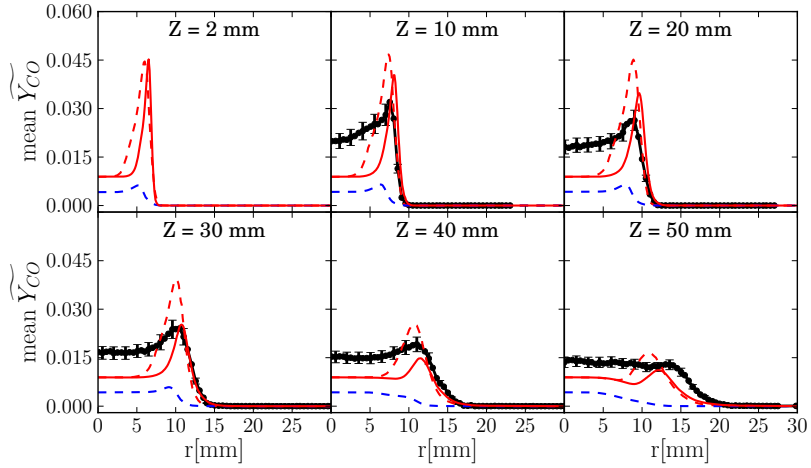

(a) Mean CO mass fraction profiles

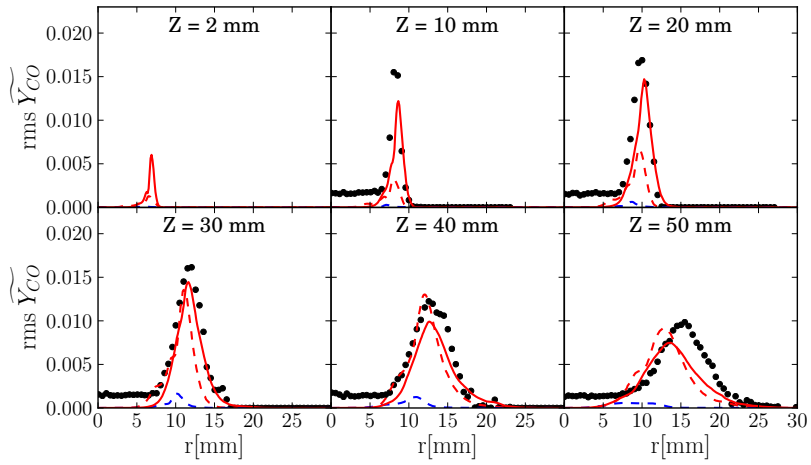

(b) RMS CO mass fraction profiles

Figure 6.19: *Mean and RMS profiles of CO mass fraction for different distances from the burner exit. Symbols: (● ●) Experimental data. Lines: Numerical simulations (- -) case bfer-c, (-- --) case virtual-c, (——) case virtual-f*

Overall agreement between the virtual sub-mechanism and LIF measurements is reasonable in comparison with the global scheme predictive capabilities. For all axial positions, the BFER mechanism predicts a quasi-constant CO mass fraction profile, underestimating largely the CO concentration in the flame front. This behavior is consistent with results presented by Franzelli (2011). Simulations using the virtual chemistry approach present however an overestimation of the peak of CO production within the mean reaction zone. This undesirable behavior, attenuated when the mesh is refined, is explained by the artificial thickening of the flame front. As the width of CO mass fraction profiles is in-

creased by a factor F, the total mass of CO contained in the flame front is also increased in the same extent (Mehl 2018; Maio et al. 2019). As an example, Fig. 6.20 shows the impact of the flame thickening on the CO mass fraction profile in a 1-D laminar premixed flame. A reference laminar well resolved solution is artificially thickened using the TFLES model. The total quantity of CO initially presents within the reference laminar flame front reads:

$$m^0_{\mathrm{CO}} = \int_{-\infty}^{+\infty} \rho Y_{\mathrm{CO}} dx_n \tag{6.1}$$

where x_n is the direction normal to the flame front, ρ and Y_{CO} are the density and the CO mass fraction of the laminar flame front, respectively. Figure 6.20 shows that the TFLES model conserves the CO peak and consequently increases artificially the mass of CO contained within the flame layer. A simple integration shows that $m^{\mathrm{TFLES}}_{\mathrm{CO}} = F m^0_{\mathrm{CO}}$. The TFLES approach therefore contributes to the overestimation of the CO peak within the mean flame brush by a factor F and this phenomenon decreases linearly when the mesh is refined.

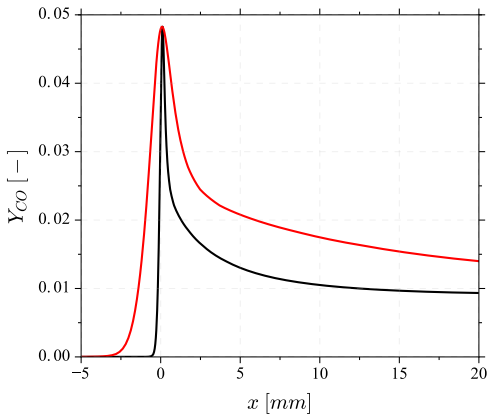

Figure 6.20: *Spatial evolution of CO mass fraction for a 1-D methane/air premixed flame at an equivalence ratio $\phi = 1.0$. Legend: ▬: DNS calculation, ▬: Thickened model with F=5*

Figure 6.19 also exhibits discrepancies between numerical and experimental data in the burnt gases located within the bluff-body recirculation zone ($r < 6$ mm). The experimental study proposed by (Barlow et al. 2012) shows that atom balances are not conserved across the flame brush leading to an increase by about 10% of the mean equivalence ratio. These phenomena results from complex preferential diffusive transport in the direction tangential to the flame front and are not captured by the virtual mechanism proposed in the present thesis.

6.3.4 Summary

Virtual optimized chemistry has been validated on a turbulent stratified flame. The Cambridge SwB5 case has been computed using global and virtual mechanisms both coupled with the TFLES turbulent combustion model. The mean flame position and its dynamic are well represented by both chemical models which give very similar results. The main virtual mechanism improves the temperature level in the recirculation zone and the capture of the flame temperature profile in the burnout zone. A particular attention was paid to the prediction of the mean and RMS of CO mass fraction. Virtual mechanisms better capture the CO equilibrium value in burnt gases. However, differential diffusion effects, neglected in this study, are found to control the local equivalence ratio within the central recirculation zone leading to an increase in CO mass fraction at this location (Barlow et al. 2012; Nambully et al. 2014a; Mercier et al. 2015).

6.4 Conclusion

In this chapter the virtual optimized chemistry approach coupled to the TFLES model was applied on two turbulent flame configurations.
First adiabatic Large-Eddy Simulations were performed on the swirled premixed burner PRECCINSTA. Results obtained with virtual optimized schemes are in good agreement with previous numerical studies, but show some discrepancies with experimental data due to simplification of the thermal wall conditions. Complementary non-adiabatic simulations with dedicated virtual kinetic schemes provide very good agreement with Raman temperature and species measurements. The use of a turbulent combustion model based on thickening of the flame front however leads to a slight overestimation of CO concentration in the reaction zone. Alternative formulations based on Filtered Wrinkled Flame models (Mehl 2018; Mercier et al. 2019) would probably results in improvement of CO formation capture.
Then, virtual optimized kinetic schemes were tested on the stratified jet-flame Cambridge. An overall good agreement between virtual kinetic solution and experiments is obtained regarding the prediction of flame position and dynamics. However as preferential diffusion effects are not taken into account modification of the composition are not captured and CO concentrations are underestimated. Further developments will consist in extending the virtual optimized mechanisms to account for differential diffusion effects.
Virtual optimized chemistry has been successfully used in gaseous turbulent flames. Next part aims at assessing the predictive capabilities of the newly developed approach in an aeronautical two-phase flow burner.

Part IV

Application of virtual chemistry in industrial scale turbulent configuration

Chapter 7

Two phase flow modeling

Contents

In this chapter, the modeling approach used to describe the disperse phase for the HERON configuration is presented. First the Lagrangian point particle method and the equations describing particles evolution are introduced. Then, the models used to close the external forces as well as mass and heat transfer due to evaporation process are described. Finally, the coupling of virtual chemistry with the evaporation model is investigated, focusing on the transport properties of the evaporated species.

7.1 Spray modeling challenges

As discussed in the introduction, aeronautical combustion chambers inject liquid fuel that atomizes to form a spray of droplets. The break-up mechanism converting the liquid continuous core into ligaments and droplets is the result of a competition between surface tension and aerodynamic forces leading to interface instabilities (see Fig. 7.1). The numerical resolution of such a phenomenon requires the use of highly resolved meshes, with typical cell sizes smaller than the minimum droplet diameter, which is unreachable for the simulation of industrial combustion chamber. For reacting calculations, Direct Numerical Simulation of liquid jet atomization is therefore not possible. Instead, a liquid spray is directly injected in the combustion chamber using an injector model. The latter aims at representing targeted droplet diameter and velocity distributions given by empirical relationships or experimental data. Once the liquid spray is injected, major challenges raised by spray modeling concerns i) the accurate description of the interactions between the droplets and the turbulence and ii) the proper prediction of the disperse phase evaporation. As these two strongly linked processes directly influence the local mixture composition, the flame structure and pollutant emissions, the simulation strategy and the choices of the associated physical models constitute essential modeling parameters.

In this chapter, the focus is made on the approaches used to describe the spray and on the modeling of the interactions between the liquid and gaseous phases.

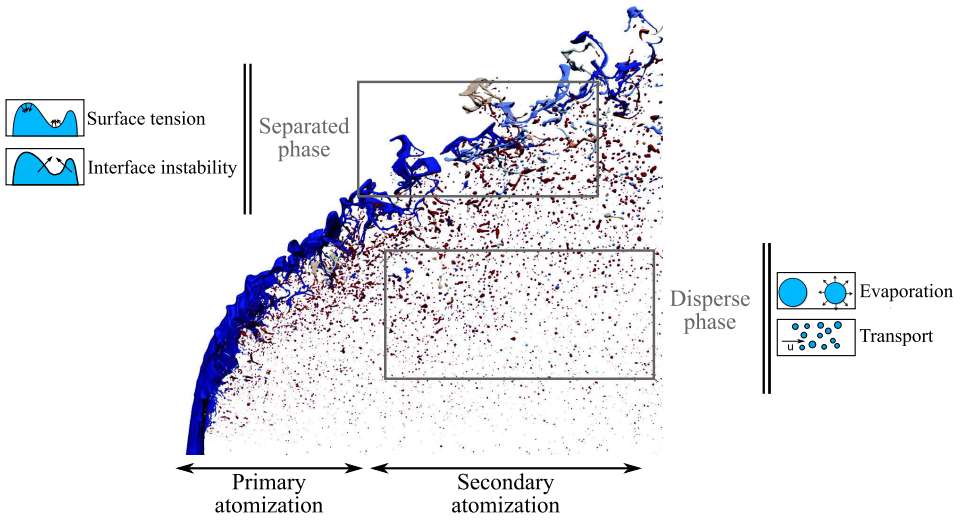

Figure 7.1: *Atomization process of a liquid jet in cross flow. Instantaneous snapshot of the liquid jet is reproduced from (Leparoux et al. 2018)*

7.2 Simulation approach: Eulerian vs Lagrangian

In the LES context, two main numerical approaches can be used to describe the liquid spray:

- **Euler-Euler** approaches consider the spray as a continuous medium whose properties correspond to the mean statistical properties of the droplets (Fevrier et al. 2005). As the Euler-Euler method uses the same Eulerian reference framework for both the gas and the liquid phases, the computational procedure for the coupling between disperse and carrier is highly facilitated. Also, the Eulerian representation of the spray features intrinsic capabilities for parallel computing. A third advantage of Eulerian approach is that the statistical convergence of spray properties is inherently obtained. However, the treatment of sprays with droplets of different sizes or velocities at the same location is not straightforward. Dedicated Eulerian models based on discretization of the phase space (Laurent and Massot 2001) or on the transport of high order moments (Vié et al. 2013) must be used to account for spray polydispersity and polykineticity[1]. Moreover, dedicated numerical techniques are required to handle stiff gradients and vacuum regions (Dombard 2011).
- In the **Euler-Lagrange** formalism, the gaseous flow description is based on continuum mechanics with an Eulerian point view, while the disperse phase is modeled by a set of particles tracked in a Lagrangian framework. To account for the exchanges between the gas and the liquid, the Lagrangian approach requires i) an interpolation step to calculate the gaseous phase properties at the droplets location and ii) a projection step to evaluate the feedback of the spray on the carrier phase. These operations must be sufficiently precise to avoid numerical errors and therefore impose a non-negligible overcost. More importantly, efficient parallelization of Lagrangian calculation requires the use of efficient double-constraint dynamic load balancing (Enjalbert 2011). If the Lagrangian method raises more computational difficulties than Euler-Euler method for massively parallel computing, it however allows to treat polydisperse and polykinetic sprays without modeling efforts. Additionally, the transport of the Lagrangian particles is relatively simple from a numerical point of view. Contrarily to Eulerian-based methods no numerical artifact is required.

In this work, the Lagrangian point particle method is considered to describe the liquid spray. This choice was motivated by both modeling and numerical reasons. First, as the droplet size distribution is a parameter of primary importance, the ability of the Lagrangian formalism to handle polydisperse flows without modeling effort was greatly favored. Then, the numerical robustness of

[1] i.e. droplets of different velocities at the same location

the Lagrangian approach constitutes a non-negligible advantage over Eulerian methods.

7.2.1 Deterministic Lagrangian model framework

In the Lagrangian framework, liquid droplets are modeled by a set of discrete particles or material points whose evolution in the gaseous flow environment is ruled by laws of point mechanics. The impact of the particles on the carrier phase is approximated with the point source approach. Mass, momentum and energy source terms from the liquid particles are interpolated on the Eulerian mesh and applied to the conservation equations describing the gaseous phase. This formalism relies on the following assumptions:

- The droplet size is considered negligible compared to all resolved scales of the flow (Maxey and Riley 1983)
- The liquid volume fraction α_l is assumed small ($\alpha_l < 10^{-4}$). In these conditions the spray, qualified as diluted, is viewed as a set of isolated and not colliding particles.
- The droplets diameter d_p is supposed sufficiently small so that the surface tension forces are strongest than deformation forces. The deformations effects are therefore neglected leading to perfectly spherical particles.
- The droplet diameter is smaller than the LES mesh size ($d_p/\Delta_x << 1$) to allow the interpolation of particle properties on the Eulerian mesh. Moreover, models describing the two-way coupling between the liquid and gaseous phases require the evaluation of non-perturbed gas properties in the vicinity of the droplet. The distance between particles and nodes of the cell containing the droplet must therefore be sufficiently high.

These hypotheses are generally valid except at the exit of the injection system where high concentration of liquid ligaments and non spherical droplets may be encountered.

The approach is qualified as deterministic, in opposition with stochastic or probabilistic approach, since each physical droplet is modeled by one material particle individually followed in the flow. The set of transported particles therefore corresponds to a unique realization of the spray. For the case simulated here, this strategy does not lead to prohibitive numerical cost because the droplets are rapidly evaporated by the flame stabilized closed to injection system.

7.2.2 Lagrangian particles equations

Each particle p, characterized by its position $\mathbf{X}_p$, velocity $\mathbf{u}_p$, mass m_p and temperature T_p (or equivalently sensible enthalpy $h_{s,p}$), is tracked in a Lagrangian framework. The evolution of its trajectory and properties is governed by the

following system of equations:

$$\frac{\mathrm{d}\mathbf{X}_p}{\mathrm{d}t} = \mathbf{u}_p \tag{7.1}$$

$$\frac{\mathrm{d}}{\mathrm{d}t}\left(m_p \mathbf{u}_p\right) = \mathbf{F}_p \tag{7.2}$$

$$\frac{\mathrm{d}m_p}{\mathrm{d}t} = \dot{m}_p \tag{7.3}$$

$$\frac{\mathrm{d}}{\mathrm{d}t}\left(m_p h_{s,p}\right) = \frac{\mathrm{d}}{\mathrm{d}t}\left(m_p c_{p,l} T_p\right) = Q_p \tag{7.4}$$

where in Eq. (7.2) $\mathbf{F}_p$ refers to the external forces applied to the particle p. The source term $\dot{m}_p$ in Eq. (7.3) denotes the evaporation rate of the particle p. Finally, $c_{p,l}$ is the heat capacity at constant pressure of the liquid phase and Q_p represents the rate of heat exchange from the gaseous phase. The liquid heat capacity $c_{p,l}$ is assumed constant.
The source terms of equations (7.2)–(7.4) are unclosed contributions that need to be modeled. Section 7.3 presents the modeling assumptions used in this thesis.

7.2.3 Coupling with the gaseous phase

The effects of the liquid droplets on the carrier phase are accounted for through coupling terms $S^{p\to g} = \{S_m^{p\to g}, S_{qdm}^{p\to g}, S_{Fuel}^{p\to g}, S_E^{p\to g}\}$ respectively applied to the filtered conservation equations (5.3)–(5.6) for mass, momentum, fuel mass fraction and energy. These different local coupling terms are evaluated by projection of the mass $\dot{m}_p$, momentum $\mathbf{F}_p$ and energy Q_p fluxes of each particle on the Eulerian grid:

$$S_m^{p\to g}(\mathbf{x}) = -\frac{1}{\Delta V}\sum_{n=1}^{N_p^V} \Psi\left(\mathbf{x}_p^n\right)\dot{m}_p^n \tag{7.5}$$

$$S_{qdm}^{p\to g}(\mathbf{x}) = -\frac{1}{\Delta V}\sum_{n=1}^{N_p^V} \Psi\left(\mathbf{x}_p^n\right)\left(\mathbf{F}_p^n + \dot{m}_p^n \mathbf{u}_p^n\right) \tag{7.6}$$

$$S_{Fuel}^{p\to g}(\mathbf{x}) = -\frac{1}{\Delta V}\sum_{n=1}^{N_p^V} \Psi\left(\mathbf{x}_p^n\right)\dot{m}_p^n \tag{7.7}$$

$$S_E^{p\to g}(\mathbf{x}) = -\frac{1}{\Delta V}\sum_{n=1}^{N_p^V} \Psi\left(\mathbf{x}_p^n\right)\left(Q_p^n + \mathbf{F}_p^n \mathbf{u}_p^n + \frac{1}{2} m_p^n \|\mathbf{u}_p\|^2\right) \tag{7.8}$$

where ΔV is the control volume at the location $\mathbf{x}$, N_p^V the number of particles contained in ΔV, and the superscript n identifies the n^{th} particle. The function $\Psi\left(\mathbf{x}_p^n\right)$ is an interpolation function depending on the mesh type.

7.3 Closing models

The spray dynamics and evaporation are modeled using the isolated droplet canonical problem. In the following sections, the source terms $\mathbf{F}_p$, $\dot{m}_p$ and Q_p are closed.

7.3.1 External forces $\mathbf{F}_p$

In this thesis, only the drag force from the surrounding gas flow and the effects of gravity are accounted for. The density of the liquid phase being substantially larger than the gaseous one ($\rho_l/\rho \propto O(3)$), the added mass term and the Basset force can be neglected (Apte et al. 2003). Also, buoyancy and lift forces are not considered. With these hypotheses, the external forces $\mathbf{F}_p$ applied on the particle p reads:

$$\mathbf{F}_p = \frac{m_p}{\tau_p}(\mathbf{u} - \mathbf{u}_p) + m_p\mathbf{g} \tag{7.9}$$

where $\mathbf{u}$ is the resolved gas velocity vector interpolated at the particle position $\mathbf{x}_p$ and $\mathbf{g}$ is the gravitational acceleration vector. The particle relaxation time τ_p is given by:

$$\tau_p = \frac{4}{3C_D\mathrm{Re}_p}\frac{\rho_l}{\rho}\frac{d_p^2}{\nu} \tag{7.10}$$

where C_D is the drag coefficient whose value depends on the flow regime described by the particle Reynolds number $\mathrm{Re}_p = d_p|\mathbf{u}_p - \mathbf{u}|/\nu$. The correlation proposed by Schiller and Nauman (1935) valid for the flow conditions encountered in aeronautical combustion chamber ($\mathrm{Re}_p \in [5; 800]$) is used:

$$C_D = \frac{24}{\mathrm{Re}_p}\left(1 + 0.15\mathrm{Re}_p^{0.687}\right) \tag{7.11}$$

It must be emphasized that the direct effect of sub-grid scale fluctuations of the flow properties on the particles motion is neglected. According to Apte et al. (2003) this hypothesis is valid only if the energy content of the sub-filter scale is low in comparison with the resolved scale energy and if the relaxation time of the particle is higher than the sub-grid scale fluctuations time scales.

7.3.2 Evaporation and heat exchange rate

A wide range of models of varying complexities have been proposed to describe the mass and heat transfer between the liquid and the gaseous phases (Spalding 1953; Yao et al. 2003; Sirignano 2010; Sazhin 2014). In this work, the Abramzon Sirignano model (Abramzon and Sirignano 1989) derived from the Spalding formulation (Spalding 1953) is used. This model is based on the reference problem of an isolated droplet depicted in Fig. 7.2.

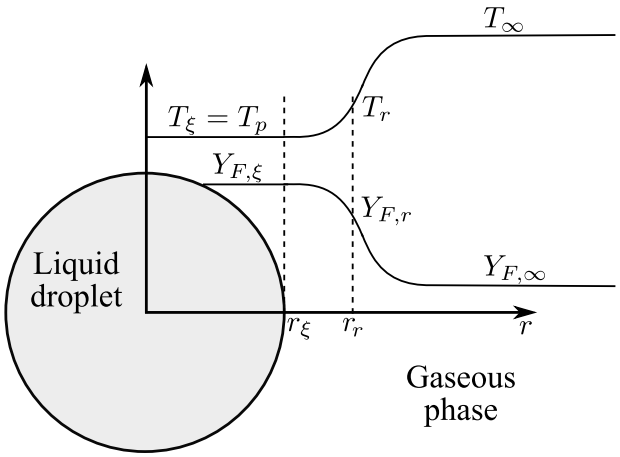

Figure 7.2: *Schematic of an isolated droplet evaporating in a gaseous flow environment at temperature $T = T_\infty$ and fuel mass fraction $Y_{F,\infty}$. Qualitative evolution of the temperature and the gaseous fuel mass fraction are illustrated.*

The Spalding and Abramzon Sirignano models, characterized as infinite liquid conduction models, rely on the following hypotheses:

- The thermal conductivity of the liquid λ_l is infinitely high, leading to uniform droplet temperature. The resolution of the droplet internal flow is then not required, thermal budget at the droplet's surface is sufficient.
- The liquid thermal diffusivity being lower than the gas one ($D_{th,l}/D < 1$), the thermal response of the gaseous phase is quasi steady.
- The liquid/gas interface is in a thermodynamic equilibrium state. The Clausius-Clapeyron law may therefore be used to compute the saturating fuel molar fraction at the droplet's surface $X_{F,\xi}$.
- The properties of the gas surrounding the droplet are constant from the droplet surface (ξ) to the far-field (∞). Hubbard et al. (1975) proposed to evaluate the surrounding gas properties at a reference point characterized by a temperature T_r and a composition $Y_{k,r}$ defined by:

$$T_r = \frac{2}{3}T_\xi + \frac{1}{3}T_\infty \tag{7.12}$$

$$Y_{k,r} = \frac{2}{3}Y_{k,\xi} + \frac{1}{3}Y_{k,\infty} \tag{7.13}$$

This is the so-called "two-third/one-third" rule.

The mass transfer and heat exchange between phases are evaluated by integrating the mass and energy conservation equations of the droplet system.

7.3.2.1 Mass transfer

The integration of the mass conservation equation describing the isolated droplet gives the following evaporation rate:

$$\dot{m}_p = -\pi d_p \left[\rho D_F\right]_r \mathrm{Sh} \ln\left(1 + B_M\right) \tag{7.14}$$

where B_M stands for the Spalding mass number and Sh is the Sherwood number characterizing the ratio of the total rate of mass transfer to the rate of diffusive mass transport. $[\rho D_F]_r$ is the product between the gas density and the diffusion coefficient of the fuel evaluated at the reference thermodynamic state r. This term is generally evaluated using the gas mixture viscosity and fuel Schmidt number:

$$\left[\rho D_F\right]_r = \frac{[\mu]_r}{\mathrm{Sc}_F} \tag{7.15}$$

Impact of the modeling of this quantity in the context of virtual and global chemistry is discussed in section 7.4.1.
In a quiescent atmosphere the Sherwood number Sh equals two. However, in most applications, the relative velocity between liquid and gas phase is non-zero. To account for the enhancement effect of convection on the evaporation process, the Ranz-Marshall correlation (Ranz and Marshall 1952) is commonly used:

$$\mathrm{Sh} = 2 + 0.55 \mathrm{Re}_p^{1/2} \mathrm{Sc}_F^{1/3} \tag{7.16}$$

The Spalding mass number B_M is defined as:

$$B_M = \frac{Y_{F,\xi} - Y_{F,\infty}}{1 - Y_{F,\xi}} \tag{7.17}$$

with the fuel mass fraction at the droplet interface $Y_{F,\xi}$ given by:

$$Y_{F,\xi} = \frac{X_{F,\xi} W_F}{W_\xi} = \frac{X_{F,\xi} W_F}{X_{F,\xi} W_F + \left(1 - X_{F,\xi}\right) W_{\neq F,\xi}} \tag{7.18}$$

where the subscript $\neq F$ refers to the mixture composed of all species except fuel. Considering that the surrounding gas properties are constant from the droplet's surface to the far field, the mean molecular weight $W_{\neq F,\xi}$ of the pseudo-mixture composed of all species except fuel reads:

$$W_{\neq F,\xi} = W_{\neq F,\infty} = \frac{\left(1 - Y_{F,\infty}\right) W_\infty}{1 - Y_{F,\infty} \dfrac{W_\infty}{W_F}} \tag{7.19}$$

The molar fraction of saturated fuel at the droplet interface $X_{F,\xi}$ is evaluated with the Clausius-Clapeyron law:

$$X_{F,\xi} = \frac{P_c}{P} \exp\left(\frac{W_F L_v\left(T_{cc}\right)}{R} \left(\frac{1}{T_{cc}} - \frac{1}{T_\xi}\right)\right) \tag{7.20}$$

where the subscript cc denotes a reference point on the saturation curve. L_v is the latent heat of vaporization defined as the enthalpy difference between the gas and the liquid state. The temperature T_ξ refers to the interface temperature equals to the droplet temperature T_p.

7.3.2.2 Heat transfer

The Lagrangian equation describing the droplet temperature evolution is obtained by integrating the energy conservation of the system represented in Fig. 7.2:

$$\frac{\mathrm{d}T_p}{\mathrm{d}t} = -\frac{1}{\tau_h}\left(T_p - \left(T_\infty - \frac{L_v\left(T_p\right)B_T}{\left[c_p\right]_r}\right)\right), \tag{7.21}$$

where τ_h is a characteristic heating time and B_T is the thermal Spalding number. The heating characteristic time τ_h is defined as:

$$\tau_h = \frac{\rho_l d_p^2}{6}\frac{\left[c_p\right]_r}{c_{p,l}}\frac{\ln\left(1+B_M\right)}{B_T}\frac{\left[\mu\right]_r}{\mathrm{Sc}_F}\mathrm{Sh} \tag{7.22}$$

This implies that the larger the droplet is the slower the heating process will be. The Spalding thermal number B_T is related to the Spalding mass transfer number B_M through the relation:

$$B_T = \left(1+B_M\right)^{\frac{\mathrm{PrSh}}{\mathrm{Sc}_F\mathrm{Nu}}} - 1 \tag{7.23}$$

with Nu the Nusselt number comparing the convective and conductive heat transfer. As the Sherwood number, its value is corrected with Ranz-Marshall correlation (Ranz and Marshall 1952) to account for the relative gas motion:

$$\mathrm{Nu} = 2 + 0.55\mathrm{Re}_p^{1/2}\mathrm{Pr}_F^{1/3} \tag{7.24}$$

7.3.2.3 Abramzon-Sirignano model

Abramzon and Sirignano (1989) extended the formalism previously introduced to better describe the convective effects due to the presence of a vapor film around the droplet. The finite thickness of the diffusive and thermal boundary layers is taken into account through the correction of the Sherwood and Nusselt numbers:

$$\mathrm{Sh}^* = 2 + \frac{\left(\mathrm{Sh}_0 - 2\right)}{F_M} \tag{7.25}$$

$$\mathrm{Nu}^* = 2 + \frac{\left(\mathrm{Nu}_0 - 2\right)}{F_T} \tag{7.26}$$

where Sh_0 and Nu_0 are the reference Sherwood and Nusselt numbers given by the Ranz-Marshall correlation described in equations (7.16) and (7.24). The

correction functions F_M and F_T were fitted from a vaporizing edge problem. The following correlations were proposed:

$$F_l = (1 + B_l)^{0.7} \frac{\ln(1 + B_l)}{B_l} \quad \text{for} \quad l = M, T \tag{7.27}$$

The thermal Spalding number B_T is also corrected to account for the finite thickness of the thermal boundary layer:

$$B_T = (1 + B_M)^{\beta} - 1 \tag{7.28}$$

with

$$\beta = \left[\frac{c_{p,F}}{c_p}\right]_r \frac{\mathrm{PrSh}^*}{\mathrm{Sc}_F \mathrm{Nu}^*} \tag{7.29}$$

Due to the interdependence between B_T and Nu^*, the heat transfer at the droplet's surface is evaluated through an iterative procedure.

7.4 Coupling virtual chemistry with evaporation model

As discussed by numerous authors, the evaporation rate $\dot{m}_p$ and heat exchange Q_p strongly depend on the thermodynamic and transport properties of the vapor film (Sanjosé 2009; Shashank and Pitsch 2011; Sierra 2012). In the context of virtual optimized chemistry, the thermodynamic properties of the virtual species are optimized so as to retrieve the mixture-averaged properties of the reference real mixture. However, in this thesis the transport properties of the virtual species are closed with simplified models that are not fitted to reproduce evaporation fluxes. The impact of this modeling assumption is discussed in the following.

7.4.1 Impact of simplified transport properties on evaporation fluxes

Global and virtual chemistry approaches, based on optimization of reaction rate parameters, use simplified models to describe the transport properties of the gaseous phase. As discussed in Chapter 1, with simplified transport models the transport properties of the gaseous flow are expressed as follows:

- The mixture viscosity μ is evaluated from a temperature dependent function (power or Sutherland law) whose parameters are fitted from complex calculations
- The thermal conductivity λ is computed from the viscosity, heat capacity and a constant Prandtl number : $\lambda = (\mu c_p)/\mathrm{Pr}$
- The molecular diffusion coefficients are computed considering unity Lewis numbers for all species leading to $D_k = \lambda/(c_p\rho) = \mu/(\rho\mathrm{Pr})$

Sanjosé (2009) and Sierra (2012) showed that these simplified transport models greatly impact the prediction of the evaporation mass and heat fluxes. Contrarily to small hydrocarbons such as methane, liquid fuels feature Lewis number that are well above unity, generally $\mathrm{Le}_F \approx 2-3$. When unity Lewis number are considered for liquid heavy hydrocarbons, the fuel vapor tends to diffuse too rapidly, and evaporation processes are subsequently accelerated.
To better account for the impact of complex transport properties on the evaporation rate, Sierra (2012) proposed to correct the original simplified transport model. While keeping constant the transport properties used for kinetic modeling, modified mixture viscosity as well as Prandtl and Schmidt numbers are introduced in the expression of the heat source Q_p and mass exchange term $\dot{m}_p$. The modified Prandtl and fuel Schmidt numbers, called Pr^{evap} and Sc_F^{evap}, are fitted from evaporation calculations using complex mixture-averaged transport properties (Hirschfelder et al. 1954). The mixture viscosity of the gas is evaluated from the mixture-averaged Wilke formula where the individual species viscosities μ_k^{evap} are closed with a temperature dependent power law fitted on a complex transport database:

$$\mu_k^{evap} = \mu_{ref,k} \left(\frac{T}{T_{ref,k}} \right)^{\beta_k} \tag{7.30}$$

To illustrate the effect of this new formulation, evaporation calculations performed with i) the simplified transport model, ii) the corrected simplified transport model and iii) complex mixture-averaged transport coefficients, are compared (Sierra 2012). Figure 7.3 (left) shows the temporal evolution of the droplet surface predicted by these three different transport models. The influence of the transport modeling strategies on the liquid temperature evolution is also displayed in Fig. 7.3 (right). Detailed information on the transport coefficients used for these simulations are presented in Table 7.1.

Transport Model	Pr^{evap}	Sc_F^{evap}	μ^{evap}
Mixture-averaged	Variable	Variable	Wilke formula
Simplified w/o correction	0.71	2.10	Power law
Simplified w/ correction	0.82	1.48	Wilke formula

Table 7.1: *Details about transport models used for evaporation calculation.*

The evaporation calculation performed with the simplified transport model shows important discrepancies with the reference mixture-averaged computation. The evaporation time predicted by the simplified model is 40 % lower than the one evaluated with complex binary transport coefficients. Also, the wet bulb temperature, corresponding to the equilibrium droplet temperature in

a gaseous environment, is strongly overestimated with the simplified transport formulation. The corrected version of the simplified transport model allows a very good agreement with complex transport calculations for both droplet surface and temperature evolutions.

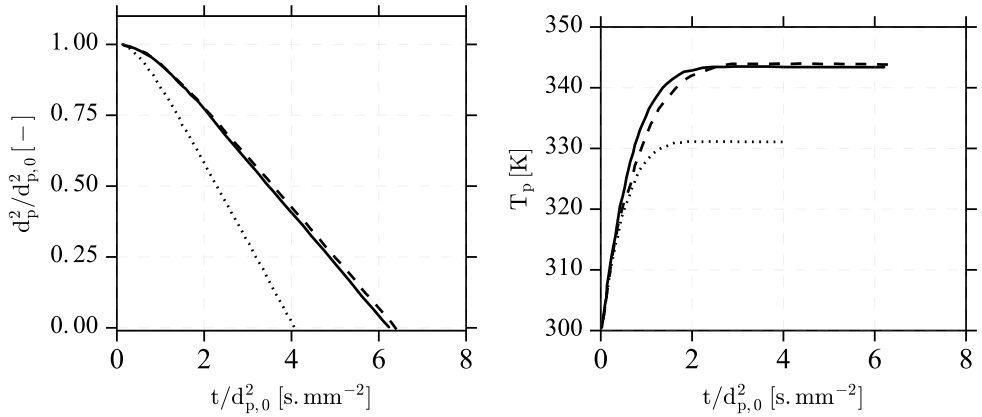

Figure 7.3: *Temporal evolution of the dimensionless droplet surface (left) and temperature (right). N-heptane evaporating droplet in a quiescent N_2 atmosphere at $T = 623\,K$. Numerical simulations performed with the Abramzon Sirignano formalism and with different transport models: Mixture-averaged (—), Simplified without correction (--), Simplified with correction (--). Reproduced from (Sierra 2012).*

7.4.2 Transport properties for virtual species

The previous section has shown that the effects of complex transport properties on evaporation fluxes can be described, at a low computational cost, by considering i) the local composition of the mixture for the evaluation of the mixture viscosity and ii) by using dedicated Prandtl and fuel Schmidt numbers. As far as virtual chemistry is concerned, the first modification related to viscosity evaluation through the Wilke formula is not applied. As mixture-averaged formulation of the viscosity requires the knowledge of each individual species viscosities, optimization of the viscosities of virtual products and intermediate species would be required. Optimization of virtual species transport properties has not been performed in this thesis and is left for future work. As a result, evaporation calculations involving a set of virtual species are performed with modified Prandtl and fuel Schmidt numbers, but viscosity is evaluated with a classical power law.

The effect of such models is assessed by studying an evaporating kerosene droplet in the cold conditions of the HERON configuration (T_3^{HERON}, P_3^{HERON}). Figure 7.4 shows the droplet surface and temperature temporal evolution obtained with the three transport closures described in Table 7.2.

Transport Model	Pr^{evap}	Sc_F^{evap}	μ^{evap}
Simplified w/o correction	0.69	0.69	Power law
Simplified w correction virtual	0.70	2.29	Power law
Simplified w/ correction	0.70	2.29	Wilke formula

Table 7.2: *Details about transport models used for evaporation calculation performed with virtual species.*

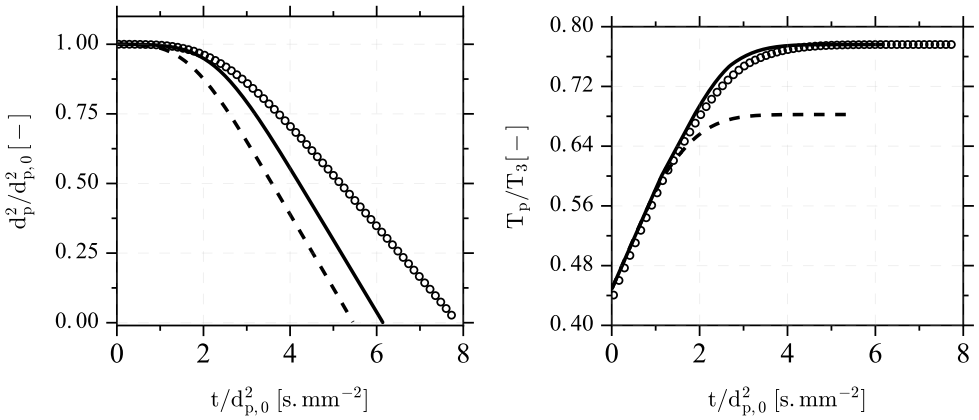

Figure 7.4: *Temporal evolution of the dimensionless droplet surface (left) and temperature (right). Kerosene evaporating droplet in a quiescent air atmosphere at* $T = T_3^{HERON}$ *. Numerical simulations performed with the Abramzon Sirignano formalism and with different transport models: Simplified without correction (--), Simplified with correction (∘), Simplified with correction virtual (—)*

As previously observed for the n-heptane evaporating droplet, the simplified model without correction underestimates the evaporation time and under-predicts the wet bulb temperature. The formulation adapted for virtual chemistry reproduces well the diameter reduction at the beginning of the evaporation process. However, as evaporation continues the slope of the curve predicted by the adapted model is overestimated leading to an underestimation of the evaporation time by 20 %. Concerning the droplet temperature, the wet bulb temperature is well captured by the model adapted for virtual chemistry.

As a conclusion, the correction of the Prandtl and Schmidt numbers allows to improve the description of the droplet temperature along the whole evaporation process, and slightly enhance the evaluation of the evaporation time. It means that, in the cold flow conditions of the Heron configuration, the liquid phase is expected to evaporate 20 % too rapidly when virtual optimized chemistry is used. The impact of this error will be evaluated by comparing the

characteristic evaporation time to the convective time in the injection system so as to identify if the evaporation process is complete before flame stabilization.

Chapter 8

LES of a Two-Phase Industrial Injector

Contents

The objective of this chapter is to test the virtual chemistry approach on an industrial two-phase injector. The high pressure HERON (High prEssuRe facility for aerO-eNgines) test bench, experimented at CORIA laboratory is selected. This two-phase burner equipped with a Lean-Premixed aero-engine injection system, and operated at high pressure and temperature is a challenging test case for virtual chemistry. The virtual optimized mechanism designed to capture the flame/flow field interaction in gaseous kerosene/air flames is combined with the Dynamic Thickened Flame model for LES (DTFLES) and the so-called efficiency function. A particular attention is given to the capabilities of this modeling strategy to predict the flame shape and stabilization.

8.1 Objectives

Spray flames encountered in aeronautical combustion chambers feature highly complex structures resulting from tight interactions between fuel atomization, spray evaporation, turbulent flow motions and combustion kinetics effects (Hollmann and Gutheil 1996; Reveillon and Vervisch 2005; Luo et al. 2011). Even if liquid break-up is complete, spray dispersion and evaporation may strongly affect the mixture homogeneity leading to partially-premixed combustion mode where both premixed and non-premixed regimes are encountered. In these conditions, the fine description of flame stabilization and pollutant formation requests a reliable representation of complex chemistry processes (Franzelli et al. 2017).

Virtual optimized chemistry approach has already been challenged on gaseous laminar flames (Chapter 4) and gaseous turbulent flame configurations (Chapter 6). The objective of the current Chapter is to test the virtual kinetic models on a representative two-phase burner. A Lean-Premixed (LP) aero-engine injection system designed by the French engine manufacturer Safran Helicopter Engines is considered in this work. This low-NO_x injector was experimentally investigated at CORIA laboratory on a mono-sector high pressure combustion chamber called HERON (High prEssuRe facility for aerO-eNgines). Laser-based experimental diagnostics specifically developed for elevated pressure conditions (Salaün et al. 2016; Malbois et al. 2017a) were used to study the flame structure and pollutant formation on a wide range of relevant aero-engines operating conditions. Measurement campaigns performed on this configuration allowed to build an extensive and high-quality experimental database essential to i) gain a better understanding on the flame structure and to ii) validate two-phase turbulent combustion models.

Malbois et al. (2017b) recently published an analysis of the impact of Fuel Air Ratio (FAR), pre-heated air temperature and initial pressure on the flame shape and pollutant emissions. Interestingly, it was shown that depending on the operating pressure and FAR, two types of flames can be stabilized. As shown in Fig. 8.1, depicting OH concentration images, in nearly all cases a straight and confined tulip-shape flame is observed. For low pressures a transition from tulip-shape to V-shape flame occurs near Lean Blow-out (LBO) conditions. As regards with exhaust pollutant emissions, in accordance with the literature it was found that NO_x concentration increases with the FAR and operating pressure while opposite trend was observed for CO.

Large-Eddy-Simulation of the LP injector was conducted by Domingo Alvarez (2019) using a premixed-based tabulated chemistry strategy (FPI) coupled with a Presumed-Conditional Moments (PCM) approach to model turbulent chemistry interactions. In this work, two droplet size distributions were tested to study the impact of the spray distribution on the flame shape and stabilization. It appeared that the flame shape and stabilization processes are strongly affected by droplet size distribution. With the polydisperse spray characterized

by a small mean droplet diameter of $D_{32} \approx 12\,\mu$m a confined V-shape flame is obtained, while a M-shape flame is observed when larger droplets are injected ($D_{32} \approx 32\,\mu$m) (Domingo Alvarez et al. 2018).

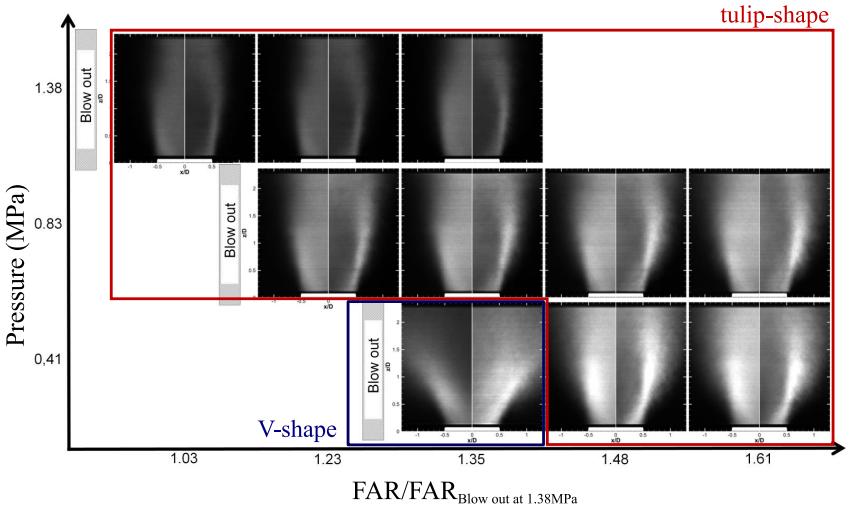

Figure 8.1: *Mean and standard deviation of OH-PLIF images for various initial pressure and fresh gases Fuel/Air ratio. Reproduced from (Malbois et al. 2017b)*

In this Chapter, the virtual optimized kinetic scheme dedicated to kerosene/air combustion description (Chapter 4) is coupled with the TFLES model (Chapter 5) and two-phase flow models (Chapter 7) to be tested on the HERON test bench. Details on the experimental and numerical set-up are provided in sections 8.2 and 8.3 respectively. Eventually, numerical results obtained with the virtual optimized chemistry approach are analyzed and compared against experimental measurements in Section 8.4.

8.2 Experimental set-up

8.2.1 The HERON test bench

A global view of the HERON combustion chamber, experimented at CORIA laboratory, is presented in Fig. 8.2. The facility is composed by four main parts, namely: a plenum, a LP injection system, a squared section combustion chamber and a sonic throttle. The swirled injection system is fed with liquid kerosene (Jet A1) through the fuel supply line enclosed in a water-cooled cylinder. Pre-heated air is provided in the plenum through a large diameter air-intake. A fixed 41 % of the total air mass flow rate passes through the four thin lateral films mounted between the plenum and the combustion chamber. The fresh air layers formed along the walls of the combustor allow the protection of the optical access used for flame visualization. The remaining 59 %

of the supplied air flows through the LP injection system and mixes with the fuel. Combustion process is initiated on the pre-vaporizer duct and is pursued in the combustion chamber. Hot gases issued from the combustion process are accelerated through a convergent. The exit of the combustion chamber is equipped with a supersonic nozzle whose section can be partially obstructed by a needle to control the pressure inside the combustion chamber. Before the sonic throttle, air at atmospheric condition is injected through eight tubes to both protect the nozzle from mechanic deformations and to quench the burnt gases.

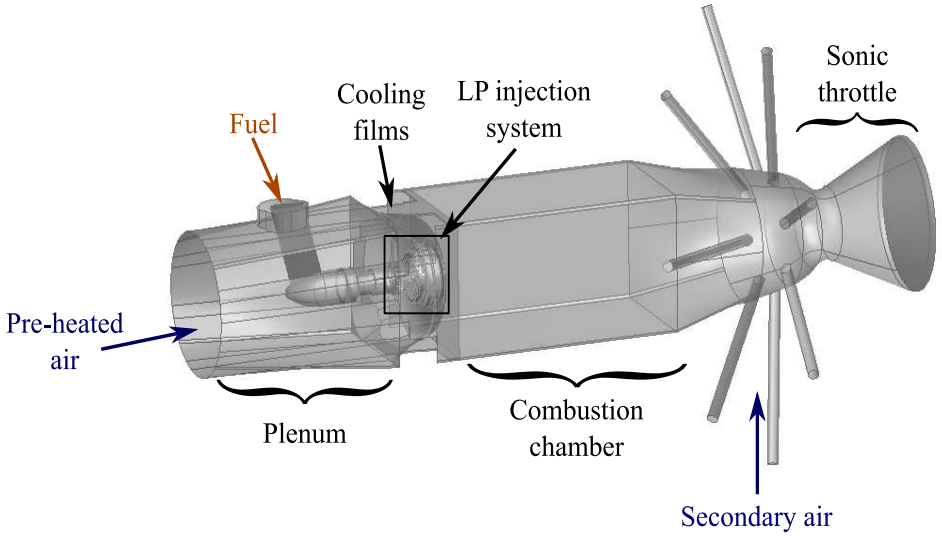

Figure 8.2: *Sketch of the HERON combustion chamber.*

Experimentally, a wide range of operating conditions have been analyzed in terms of operating pressure, Fuel Air Ratio (FAR) and preheated air temperature. In this work, Large Eddy Simulations are performed for one unique operating point. Characteristics of the simulated operating point are provided in Table 8.1.

	Pressure [MPa]	FAR / $\text{FAR}_{BO}^{P=1.38\,MPa}$ [−]	Mass flow rates [g.s^{-1}]	Temperature [K]
Main air stream	0.83	1.35	108.0	[500, 670]
Secondary air stream			20.0	≈ 300
Liquid fuel			[0, 10]	≈ 300

Table 8.1: *Characteristics of the simulated operating point. For confidentiality reasons, exact operating conditions are not disclosed.*

8.2.2 The Lean-Premixed injection system

A 2-D schematic of the LP injection system geometry provided by Safran Helicopter Engine is presented in Fig. 8.3. The device is composed by two swirled stages:

- A first radial swirler redirects the pre-heated air flowing from the plenum through a converging axial canal. Because of the inclined position of the guide vanes the air exiting from the radial swirler features a swirling motion.
- Further downstream, a second axial swirler discharges swirled air in the pre-vaporizer duct.

Fuel is injected in the pre-vaporizer duct through 9 small holes, of diameter d_j, located at the tip of the conical injector. The high velocity swirling air-stream coming from the two swirlers imposes high aerodynamic forces on the surface of the slow-moving fuel leading to efficient atomization of the liquid core.

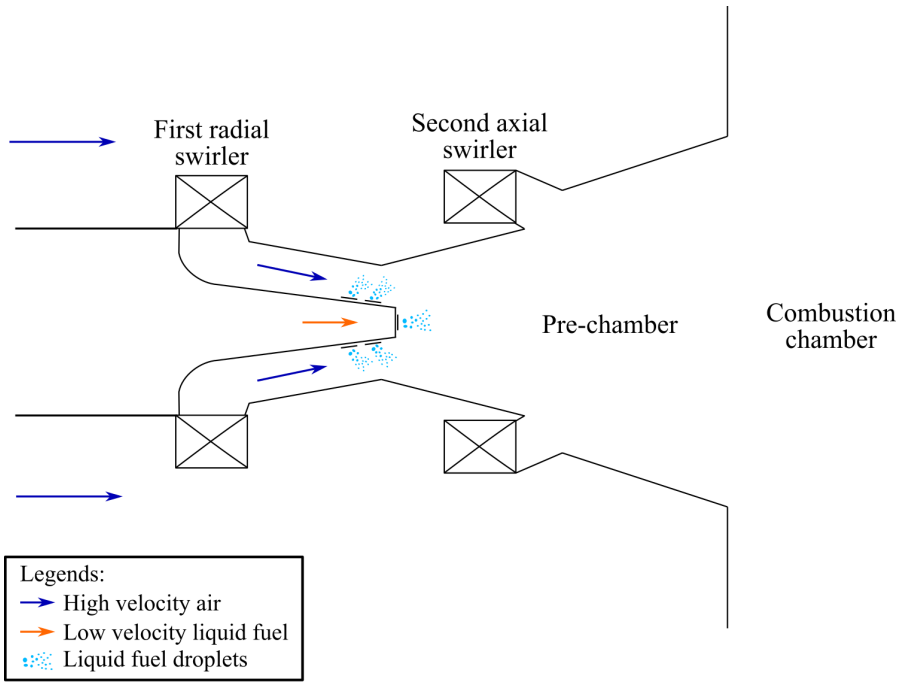

Figure 8.3: *2-D cut view of the LP injection system geometry*

8.2.3 Experimental measurements

Advanced and innovative laser-based experimental diagnostics were developed at CORIA laboratory to analyze and understand the combustion dynamics in the HERON test rig (Malbois et al. 2017a; Malbois et al. 2017b). Planar Laser-Induced-Fluorescence (PLIF) measurements of OH gradients is used to visualize

the flame front location and structure, while the distribution of kerosene vapor is accessed through kerosene-PLIF measurements. Simultaneous measurements of OH and kerosene fluorescence have also been performed to correlate the instantaneous position of the reactive layer and the distribution of equivalence ratio. In combination with these two diagnostics, CH^* chemiluminescence is measured to identify the reaction zone position and flame length. Instantaneous 2-D distribution of Nitrogen Oxides concentration are also available. In terms of flow dynamics, velocity was characterized through Particle Image Velocimetry (PIV) measurements. Finally, global information on the composition of the quenched combustion products (NO, CO, CO_2, O_2 and HC) at the exit of the combustion chamber are evaluated using exhaust gas analyzers.

Complementary measurements were performed in the context of the TLC (Towards Lean Combustion) project at DLR. The objective of this measurement campaign was to characterize the atomization, evaporation and fuel/air mixing processes in the injection system. Particularly, droplets sizes distribution and liquid phase velocity were measured via Phase-Doppler Anemometry (PDA). Unfortunately, these essential quantities were acquired at different operating conditions and in a different combustor rig (Koopman et al. 2005). Therefore, these results cannot be used directly as boundary conditions for numerical simulations.

8.3 Numerical set-up

Large Eddy Simulations of the HERON test-bench were performed with the compressible, massively-parallel solver AVBP (Schönfeld and Rudgyard 1999). Temporal integration of convective terms is explicitly performed with the Finite Element Two-step Taylor-Galerkin Colin (TTGC) scheme (Colin and Rudgyard 2000). Diffusion terms are integrated using a second order Finite Element 2-Δ scheme. The sub-grid stress tensor is closed using a Boussinesq assumption, with the turbulent viscosity given by the sigma model (Nicoud et al. 2011).

8.3.1 Computational domain, boundary conditions and mesh

The computational domain illustrated in Fig. 8.4 is derived from the real test rig geometry depicted in Fig. 8.2. Two main geometric simplifications were however performed to alleviate numerical difficulties and reduce the number of computational grid points:

- **Film cooling removal:** The prediction of the correct mass flow repartition between the injection system and the cooling films is of paramount importance to reproduce the targeted global fuel/air ratio FAR_{global}. Unfortunately, numerical resolution of the flow in the thin lateral films (about 1 mm thickness) imposes both high mesh resolution and numeri-

cal challenges associated with corner walls treatment. For the operating point investigated, experimental measurements show that the flame is straight and confined. The effects of cooling films on flame stabilization are then assumed negligible. To ensure a correct repartition of mass flow rates and reduce the computational efforts, films are not simulated but are modeled by an inlet film boundary condition. Contrarily to classical inlet boundary condition, fluxes are not imposed on the nodes but on faces.

- **Secondary air tubes reduction** The secondary air tubes mounted upstream of the sonic throttle are truncated to reduce the number of computational cells. Established turbulent flow with an arbitrary power law profile is assumed at the inlet of the eight pipes.

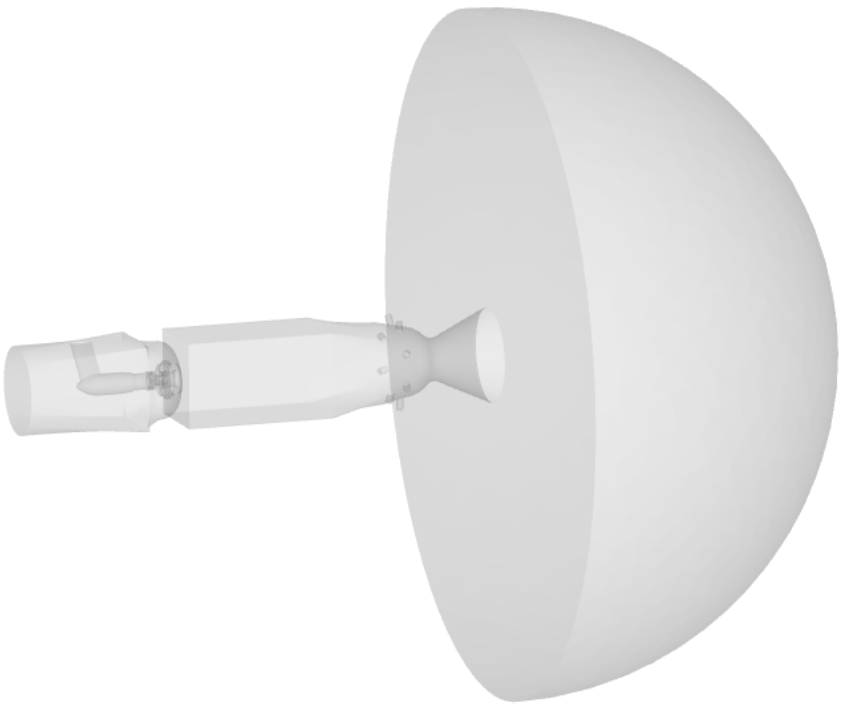

Figure 8.4: *HERON computational domain.*

Inlet and outlet boundary conditions are prescribed using the non-reflective Navier-Stokes Characteristic Boundary Conditions (NSCBC) approach to ensure a proper treatment of acoustic waves. Moreover, to limit the interaction between the outlet of the convergent and the combustion chamber, the computational domain has been extended far downstream in the axial direction. All burner walls are modeled with adiabatic and non-slipping boundary conditions.

The computational domain is discretized with 65.2 M tetrahedral elements and 11.4 M nodes. Figure 8.5 presents a view of the grid size distribution in the region of interest. A characteristic grid size of $\Delta_x^0 = 0.2\,\text{mm}$ is used in the swirlers, in the pre-vaporizer duct, and at the exit of the cooling films. The mesh is then coarsened in the axial and radial direction. A typical cell size of $\Delta_x = 2\Delta_x^0$ is obtained at 40 mm of the pre-chamber exit plane.

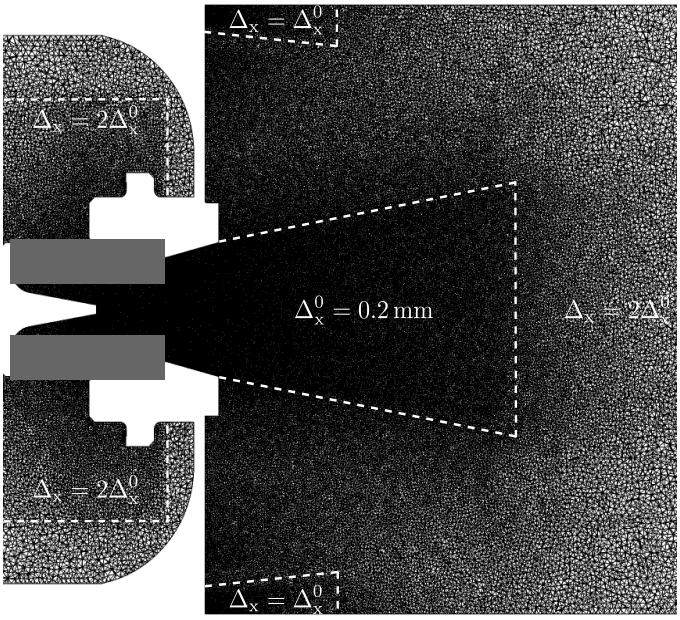

Figure 8.5: *Representation of the mesh and repartition of the points on the combustion chamber middle plane.*

8.3.2 Spray modeling

8.3.2.1 Liquid fuel injection modeling

As previously discussed in Chapter 7 the coupled simulation of fuel atomization, liquid spray evaporation and combustion imposes prohibitive computational costs and important numerical difficulties. Reactive two-phase flow calculations do not resolve break-up processes but directly inject a liquid spray with presumed granulometry and velocity profile. Major difficulties are then associated with the choice of the fuel droplets size and velocity.
Figure 8.6 presents simplified views of two possible scenarios regarding liquid spray behavior in the studied atomizer. In the first possible situation, the fuel droplets issued from the eight side holes do not interact with the walls and are simply transported in the pre-chamber (Fig. 8.6.a). The second scenario, depicted in Fig. 8.6.b, assumes that the fog of droplets hits the atomizer wall and feed a liquid film formed along the solid walls. At the tip of the injector walls,

the accumulated liquid fuel is disintegrated into ligaments and fine droplets under the effects of high shearing forces. As the spray injection models associated with each configuration are very different it is important to discriminate between the two situations. To evaluate the probability that the liquid jet interact with the injector walls, correlations issued from experimental studies of kerosene jet in cross flow configurations (Becker and Hassa 2002; Ragucci et al. 2007; Freitag and Hassa 2008) are used. These different studies provide analytic expressions of the liquid jet penetration and jet breakdown point location as a function of nozzle geometry dimensions and two dimensionless aerodynamic parameters: the aerodynamic Weber number We_{aero} and the momentum flux ratio q. Unfortunately, for the present configuration and operating point the small momentum flux ratio ($q \approx 0.3$) does not match the validity domain of published experimental correlations.

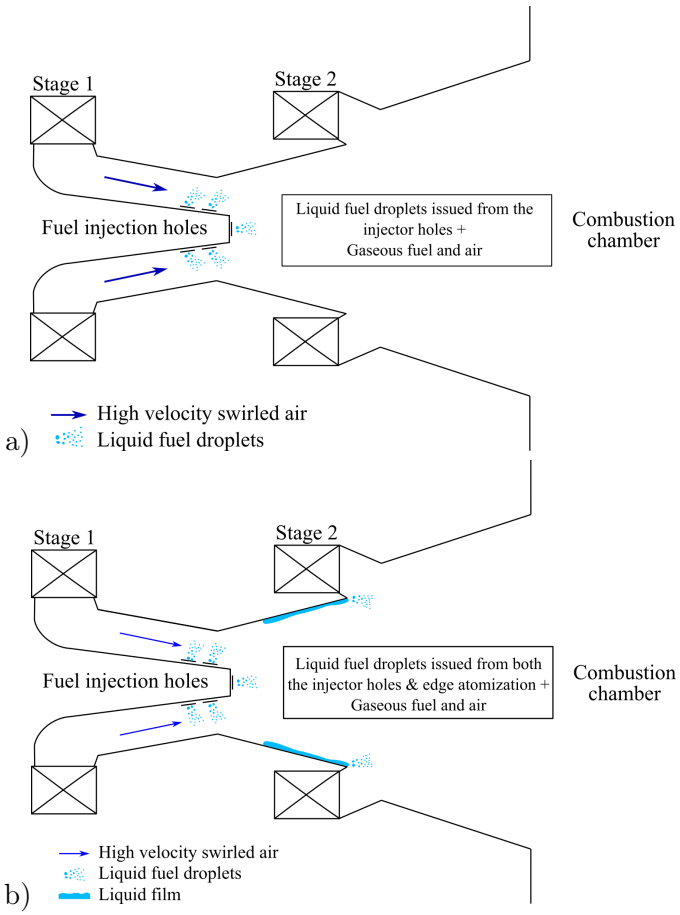

Figure 8.6: *Schematic of two possible scenarios regarding liquid spray behavior. A first possible situation assumes no interaction between the fuel droplets and atomizer walls (top). While in a second potential scenario, the cloud of droplets form a liquid film along the wall injector that is further atomized at the edge (bottom).*

Considering the highly uncertain spray behavior a simple spray injection model based on Safran Helicopter Engine design practice is considered. In this work, the spray droplet size distribution is assumed to follow a Weitbull probability distribution. This probability function, proposed by Yoon et al. (2004), parametrizes the liquid droplet diameter distribution by two moments of the spray statistics, namely the Sauter-mean diameter D_{32} and a spread coefficient γ:

$$f(D) = \frac{\gamma D^{\gamma-1}}{X^{\gamma}} \exp\left(-\left(\frac{D}{X}\right)^{\gamma}\right) \tag{8.1}$$

where X is a characteristic droplet size linked with the Sauter-mean diameter through the following relation:

$$D_{32} = \frac{X\Gamma\left(\frac{3}{\gamma}+1\right)}{\Gamma\left(\frac{2}{\gamma}+1\right)} \tag{8.2}$$

As no experimental measurements are provided to evaluate these parameters, estimates based on experimental correlations are used. In view of the atomizer geometry and main flow field features, the LP injector can be compared to an airblast atomizer. With this assumption, the Sauter-mean diameter is evaluated with the Lefebvre and Rizk equation for the mean drop size (Lefebvre 1989):

$$D_{32} = D_{32}^{\sigma} + D_{32}^{\mu} \tag{8.3}$$

$$D_{32} = C_1 d_j \left[\frac{\sigma}{\rho U_r^2 d_j}(1+FAR)\right]^{0.4} + C_2 d_j \left(\frac{\mu_l^2}{\sigma \rho_l d_j}\right)^{0.5}(1+FAR) \tag{8.4}$$

where σ is the surface tension and U_r is the relative velocity between the gaseous and liquid phase. The constant parameters C_1 and C_2 are respectively equal to 0.48 and 0.15. The second parameter γ, characterizing the dispersion of the diameter distribution, is deduced from PDA measurements performed at higher pressures in the context of the TLC project (Koopman et al. 2005). As the shape of the diameter distribution is assumed unchanged when varying the operating conditions and geometry of the combustor, the spread parameter γ equal to 3.1 determined experimentally is used in this study.

Droplets are injected with the same constant velocity evaluated from the fuel mass flow rate. As regards with spray/solid wall interactions a classic elastic rebound model is used.

8.3.3 Turbulent combustion modeling

The under-resolution of chemical reaction rates on the LES grid is accounted for the TFLES model. The species flame sensors introduced in Chapter 5 are used

to evaluate the global flame sensor and thickening factor. Impact of the sub-grid flame wrinkling on the resolved flame surface is modeled with the efficiency function proposed by (Charlette et al. 2002a) with a constant β parameter set to 0.5.
In this complex flow environment, a strong stratification of the reactive mixture is likely to be encountered. The flame parameters characterizing the thickening factor and efficiency function are therefore expressed as a function of the local mixture composition:

$$S_k = f\Big(\delta_{r,k}\left(\phi\right)\Big) \quad \text{for} \quad k \in [1, N_s] \tag{8.5}$$

$$F_k = f\Big(\delta_{r,k}\left(\phi\right), \max\left(\dot{\omega}_k\right)\left(\phi\right)\Big) \quad \text{for} \quad k \in [1, N_s] \tag{8.6}$$

$$\Xi = f\Big(\delta_L\left(\phi\right), S_L\left(\phi\right)\Big) \tag{8.7}$$

In practice, the parameters dependent on the equivalence ratio are evaluated from 1-D laminar premixed flames calculations and are tabulated as a function of the nitrogen mass fraction, that may be seen as a passive scalar.
Estimate of the global thickening factor variation with the equivalence ratio is provided in Fig. 8.7. To allow the resolution of the kerosene source term, on at least three points, on a grid of characteristic cell size of $\Delta_x = 0.2$ mm, thickening factors varying from 6 to 32 are required.

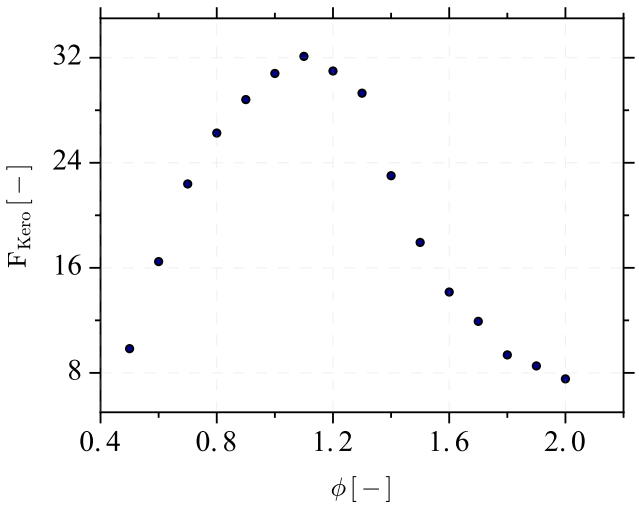

Figure 8.7: *Evolution of the kerosene thickening factor F_{kero} with the equivalence ratio for a grid size of $\Delta_x = 0.2\,\text{mm}$.*

8.4 Results analysis

In a first part, the LES results obtained with the numerical set-up presented in section 8.3 are analyzed. A special attention is given to the flow structure, the

spray behavior and the flame structure. Numerical results are then compared to experimental data to evaluate the capabilities of the numerical strategy to predict the flame shape and stabilization.

8.4.1 Flow, spray and flame topology

Aerodynamic fields, spray characteristics and flame topology and structure are first investigated.

8.4.1.1 Aerodynamic fields

Figure 8.8 illustrates the mean resolved velocity fields extracted on the combustion chamber center plane.

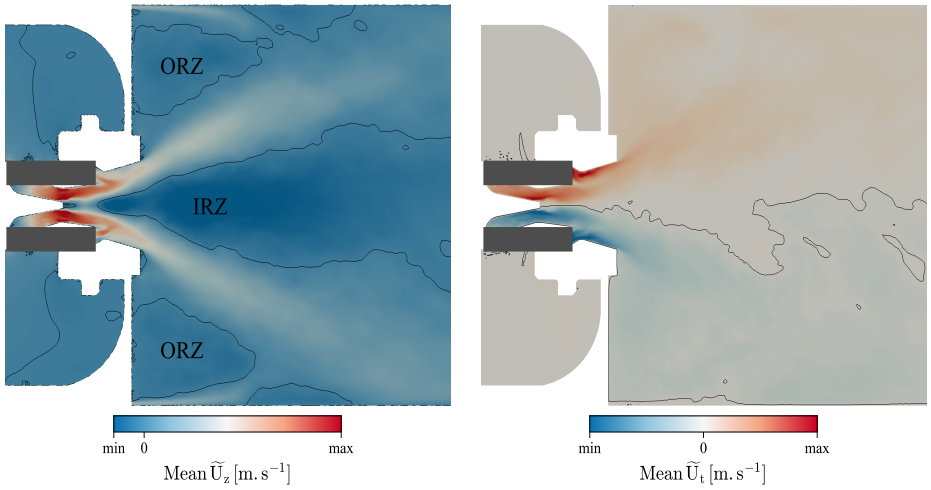

(a) Mean axial velocity field (b) Mean tangential velocity field

Figure 8.8: *Mean fields of resolved axial and tangential velocity components. The black lines identify the zero axial (left) and tangential (right) velocity iso-surfaces.*

Typical characteristics of a swirled flow are identified from both axial and tangential velocity fields:

- The rapid change of tangential velocity sign observed near the combustion chamber centerline suggests the rotating motion of the flow.
- Due to the intense swirling flow motion one may observe an Inner-Recirculation Zone (IRZ) on the injection system centerline. The IRZ is characterized by negative axial velocities and is surrounded by a conically shaped-jet featuring high axial velocity.
- On the whole circumference of the high velocity jet, near the combustion chamber walls, small Outer-Recirculation Zones (ORZ) are noticed. These negative axial velocity regions are surrounded by moderate velocity jets issued from the film cooling systems.

8.4.1.2 Spray dynamics and evaporation

To illustrate the liquid spray behavior instantaneous views of the complete set of Lagrangian particles colored by their radius and temperature are shown in Fig. 8.9.

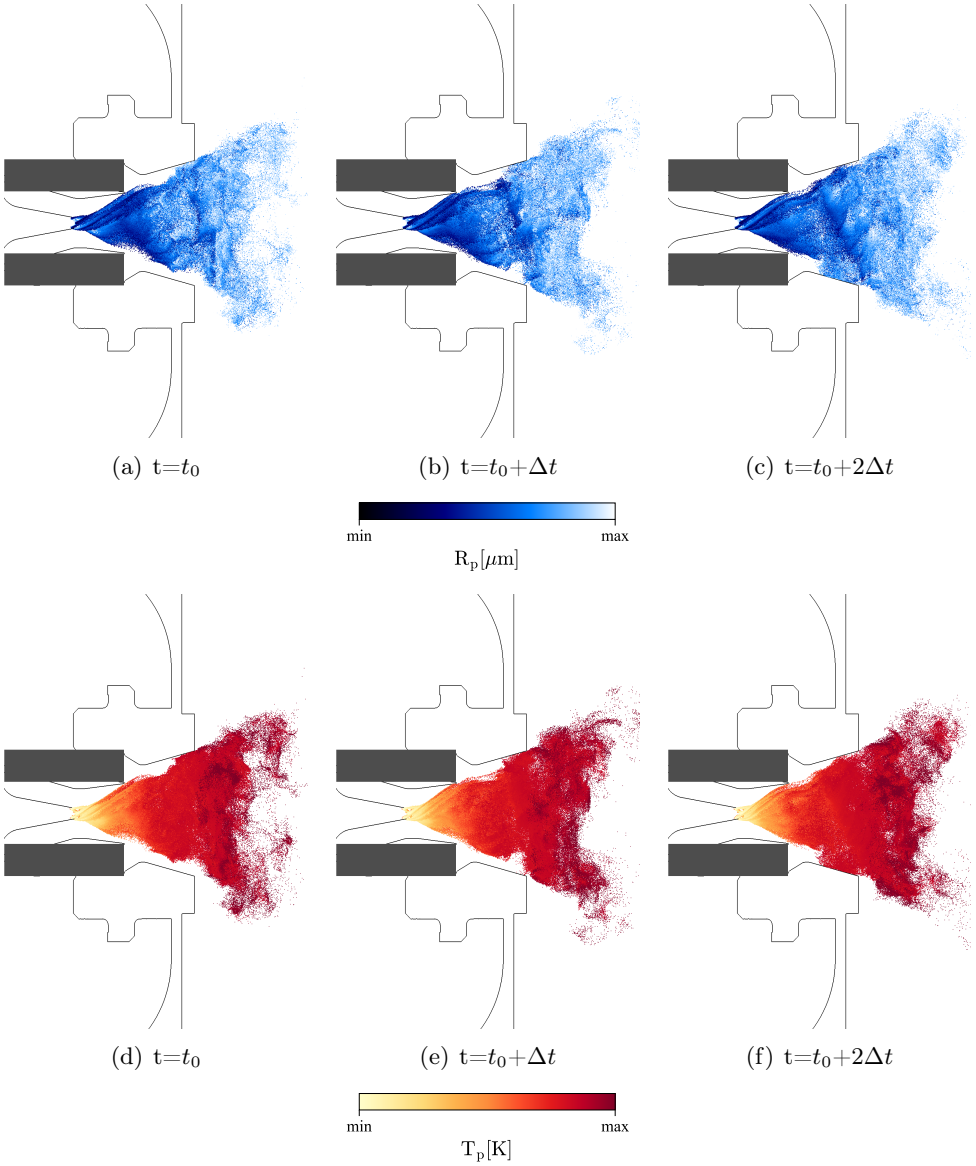

Figure 8.9: *Instantaneous view of the particles colored by their radius (top) and temperature (bottom) at equidistant times* $\Delta t = 0.1$ ms.

The cold and large droplets issuing from the injection system holes are progressively heated up by the hot gaseous mixture and rapidly evaporate leading to their size reduction. As regards with spray dynamics, Fig. 8.9 suggests a

swirling motion of the cloud of droplets due to an important coupling between the spray and the gaseous flow motions. The particles feature small Stokes numbers ($St_p \approx 0.1$) with respect to the convective[1] and the swirling[2] times of the LP system, and therefore rapidly reach an equilibrium state with the gaseous phase. As a result of the coupling between the disperse and carrier phases, the spray strongly interacts with the injection system walls. Periodically, the liquid droplets hit the pre-chamber duct walls and the splitting wall between the first and second swirler. As a simple rebound type boundary condition is used to model the interaction between the spray and the combustion chamber walls, splashing, filming or sticking phenomena are not accounted for.

Figure 8.10 presents three instantaneous fields of resolved mixture fraction.

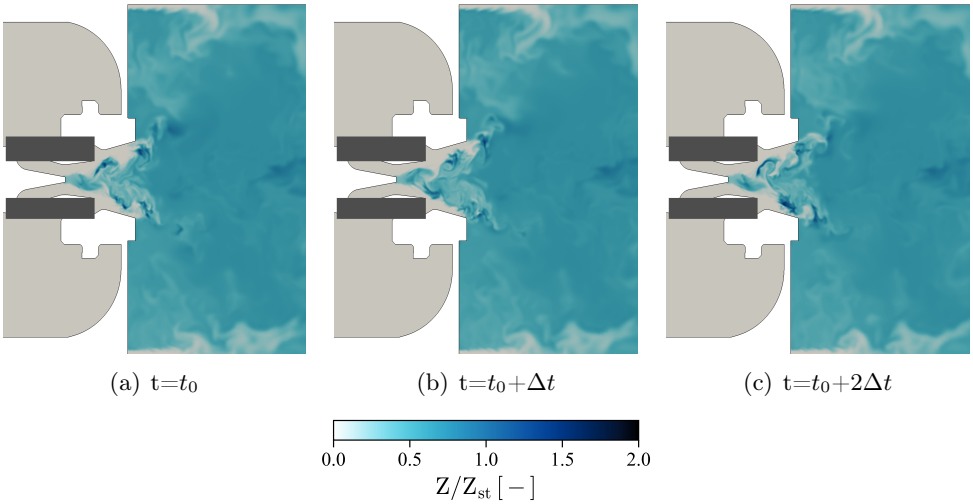

Figure 8.10: *Instantaneous fields of resolved mixture fraction at equidistant times* $\Delta t = 80\,\mu s$.

In the pre-vaporizer duct, the liquid spray evaporates and creates a stratified gaseous kerosene-air mixture. The mixture fraction fields present a characteristic pattern with high concentration fuel regions preferentially located along an helical shape whose position temporally alternates. This typical behavior is due to the interaction between the liquid spray and an hydrodynamics instability called Precessing Vortex Core (PVC) (Syred 2006). This instability, revealed in Fig. 8.11 with low pressure iso-surface (red), imposes its helicoidal motion to the liquid spray and consequently to the evaporated fuel. This is particularly visible in Fig. 8.11 depicting the iso-surface of lean kerosene mass fraction (blue). It may be also noted that the hydrodynamic instability and

[1] $\tau^c = L/U_z$ with L the pre-chamber length and U$_z$ the characteristic axial gaseous velocity
[2] $\tau^s = 2\pi/\omega$ with ω the characteristic orthoradial gaseous velocity

the resulting preferential helicoidal evaporation are phase-shifted because of the drag relaxation and evaporation time of the liquid droplets.

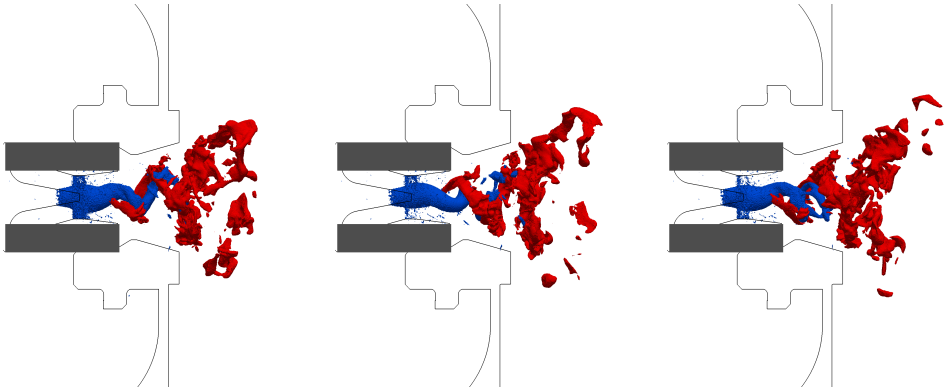

(a) t=t_0 (b) t=t_0+Δt (c) t=t_0+2Δt

Figure 8.11: *Instantaneous iso-surfaces of low pressure (blue) and lean fuel mass fraction (red) at equidistant times* $\Delta t = 80\,\mu$s.

The PVC and its interaction with the spray are analyzed in Fig. 8.12 showing the pressure and kerosene mass fraction signals as well as the associated Power Spectral Density (PSD). The spectral analysis of the pressure signal correlated to the pressure iso-surface temporal evolution allows to identify the characteristic frequency of the PVC f_{PVC} to 6.5 kHz. The PSD of the kerosene mass fraction signal also shows a predominant peak at 6.5 kHz demonstrating the strong interaction between the PVC and the liquid phase. The first modes identified in the PSD of the pressure signal are suspected to be acoustic modes. Rough estimates of the first longitudinal and transverse modes frequencies may be given by $f^L_{1/4} = c/(4L)$ and $f^T_{1/2} = c/(2l)$, where c is the sound of speed, while L and l are the longitudinal and transverse characteristic lengths of the combustion chamber. With $f^L_{1/4} \approx 800$ Hz and $f^T_{1/2} \approx 4800$ Hz the first two peaks may be attributed to half ($f^L_{1/2} \approx 1600$ Hz) and three quarter ($f^L_{3/4} \approx 2400$ Hz) wave longitudinal modes, while the third mode could be related to the half wave transverse mode. The last peak of low Power Spectral Density at $f = 13.5$ kHz $\approx 2f_{PVC}$ is presumed to be associated with the intermittent presence of a double PVC structure (Syred 2006). This specific instability characterized by two PVC branches is illustrated in Fig. 8.13.

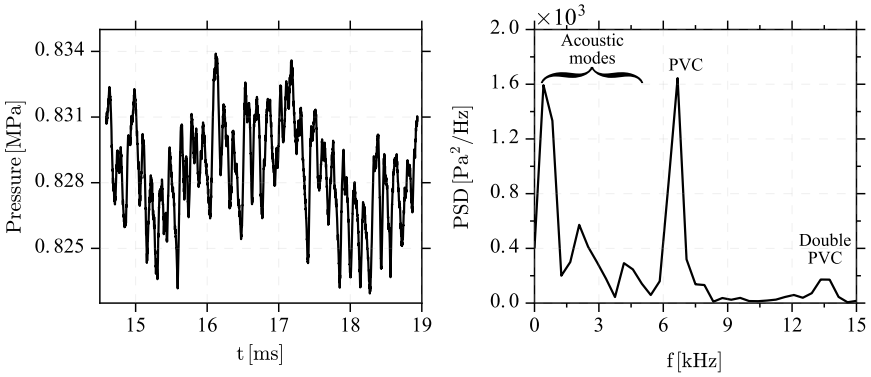

(a) Pressure signal

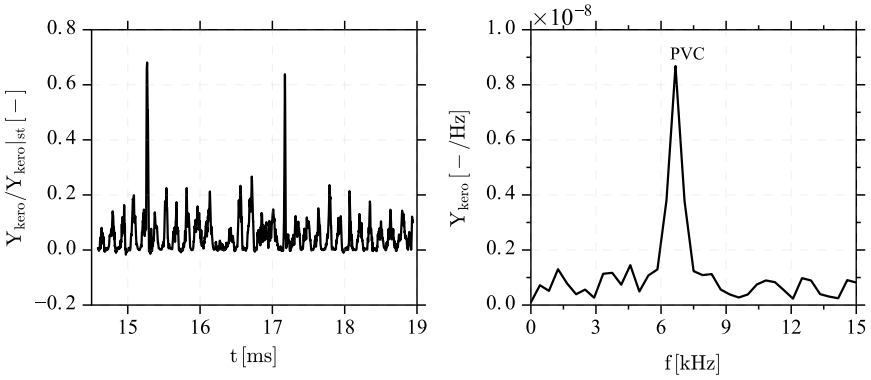

(b) Kerosene mass fraction signal

Figure 8.12: *Pressure and kerosene mass fraction signals measured in the pre-vaporizer chamber and associated PSD. The pressure signal is measured by a probe located at $x^* = 0.21$ while the kerosene probe is located at $x^* = 0.33$. Normalized coordinates $x^* = x/L$ are used, where x denotes the distance to the injector exit and L stands for an arbitrary length.*

Figure 8.13: *Instantaneous iso-surface of low pressure identifying a double PVC.*

8.4.1.3 Flame shape and structure

Flame shape and stabilization

The flame stabilization and shape are presented in Figs. 8.14 and 8.15 showing the instantaneous and mean fields of temperature and heat release rate. These figures suggest that the flame stabilizes in the combustion chamber, far from the injection system. The flame features the typical characteristics of an M-shape flame with a large opening angle and two reaction regions. On the combustion chamber axis a first inner flame front stabilizes along the inner recirculation zone. Hot gases issued from the the inner reactive region are transported by the reverse flow towards the injection system ensuring flame stabilization. On the exit plane of the pre-vaporizer chamber a second outer reaction zone attached to the walls consumes the fresh kerosene/air mixture formed in the outer region of the pre-chamber.

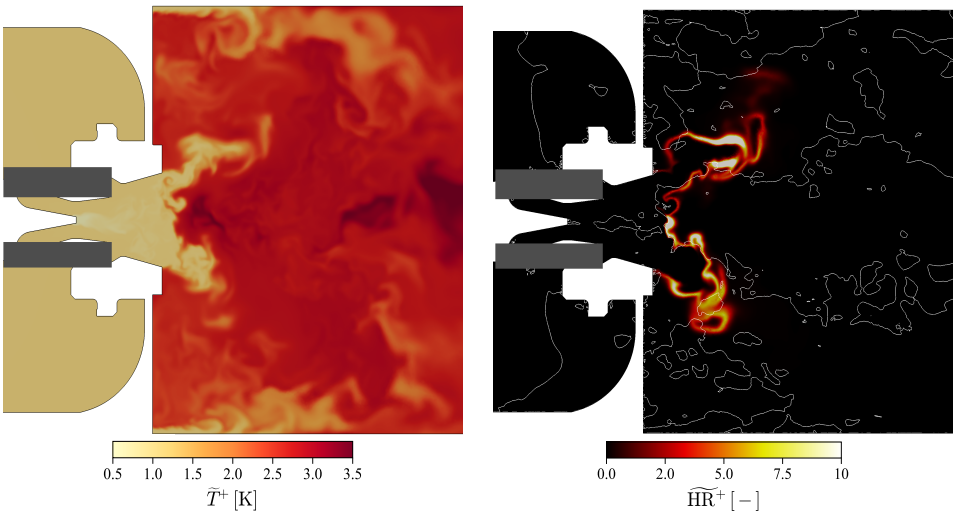

(a) Instantaneous temperature field (b) Instantaneous heat release rate field

Figure 8.14: *Instantaneous fields of resolved temperature and heat release rate. The white line in Fig. 8.14.b identifies the zero axial velocity.*

The dimensionless field of temperature presented in Fig. 8.14.a demonstrates that the gaseous temperature is affected by evaporation processes occurring near the tip nozzle. As the cold liquid fuel droplets evaporate in the pre-heated environment an important part of the gaseous sensible energy is used to heat-up droplets leading to carrier phase temperature reduction of about 200 K.
Figure 8.14.b, depicting the instantaneous field of heat release rate, shows variations of the chemical activity along the flame front. This observation may be accounted for by the important mixture stratification discussed in sub-section 8.4.1.2. Also, the mean field of heat release shows intense chemical activity in

the two external reacting branches, while low values of reaction rates are observed on the combustor axis. These behavior suggest that the outer reaction zone is anchored to the combustion chamber walls where the fresh gases meet the ORZ burnt gases. On the contrary on the combustion chamber center, the thin flame front position fluctuates importantly leading to lower mean heat release rate. Detailed discussions on this topic are provided in sub-section 8.4.2.2.

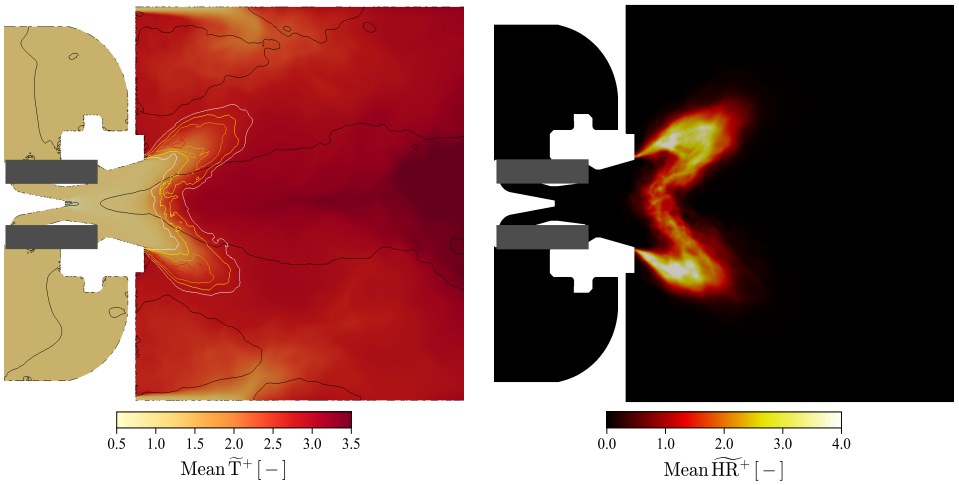

(a) Mean temperature field (b) Mean heat release rate field

Figure 8.15: *Mean fields of resolved temperature and heat release rate. The black line in Fig. 8.15.a identifies the zero axial velocity, while the four white to red lines represent iso-surface of heat release rate.*

Flame structure

The flame structure is analyzed by plotting the chemical trajectories in the Z-phase space. Fig. 8.17 shows the repartition of resolved temperature as a function of mixture fraction for different axial planes whose position are depicted in Fig. 8.16. To discriminate mixing-dominated regions from reactive-controlled zones the temperature scatter plots are colored by the local heat release rate.

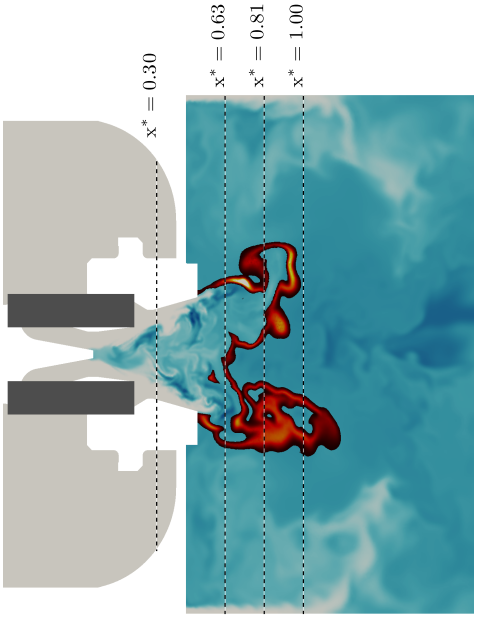

Figure 8.16: *Post-treatment planes positions and instantaneous resolved mixture fraction field. In red colors the iso-volume of resolved heat release rate identifies the reaction zone. Normalized coordinates $x^* = x/L$ are used, where x denotes the distance to the injector exit and L stands for an arbitrary length.*

In the pre-vaporizer duct at $x^* = 0.30$, mixing occurs between fresh air and kerosene issued from the liquid spray evaporation. In this zone, the mixture and aerodynamic conditions do not allow flame stabilization. Further downstream, at $x^* = 0.63$ where the central foot of the flame stabilizes, a weakly-stratified lean reaction zone characterized by high release rate is observed. Moreover, two mixing lines describing the mixing processes between i) fresh air and evaporated fuel and ii) fresh air and burnt gases are noticed. Along the third and fourth planes, the reacting points identify a lean premixed flame with small stratification level.
To sum-up the inhomogeneous lean mixture, issued from the coupling between efficient evaporation and the PVC, feeds an M-shaped flame that mainly burns under premixed/weakly stratified combustion mode.

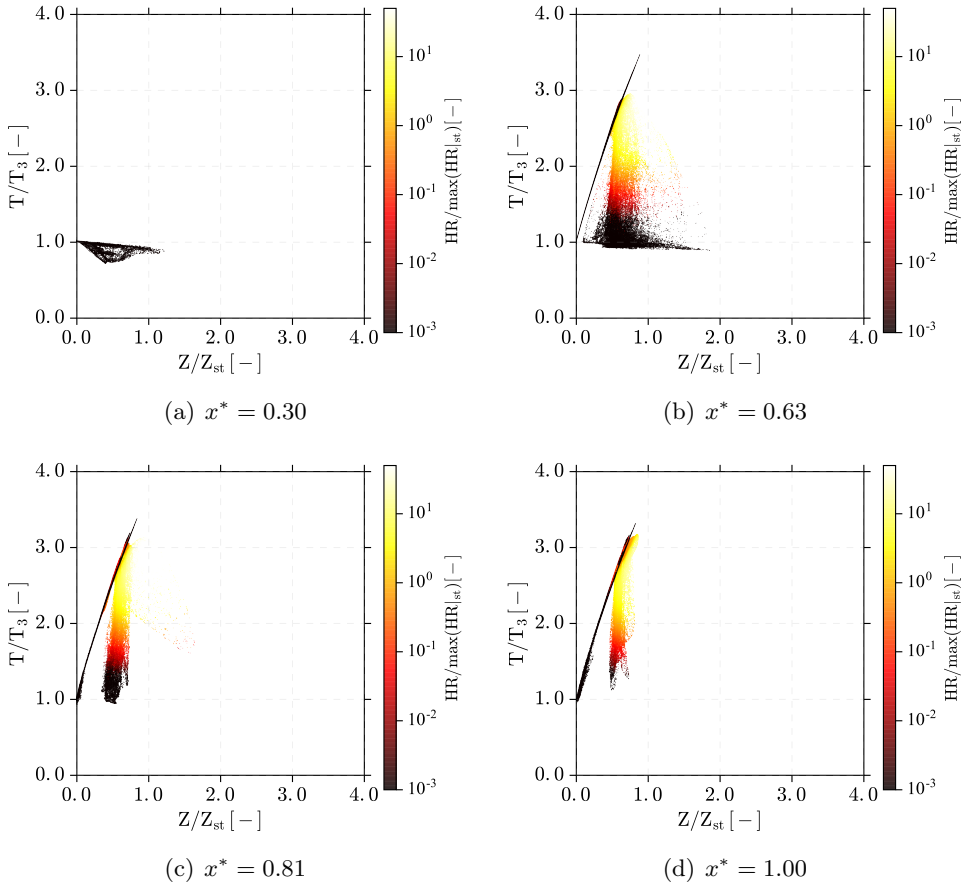

(a) $x^* = 0.30$ (b) $x^* = 0.63$

(c) $x^* = 0.81$ (d) $x^* = 1.00$

Figure 8.17: *Scatter plots of resolved temperature colored by heat release rate as a function of mixture fraction for different axial positions indicated in Fig. 8.16.*

8.4.2 Comparison with experimental measurements

8.4.2.1 Flame shape and aerodynamic fields

Capabilities of the numerical approach to predict the flame shape, stabilization and structure are assessed by comparing simulation results against OH-PLIF and PIV measurements.

Figure 8.18 compares the mean field of heat release rate predicted by the virtual chemistry calculation to the average of both OH-PLIF images and OH-PLIF gradient images. Important differences in terms of flame shape and stabilization are observed. The mean of OH-PLIF gradient images (Fig. 8.18.a (bottom)) demonstrates that the flame features a typical tulip-shape where burnt gases, represented by OH species, are confined in the middle region of the combustor. Additionally, the presence of OH species at the exit plane of the injection

system indicates that part of the kerosene is burnt in the pre-chamber region and that flame stabilizes upstream of the combustion chamber. As discussed previously, Large-Eddy Simulation performed with the virtual chemistry approach predicts an M-shape flame with two anchoring points located on the combustion chamber walls and on the burner axis.

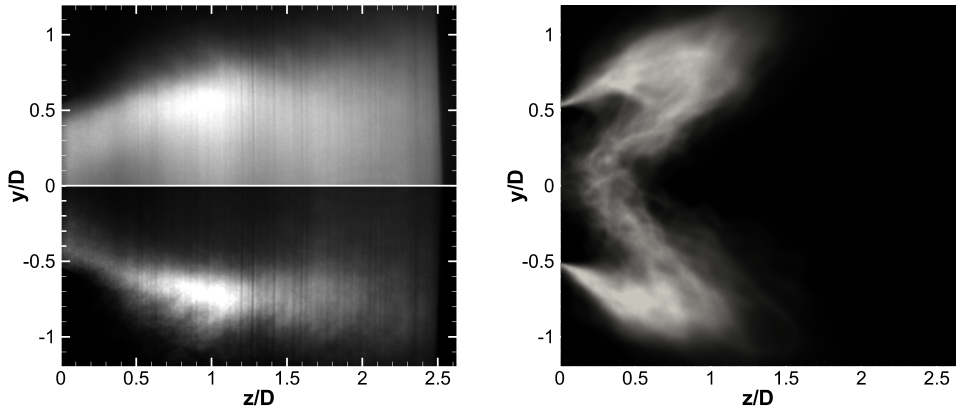

(a) Mean OH-PLIF and OH-PLIF gradients (b) Mean heat release rate LES

Figure 8.18: *Qualitative flame shape and stabilization comparison. Mean OH-PLIF images (top) and mean OH-PLIF gradients images (bottom) are compared to the heat release rate predicted numerically.*

Qualitative comparison between the mean aerodynamic fields measured by Particle Image Velocimetry (PIV) and obtained through numerical simulation is provided in Fig. 8.19. The mean axial velocity fields show a misprediction of the mean flow opening angle, along with an important overestimation of the inner-recirculation zone width, and an under-prediction of the outer-recirculation zones size. These discrepancies are due to the different flame stabilizations. Numerically, the flame is importantly lifted and allows the formation of a large inner recirculation zone. On the contrary, experimental measurements show that the flame stabilizes in the narrow pre-chamber leading to a confined inner recirculation zone and small opening of the flow angle. Mean radial velocity fields illustrated in Fig.8.19 (bottom) indicates an overestimation of the radial velocity component. Again this misprediction may be attributed to the different flame shapes between experiment and LES.

Qualitative comparison between numerical simulation and experimental measurements shows that the numerical simulation does not capture the proper flame stabilization and shape. Possible reasons accounting for the discrepancies between experiments and numerical results are numerous and of different nature. A plausible cause related to aerodynamic modeling and interaction between the flame and flow field is discussed in the next subsection.

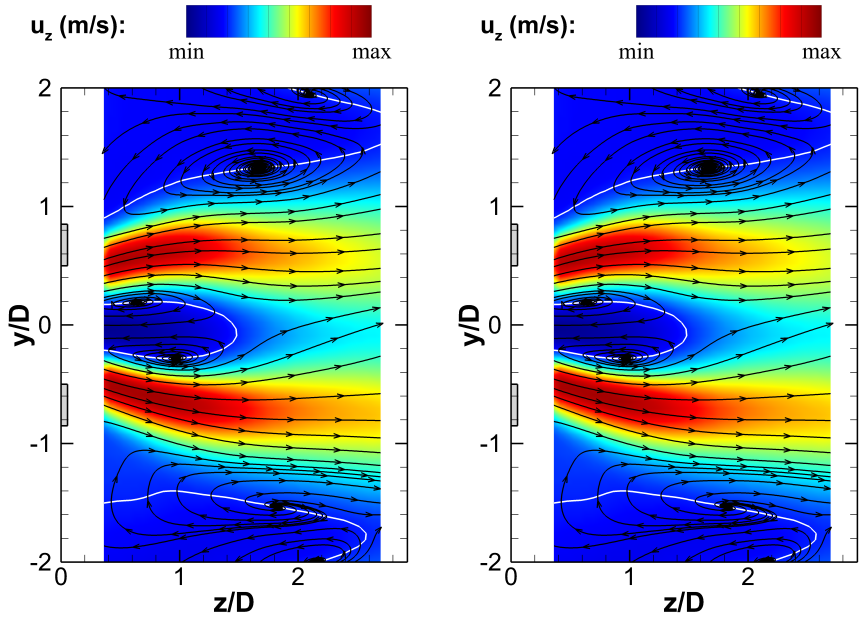

(a) Mean axial velocity PIV measurements

(b) Mean resolved axial velocity LES

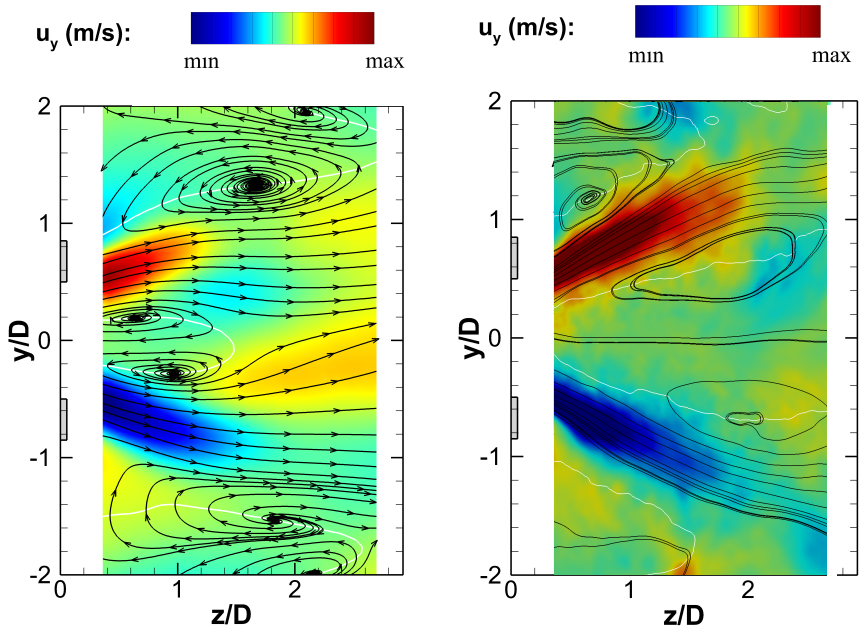

(c) Mean radial velocity PIV measurements

(d) Mean resolved radial velocity LES

Figure 8.19: *Mean fields of axial and radial velocity. The white lines identify the zero axial velocity, while the black lines represent pseudo-streamlines.*

8.4.2.2 Flame/flow interactions dynamics and stabilization scenario

The dynamic behavior of the flame and its interaction with the inner recirculation zone is analyzed in Fig. 8.20 showing four instantaneous snapshots of heat release rate and iso-surfaces of zero axial velocity.

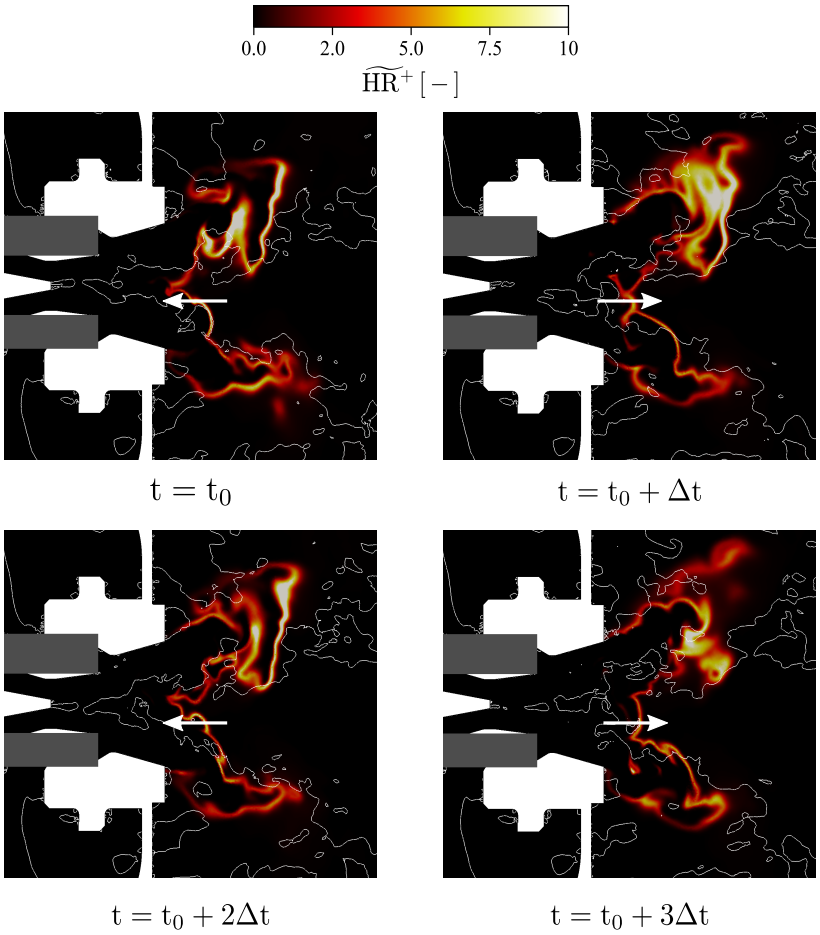

Figure 8.20: *Instantaneous fields of resolved heat release rate at equidistant times* $\Delta t = 80\,\mu s$. *The white lines identify iso-surface of zero axial velocity, while the white arrows schematically represent the movement of the flame front.*

As classically observed in swirled combustion chamber, the flame stabilizes along the iso-surfaces of zero axial velocity. However the snapshots of Fig. 8.20 reveal that the IRZ shape varies significantly from one instant to the other. In the first cut view, a continuous highly fragmented IRZ is observed in the pre-vaporizer chamber. As both thermodynamic (local mixture and temperature) and kinematic (reverse flow) conditions are favorables the flame front propagates towards the fresh gases. As the flame moves to the nozzle tip, the

IRZ is intensely perturbed and starts to break up. As shown in the second instantaneous view, at $t = t_0 + \Delta t$, the IRZ is cut into two pieces preventing the flame front to pursue its propagation in the reverse direction. The same process repeats for the third and fourth snapshots. This series of four instantaneous fields therefore demonstrates that the fragmentation of the IRZ prevents the flame to stabilize in the pre-vaporizer duct leading to a highly unstable position of the inner flame front anchoring point. In such perturbed flow environment, the tulip-shape-like anchoring of the flame observed in experiments does not seem possible.

To complete this explanation, the temporal evolution of the central flame anchoring position is studied. Figure 8.21 illustrates the axial movement of the lowest point of the iso-surface of heat release rate. In accordance with the mean heat release field, Fig. 8.21 shows that in average the inner flame front stabilizes few millimeters downstream of the combustion chamber inlet. This simple analysis also evidences that the position of the inner flame front stabilization point importantly fluctuates with time. Within the time investigated, the flame front position is shown to vary by 8 mm between the lowest and highest point.

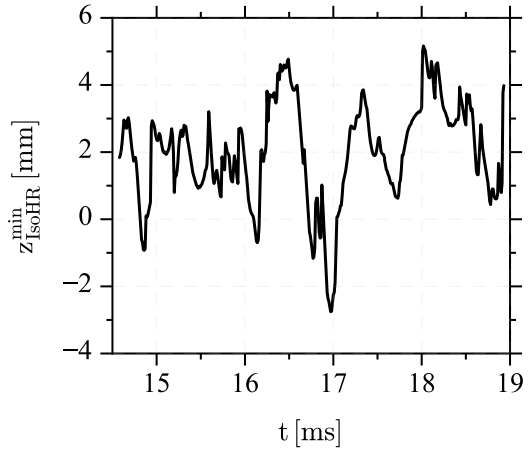

Figure 8.21: *Temporal evolution of the axial coordinate of the lowest point of the iso-surface of heat release. $z = 0$ corresponds to the axial position of the combustion chamber wall.*

The flame stabilization and shape seem tightly influenced by the dynamic behavior of the IRZ. If the physical reasons accounting for the IRZ destabilization are not explicitly identified, the analysis of the aerodynamic fields in cold flow conditions brings interesting elements of response. Fig. 8.22 depicting four instantaneous axial velocity fields shows that the fragmentation of the IRZ is also obtained in non-reacting conditions. This observation therefore suggests that the dynamic behavior of the IRZ is not necessarily due to complex inter-

actions between the flame front and the flow motions, but is mainly governed by the aerodynamics of the injection system. A possible source of error is the misprediction of the mass flow splitting between the two stages of the injector. In this situation, one of the two swirl stage could discharge a too important mass flow rate that would affect the IRZ and provoke its fragmentation.

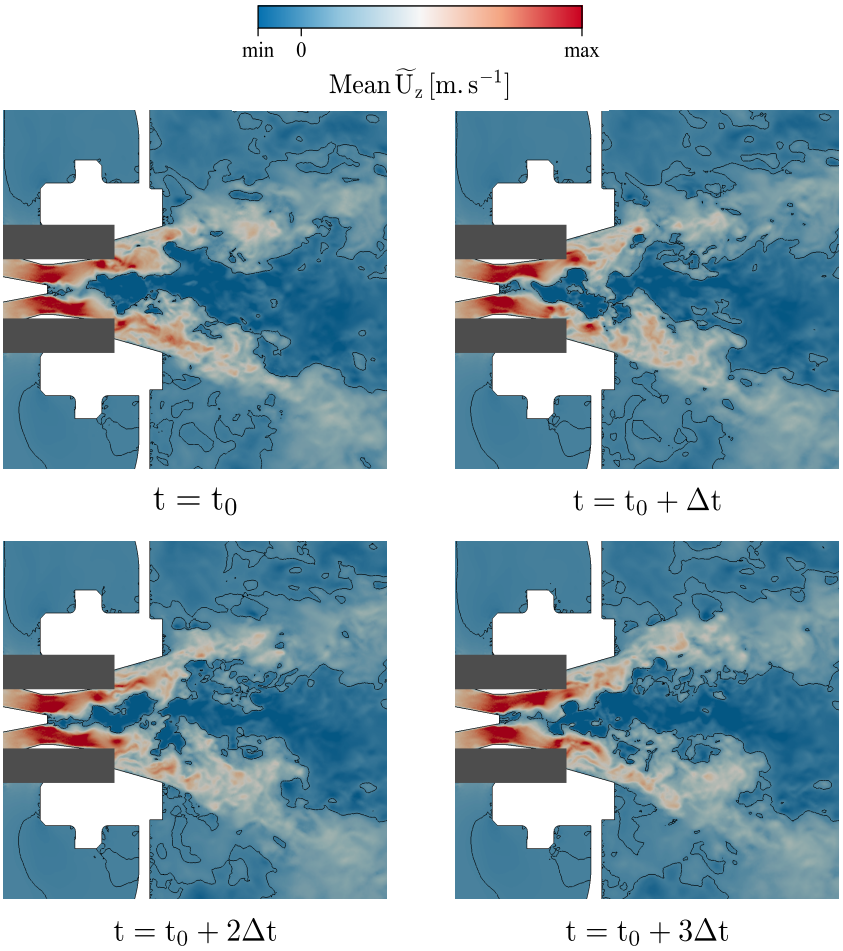

Figure 8.22: *Instantaneous fields of resolved axial velocity at equidistant times* $\Delta t = 80\,\mu$s *in non-reacting conditions. The white lines identify iso-surface of zero axial velocity.*

8.5 Summary and perspectives

In this chapter, the virtual optimized chemistry approach has been first used in the LES of a two-phase Lean Premixed injection system. Qualitative comparisons between numerical results and experiments show that the flame shape and stabilization are not well reproduced. Experimental measurements evidence that a narrow tulip-shape flame stabilizes in the pre-vaporizer duct, while numerically an M-shape flame with a wide opening angle stabilizes in the combustion chamber. A possible reason accounting for the different flame shapes is explored by analyzing the interaction between the flame and the inner recirculation zone. It appeared that the inner recirculation zone is irregularly fragmented preventing the flame to propagate with the reverse flow and to stabilize in the pre-vaporizer chamber. The dynamic behavior of the inner recirculation zone also observed in cold flow conditions is assumed to be associated with a misprediction of the flow motions in the injection system. To confirm this hypothesis additional calculations with finer mesh in the near wall region of the injector would be of great interest.

From these results it is unfortunately difficult to conclude on the predictive capability of the chemical model. To gain a better understanding on the dominant physical processes, a parametric study investigating the impact of each physical sub-model should be performed. First, the virtual optimized chemistry approach should be challenged in two-phase flow canonical problems. If required, the virtual kinetic schemes will be trained to capture spray flames complex chemical structure. Regarding spray modeling, high uncertainty lies in the choice of the injected droplet size distribution. As this spray property strongly impacts the evaporation and the subsequent mixture conditions, it is highly necessary to better characterize the droplet diameter distribution either through experimental measurement or through primary atomization calculation. Moreover, as the numerical simulation shows that the spray strongly interacts with the injection system walls, complementary calculations using refined spray/wall interaction models must be performed. Eventually, impact of the heat losses at the combustion chamber walls must be evaluated with non-adiabatic calculations.

Conclusion

The thesis main intent was to develop a reliable flame chemistry model applicable in Large-Eddy Simulations of industrial combustion chambers. An original and reduced-cost chemical modeling strategy, called virtual optimized chemistry, has been proposed. This approach relies on building-up virtual optimized schemes that are composed of virtual species and reactions. Contrarily to conventional kinetic mechanisms, virtual species do not model real chemical compounds but constitute degrees of freedom of the model. Similarly, virtual reactions ruling the production and destruction of virtual species do not represent real chemical paths but compose a mathematical architecture. In this framework, virtual species properties and reaction rate parameters are optimized to retrieve quantities of interest such as flame temperature and pollutant species, on a range of selected flame configurations. An automated procedure, based on genetic algorithm, allows to identify i) the physical properties of virtual species that best describe mixture-averaged properties of a real reference mixture, ii) the set of kinetic rate coefficients allowing a proper capture of a reference database composed by a collection of laminar flamelets. Flame/flow field interactions and pollutant species formation processes are originally modeled by different sub-mechanisms.

The virtual optimized chemistry approach has been first applied for the derivation of methane/air virtual schemes capable of addressing combustion chemistry on mixed flame regimes. A main virtual mechanism dedicated to the prediction of flame heat release and a satellite scheme devoted to the description of CO were developed and tested in 1-D laminar flames. Comparisons of the reduced schemes with the reference complex kinetic model show that virtual optimized chemistry captures well the targeted flame properties in both premixed and non-premixed flame configurations. Analysis of the impact of the reference database demonstrated that the description of CO formation in both premixed and non-premixed is achieved when both flame archetypes are included in the targeted flame library.
The new chemical model has also been used for the generation of virtual schemes devoted to the description of kerosene/air combustion in high pressure and high temperature conditions. While keeping the same mechanism architecture than for methane, the CO concentrations and heat release rate are well captured, suggesting that the size of the reduced virtual scheme does not depend on the number of reactions and species involved in the reference mechanism.

Virtual optimized schemes for methane oxidation are combined with the Thickened Flame model for LES and are subsequently tested on two gaseous turbu-

lent configurations. Simulations performed on the lean-premixed swirled burner PRECCINSTA show that the virtual mechanism captures well the flame dynamics and mean flame position. As non-adiabatic effects play an important role in this burner, the original adiabatic virtual model is not able to capture the flame shape and the CO recombination processes due to enthalpy decrease. However, virtual schemes tailored to account for non-adiabatic effects are in very good agreement with experimental data. Virtual optimized kinetic schemes were then tested on a stratified jet-flame. As noticed in the first test case, flame position and dynamics are well reproduced by the reduced virtual model. However, CO concentrations are mispredicted both in the flame front and in the burnt gases region. These discrepancies are the results of i) preferential diffusion effects that are not accounted for and ii) the use of a turbulent combustion model based on thickening of the flame front.

Eventually, the virtual mechanism for kerosene/air combustion is tested on a representative two-phase injection system. Comparison between numerical simulation and experimental measurements shows that the LES does not capture the proper flame stabilization and shape. Due to important uncertainties on the spray characteristics it is difficult to identify the reasons accounting for these differences and to therefore conclude on the predictive capabilities of the virtual chemistry approach.

Perspectives

The various points investigated during this thesis, as well as limitations of the virtual model, offer numerous and varied perspectives:

Virtual optimized mechanisms generation

- Though efficient evolutionary algorithm is used for the evaluation of both virtual species properties and reaction rate parameters, the virtual optimized schemes architectures are identified through an iterative procedure based on multiple tests. To improve the efficiency of the mechanism generation and the optimality of the resulting schemes an automated method should be developed. Particularly, nature (consecutive, competing, equilibrium) and number of the virtual chemical reactions must be identified without *a priori* knowledge of the complex underlying chemical processes.
- Genetic optimization procedures are particularly adapted to handle minimization problems based on complex fitness functions featuring highly structured landscapes (multiple valleys), noise and insufficient information. Due to the inherent randomness of the method Genetic Algorithm (GA) are able to depart from local optima and identify the global optimum. However, if the computational resources allocated for optimization are not sufficient GA may fail to explore the valley and efficiently eval-

uate the fittest set of parameters. This problem is illustrated in Fig. 4 where the cost-function decreases importantly during the last iterations of the procedure. To overcome this difficulty, GA could be coupled with a deterministic optimization method such as gradient based algorithms, that is known to converge rapidly towards local optimum when the initial guess is close to optimum.

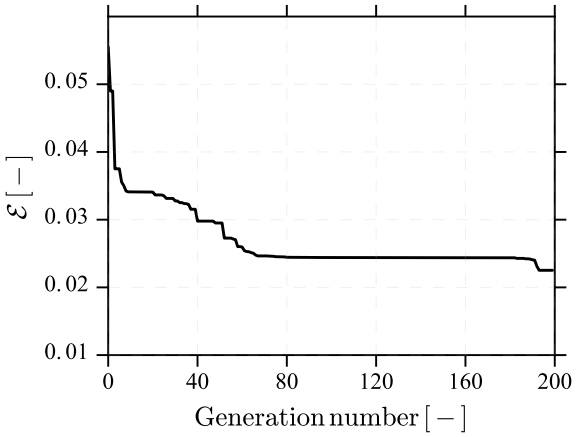

Figure 4: *Evolution of the cost function $\mathcal{E}$ as a function of the number of generations. At the end of the optimization procedure sudden improvement of the fitness function occurs demonstrating the potential difficulty of GA to locally explore a valley.*

Virtual optimized mechanisms validity domain

- In the present work, the transport properties of the virtual species are closed with simplified models that do not account for preferential diffusion effects. Results obtained on the 2-D burner and on the stratified jet flame Cambridge clearly evidenced the need to account for these phenomena. A first step would be to include the virtual species molecular diffusion coefficients in the set of parameters to optimize. Then, in order to capture the complex interactions between flame curvature, strain rate and differential diffusion effects, the reference database used to build the main virtual mechanism should be complemented with laminar non-premixed and strained premixed flames.
- The concept of satellite mechanisms dedicated to the prediction of a pollutant species has been successfully applied for the derivation of virtual schemes aiming at describing CO. The new strategy should be challenged on other pollutant species of interest for industrial applications such as nitrogen oxides or soot precursors. Though the methodology can theoretically be transposed to any chemical species, difficulties associated with the capture of chemical processes evolving with different time scales should be addressed. For instance, NO_x formation proceeds through two

chemical paths occurring both in the thin flame front region and in the post-flame zone on very large length and time scales. A strategy aiming at describing the complex formation of NO_x using the virtual chemistry approach is currently under development within the PhD Thesis of Maio (2019). As illustrated in Fig. 5, this approach consists in first optimizing reactions accounting for prompt NO_x production in the flame front zone, and second optimizing chemical reactions describing thermal NO_x formed in the post-flame zone.

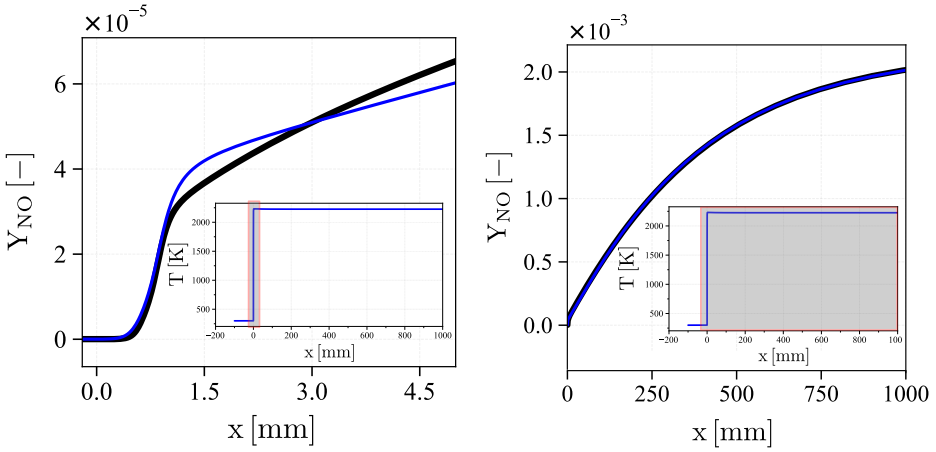

First step: Optimization of the fast reactions describing prompt NOx formation

Second step: Optimization of the slow reactions describing thermal NOx formation

Figure 5: *Spatial evolution of the NO_x mass fraction for a stoichiometric premixed methane/air flame.*

- Virtual optimized schemes dedicated to the prediction of gaseous kerosene-air combustion have been used for the Large-Eddy-Simulation of the two-phase flow industrial burner HERON. To improve the reliability of the approach in an aeronautical context, extension of the current virtual chemistry approach in a two-phase flow environment would be of great interest. Capabilities of the virtual optimized concept to properly account for evaporation processes in both fresh gases and hot combustion products should be improved. Moreover, complex interactions between liquid droplets and turbulent flame fronts should be investigated.
- To ensure representativity of the virtual optimized chemistry in aeronautical combustion chambers, virtual mechanisms were optimized to reproduce mixed combustion regimes were both premixed and non-premixed flame archetypes are encountered. The domain of application of the newly developed chemical description approach could be enlarged to other applications such as Diesel Internal Combustion engines, SCRAMJET combustors, or diluted combustion systems. To achieve this goal, the virtual optimized concept should be tested and extended to a wider range of

canonical flame problems including homogeneous auto-ignition or cold flames configurations for example.

Flame-turbulence interaction modeling

- The Thickened-Flame model for LES has been first considered to ensure the coupling between turbulence and virtual optimized mechanisms. Unfortunately, as observed on the stratified Cambridge jet flame, this robust and simple turbulent combustion model is not able to describe the concentration of intermediate species, such as CO, when flame wrinkling occurs. An alternative strategy aiming at modeling for the effect of subgrid scale wrinkling on pollutants has been recently proposed in the thesis of Mehl (2018). This turbulent combustion model, called Filtered Optimized Chemistry (FOC) model, consists in optimizing virtual reaction mechanisms to capture a collection of Filtered Wrinkled Flamelets that accounts for the impact of flame wrinkling on the flame structure. The Filtered Optimized Chemistry model has been used for the simulation of the Cambridge swirled burner showing important improvement over the TFLES model regarding the prediction of CO. This promising approach developed for premixed flame archetype should be extended to operate in stratified and pure diffusion regimes so as to be applied in industrial combustion chambers.

Appendix A

Genetic algorithm

This appendix gives details on the optimization tool MelOptim. Initialization, selection procedure, genetic operators and reduction technique used in the optimization code are discussed.

Population initialization
Pseudorandom numbers, used for population initialization, are generated through a classical Mersenne Twister algorithm.

Selection operation
The selection operator is based on a **k-tournament algorithm**. The main steps of this stochastic procedure may be summarized as follow:

- Random selection of k members from the previous generation
- Ranking the potential solutions according to the cost function
- Generation of a random number $\mathcal{R}$ between 0 and 1
- If $\mathcal{R} < P_{\mathcal{T}}$ the fittest indidvidual among the pool of k individual is selected, otherwise, the second ranking individual is selected with a probability $P_{\mathcal{T}}\,(1 - P_{\mathcal{T}})$

These steps are repeated until an individual is selected, or until the lowest ranking is reached.
In this work, the classical binary tournament involving k=2 individuals is used. This simple and low CPU demanding algorithm enables an easy control of the selective pressure and population diversity by adjusting the value of the tournament probability p_T. In this work, the intermediate value $p_T = 0.7$ was found to adequately balance between strong selective pressure promoted with $p_T = 1.0$ (determinist selection) and weak selective pressure promoted with $p_T = 0.5$ (random selection).

Crossover or recombination
In real coded evolutionary algorithms, a wide range of crossover operators were proposed (Wright 1991; Goldberg 1990; Eshelman and Schaffer 1993). The Simulated Binary Crossover (SBX) introduced by Deb and Agrawal (1995) is

considered in this study. The general procedure to create two children from SBX operator are:

- Generation of a random number $\mathcal{R}$ between 0 and 1
- Calculation of the spread factor β characterizing the ratio of the absolute difference in children values to that of the parent values:

$$\beta = \begin{cases} 2\mathcal{R}^{\frac{1}{1+\eta}} & \text{if } \mathcal{R} \leq 0.5 \\ \left(\dfrac{1}{2\left(1-\mathcal{R}\right)}\right)^{\frac{1}{1+\eta}} & \text{otherwise} \end{cases} \tag{A.1}$$

- Evaluation of the children C_1 and C_2 from the parents P_1 and P_2:

$$C_{1,k} = 0.5\left[\left(1+\beta\right)P_{1,k} + \left(1-\beta\right)P_{2,k}\right] \tag{A.2}$$

$$C_{2,k} = 0.5\left[\left(1-\beta\right)P_{1,k} + \left(1+\beta\right)P_{2,k}\right] \tag{A.3}$$

  where k is the gene index (unknown thermochemical or kinetic parameter).

Main advantage of this recombination operation is to avoid bias towards any parent solution. Moreover, as the spread factor is built so that children solutions has a spread which is proportional to that of the parent solutions, solution dispersion reduces as generations evolve to ease convergence. Application of the SBX crossover is performed with a probability $\mathcal{P}_c$ equal to 0.7 to ensure a satisfactory exploitation of the evaluation step.

Mutation

The non-uniform mutation operator proposed by Michalewicz (2013) is used in this work. This dynamic mutation operator is designed to allow a fine local tuning of the population diversity with time. If the kth gene g_k of parent P is selected for mutation the gene k $g_k^{'}$ of the associated children C reads:

$$g_k^{'} = \begin{cases} g_k + \Delta\left(n, g_k^{\max} - g_k\right) & \text{if } \mathcal{R} = 0 \\ g_k - \Delta\left(n, g_k - g_k^{\min}\right) & \text{if } \mathcal{R} = 1 \end{cases} \tag{A.4}$$

where n is the number of generations performed, and the superscripts min and max denote the minimum and maximum bounds for the kth parameter to optimize. The function $\Delta\left(n, y\right)$ returns a value in the range [0, y] such that the probability of $\Delta\left(n, y\right)$ to be close to 0 increases when n increases. The function used by Martin Martin (2005) is considered:

$$\Delta\left(n, y\right) = y\mathcal{R}\left(1 - \frac{n}{N_{gen}}\right)^b \tag{A.5}$$

where N_{gen} is the maximal generation number allowed, $\mathcal{R}$ is a random number in the interval [0, 1] and b is a system parameter determining the degree of non-uniformity.

Each solution has a probability $\mathcal{P}_m = 0.1$ to mute. This value was found to allow a good balance between space exploitation and exploration.

Reduction operation
After children population evaluation, a reduction or filtering operation relying on k-tournament selection is applied. To ensure population diversity the reduction operation prevents an individual to be selected twice in the new generation.

Appendix B

Optimization of product species thermodynamic properties

This appendix describes the optimization procedure used for the optimization of the thermodynamic properties of the virtual products.

The in-house genetic algorithm presented in Chapter 3 is used to minimize the cost function defined in Eq. 3.24 and expressed as:

$$\mathcal{E}_{\text{thermo}}^{\text{main}}\left(\mathcal{X}\right)\left(N_p^{v_m}, \alpha_{P_k}^{v_m}\left(\phi_i\right), a_{lP_k}^{v_m}\right) = \sum_{i=1}^{N_c}\sum_{l=1}^{N_T}\left[\overline{a}_{lP}^{v_m}|^{eq}\left(\phi_i\right) - \sigma_l\left(\phi_i\right)\right] \quad \text{(B.1)}$$

where $\sigma_l\left(\phi_i\right)$ is given by:

$$\sigma_l\left(\phi_i\right) = \overline{a}_l^d|^{eq}\left(\phi_i\right) - \overline{a}_{lA}^{v_m}|^{eq}\left(\phi_i\right) \quad \text{(B.2)}$$

The function $\overline{a}_{lA}^{v_m}|^{eq}\left(\phi_i\right)$ is entirely defined by real species properties and equilibrium concentration of reactants, while $\overline{a}_l^d|^{eq}\left(\phi_i\right)$ is obtained through equilibrium calculations with detailed chemistry. Therefore, $\sigma_l\left(\phi_i\right)$ is known and constitutes the target coefficient of the optimization procedure. Figure B.1 shows the evolution of the 6 coefficients σ_l versus the equivalence ratio.
The term $\overline{a}_{lP}^{v_m}|^{eq}\left(\phi_i\right)$ is unknown and needs to be optimized in order to minimize the cost function $\mathcal{E}_{\text{thermo}}^{\text{main}}$ defined by Eq. (B.1):

$$\overline{a}_{lP}^{v_m}|^{eq}\left(\phi_i\right) = \sum_{k=1}^{N_p^{vm}} a_{lP_k}^{v_m}\alpha_{P_k}^{v_m}Y_P^{v_m}|^{eq}\left(\phi_i\right) \quad \text{for} \quad l \in [1, N_T] \quad \text{(B.3)}$$

The optimization calculation requires the evaluation of $\mathrm{N}_T \times \mathrm{N}_p^{v_m}$ thermodynamic coefficients $a_{lP_k}^{v_m}$, and $\left(N_p^{v_m} - 1\right) \times N_c$ stoichiometric coefficients $\alpha_{P_k}^{v_m}$. For only two products and $\mathrm{N}_c = 31$ equivalence ratio conditions, 43 variables have to be determined.
To ease the optimization procedure, the problem is divided into two parts. We first consider that for each of $\mathrm{N}_p^{v_m}$ products, a subset of m thermodynamic coefficients $a_{lP_k}^{v_m}$ is known and ensure a perfect reproduction of the corresponding

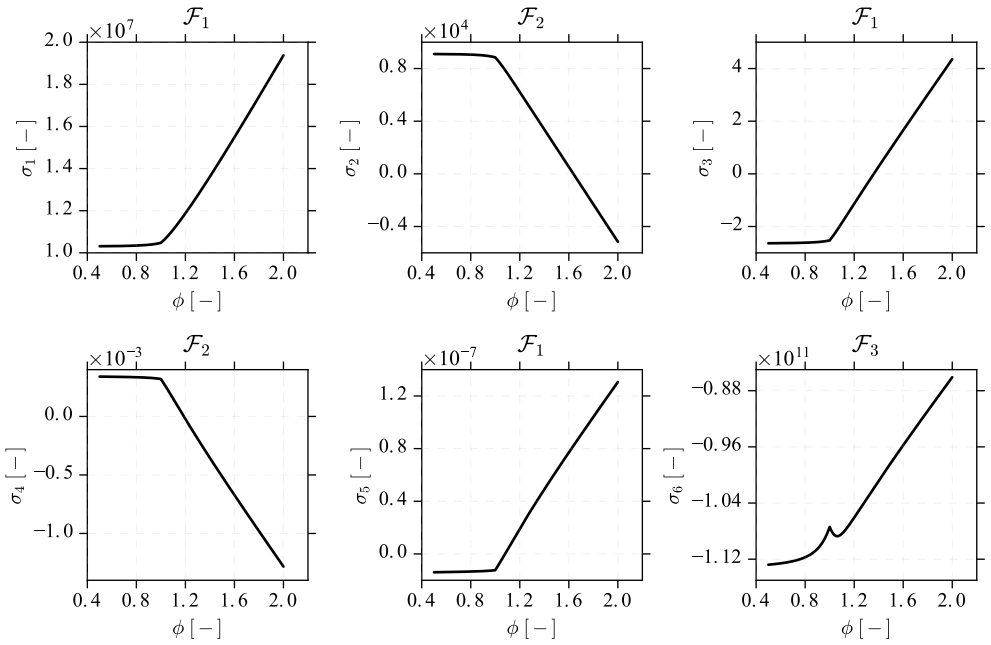

Figure B.1: *Evolution of the target coefficients σ_l versus the equivalence ratio. Three distinctive families of curves may be identified: $\mathcal{F}_1 = \{\sigma_1, \sigma_3, \sigma_5\}$, $\mathcal{F}_2 = \{\sigma_2, \sigma_4\}$ and $\mathcal{F}_3 = \{\sigma_6\}$.*

target coefficients over the whole flammability range. This hypothesis can be expressed through the following system expressed in its general form for the equivalence ratio ϕ_i:

$$\begin{cases} \sum\limits_{k=1}^{N_p^{vm}} a_{1P_k}^{vm} \alpha_{P_k}^{vm} Y_P^{vm}|^{eq}(\phi_i) & = \sigma_1(\phi_i) \\ \dots & \\ \sum\limits_{k=1}^{N_p^{vm}} a_{mP_k}^{vm} \alpha_{P_k}^{vm} Y_P^{vm}|^{eq}(\phi_i) & = \sigma_m(\phi_i) \end{cases} \tag{B.4}$$

With the arbitrary constraint $\sum\limits_{k=1}^{N_p^{vm}} \alpha_{P_k}^{vm} = 1$, Eq. B.4 can be rewritten:

$$\begin{cases} \sum\limits_{k=1}^{N_p^{vm}-1} \left[a_{l_1 k}^{vm} \alpha_{P_k}^{vm}(\phi_i)\right] + a_{l_1 N_p}^{vm} \left(1 - \sum\limits_{k=1}^{N_p^{vm}-1} \alpha_{P_k}^{vm}(\phi_i)\right) & = \dfrac{\sigma_{l_1}}{Y_P^{vm}|^{eq}}(\phi_i) \\ \dots & \\ \sum\limits_{k=1}^{N_p^{vm}-1} \left[a_{l_m k}^{vm} \alpha_{P_k}^{vm}(\phi_i)\right] + a_{l_m, N_p}^{vm} \left(1 - \sum\limits_{k=1}^{N_p^{vm}-1} \alpha_{P_k}^{vm}(\phi_i)\right) & = \dfrac{\sigma_{l_m}}{Y_P^{vm}|^{eq}}(\phi_i) \end{cases} \tag{B.5}$$

If $m = N_p^{v_m} - 1$, the system Eq. (B.5) exhibits $N_p^v - 1$ equations and $N_p^{v_m} - 1$ unknown functions $\alpha_{P_k}^{v_m}(\phi)$. The stoichiometric coefficients $\alpha_{P_k}^{v_m}(\phi_i)$ can be evaluated by inverting the N_c systems of Eq. (B.5). Thus for any set of $m = N_p^{v_m} - 1$ thermodynamic coefficients, the evolution of the product stoichiometric coefficients in the composition space can be calculated. However, the physical consistency (bounded behavior) of the resulting $\alpha_{P_k}^{v_m}(\phi)$ coefficients is not necessarily obtained. Then the identification of the best subset of $N_p^{v_m} - 1$ thermodynamic coefficients and associated $\alpha_{P_k}^{v_m}(\phi)$ is done through genetic optimization with the objective to respect the physical constraint: $0 < \alpha_{P_k}^{v_m}(\phi_i) < 1$. Practically, the physical behavior of the stoichiometric coefficients is ensured by minimizing the cost function $\mathcal{E}_{\text{thermo 1}}^{\text{main}}$:

$$\mathcal{E}_{\text{thermo 1}}^{\text{main}} = \sum_{k=1}^{N_p^{v_m}} \delta_{P_k} \tag{B.6}$$

where δ_{P_k} is defined as:

$$\delta_{P_k} = \begin{cases} 0 & \text{if} \quad \alpha_{P_k}^{v_m}(\phi_i) \in]0;1[\\ 1 & \text{else} \end{cases} \tag{B.7}$$

The second part of the optimization procedure aims at evaluating the $m' = N_T - m$ residual thermodynamic coefficients. The optimization algorithm is again used to minimize the fitness function $\mathcal{E}_{\text{thermo 2}}^{\text{main}}$:

$$\mathcal{E}_{\text{thermo 2}}^{\text{main}} = \sum_{i=1}^{N_c} \sum_{l=m}^{N_T} \left[\overline{a}_{lP}^{v} |^{eq}(\phi_i) - \sigma_l(\phi_i) \right] \tag{B.8}$$

In practice, the choice of the m thermodynamic coefficients optimized during the first stage of the procedure is important. Figure B.1 shows that three families of coefficients can be identified considering their evolution in the composition space. The coefficients σ_1, σ_3 and σ_5, belonging to the family called $\mathcal{F}_1$, feature a constant behavior for lean mixtures and the same increasing trend in the rich zone. The second family of coefficients $\mathcal{F}_2$, including the terms σ_2 and σ_4, is constant for lean injection conditions and shows a decrease with the equivalence ratio for rich mixtures. Finally the coefficient σ_6 presents a distinct behavior with a discontinuity near the stoichiometry. To summarize, if $m = 3$ thermodynamic coefficients are used to identify the evolution of $N_p^{v_m} = 4$ virtual product stoichiometric coefficients $\alpha_{P_k}^{v_m}(\phi_i)$, given the self-similar behavior of σ_l profiles, optimization of the $m' = 3$ remaining coefficients is therefore easier. If the m chosen coefficients are for instance the first, second and last one, one can expect a rapid and efficient convergence of the optimization algorithm. As a conclusion, this a priori study shows a minimum number of four virtual products is required to describe the equilibrium state thermodynamic properties (c_p and h) of the mixture on the whole flammability range.

Appendix C

Virtual chemistry approach for fuels of varying complexity

Validation of the virtual chemistry concept is complemented by the derivation of three virtual optimized schemes for : ethylene, propane and n-heptane oxidation. Capabilities of the virtual optimized mechanisms to capture the equilibrium flame temperature and laminar flame speed are assessed.

The virtual optimized chemistry strategy, presented in Chapter 3 and applied to methane/air and kerosene/air combustion, is used for the derivation of reduced virtual schemes dedicated to the prediction of the oxidation of hydrocarbons fuels ranging from ethylene to n-heptane. Following the global procedure presented in Fig. 3.8, the three detailed chemical mechanisms indicated in Table C.1 are used as reference to build-up the corresponding virtual optimized mechanisms. Despite the various sizes of the reference complex schemes (the number of species ranges from 106 to 297 and the number of elementary reactions varies from 784 to 16797), all corresponding reduced virtual schemes are composed by the same number of virtual species and virtual reactions. For both the main virtual scheme and the sub-mechanism for CO prediction a total of 11 virtual species interacting through 5 virtual reactions are considered.

Hydrocarbons	Detailed mechanisms	Ref.	Virtual mechanisms
Ethylene (C_2H_4)	297 species 16797 reactions	(Saggese et al. 2015)	**Main scheme:** 8 species / 2 reactions **Sub-scheme for CO:** 3 species / 3 reactions
Propane (C_3H_8)	111 species 784 reactions	(Wang et al. 2007)	
N-heptane (C_7H_{16})	106 species 1738 reactions	(Stagni et al. 2013)	

Table C.1: *Hydrocarbons and associated reference kinetic schemes*

Figure C.1 presents the adiabatic flame temperatures obtained with mixtures

composed of real properties reactant species (F, O_2, N_2) as well as four virtual products with optimized thermodynamic properties. Reference equilibrium calculations performed with the full set of species included in the detailed scheme of Table C.1 are shown as reference in Fig. C.1. For each fuel investigated, a very good agreement is obtained between virtual and complex equilibrium computations on the whole range of fresh gases composition. Even for heavy hydrocarbons such as n-heptane, only four virtual products are required to describe the equilibrium state.

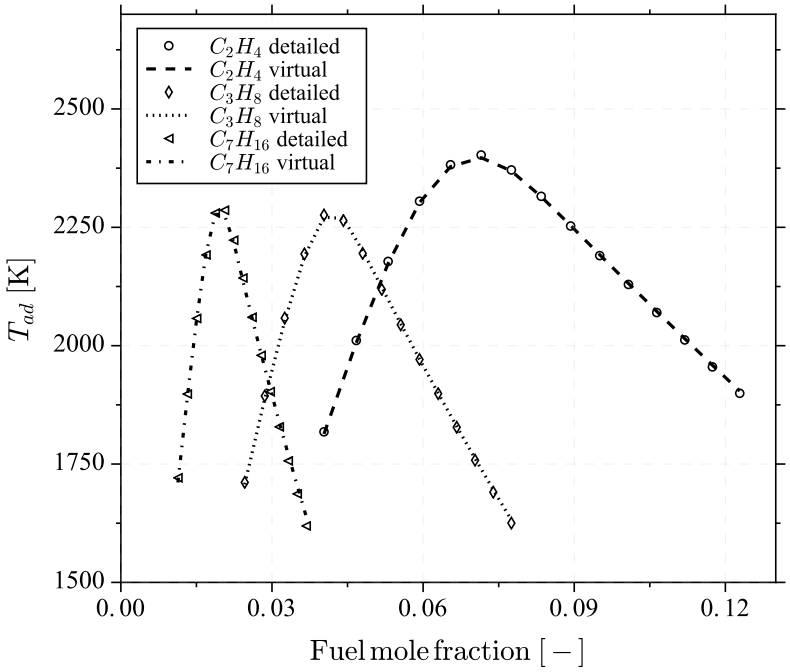

Figure C.1: *Adiabatic flame temperature versus fuel mole fraction for air/hydrocarbon mixtures at fresh gas temperature* $T_f = 300\,\mathrm{K}$ *and pressure* $P = 1\,\mathrm{atm}$. *Equilibrium calculations including four virtual products (black lines) are compared to reference equilibrium computations (symbols).*

Capabilities of the two-step virtual scheme to capture the laminar flame speed is investigated in Fig. C.2 comparing the laminar flame speed predicted by both the virtual mechanisms and the reference mechanisms. For all hydrocarbons considered, the two-step virtual schemes associated with equivalence ratio dependent correction function captures very well the laminar flame consumption speed over the whole flamability range.

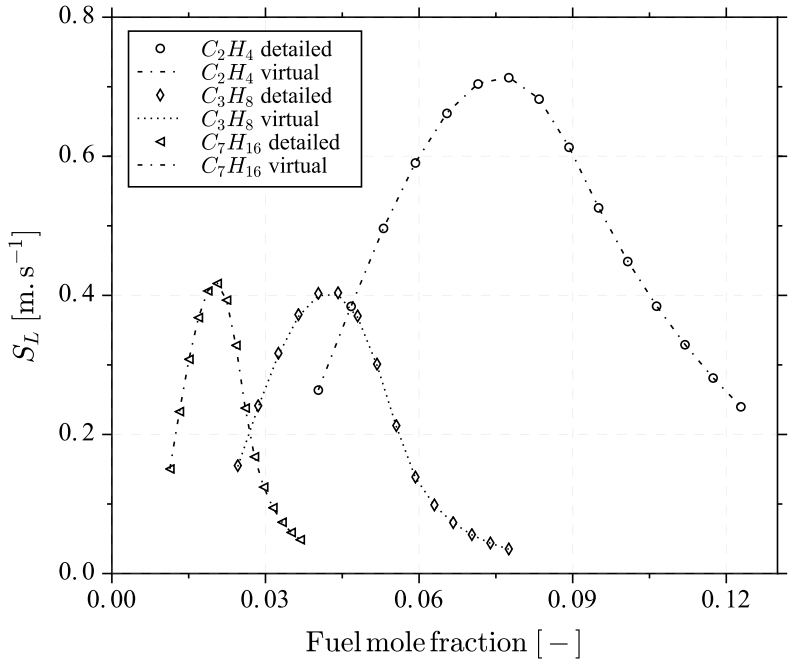

Figure C.2: *Evolution of the laminar flame speed S_L with the fuel mole fraction for fuels of varying complexity at fresh gas temperature $T_f = 300\,\mathrm{K}$ and pressure $P = 1\,\mathrm{atm}$. Detailed kinetic schemes (symbols) and main virtual optimized schemes (lines) are compared.*

Appendix D

Résumé détaillé en français

La nature conflictuelle des contraintes de performances, d'opérabilité et de respect des normes environnementales conduit les motoristes à optimiser finement la géométrie de la chambre de combustion afin d'identifier le meilleur design. La Simulation aux Grande Echelles (SGE) est aujourd'hui un outil performant et est déployé de manière courante dans les Bureaux d'Etudes pour la prédiction des propriétés macroscopiques des écoulements réactifs. Toutefois, la description des phénomènes influencés par les effets de chimie complexe, tels que la stabilisation, l'extinction de flamme et la formation des polluants, reste un problème crucial. En effet, la prédiction des effets de chimie complexe nécessite l'utilisation de modèles cinétiques détaillés imposant des coûts de calculs prohibitifs, des problèmes de raideur numérique et des difficultés de couplage avec les échelles non résolues turbulentes.
Afin d'inclure une description des processus chimiques dans les simulations numériques de chambres de combustion industrielles de nombreuses approches ont été proposées dans la littérature. Les schémas cinétiques semi-globaux, conçus pour reproduire les propriétés globales de flamme à l'aide de 5 à 8 espèces majoritaires (Westbrook and Dryer 1981; Jones and Lindstedt 1988; Franzelli et al. 2010), sont largement utilisés pour leurs faibles coûts de calcul et leur couplage relativement facile avec la turbulence. Cependant, ces mécanismes ne sont pas en mesure de capturer les processus de formation des espèces polluantes, et ne parviennent pas à décrire la structure chimique complexe des flammes rencontrées dans les chambres de combustion. Les méthodes de chimie tabulée, basée sur la paramétrisation de la structure de flamme en fonction d'un faible nombre de paramètres de contrôle (Peters 1984; Gicquel et al. 2000; Van Oijen et al. 2001; Pierce and Moin 2004), constituent une alternative attractive pour la description des effets de chimie complexe à très faible coûts CPU. Cette approche soulève toutefois de nombreux problèmes de modélisation (choix de l'archétype de flamme et des variables de contrôle, fermeture des équations de transport) et des difficultés pratiques lorsqu'elle est utilisée dans des configurations réelles. Enfin, si les schémas analytiques fournissent une description précise de la structure de la flamme et des espèces intermédiaires dans une large gamme de conditions (Luche 2003; Lu and Law 2008), ils impliquent également des coûts de calculs élevés dans le cas de carburants lourds et peuvent conduire à des problèmes de raideurs numériques.

Dans cette thèse, une nouvelle approche de modélisation, appelée chimie virtuelle optimisée, a été développée pour répondre aux principales limitations mentionnées ci-dessus. L'approche de chimie virtuelle repose sur la construction de schémas virtuels optimisés, composés d'espèces et de réactions virtuelles. Contrairement aux mécanismes cinétiques classiques, les espèces virtuelles ne modélisent pas des composés chimiques réels mais constituent des degrés de liberté du modèle. De même, les réactions virtuelles qui régissent la production et la destruction d'espèces virtuelles ne représentent pas des voies chimiques réelles mais constituent une architecture mathématique. Dans ce cadre, les propriétés des espèces virtuelles et les paramètres cinétiques fermant les vitesses de réaction sont calibrés pour reproduire des quantités d'intérêt telles que la température de la flamme et les espèces polluantes, sur une gamme de configurations de flamme sélectionnées. Une procédure automatisée, basée sur un algorithme génétique, permet d'identifier i) les propriétés physiques des espèces virtuelles qui décrivent le mieux les propriétés moyennes du mélange réel de référence, ii) l'ensemble des paramètres cinétiques permettant de prédire précisément une base de données de référence composée d'une collection de flammes 1-D laminaires. Le couplage entre la flamme et l'écoulement et les processus de formation des espèces polluantes sont modélisés par différents sous-mécanismes.
L'approche de chimie virtuelle optimisée a d'abord été appliquée à la dérivation de schémas dédiés à la combustion du mélange méthane/air en condition atmosphérique. Un mécanisme virtuel principal consacré à la prédiction du dégagement de chaleur et un schéma satellite dédié à la description du CO ont été développés et testés sur des configurations de flammes 1-D laminaires. La comparaison des schémas réduits au modèle cinétique complexe de référence montre que la chimie virtuelle optimisée capture bien les propriétés de flamme ciblées à la fois dans le cas de flammes pré-mélangées et non pré-mélangées de diffusion. Il a été démontré que la description de la formation de CO dans les flammes pré-mélanges et non pré-mélanges est obtenue lorsque les deux archétypes de flamme sont inclus dans la base de données utilisée pour la calibration du schéma virtuel. Le nouveau modèle chimique a également été utilisé pour la génération de schémas virtuels consacrés à la description de l'oxydation du kérosène à haute pression et à haute température. En conservant la même structure de mécanisme que pour le méthane, les concentrations de CO et le taux de dégagement de chaleur sont bien capturés par les mécanismes virtuels. Ceci suggère que la taille du schéma virtuel réduit ne dépend pas de la complexité du carburant.
Les schémas virtuels optimisés pour décrire l'oxydation du méthane sont combinés avec le modèle TFLES et sont ensuite testés sur deux configurations turbulentes gazeuses. Les simulations réalisées sur le brûleur PRECCINSTA montrent que les mécanismes virtuels capturent bien la dynamique de flamme et la position moyenne de la flamme. Comme les effets non-adiabatiques jouent un rôle important dans ce brûleur, le modèle virtuel adiabatique original n'est pas capable de capturer la forme de la flamme et les processus de recombinai-

son du CO. Toutefois, les schémas virtuels conçus pour tenir compte des effets non-adiabatiques sont en très bon accord avec les données expérimentales. Les schémas cinétiques virtuels optimisés ont ensuite été testés sur une flamme faiblement stratifiée : la flamme Cambridge. La position et la dynamique de la flamme sont bien reproduites par le modèle virtuel réduit. Cependant, les concentrations de CO sont mal prédites tant dans le front de flamme que dans la région des gaz brûlés. Ces écarts sont le résultat i) d'effets de diffusion préférentiels non pris en compte dans l'actuelle formulation de l'approche et ii) de l'utilisation d'un modèle de combustion turbulente basé sur l'épaississement du front de flamme qui tend à surestimer les niveaux d'espèces intermédiaires.
Enfin, le mécanisme virtuel calibré pour la combustion du kérosène et l'air est testé sur un système d'injection diphasique industriel monté sur le banc HERON haute pression. La comparaison entre la simulation numérique et les mesures expérimentales montre que le calcul ne décrit pas correctement la forme de la flamme. En raison des incertitudes importantes sur les caractéristiques du spray, il est difficile d'identifier les raisons qui expliquent ces différences et donc de tirer des conclusions sur les capacités prédictives de l'approche de chimie virtuelle.

References

Abou-Taouk, A., B. Farcy, P. Domingo, L. Vervisch, S. Sadasivuni, and L.-E. Eriksson (2016). Optimized reduced chemistry and molecular transport for Large Eddy Simulation of partially premixed combustion in a gas turbine. *Combustion Science and Technology 188*(1), 21–39. *(p. 54)*

Abou-Taouk, A., S. Sadasivuni, D. Lörstad, and L.-E. Eriksson (2013). Evaluation of global mechanisms for LES analysis of SGT-100 DLE combustion system. In *ASME Turbo Expo 2013: Turbine Technical Conference and Exposition*. American Society of Mechanical Engineers. *(p. 54)*

Abramzon, B. and W. Sirignano (1989). Droplet vaporization model for spray combustion calculations. *International Journal of Heat and Mass Transfer 32*(9), 1605–1618. *(p. 176, 179)*

Agosta, A., N. Cernansky, D. Miller, T. Faravelli, and E. Ranzi (2004). Reference components of jet fuels: kinetic modeling and experimental results. *Experimental Thermal and Fluid Science 28*(7), 701–708. *(p. 114)*

Airbus (2018). Global market forecast, 2018. `https://www.airbus.com/aircraft/market/global-market-forecast.html`. *(p. 1)*

Angelberger, C., D. Veynante, F. Egolfopoulos, and T. Poinsot (1998). Large eddy simulations of combustion instabilities in premixed flames. In *Proceedings of the Summer Program*, pp. 61–82. Center for Turbulence Research, NASA Ames/Stanford Univ. *(p. 132)*

Apte, S. V., K. Mahesh, P. Moin, and J. C. Oefelein (2003). Large-eddy simulation of swirling particle-laden flows in a coaxial-jet combustor. *International Journal of Multiphase Flow 29*(8), 1311–1331. *(p. 176)*

Arrhenius, S. (1889). On the reaction velocity of the inversion of cane sugar by acids. *Zeitschrift fur physikalische Chemie 4*, 226. *(p. 22)*

Auzillon, P., B. Fiorina, R. Vicquelin, N. Darabiha, O. Gicquel, and D. Veynante (2011). Modeling chemical flame structure and combustion dynamics in LES. *Proceedings of the Combustion Institute 33*(1), 1331–1338. *(p. 135)*

Barlow, R. S., M. J. Dunn, M. S. Sweeney, and S. Hochgreb (2012). Effects of preferential transport in turbulent bluff-body-stabilized lean premixed CH_4/air flames. *Combustion and Flame 159*(8), 2563–2575. *(p. 18, 140, 156, 158, 166, 167)*

Becker, J. and C. Hassa (2002). Breakup and atomization of a kerosene jet in crossflow at elevated pressure. *Atomization and Sprays 12*(1-3), 49–67. *(p. 193)*

Bénard, P., G. Lartigue, V. Moureau, and R. Mercier (2019). Large-Eddy simulation of the lean-premixed PRECCINSTA burner with wall heat loss. *Proceedings of the Combustion Institute 37*(4), 5233–5243. *(p. 147,*

151, 154, 155)

Boeing (2017). Current market outlook, 2017. https://www.boeing.com/commercial/market/current-market-outlook-2017/. *(p. 1)*

Boger, M., D. Veynante, H. Boughanem, and A. Trouvé (1998). Direct numerical simulation analysis of flame surface density concept for large eddy simulation of turbulent premixed combustion. In *Symposium (International) on Combustion*, Volume 27, pp. 917–925. Elsevier. *(p. 131)*

Brown, N. J., G. Li, and M. L. Koszykowski (1997). Mechanism reduction via principal component analysis. *International Journal of Chemical Kinetics 29*(6), 393–414. *(p. 46)*

Bui-Pham, M., K. Seshadri, and F. Williams (1992). The asymptotic structure of premixed methane-air flames with slow CO oxidation. *Combustion and Flame 89*(3-4), 343–362. *(p. 93)*

Butler, T. and P. O'Rourke (1977). A numerical method for two dimensional unsteady reacting flows. *Symposium (International) on Combustion 16*(1), 1503–1515. *(p. 131)*

Bykov, V. and U. Maas (2007). The extension of the ILDM concept to reaction–diffusion manifolds. *Combustion Theory and Modelling 11*(6), 839–862. *(p. 55)*

Cailler, M., N. Darabiha, D. Veynante, and B. Fiorina (2017a). Building-up virtual optimized mechanism for flame modeling. *Proceedings of the Combustion Institute 36*(1), 1251–1258. *(p. 79)*

Cailler, M., R. Mercier, V. Moureau, N. Darabiha, and B. Fiorina (2017b). Prediction of CO emissions in LES of turbulent stratified combustion using virtual chemistry. In *55th AIAA Aerospace Sciences Meeting, AIAA SciTech Forum*. *(p. 156)*

Cavazzuti, M. (2013). Deterministic optimization. In *Optimization Methods*, pp. 77–102. Springer. *(p. 66)*

Charlette, F., C. Meneveau, and D. Veynante (2002a). A power-law flame wrinkling model for LES of premixed turbulent combustion Part I: non-dynamic formulation and initial tests. *Combustion and Flame 131*(1), 159–180. *(p. 32, 132, 144, 158, 159, 195)*

Charlette, F., C. Meneveau, and D. Veynante (2002b). A power-law flame wrinkling model for LES of premixed turbulent combustion Part II: dynamic formulation. *Combustion and Flame 131*(1-2), 181–197. *(p. 132)*

Chen, J. (1997). Development of reduced mechanisms for numerical modelling of turbulent combustion. In *Workshop on Numerical Aspects of Reduction in Chemical Kinetics, CERMICS-ENPC, Cité Descartes, Champus sur Marne, France*. *(p. 49)*

Coffee, T. and J. Heimerl (1981). Transport algorithms for premixed, laminar steady-state flames. *Combustion and Flame 43*, 273–289. *(p. 17)*

Colin, O., F. Ducros, D. Veynante, and T. Poinsot (2000a). A thickened flame model for large eddy simulations of turbulent premixed combustion. *Physics of fluids 12*(7), 1843–1863. *(p. 9, 10, 32, 131, 132, 144)*

Colin, O. and M. Rudgyard (2000b). Development of high-order taylor–galerkin schemes for LES. *Journal of Computational Physics 162*(2), 338–371. *(p. 144, 190)*

Dagaut, P. (2002). On the kinetics of hydrocarbons oxidation from natural gas to kerosene and diesel fuel. *Physical Chemistry Chemical Physics 4*(11), 2079–2094. *(p. 114)*

Dagaut, P. and M. Cathonnet (2006). The ignition, oxidation, and combustion of kerosene: A review of experimental and kinetic modeling. *Progress in Energy and Combustion Science 32*(1), 48–92. *(p. 41, 114)*

Dagaut, P., F. Karsenty, G. Dayma, P. Diévart, K. Hadj-Ali, A. Mzé-Ahmed, M. Braun-Unkhoff, J. Herzler, T. Kathrotia, T. Kick, et al. (2014). Experimental and detailed kinetic model for the oxidation of a gas to liquid (GtL) jet fuel. *Combustion and Flame 161*(3), 835–847. *(p. 41)*

Dagaut, P., M. Reuillon, J.-C. Boettner, and M. Cathonnet (1994). Kerosene combustion at pressures up to 40 atm: Experimental study and detailed chemical kinetic modeling. *Symposium (International) on Combustion 25*(1), 919–926. *(p. 114)*

Darabiha, N. and S. Candel (1992). The influence of the temperature on extinction and ignition limits of strained hydrogen-air diffusion flames. *Combustion Science and Technology 86*(1-6), 67–85. *(p. 8, 26, 69, 105)*

Darwin, C. (1872). *The origin of species by means of natural selection: or, the preservation of favored races in the struggle for life*, Volume 1. Modern library. *(p. 67)*

De, A. and S. Acharya (2009). Large eddy simulation of a premixed bunsen flame using a modified thickened-flame model at two Reynolds number. *Combustion Science and Technology 181*(10), 1231–1272. *(p. 133)*

Deb, K. and R. B. Agrawal (1995). Simulated binary crossover for continuous search space. *Complex Systems 9*(2), 115–148. *(p. 217)*

Dixon-Lewis, G. (1968). Flame structure and flame reaction kinetics II. Transport phenomena in multicomponent systems. *Proceedings of the Royal Society of London A: Mathematical, Physical and Engineering Sciences 307*(1488), 111–135. *(p. 17)*

Dombard, J. (2011). *Direct Numerical Simulation of non-isothermal dilute sprays using the Mesoscopic Eulerian Formalism*. Ph. D. thesis, Institut National Polytechnique de Toulouse. *(p. 173)*

Domingo, P., L. Vervisch, and K. Bray (2002). Partially premixed flamelets in LES of nonpremixed turbulent combustion. *Combustion Theory and Modelling 6*(4), 529–551. *(p. 36)*

Domingo, P., L. Vervisch, and J. Réveillon (2005). DNS analysis of partially premixed combustion in spray and gaseous turbulent flame-bases stabilized in hot air. *Combustion and Flame 140*(3), 172–195. *(p. 36)*

Domingo Alvarez, P. (2019). *Simulation aux grandes échelles de la combustion haute pression pour la validation à priori de diagnostiques optiques*. Ph. D. thesis, Normandie Université. *(p. 186)*

Domingo Alvarez, P., P. Bénard, G. Lartigue, V. Moureau, and F. Grisch (2018). LES evaluation of the spray characteristics impact on the flame in a lean-premixed injection system. In *Poster presented at the 37th International Symposium on Combustion*. *(p. 187)*

Duboc, B., P. Domingo, and G. Ribert (2015). Simulating kerosene/air flames with hybrid transported-tabulated chemistry. In *Proceedings of the European Combustion Meeting*. *(p. 58)*

Edwards, K., T. Edgar, and V. Manousiouthakis (1998). Kinetic model reduction using genetic algorithms. *Computers & chemical engineering 22*(1-2), 239–246. *(p. 46)*

Edwards, T. and L. Q. Maurice (2001). Surrogate mixtures to represent complex aviation and rocket fuels. *Journal of Propulsion and Power 17*(2), 461–466. *(p. 114)*

El Bakali, A., P. Dagaut, and M. Cathonnet (1999). Cinétique de combustion du kérosène à pression atmosphérique. In *CNRS, Rapport interne*. *(p. 115)*

Elliott, L., D. Ingham, A. Kyne, N. Mera, M. Pourkashanian, and C. Wilson (2004). Genetic algorithms for optimisation of chemical kinetics reaction mechanisms. *Progress in Energy and Combustion Science 30*(3), 297–328. *(p. 67)*

Elliott, L., D. B. Ingham, A. G. Kyne, N. S. Mera, M. Pourkashanian, and S. Whittaker (2006). Reaction mechanism reduction and optimisation for modelling aviation fuel oxidation using standard and hybrid genetic algorithms. *Computers & Chemical Engineering 30*(5), 889–900. *(p. 46)*

Embouazza, M. (2005). *Etude de l'auto-allumage par réduction des schémas cinétiques chimiques: application à la combustion homogène diesel*. Ph. D. thesis, Ecole Centrale de Paris. *(p. 55)*

Enjalbert, N. (2011). *Modélisation avancée de la combustion turbulente diphasique en régime de forte dilution par les gaz brûlés*. Ph. D. thesis, Rouen, INSA. *(p. 173)*

Ern, A. and V. Giovangigli (1994). *Multicomponent transport algorithms*, Volume 24. Springer Science & Business Media. *(p. 15, 17)*

Ern, A. and V. Giovangigli (1998). Thermal diffusion effects in hydrogen-air and methane-air flames. *Combustion Theory and Modelling 2*(4), 349–372. *(p. 18)*

Eshelman, L. J. and J. D. Schaffer (1993). Real-coded genetic algorithms and interval-schemata. In *Foundations of Genetic Algorithms*, Volume 2, pp. 187–202. Elsevier. *(p. 217)*

Euler, M., R. Zhou, S. Hochgreb, and A. Dreizler (2014). Temperature measurements of the bluff body surface of a swirl burner using phosphor thermometry. *Combustion and Flame 161*(11), 2842–2848. *(p. 156)*

Farcy, B., A. Abou-Taouk, L. Vervisch, P. Domingo, and N. Perret (2014). Two approaches of chemistry downsizing for simulating selective non catalytic reduction DeNOx process. *Fuel 118*, 291–299. *(p. 54, 67)*

Felden, A. (2017). *Development of Analytically Reduced Chemistries (ARC) and applications in Large Eddy Simulations (LES) of turbulent combustion*. Ph. D. thesis, Institut National Polytechnique de Toulouse. *(p. 7)*

Felden, A., L. Esclapez, E. Riber, B. Cuenot, and H. Wang (2018). Including real fuel chemistry in LES of turbulent spray combustion. *Combustion and Flame 193*, 397–416. *(p. 50, 52)*

Fernandez-Tarrazo, E., A. L. Sánchez, A. Liñán, and F. A. Williams (2006). A simple one-step chemistry model for partially premixed hydrocarbon combustion. *Combustion and Flame 147*(1), 32–38. *(p. 52, 53, 79, 91)*

Fevrier, P., O. Simonin, and K. D. Squires (2005). Partitioning of particle velocities in gas–solid turbulent flows into a continuous field and a spatially uncorrelated random distribution: theoretical formalism and numerical study. *Journal of Fluid Mechanics 533*, 1–46. *(p. 173)*

Fichet, V. (2008). *Modélisation de la combustion du gaz naturel par réseaux de réacteurs avec cinétique chimique détaillée*. Ph. D. thesis, Ecole Centrale Paris. *(p. 55)*

Fiorina, B., R. Baron, O. Gicquel, D. Thevenin, S. Carpentier, and N. Darabiha (2003). Modelling non-adiabatic partially premixed flames using flame-prolongation of ILDM. *Combustion Theory and Modelling 7*(3), 449–470. *(p. 88, 109)*

Fiorina, B., O. Gicquel, L. Vervisch, S. Carpentier, and N. Darabiha (2005). Approximating the chemical structure of partially premixed and diffusion counterflow flames using FPI flamelet tabulation. *Combustion and Flame 140*(3), 147–160. *(p. 55, 99)*

Fiorina, B., R. Mercier, G. Kuenne, A. Ketelheun, A. Avdić, J. Janicka, D. Geyer, A. Dreizler, E. Alenius, C. Duwig, et al. (2015b). Challenging modeling strategies for LES of non-adiabatic turbulent stratified combustion. *Combustion and Flame 162*(11), 4264–4282. *(p. 55)*

Fiorina, B., D. Veynante, and S. Candel (2015a). Modeling combustion chemistry in large eddy simulation of turbulent flames. *Flow, Turbulence and Combustion 94*(1), 3–42. *(p. 42, 56, 130)*

Fiorina, B., R. Vicquelin, P. Auzillon, N. Darabiha, O. Gicquel, and D. Veynante (2010). A filtered tabulated chemistry model for LES of premixed combustion. *Combustion and Flame 157*(3), 465 – 475. *(p. 131, 141)*

Flightpath, A. (2011). 2050-Europe's vision for aviation. `http://www.acare4europe.org`. *(p. 2)*

Franzelli, B., B. Fiorina, and N. Darabiha (2013). A tabulated chemistry method for spray combustion. *Proceedings of the Combustion Institute 34*(1), 1659–1666. *(p. 55)*

Franzelli, B., E. Riber, B. Cuenot, and M. Ihme (2015). Numerical modeling of soot production in aero-engine combustors using large eddy simulations. In *Proceedings of ASME Turbo Expo 2015*. *(p. 57)*

Franzelli, B., E. Riber, L. Y. Gicquel, and T. Poinsot (2012). Large Eddy Simulation of combustion instabilities in a lean partially premixed swirled

flame. *Combustion and Flame 159*(2), 621–637. *(p. 53, 87, 133, 141, 143, 158)*

Franzelli, B., E. Riber, M. Sanjosé, and T. Poinsot (2010). A two-step chemical scheme for kerosene–air premixed flames. *Combustion and Flame 157*(7), 1364–1373. *(p. 6, 32, 53, 91, 229)*

Franzelli, B., A. Vié, M. Boileau, B. Fiorina, and N. Darabiha (2017). Large eddy simulation of swirled spray flame using detailed and tabulated chemical descriptions. *Flow, Turbulence and Combustion 98*(2), 633–661. *(p. 52, 186)*

Franzelli, B. G. (2011). *Impact of the chemical description on direct numerical simulations and large eddy simulations of turbulent combustion in industrial aero-engines*. Ph. D. thesis, Institut National Polytechnique de Toulouse. *(p. 103, 133, 134, 141, 151, 165)*

Freitag, S. and C. Hassa (2008). Spray characteristics of a kerosene jet in cross flow of air at elevated pressure. In *Proceedings ILASS-Europe*. *(p. 193)*

Fureby, C. (2005). A fractal flame-wrinkling large eddy simulation model for premixed turbulent combustion. *Proceedings of the Combustion Institute 30*(1), 593–601. *(p. 132)*

Galpin, J., A. Naudin, L. Vervisch, C. Angelberger, O. Colin, and P. Domingo (2008). Large-eddy simulation of a fuel-lean premixed turbulent swirl-burner. *Combustion and Flame 155*(1-2), 247–266. *(p. 130, 141, 143, 146, 151)*

Gao, F. and E. E. O'Brien (1993). A large-eddy simulation scheme for turbulent reacting flows. *Physics of Fluids A: Fluid Dynamics 5*(6), 1282–1284. *(p. 130)*

Gentle, J. E., W. K. Härdle, and Y. Mori (2012). *Handbook of computational statistics: concepts and methods*. Springer Science & Business Media. *(p. 66)*

Germano, M., U. Piomelli, P. Moin, and W. H. Cabot (1991). A dynamic subgrid-scale eddy viscosity model. *Physics of Fluids A: Fluid Dynamics 3*(7), 1760–1765. *(p. 128)*

Gicquel, O., N. Darabiha, and D. Thévenin (2000). Laminar premixed hydrogen / air counterflow flame simulations using flame prolongation of ILDM with differential diffusion. *Proceedings of the Combustion Institute 28*(2), 1901–1908. *(p. 6, 55, 87, 88, 229)*

Goldberg, D. E. (1989). *Genetic Algorithms in Search, Optimization and Machine Learning* (1st ed.). Boston, MA, USA: Addison-Wesley Longman Publishing Co., Inc. *(p. 67)*

Goldberg, D. E. (1990). The theory of virtual alphabets. In *International Conference on Parallel Problem Solving from Nature*, pp. 13–22. Springer. *(p. 217)*

Goodwin, D. G. (2002). Cantera: An object-oriented software toolkit for chemical kinetics, thermodynamics, and transport processes. `http://www.cantera.org`. *(p. 26)*

Goussis, D. A. and U. Maas (2011). Model reduction for combustion chemistry. In *Turbulent Combustion Modeling*, pp. 193–220. Springer. *(p. 49)*

Hannebique, G., P. Sierra, E. Riber, and B. Cuenot (2013). Large eddy simulation of reactive two-phase flow in an aeronautical multipoint burner. *Flow, Turbulence and Combustion 90*(2), 449–469. *(p. 36)*

Hélie, J. and A. Trouvé (1998). Turbulent flame propagation in partially premixed combustion. *Symposium (International) on Combustion 27*(1), 891–898. *(p. 30, 31)*

Hermeth, S., G. Staffelbach, L. Y. Gicquel, V. Anisimov, C. Cirigliano, and T. Poinsot (2014). Bistable swirled flames and influence on flame transfer functions. *Combustion and Flame 161*(1), 184–196. *(p. 54, 87)*

Hernández, I., G. Staffelbach, T. Poinsot, J. C. R. Casado, and J. B. Kok (2013). LES and acoustic analysis of thermo-acoustic instabilities in a partially premixed model combustor. *Comptes Rendus Mécanique 341*(1), 121–130. *(p. 87)*

Hilbert, R., F. Tap, H. El-Rabii, and D. Thévenin (2004). Impact of detailed chemistry and transport models on turbulent combustion simulations. *Progress in Energy and Combustion Science 30*(1), 61–117. *(p. 18)*

Hirschfelder, J. O., C. F. Curtiss, R. B. Bird, and M. G. Mayer (1954). *Molecular theory of gases and liquids*, Volume 26. Wiley New York. *(p. 18, 86, 181)*

Holland, J. H. et al. (1975). *Adaptation in natural and artificial systems: an introductory analysis with applications to biology, control, and artificial intelligence*. University of Michigan Press Ann Arbor. *(p. 67)*

Hollmann, C. and E. Gutheil (1996). Modeling of turbulent spray diffusion flames including detailed chemistry. In *Symposium (international) on combustion*, Volume 26, pp. 1731–1738. Elsevier. *(p. 186)*

Hong, G. I., J. H. Chen, and J.-Y. Chen (1999). Chemical response of methane/air diffusion flames to unsteady strain rate. *Combustion and Flame 118*(1), 204–212. *(p. 41, 108)*

Hubbard, G., V. Denny, and A. Mills (1975). Droplet evaporation: effects of transients and variable properties. *International Journal of Heat and Mass Transfer 18*(9), 1003–1008. *(p. 177)*

IATA (2017). 20 years, passenger forecast. `http://airlines.iata.org/data/20-year-passenger-forecast`. *(p. 1)*

ICAO (2017). Civil aviation statistics of the world and ICAO staff estimates. `https://data.worldbank.org/indicator/IS.AIR.PSGR`. *(p. 1)*

Ihme, M. and H. Pitsch (2008). Modeling of radiation and nitric oxide formation in turbulent nonpremixed flames using a flamelet/progress variable formulation. *Physics of Fluids 20*(5), 055110. *(p. 56)*

Ihme, M., C. Schmitt, and H. Pitsch (2009). Optimal artificial neural networks and tabulation methods for chemistry representation in LES of a bluff-body swirl-stabilized flame. *Proceedings of the Combustion Institute 32*(1), 1527–1535. *(p. 56)*

Ihme, M., L. Shunn, and J. Zhang (2012). Regularization of reaction progress variable for application to flamelet-based combustion models. *Journal of Computational Physics 231*(23), 7715–7721. *(p. 56)*

Jaouen, N. (2017c). *An automated approach to derive and optimise reduced chemical mechanisms for turbulent combustion*. Ph. D. thesis, Normandie Université. *(p. 57)*

Jaouen, N., L. Vervisch, and P. Domingo (2017b). Auto-thermal reforming (ATR) of natural gas: An automated derivation of optimised reduced chemical schemes. *Proceedings of the Combustion Institute 36*(3), 3321–3330. *(p. 52, 57)*

Jaouen, N., L. Vervisch, P. Domingo, and G. Ribert (2017a). Automatic reduction and optimisation of chemistry for turbulent combustion modelling: Impact of the canonical problem. *Combustion and Flame 175*, 60–79. *(p. 7, 45, 56)*

Jaravel, T. (2016). *Prediction of pollutants in gas turbines using large eddy simulation*. Ph. D. thesis, Institut National Polytechnique de Toulouse. *(p. 21, 48, 52, 57, 86, 133, 134)*

Jaravel, T., E. Riber, B. Cuenot, and G. Bulat (2017). Large eddy simulation of an industrial gas turbine combustor using reduced chemistry with accurate pollutant prediction. *Proceedings of the Combustion Institute 36*(3), 3817–3825. *(p. 7, 45, 52)*

Jones, W. and R. Lindstedt (1988). Global reaction schemes for hydrocarbon combustion. *Combustion and Flame 73*(3), 233–249. *(p. 6, 52, 53, 62, 86, 87, 229)*

Kee, R. J., G. Dixon-Lewis, J. Warnatz, M. E. Coltrin, and J. A. Miller (1986). A fortran computer code package for the evaluation of gas-phase multicomponent transport properties. *Sandia National Laboratories Report SAND86-8246 13*, 80401–1887. *(p. 19)*

Kee, R. J., F. M. Rupley, E. Meeks, and J. A. Miller (1996). Chemkin-III: A fortran chemical kinetics package for the analysis of gas-phase chemical and plasma kinetics. *(p. 26, 82)*

Kerstein, A. R., W. T. Ashurst, and F. A. Williams (1988). Field equation for interface propagation in an unsteady homogeneous flow field. *Physical Review A 37*(7), 2728. *(p. 131)*

Knudsen, E. and H. Pitsch (2008). A dynamic model for the turbulent burning velocity for large eddy simulation of premixed combustion. *Combustion and Flame 154*(4), 740–760. *(p. 132)*

Koopman, J., C. Hassa, M. Fischer, G. Stockhausen, M. Jarius, C. Willert, J. Becker, I. Röhle, and L. Wehr (2005). Modelling of low emissions combustors using large eddy simulations. work package 4: Reacting flow, temperature and species data. *(p. 190, 194)*

Kraushaar, M. (2011). *Application of the compressible and low-Mach number approaches to Large Eddy Simulation of turbulent flows in aero-engines*. Ph. D. thesis, Institut National Polytechnique de Toulouse. *(p. 110, 157)*

Kuenne, G., A. Ketelheun, and J. Janicka (2011). LES modeling of premixed combustion using a thickened flame approach coupled with FGM tabulated chemistry. *Combustion and Flame 158*(9), 1750–1767. *(p. 55, 133)*

Lam, S. (1985). Singular perturbation for stiff equations using numerical methods. In *Recent Advances in the Aerospace Sciences*, pp. 3–19. Springer. *(p. 50, 108)*

Lam, S. (1993). Using CSP to understand complex chemical kinetics. *Combustion Science and Technology 89*(5-6), 375–404. *(p. 89)*

Lam, S. and D. Goussis (1994). The CSP method for simplifying kinetics. *International Journal of Chemical Kinetics 26*(4), 461–486. *(p. 7, 50, 89)*

Laurent, F. and M. Massot (2001). Multi-fluid modelling of laminar polydisperse spray flames: origin, assumptions and comparison of sectional and sampling methods. *Combustion Theory and Modelling 5*(4), 537–572. *(p. 173)*

Lecocq, G., I. Hernández, D. Poitou, E. Riber, and B. Cuenot (2013). Soot prediction by Large-Eddy Simulation of complex geometry combustion chambers. *Comptes Rendus Mécanique 341*(1-2), 230–237. *(p. 57)*

Lefebvre, A. H. (1989). Properties of sprays. *Particle & Particle Systems Characterization 6*(1-4), 176–186. *(p. 194)*

Lefebvre, A. H. (2010). *Gas turbine combustion: alternative fuels and emissions*. CRC press. *(p. 3)*

Legier, J.-P. (2001). *Simulations numériques des instabilités de combustion dans les foyers aéronautiques*. Ph. D. thesis, Institut National Polytechnique de Toulouse. *(p. 158)*

Legier, J.-P., T. Poinsot, and D. Veynante (2000). Dynamically thickened flame LES model for premixed and non-premixed turbulent combustion. In *Proceedings of the summer program*, pp. 157–168. Center for Turbulence Research, NASA Ames/Stanford Univ. *(p. 132, 133)*

Lepage, V. (2000). *Elaboration d'une méthode de réduction de schémas cinétiques détaillés. Application aux mécanismes de combustion du gaz naturel et du n-décane*. Ph. D. thesis, Université d'Orléans. *(p. 7, 49, 52)*

Leparoux, J., R. Mercier, V. Moureau, and H. Musaeffendic (2018). Primary atomization simulation applied to a jet in crossflow aeronautical injector with dynamic mesh adaptation. In *Proceedings of 14 th Triennal International Conference on Liquid Atomization and Spray Systems (ILASS Europe 2018)*. *(p. 172)*

Li, J., Z. Zhao, A. Kazakov, and F. L. Dryer (2004). An updated comprehensive kinetic model of hydrogen combustion. *International journal of chemical kinetics 36*(10), 566–575. *(p. 40)*

Liñán, A. and F. A. Williams (1993). *Fundamental aspects of combustion*. New York, NY (United States); Oxford University Press. *(p. 79)*

Lindstedt, R. and L. Maurice (2000). Detailed chemical-kinetic model for aviation fuels. *Journal of Propulsion and Power 16*(2), 187–195. *(p. 114)*

Løvås, T., P. Amnéus, F. Mauss, and E. Mastorakos (2002b). Comparison of automatic reduction procedures for ignition chemistry. *Proceedings of the Combustion Institute 29*(1), 1387–1393. *(p. 50)*

Løvås, T., F. Mauss, C. Hasse, and N. Peters (2002a). Development of adaptive kinetics for application in combustion systems. *Proceedings of the Combustion Institute 29*(1), 1403–1410. *(p. 50)*

Løvås, T., D. Nilsson, and F. Mauss (2000). Automatic reduction procedure for chemical mechanisms applied to premixed methane/air flames. *Proceedings of the Combustion Institute 28*(2), 1809–1815. *(p. 7)*

Lu, T. and C. K. Law (2005). A directed relation graph method for mechanism reduction. *Proceedings of the Combustion Institute 30*(1), 1333–1341. *(p. 7, 44, 45, 89)*

Lu, T. and C. K. Law (2006a). Linear time reduction of large kinetic mechanisms with directed relation graph: n-Heptane and iso-octane. *Combustion and Flame 144*(1), 24–36. *(p. 45)*

Lu, T. and C. K. Law (2006b). On the applicability of directed relation graphs to the reduction of reaction mechanisms. *Combustion and Flame 146*(3), 472–483. *(p. 45, 89)*

Lu, T. and C. K. Law (2006c). Systematic approach to obtain analytic solutions of quasi steady state species in reduced mechanisms. *The Journal of Physical Chemistry A 110*(49), 13202–13208. *(p. 49)*

Lu, T. and C. K. Law (2008). A criterion based on computational singular perturbation for the identification of quasi steady state species: A reduced mechanism for methane oxidation with NO chemistry. *Combustion and Flame 154*(4), 761–774. *(p. 7, 48, 50, 51, 52, 86, 87, 89, 229)*

Lu, T. and C. K. Law (2009). Toward accommodating realistic fuel chemistry in large-scale computations. *Progress in Energy and Combustion Science 35*(2), 192–215. *(p. 40)*

Lu, T., C. S. Yoo, J. Chen, and C. K. Law (2010). Three-dimensional direct numerical simulation of a turbulent lifted hydrogen jet flame in heated coflow: a chemical explosive mode analysis. *Journal of Fluid Mechanics 652*, 45–64. *(p. 36)*

Luche, J. (2003). *Elaboration of reduced kinetic models of combustion. Application to a kerosene mechanism*. Ph. D. thesis, Université d'Orléans. *(p. 7, 52, 114, 229)*

Luche, J., M. Reuillon, J.-C. Boettner, and M. Cathonnet (2004). Reduction of large detailed kinetic mechanisms: application to kerosene/air combustion. *Combustion Science and Technology 176*(11), 1935–1963. *(p. 48)*

Luo, K., H. Pitsch, M. Pai, and O. Desjardins (2011). Direct numerical simulations and analysis of three-dimensional n-heptane spray flames in a model swirl combustor. *Proceedings Combustion Institute 33*(2), 2143–2152. *(p. 31, 186)*

Maas, U. and S. B. Pope (1992a). Implementation of simplified chemical kinetics based on intrinsic low-dimensional manifolds. *Proceedings of the*

Combustion Institute 24(1), 103–112. *(p. 55)*

Maas, U. and S. B. Pope (1992b). Simplifying chemical kinetics: intrinsic low-dimensional manifolds in composition space. *Combustion and Flame 88*(3), 239–264. *(p. 54, 55)*

Magnussen, B. F. and B. H. Hjertager (1977). On mathematical modeling of turbulent combustion with special emphasis on soot formation and combustion. In *Symposium (international) on Combustion*, Volume 16, pp. 719–729. Elsevier. *(p. 130)*

Maio, G. (2019). Ph. D. thesis, Paris Saclay. *(p. 214)*

Maio, G., M. Cailler, R. Mercier, and B. Fiorina (2019). Virtual chemistry for temperature and CO prediction in LES of non-adiabatic turbulent flames. *Proceedings of the Combustion Institute 37*(2), 2591–2599. *(p. 151, 153, 166)*

Malbois, P., E. Salaün, F. Frindt, G. Cabot, L. Bouheraoua, H. Verdier, S. Richard, M. Boukhalfa, B. Renou, and F. Grisch (2017). Simultaneous equivalence ratio and flame structure measurements in a lean-premixed aero-engine injection system under relevant operating conditions. In *Proceedings of the European Combustion Meeting*. *(p. 186, 189)*

Malbois, P., E. Salaun, F. Frindt, G. Cabot, B. Renou, F. Grisch, L. Bouheraoua, H. Verdier, and S. Richard (2017). Experimental investigation with optical diagnostics of a lean-premixed aero-engine injection system under relevant operating conditions. In *ASME Turbo Expo 2017*. American Society of Mechanical Engineers. *(p. 186, 187, 189)*

Marinov, N. M., W. J. Pitz, C. K. Westbrook, A. M. Vincitore, M. J. Castaldi, S. M. Senkan, and C. F. Melius (1998). Aromatic and polycyclic aromatic hydrocarbon formation in a laminar premixed n-butane flame. *Combustion and Flame 114*(1), 192–213. *(p. 41)*

Martin, C.-E. (2005). *Etude énergétique des instabilités thermo-acoustiques et optimisation génétique des cinétiques réduites*. Ph. D. thesis, Institut National Polytechnique de Toulouse. *(p. 52, 54, 67, 79, 218)*

Mason, E. and S. Saxena (1958). Approximate formula for the thermal conductivity of gas mixtures. *The Physics of Fluids 1*(5), 361–369. *(p. 18)*

Masri, A. (2015). Partial premixing and stratification in turbulent flames. *Proceedings of the Combustion institute 35*(2), 1115–1136. *(p. 31)*

Maxey, M. R. and J. J. Riley (1983). Equation of motion for a small rigid sphere in a nonuniform flow. *The Physics of Fluids 26*(4), 883–889. *(p. 174)*

McBride, B. J., S. Gordon, and M. A. Reno (1993). Coefficients for calculating thermodynamic and transport properties of individual species. *(p. 71)*

Meares, S. and A. R. Masri (2014). A modified piloted burner for stabilizing turbulent flames of inhomogeneous mixtures. *Combustion and Flame 161*(2), 484 – 495. *(p. 31)*

Mehl, C. (2018). *Large Eddy Simulations and complex chemistry for modeling*

the chemical structure of turbulent flames. Ph. D. thesis, Paris Saclay. *(p. 151, 166, 167, 215)*

Meier, W., P. Weigand, X. R. Duan, and R. Giezendanner-Thoben (2007). Detailed characterization of the dynamics of thermoacoustic pulsations in a lean premixed swirl flame. *Combustion and Flame 150*(1), 2–26. *(p. 9, 140, 142, 143)*

Menon, S. and W. H. Calhoon Jr (1996). Subgrid mixing and molecular transport modeling in a reacting shear layer. In *Symposium (International) on Combustion*, Volume 26, pp. 59–66. Elsevier. *(p. 130)*

Mercier, R. (2015). *Turbulent combustion modeling for Large Eddy Simulation of non-adiabatic stratified flames*. Ph. D. thesis, Ecole Centrale Paris. *(p. 126, 158)*

Mercier, R., P. Auzillon, V. Moureau, N. Darabiha, O. Gicquel, D. Veynante, and B. Fiorina (2014). LES modeling of the impact of heat losses and differential diffusion on turbulent stratified flame propagation: application to the TU darmstadt stratified flame. *Flow, Turbulence and Combustion 93*(2), 349–381. *(p. 55, 88)*

Mercier, R., C. Mehl, V. Moureau, and B. Fiorina (2019). Filtered wrinkled flamelets model for large eddy simulation of turbulent premixed combustion. *Combustion and Flame 205*, 93–108. *(p. 167)*

Mercier, R., V. Moureau, D. Veynante, and B. Fiorina (2015b). LES of turbulent combustion: on the consistency between flame and flow filter scales. *Proceedings of the Combustion Institute 35*(2), 1359–1366. *(p. 141, 143)*

Mercier, R., T. Schmitt, D. Veynante, and B. Fiorina (2015a). The influence of combustion SGS sub-models on the resolved flame propagation. application to the LES of the Cambridge stratified flames. *Proceedings of the Combustion Institute 35*(2), 1259–1267. *(p. 140, 156, 157, 159, 167)*

Michalewicz, Z. (2013). *Genetic algorithms+ data structures= evolution programs*. Springer. *(p. 218)*

Miguel-Brebion, M., D. Mejia, P. Xavier, F. Duchaine, B. Bédat, L. Selle, and T. Poinsot (2016). Joint experimental and numerical study of the influence of flame holder temperature on the stabilization of a laminar methane flame on a cylinder. *Combustion and Flame 172*, 153–161. *(p. 51)*

Mizobuchi, Y., J. Shinjo, S. Ogawa, and T. Takeno (2005). A numerical study on the formation of diffusion flame islands in a turbulent hydrogen jet lifted flame. *Proceedings of the Combustion Institute 30*(1), 611–619. *(p. 36)*

Moin, P., K. Squires, W. Cabot, and S. Lee (1991). A dynamic subgrid-scale model for compressible turbulence and scalar transport. *Physics of Fluids A: Fluid Dynamics 3*(11), 2746–2757. *(p. 129)*

Monchick, L. and E. Mason (1961). Transport properties of polar gases. *The Journal of Chemical Physics 35*(5), 1676–1697. *(p. 19)*

Mongia, H. (2010). On initiating 3rd generation of correlations for gaseous

emissions of aero-propulsion engines. In *48th AIAA Aerospace Sciences Meeting Including the New Horizons Forum and Aerospace Exposition*, Volume 1529, pp. 4–7. *(p. 3)*

Montgomery, C. J., C. Yang, A. R. Parkinson, and J.-Y. Chen (2006). Selecting the optimum quasi-steady-state species for reduced chemical kinetic mechanisms using a genetic algorithm. *Combustion and Flame 144*(1), 37–52. *(p. 49, 50)*

Moureau, V., P. Domingo, and L. Vervisch (2011a). Design of a massively parallel CFD code for complex geometries. *Comptes Rendus Mécanique 339*(2-3), 141 – 148. *(p. 110, 153, 157)*

Moureau, V., P. Domingo, and L. Vervisch (2011b). From large-eddy simulation to direct numerical simulation of a lean premixed swirl flame: Filtered laminar flame-PDF modeling. *Combustion and Flame 158*(7), 1340–1357. *(p. 141)*

Moureau, V., P. Minot, H. Pitsch, and C. Bérat (2007). A ghost-fluid method for large-eddy simulations of premixed combustion in complex geometries. *Journal of Computational Physics 221*(2), 600–614. *(p. 141, 143)*

Mueller, M. E. and H. Pitsch (2012). A methodology for soot prediction including thermal radiation in complex industrial burners. *Combustion and Flame 159*(6), 2166–2180. *(p. 55)*

Nambully, S., P. Domingo, V. Moureau, and L. Vervisch (2014a, 1). A filtered-laminar-flame PDF sub-grid scale closure for LES of premixed turbulent flames. part I: Formalism and application to a bluff-body burner with differential diffusion. *Combustion and Flame 161*(7), 1756–1774. *(p. 88, 140, 158, 167)*

Nambully, S., P. Domingo, V. Moureau, and L. Vervisch (2014b, 2). A filtered-laminar-flame PDF sub-grid-scale closure for LES of premixed turbulent flames. part II: Application to a stratified bluff-body burner. *Combustion and Flame 161*(7), 1775–1791. *(p. 156)*

Nguyen, P.-D., L. Vervisch, V. Subramanian, and P. Domingo (2010). Multidimensional flamelet-generated manifolds for partially premixed combustion. *Combustion and Flame 157*(1), 43–61. *(p. 56)*

Nicoud, F., H. Baya Toda, O. Cabrit, S. Bose, and J. Lee (2011). Using singular values to build a subgrid-scale model for large eddy simulations. *Physics of Fluids 23*(8), 085106. *(p. 128, 157, 190)*

Nicoud, F. and F. Ducros (1999). Subgrid-scale stress modelling based on the square of the velocity gradient tensor. *Flow, Turbulence and Combustion 62*(3), 183–200. *(p. 128, 144)*

Niu, Y.-S., L. Vervisch, and P. D. Tao (2013). An optimization-based approach to detailed chemistry tabulation: Automated progress variable definition. *Combustion and Flame 160*(4), 776–785. *(p. 56)*

Paulhiac, D. (2015). *Modélisation de la combustion d'un spray dans un brûleur aéronautique*. Ph. D. thesis, Institut National Polytechnique de Toulouse. *(p. 53)*

Pecquery, F., V. Moureau, G. Lartigue, L. Vervisch, and A. Roux (2014). Modelling nitrogen oxide emissions in turbulent flames with air dilution: Application to LES of a non-premixed jet-flame. *Combustion and Flame 161*(2), 496–509. *(p. 56, 57)*

Penner, J. E., D. H. Lister, D. J. Griggs, D. J. Dokken, and M. McFarland (1999). Aviation and the global atmosphere: A special report of IPCC working groups I and III, Intergovernmental panel on climate change. *(p. 2)*

Pepiot, P. (2008). *Automatic strategies to model transportation fuel surrogates*. Ph. D. thesis, Stanford University. *(p. 45, 48, 52, 105)*

Pepiot, P. and H. Pitsch (2005). Systematic reduction of large chemical mechanisms. In *4th Joint Meeting of the US Sections of the Combustion Institute*, Volume 2123, pp. 2005. Drexel University Pittsburgh, PA, USA. *(p. 45)*

Pepiot-Desjardins, P. and H. Pitsch (2008). An efficient error-propagation-based reduction method for large chemical kinetic mechanisms. *Combustion and Flame 154*(1), 67–81. *(p. 7, 45, 47)*

Perry, B. A., M. E. Mueller, and A. R. Masri (2017). A two mixture fraction flamelet model for large eddy simulation of turbulent flames with inhomogeneous inlets. *Proceedings of the Combustion Institute 36*(2), 1767–1775. *(p. 55)*

Peters, N. (1984). Laminar diffusion flamelet models in non-premixed turbulent combustion. *Progress in Energy and Combustion Science 10*(3), 319–339. *(p. 6, 55, 229)*

Pierce, C. D. and P. Moin (2004). Progress-variable approach for large-eddy simulation of non-premixed turbulent combustion. *Journal of Fluid Mechanics 504*, 73–97. *(p. 6, 55, 229)*

Pitsch, H. (2006). Large-eddy simulation of turbulent combustion. *Annual Review of Fluid Mechanics 38*, 453–482. *(p. 127)*

Pitsch, H. and L. Duchamp De Lageneste (2002). Large-eddy simulation of premixed turbulent combustion using a level-set approach. *Proceedings of the Combustion Institute 29*(2), 2001–2008. *(p. 132)*

Pitsch, H. and M. Ihme (2005). An unsteady/flamelet progress variable method for LES of nonpremixed turbulent combustion. In *43rd AIAA Aerospace Sciences Meeting and Exhibit*, pp. 557. *(p. 55)*

Pitsch, H. and N. Peters (1998). A consistent flamelet formulation for non-premixed combustion considering differential diffusion effects. *Combustion and Flame 114*(1-2), 26–40. *(p. 29)*

Poinsot, T. and D. Veynante (2012). *Theoretical and numerical combustion*. Third Edition by T. Poinsot. *(p. 18, 127, 128, 130)*

Polifke, W., W. Geng, and K. Döbeling (1998). Optimization of rate coefficients for simplified reaction mechanisms with genetic algorithms. *Combustion and Flame 113*(1-2), 119 – 134. *(p. 53, 54, 65, 67)*

Pope, S. (1994). Lagrangian PDF methods for turbulent flows. *Annual review*

of fluid mechanics 26(1), 23–63. *(p. 131)*

Pope, S. B. (2000). *Turbulent flows*. Cambridge University Press. *(p. 126, 127)*

Proch, F., P. Domingo, L. Vervisch, and A. M. Kempf (2017). Flame resolved simulation of a turbulent premixed bluff-body burner experiment. Part I: Analysis of the reaction zone dynamics with tabulated chemistry. *Combustion and Flame 180*, 321–339. *(p. 140)*

Proch, F. and A. M. Kempf (2014). Numerical analysis of the cambridge stratified flame series using artificial thickened flame LES with tabulated premixed flame chemistry. *Combustion and Flame 161*(10), 2627–2646. *(p. 133, 140, 156, 161)*

Proch, F., M. Pettit, T. Ma, M. Rieth, and A. Kempf (2013). Investigations on the effect of different subgrid models on the quality of LES results. In *Workshop on Direct and Large-Eddy Simulation 9*. *(p. 157)*

Ragucci, R., A. Bellofiore, and A. Cavaliere (2007). Trajectory and momentum coherence breakdown of a liquid jet in high-density air cross-flow. *Atomization and Sprays 17*(1), 1–24. *(p. 193)*

Ranz, W. and W. Marshall (1952). Evaporation from drops. *Chemical Engineering Progress 48*(3), 141–146. *(p. 178, 179)*

Ranzi, E., A. Frassoldati, R. Grana, A. Cuoci, T. Faravelli, A. Kelley, and C. Law (2012). Hierarchical and comparative kinetic modeling of laminar flame speeds of hydrocarbon and oxygenated fuels. *Progress in Energy and Combustion Science 38*(4), 468–501. *(p. 86)*

Reveillon, J. and L. Vervisch (2005). Analysis of weakly turbulent dilute-spray flames and spray combustion regimes. *Journal of Fluid Mechanics 537*, 317–347. *(p. 186)*

Ribert, G., O. Gicquel, N. Darabiha, and D. Veynante (2006). Tabulation of complex chemistry based on self-similar behavior of laminar premixed flames. *Combustion and Flame 146*(4), 649–664. *(p. 56)*

Ribert, G., L. Vervisch, P. Domingo, and Y.-S. Niu (2014). Hybrid transported-tabulated strategy to downsize detailed chemistry for numerical simulation of premixed flames. *Flow, Turbulence and Combustion 92*(1-2), 175–200. *(p. 57, 58)*

Richard, S. (2015). Lecture notes in combustion technology for future aero gas turbines and requirements on design tools. In *Von Karman Institute Lecture Series*. *(p. 5)*

Richard, S., O. Colin, O. Vermorel, A. Benkenida, C. Angelberger, and D. Veynante (2007). Towards large eddy simulation of combustion in spark ignition engines. *Proceedings of the Combustion Institute 31*(2), 3059–3066. *(p. 132)*

Rosenberg, D. A., P. M. Allison, and J. F. Driscoll (2015). Flame index and its statistical properties measured to understand partially premixed turbulent combustion. *Combustion and Flame 162*(7), 2808–2822. *(p. 31)*

Roux, S., G. Lartigue, T. Poinsot, U. Meier, and C. Bérat (2005). Studies of

mean and unsteady flow in a swirled combustor using experiments, acoustic analysis, and large eddy simulations. *Combustion and Flame 141*(1-2), 40–54. *(p. 140, 143)*

Sagaut, P. (2006). *Large eddy simulation for incompressible flows: an introduction*. Springer-Verlag Berlin and Heidelberg. *(p. 129)*

Saggese, C., S. Ferrario, J. Camacho, A. Cuoci, A. Frassoldati, E. Ranzi, H. Wang, and T. Faravelli (2015). Kinetic modeling of particle size distribution of soot in a premixed burner-stabilized stagnation ethylene flame. *Combustion and Flame 162*(9), 3356–3369. *(p. 225)*

Salaün, E., P. Malbois, A. Vandel, G. Godard, F. Grisch, B. Renou, G. Cabot, and A. Boukhalfa (2016). Experimental investigation of a spray swirled flame in gas turbine model combustor. In *18th International Symposium on the Application of Laser and Imaging Techniques to Fluid Mechanics, Lisbon, Portugal*. *(p. 10, 186)*

Sánchez, A., A. Lépinette, M. Bollig, A. Liñán, and B. Lázaro (2000). The reduced kinetic description of lean premixed combustion. *Combustion and Flame 123*(4), 436–464. *(p. 86)*

Sanjosé, M. (2009). *Evaluation de la méthode Euler-Euler pour la simulation aux grandes échelles des chambres à carburant liquide*. Ph. D. thesis, Institut National Polytechnique de Toulouse. *(p. 180, 181)*

Sankaran, R., E. R. Hawkes, J. H. Chen, T. Lu, and C. K. Law (2007). Structure of a spatially developing turbulent lean methane–air bunsen flame. *Proceedings of the Combustion Institute 31*(1), 1291–1298. *(p. 51, 154)*

Sazhin, S. (2014). *Droplets and sprays*, Volume 345. Springer. *(p. 176)*

Schiller, L. and A. Nauman (1935). A drag coefficient correlation. *VDI Zeitung 77*, 318–320. *(p. 176)*

Schönfeld, T. and M. Rudgyard (1999). Steady and unsteady flow simulations using the hybrid flow solver AVBP. *AIAA journal 37*(11), 1378–1385. *(p. 8, 32, 144, 190)*

Shashank, E. K. and H. Pitsch (2011). Spray evaporation model sensitivities. In *Annual Research Briefs of the CTR*, pp. 213–224. Center for Turbulence Research, NASA Ames/Stanford Univ. *(p. 180)*

Sierra, P. (2012). *Modeling the dispersion and evaporation of sprays in aeronautical combustion chambers*. Ph. D. thesis, Institut National Polytechnique de Toulouse. *(p. 180, 181, 182)*

Sikalo, N., O. Hasemann, C. Schulz, A. Kempf, and I. Wlokas (2014). A genetic algorithm-based method for the automatic reduction of reaction mechanisms. *International Journal of Chemical Kinetics 46*(1), 41–59. *(p. 46)*

Sirignano, W. A. (2010). *Fluid dynamics and transport of droplets and sprays*. Cambridge University Press. *(p. 176)*

Smagorinsky, J. (1963). General circulation experiments with the primitive equations: I. the basic experiment. *Monthly weather review 91*(3), 99–

164. *(p. 128)*

Smith, G. P., D. M. Golden, M. Frenklach, B. Eiteener, M. Goldenberg, C. T. Bowman, R. K. Hanson, W. C. Gardiner, V. V. Lissianski, and Z. W. Qin (2011). Gri-mech 3.0. *(p. 74, 86, 87)*

Spalding, D. B. (1953). The combustion of liquid fuels. *Symposium (international) on combustion 4*(1), 847–864. *(p. 176)*

Stagni, A., A. Cuoci, A. Frassoldati, T. Faravelli, and E. Ranzi (2013). Lumping and reduction of detailed kinetic schemes: an effective coupling. *Industrial & Engineering Chemistry Research 53*(22), 9004–9016. *(p. 225)*

Sutherland, W. (1893). The viscosity of gases and molecular force. *The London, Edinburgh, and Dublin Philosophical Magazine and Journal of Science 36*(223), 507–531. *(p. 19)*

Sweeney, M. S., S. Hochgreb, and R. S. Barlow (2011b). The structure of premixed and stratified low turbulence flames. *Combustion and Flame 158*(5), 935 – 948. *(p. 140)*

Sweeney, M. S., S. Hochgreb, M. J. Dunn, and R. S. Barlow (2011a). A comparative analysis of flame surface density metrics in premixed and stratified flames. *Proceedings of the Combustion Institute 33*(1), 1419–1427. *(p. 9, 140, 156, 157)*

Sweeney, M. S., S. Hochgreb, M. J. Dunn, and R. S. Barlow (2012a). The structure of turbulent stratified and premixed methane/air flames I: Non-swirling flows. *Combustion and Flame 159*(9), 2896–2911. *(p. 78, 156, 157)*

Sweeney, M. S., S. Hochgreb, M. J. Dunn, and R. S. Barlow (2012b). The structure of turbulent stratified and premixed methane/air flames II: Swirling flows. *Combustion and Flame 159*(9), 2912 – 2929. *(p. 157)*

Sweeney, M. S., S. Hochgreb, M. J. Dunn, and R. S. Barlow (2013). Multiply conditioned analyses of stratification in highly swirling methane/air flames. *Combustion and Flame 160*(2), 322 – 334. *(p. 140, 157, 164)*

Syred, N. (2006). A review of oscillation mechanisms and the role of the precessing vortex core (pvc) in swirl combustion systems. *Progress in Energy and Combustion Science 32*(2), 93–161. *(p. 198, 199)*

TNF Workshops (2016-2018). International workshop on measurement and computation of turbulent (non)premixed flames. `https://public.ca.sandia.gov/TNF/abstract.html`. *(p. 31)*

Tomlin, A. S., M. J. Pilling, T. Turányi, J. H. Merkin, and J. Brindley (1992). Mechanism reduction for the oscillatory oxidation of hydrogen: sensitivity and quasi-steady-state analyses. *Combustion and Flame 91*(2), 107–130. *(p. 43)*

Tomlin, A. S., T. Turányi, and M. J. Pilling (1997). Mathematical tools for the construction, investigation and reduction of combustion mechanisms. *Comprehensive Chemical Kinetics 35*, 293–437. *(p. 43)*

Turányi, T. (1990). Reduction of large reaction mechanisms. *New Journal of chemistry 14*(11), 795–803. *(p. 42, 43)*

Turányi, T. and T. Bérces (1990). Kinetics of reactions occurring in the unpolluted troposphere, II. sensitivity analysis. *Reaction Kinetics and Catalysis Letters 41*(1), 103–108. *(p. 45)*

United Stated Environmental Protection Agency, U. (2018). Air topics. https://www.epa.gov/environmental-topics/air-topics. *(p. 2)*

Vagelopoulos, C. M. and F. N. Egolfopoulos (1998). Direct experimental determination of laminar flame speeds. In *Symposium (international) on combustion*, Volume 27, pp. 513–519. Elsevier. *(p. 86)*

Vajda, S., P. Valko, and T. Turányi (1985). Principal component analysis of kinetic models. *International Journal of Chemical Kinetics 17*(1), 55–81. *(p. 7, 46)*

Valiño, L. (1998). A field Monte Carlo formulation for calculating the probability density function of a single scalar in a turbulent flow. *Flow, Turbulence and Combustion 60*(2), 157–172. *(p. 131)*

Van Oijen, J., F. Lammers, and L. De Goey (2001). Modeling of complex premixed burner systems by using flamelet-generated manifolds. *Combustion and Flame 127*(3), 2124–2134. *(p. 6, 55, 229)*

Veynante, D. and V. Moureau (2015). Analysis of dynamic models for large eddy simulations of turbulent premixed combustion. *Combustion and Flame 162*(12), 4622–4642. *(p. 132)*

Veynante, D. and L. Vervisch (2002). Turbulent combustion modeling. *Progress in Energy and Combustion Science 28*(3), 193–266. *(p. 130)*

Vié, A., B. Franzelli, Y. Gao, T. Lu, H. Wang, and M. Ihme (2015). Analysis of segregation and bifurcation in turbulent spray flames: A 3D counterflow configuration. *Proceedings of the Combustion Institute 35*(2), 1675–1683. *(p. 21, 51)*

Vié, A., F. Laurent, and M. Massot (2013). Size-velocity correlations in hybrid high order moment/multi-fluid methods for polydisperse evaporating sprays: Modeling and numerical issues. *Journal of Computational Physics 237*, 177–210. *(p. 173)*

Violi, A., S. Yan, E. Eddings, A. Sarofim, S. Granata, T. Faravelli, and E. Ranzi (2002). Experimental formulation and kinetic model for jp-8 surrogate mixtures. *Combustion Science and Technology 174*(11-12), 399–417. *(p. 114)*

Vlachos, D. (1996). Reduction of detailed kinetic mechanisms for ignition and extinction of premixed hydrogen/air flames. *Chemical Engineering Science 51*(16), 3979–3993. *(p. 46)*

Volpiani, P. S., T. Schmitt, and D. Veynante (2017). Large eddy simulation of a turbulent swirling premixed flame coupling the TFLES model with a dynamic wrinkling formulation. *Combustion and Flame 180*, 124–135. *(p. 54, 141, 146, 151)*

Wang, G., M. Boileau, and D. Veynante (2011). Implementation of a dynamic thickened flame model for large eddy simulations of turbulent premixed combustion. *Combustion and Flame 158*(11), 2199–2213. *(p. 144)*

Wang, H., E. Dames, B. Sirjean, D. Sheen, R. Tangko, A. Violi, J. Lai, F. Egolfopoulos, D. Davidson, R. Hanson, et al. (2010). A high-temperature chemical kinetic model of n-alkane (up to n-dodecane), cyclohexane, and methyl-, ethyl-, n-propyl and n-butyl-cyclohexane oxidation at high temperatures. *JetSurF version 2*, 19. *(p. 41)*

Wang, H., X. You, A. V. Joshi, S. G. Davis, A. Laskin, F. Egolfopoulos, and C. K. Law (2007). USC Mech Version II. High-temperature combustion reaction model of H2/CO/C1-C4 compounds. *(p. 41, 225)*

Wang, P., N. Platova, J. Fröhlich, and U. Maas (2014). Large eddy simulation of the PRECCINSTA burner. *International Journal of Heat and Mass Transfer 70*, 486–495. *(p. 141)*

Warnatz, J. (1981). The structure of laminar alkane-, alkene-, and acetylene flames. *Symposium (International) on Combustion 18*(1), 369–384. *(p. 24)*

Weigand, P., X. Duan, W. Meier, U. Meier, M. Aigner, and C. Bérat (2005). Experimental investigations of an oscillating lean premixed CH_4/air swirl flame in a gas turbine model combustor. In *Proceedings of the European Combustion Meeting 2005*, pp. 235. *(p. 140)*

Weigand, P., W. Meier, X. Duan, and M. Aigner (2007). Laser-based investigations of thermoacoustic instabilities in a lean premixed gas turbine model combustor. *Journal of Engineering for Gas Turbines and power 129*(3), 664–671. *(p. 140)*

Westbrook, C. K. and F. L. Dryer (1981). Simplified reaction mechanisms for the oxidation of hydrocarbon fuels in flames. *Combustion Science and Technology 27*(1-2), 31–43. *(p. 6, 52, 53, 62, 86, 229)*

Wilke, C. (1950). A viscosity equation for gas mixtures. *The Journal of Chemical Physics 18*(4), 517–519. *(p. 18)*

Williams, F. (1985). *Combustion theory*. Benjamin/Cummings Publishing Company, Inc. *(p. 131)*

Wright, A. H. (1991). Genetic algorithms for real parameter optimization. In *Foundations of Genetic Algorithms*, Volume 1, pp. 205–218. Elsevier. *(p. 217)*

Wu, H. and M. Ihme (2016). Compliance of combustion models for turbulent reacting flow simulations. *Fuel 186*, 853–863. *(p. 36)*

Xuan, Y., G. Blanquart, and M. E. Mueller (2014). Modeling curvature effects in diffusion flames using a laminar flamelet model. *Combustion and Flame 161*(5), 1294–1309. *(p. 29)*

Yamashita, H., M. Shimada, and T. Takeno (1996). A numerical study on flame stability at the transition point of jet diffusion flames. *Proceedings of the Combustion Institute 26*(1), 27–34. *(p. 36)*

Yao, G., S. Abdel-Khalik, and S. Ghiaasiaan (2003). An investigation of simple evaporation models used in spray simulations. *Journal of Heat Transfer 125*(1), 179–182. *(p. 176)*

Yoo, C. S., T. Lu, J. H. Chen, and C. K. Law (2011). Direct numerical

simulations of ignition of a lean n-heptane/air mixture with temperature inhomogeneities at constant volume: Parametric study. *Combustion and Flame 158*(9), 1727 – 1741. *(p. 51)*

Yoon, S., J. Hewson, P. DesJardin, D. Glaze, A. Black, and R. Skaggs (2004). Numerical modeling and experimental measurements of a high speed solid-cone water spray for use in fire suppression applications. *International Journal of Multiphase Flow 30*(11), 1369–1388. *(p. 194)*

Yu, C.-L., C. Wang, and M. Frenklach (1995). Chemical kinetics of methyl oxidation by molecular oxygen. *The Journal of Physical Chemistry 99*(39), 14377–14387. *(p. 86)*

Zambon, A. and H. Chelliah (2007). Explicit reduced reaction models for ignition, flame propagation, and extinction of $C_2H_4/CH_4/H_2$ and air systems. *Combustion and Flame 150*(1), 71–91. *(p. 49)*

Zheng, X., T. Lu, and C. Law (2007). Experimental counterflow ignition temperatures and reaction mechanisms of 1,3-butadiene. *Proceedings of the Combustion Institute 31*(1), 367 – 375. *(p. 45)*

Zhou, R., S. Balusamy, M. S. Sweeney, R. S. Barlow, and S. Hochgreb (2013). Flow field measurements of a series of turbulent premixed and stratified methane/air flames. *Combustion and Flame 160*(10), 2017–2028. *(p. 140, 156)*

université PARIS-SACLAY
ÉCOLE DOCTORALE
Sciences mécaniques et énergétiques, matériaux et géosciences (SMEMAG)

Titre : Mécanismes chimiques virtuels optimisés pour la prédiction des polluants dans des flammes turbulentes

Mots clés : Structure de flamme, Prédiction des polluants, Combustion turbulente, Simulation aux Grandes Echelles, Chimie virtuelle optimisée.

Résumé : La nature conflictuelle des contraintes de performances, d'opérabilité et de respect des normes environnementales conduit les motoristes à optimiser finement la géométrie du brûleur afin d'identifier le meilleur design. La Simulation aux Grande Echelles (SGE) est aujourd'hui un outil performant et est déployé de manière courante dans les Bureaux d'Etudes pour la prédiction des propriétés macroscopiques de l'écoulement. Toutefois, de nombreux phénomènes influencés par les effets de chimie complexe, tels que la stabilisation, l'extinction de flamme et la formation des polluants, reste un problème crucial. En effet, la description des effets de chimie complexe nécessite l'utilisation de modèles cinétiques détaillés imposant des coûts de calculs prohibitifs, des problèmes de raideurs numérique et des difficultés de couplage avec les échelles non résolues turbulentes.

Afin d'inclure une description des processus chimiques, dans les simulations numériques de chambres de combustion réelles, des modèles réduits doivent être proposés. Dans cette thèse, une méthode originale, appelée chimie virtuelle optimisée, est développée. Cette stratégie a pour objectif la description de la structure chimique de la flamme et la formation des polluants dans des configurations de flamme représentatives. Les schémas cinétiques virtuels optimisés, composés de réactions virtuelles et d'espèces virtuelles, sont construits par optimisation des paramètres réactionnels et des propriétés thermochimiques des espèces virtuelles afin de capturer les propriétés de flamme d'intérêt.

Title : Virtual chemical mechanisms optimized to capture pollutant formation in turbulent flames

Keywords : Chemical flame structure, Pollutant formation, Turbulent combustion, Large-Eddy Simulation, Virtual optimized chemistry.

Abstract : The conflicting nature of performance, operability and environmental constraints leads engine manufacturers to perform a fine optimization of the burner geometry to find the best design compromise. Large Eddy Simulation (LES) is an attractive tool to achieve this challenging task, and is routinely used in design office to capture macroscopic flow features. However, the prediction of phenomena influenced by complex kinetic effects, such as flame stabilization, extinction and pollutant formation, is still a crucial issue. Indeed, the comprehensive description of combustion chemistry effects requires the use of detailed models imposing prohibitive computational costs, numerical stiffness and difficulties related to model the coupling with unresolved turbulent scales.

Reduced-cost chemistry description strategies must then be proposed to account for kinetic effects in LES of real combustion chambers. In this thesis an original modeling approach, called virtual optimized chemistry, is developed. This strategy aims at describing the chemical flame structure and pollutant formation in relevant flame configurations, at a low computational cost. Virtual optimized kinetic schemes, composed by virtual reactions and virtual species, are built through optimization of both kinetic rate parameters and virtual species thermo-chemical properties so as to capture reference target flame quantity.

Université Paris-Saclay
Espace Technologique / Immeuble Discovery
Route de l'Orme aux Merisiers RD 128 / 91190 Saint-Aubin, France